Emergence of modular and long-range correlated activity in the developing neocortex

Dissertation

zur Erlangung des Doktorgrades
der Naturwissenschaften

vorgelegt beim Fachbereich 13 - Physik
der Johann Wolfgang Goethe - Universität
in Frankfurt am Main
von

Bettina Hein
aus Schweinfurt

Frankfurt (2019)
(D 30)

Vom Fachbereich Physik der
Johann Wolfgang Goethe - Universität als Dissertation angenommen.

Dekan:

- Prof. Dr. Michael Lang
  Physikalisches Institut

Gutachter:

- Prof. Dr. Matthias Kaschube
  Frankfurt Institute for Advanced Studies
- Prof. Dr. Jochen Triesch
  Frankfurt Institute for Advanced Studies

Datum der Disputation:

Affidavit

I hereby declare that this dissertation entitled "Emergence of modular and long-range correlated activity in the developing neocortex" has been written independently and with no other sources and aids than quoted.

Bettina Hein, Frankfurt, August 28, 2019

Contents

German summary

In vielen physikalischen Systemen entwickelt sich ausgehend von einem ungeordnetem Zustand mittels einer lokalen Wechselwirkung zwischen einzelnen Systemkomponenten eine interne Ordnung. Dieses Prinzip der *Selbstorganisation* benötigt keine externen steuernden Impulse, und ist oft robust gegenüber Änderungen oder Störungen im System. Daher ist Selbstorganisation ein eleganter Mechanismus, um mit einfachen Regeln Ordnung in einem komplexen System entstehen zu lassen.
Eines der komplexesten Systeme in unserer Umwelt ist das Gehirn. Es besteht aus hierarchisch angeordneten kortikalen Arealen, welche sensorische Information verarbeiten und diese in bestimmtes Verhalten übersetzen. Ein kortikales Areal besteht aus bis zu 100 Millionen neuronaler Zellen, die mittels eines komplexen Netzwerkes miteinander verknüpft sind. Interessanterweise weist kortikale Aktivität in verschiedenen Gehirnarealen und Spezies oft zwei grundlegende Merkmale auf. Erstens, bildet kortikale Aktivität Muster bestehend aus aktiven Domänen mit einer typischen räumlichen Skala von 1 mm[164,43,45,331,154,285,48,231,389]. Wie die Ergebnisse dieser Arbeit zeigen, bleibt diese räumliche Modulation der kortikalen Aktivität auch dann bestehen, wenn sich das Gehirn in unterschiedlichen Zuständen befindet (anästhesiert und wach[389]), ist schon früh in der kortikalen Entwicklung zu beobachten und ist in spontaner[389] wie in sensorisch evozierter[231] Aktivität zu finden. Dies impliziert, dass diese beobachtete domänenartige Struktur eine grundlegende Eigenschaft kortikaler Netzwerkaktivität ist. Jedoch fehlt bislang ein biologisch plausibler Mechanismus, der die Bildung modular Aktivität beschreibt.
Zweitens sind Domänen, die mehrere Millimeter voneinander entfernt sind, in ihrer Aktivität miteinander korreliert. Diese langreichweitige Korrelation erstreckt sich über mehrere Millimeter, sowohl bei spontaner[389] als auch bei visuell evozierter Aktivität[231]. Im reifen Kortex lässt sich diese langreichweitige Korrelationsstruktur durch langreichweitige laterale Verschaltungen erklären. Jedoch zeigen meine Analysen in dieser Arbeit, dass schon der unreife Kortex, der noch keine langreichweitigen Verschaltungen besitzt, eine Korrelationsstruktur mit gleicher Reichweite aufweist. Dies motiviert die Frage, wie sich eine solche Korrelationsstruktur nur mit Hilfe lokaler Wechselwirkungen bilden kann. Eine mögliche Erklärung ist, dass modulare und langreichweitig korrelierte Aktivität mittels eines intrakortikalen Mechanismus entstehen. Dies ist konsistent mit der Idee der Selbstorganisation und bildet den Kern der vorliegenden Arbeit.
Ein zentrales Problem in Computational Neuroscience ist zu verstehen, wie neuronale Aktivität in kortikalen Netzwerken gebildet wird. Ein tieferes Verständnis wie die Aktivität zwischen Netzwerkeinheiten wechselwirkt, könnte beispielsweise beleuchten wie Information von der Außenwelt in der Form von neuronaler Aktivität zwischen Gehirnarealen übermittelt wird. Eine direkte Anwendung dieser Einsicht könnte darin liegen Behandlungsansätze für neurologische Krankheiten, die zu Abweichungen in normaler Gehirnaktivität führen, zu stimulieren.
Jüngste Weiterentwicklungen experimenteller Methoden haben neue Möglichkeiten geschaffen

die Entwicklung der neuronalen Aktivität in kortikalen Schaltkreisen zu untersuchen. Hochempfindliche, genetisch codierte Kalziumindikatoren[81] ermöglichen die zuverlässige Abbildung evozierter und spontaner kortikaler Aktivität *in vivo* . Diese neue Familie von Kalziumindikatoren ermöglicht es, eine große Anzahl von Neuronen[390,388,375] chronisch über mehrere Wochen bis Monate[81,375,389] abzubilden. In Kombination mit dem Einsatz von Frettchen, die in einem relativ frühen Stadium ihrer Entwicklung geboren werden[267], eignen sich diese Kalziumindikatoren gut, um die frühe kortikale Entwicklung der neuronalen Aktivität zu erfassen. Die Möglichkeit die Aktivität einer Vielzahl von Neuronen gleichzeitig aufzunehmen, erfordert in der vorliegenden Arbeit die Entwicklung neuer Analyse- und Modellierungsmethoden. Zusammen mit den neuartigen experimentellen Techniken, könnten diese analytischen Instrumente es ermöglichen, die Prinzipien aufzuklären, die der Entstehung und Reifung der kortikalen Aktivität zugrunde liegen.
Um die Entwicklung der kortikalen Aktivität zu untersuchen, ist der visuelle Kortex von Säugetieren ein besonders gut geeignetes System. Dieses ist zuständig für die Verarbeitung visueller Informationen, die über die Retina in das Gehirn gelangen. Die funktionale Organisation im reifen visuellen Kortex wurde eingehend untersucht und charakterisiert. Im primären visuellen Kortex rufen orientierte kantenartige Reize starke neuronale Antworten hervor[196]. Diese kortikalen Antworten sind in Primaten und Fleischfressern räumlich moduliert[285,86,344,389]. Durch eine systematische Variation der Orientierung dieser visuellen Reize wird eine geordnete Karte bestehend aus Orientierungsdomänen sichtbar, die über die Oberfläche des Kortex verteilt sind[231]. Innerhalb einer Orientierungsdomäne antworten individuelle Neurone vorzugsweise auf die gleiche Orientierung. Diese Orientierungsdomänen bedecken quasi-periodisch mit einem typischen Abstand zueinander den gesamten primären visuellen Kortex. Diese globale Organisation von Orientierungsdomänen spiegelt die langreichweitige Korrelationsstruktur in der kortikalen Aktivität wider. So sind beispielsweise weit entfernte Neurone mit ähnlicher Orientierungspräferenz in ihrer evozierten Aktivität korreliert.
Im reifen Kortex fallen spontan koaktive Domänen häufig mit diesen funktionalen Domänen zusammen[344,235,327,389]. In einer früheren Arbeit wurde gezeigt, dass im reifen visuellen Kortex spontane Aktivitätsmuster zu einem gewissen Grad den Aktivitätsmustern ähneln, die durch visuelle Stimuli evoziert wurden[235,327]. Die Autoren[235] deuteten an, dass spontane und evozierte Aktivitätsmuster sich über einen großen kortikalen Bereich ähneln. Anschließende theoretische Arbeiten untersuchten, ob die Eigenschaften der spontanen Aktivität mit solch einer langreichweitigen Ähnlichkeit vereinbar sind, führten jedoch zu keinem schlüssigen Ergebnis[159]. Darüberhinaus bleibt es unklar, bis zu welcher feinen räumlichen Skala die Ähnlichkeit zwischen spontaner und evozierter Aktivität besteht.
Eine große Anzahl an theoretischen und experimentellen Arbeiten hat Aufschluss darüber gegeben, wie kortikale Verschaltungen Aktivitätsmuster beeinflussen. Insbesondere wurde in vielen Studien untersucht, ob kortikale Aktivität eher durch Feed-Forward-Input oder durch intrakortikale Verschaltungen bestimmt ist. Theoretische Studien haben verschiedene Modelle betrachtet, um die Fähigkeit und den Umfang von Feed-Forward-Inputs und intrakortikalen Mechanismen bei der Gestaltung der räumlich-zeitlichen Eigenschaften der neuronalen Netzwerkaktivität zu untersuchen[218,224,241,420]. In ähnlicher Weise zielten experimentelle Arbeiten darauf ab, den Beitrag von Feed-Forward-Inputs im Vergleich zu intrakortikalen Verschaltungen bei der Gestaltung der Netzwerkaktivität zu analysieren[303,352,389]. Der Beitrag dieser verschiedenen Inputquellen zur Bildung der lokalen und ausgedehnten Organisation der kortikalen Aktivität ist jedoch nach wie vor unklar. Interessanterweise zeigen Experimente, die durch diese Arbeit motiviert und beschrieben wurden, dass die modulare und weitreichende korrelierte Organisation der spontanen kortikalen Aktivität nach Inaktivierung des vorgelagerten Hirnareals intakt bleibt[389]. Dieses Ergebnis deutet an, dass diese fundamentalen Eigenschaften dem Kortex nicht durch Feed-Forward-Inputs auferlegt werden.
Tatsächlich wurde in theoretischen Arbeiten umfangreich die Entstehung modularer Aktivität

basierend auf einem intrakortikalen Mechanismus im Rahmen dynamischer Netzwerkmodelle untersucht[287,411,28,226,71,44,163]. Ein solches neuronales Netzwerkmodell besteht aus einer Population von Neuronen, die über wiederkehrende Verbindungen miteinander wechselwirken. Typischerweise beruht der intrakortikale Mechanismus auf lokaler Förderung und lateraler Unterdrückung der Aktivität, was in einem breiteren Kontext als Turing-Mechanismus bezeichnet wird[430,152,296]. Eine einfache Möglichkeit diesen Mechanismus zu implementieren, besteht in einer speziellen rekurrenten Verschaltung, die aus lokaler Exzitation und lateraler Hemmung (manchmal als Mexican hat Profil bezeichnet) zusammengesetzt ist[287,411,28,71,44]. Die lokale Exzitation verstärkt lokal erhöhte Aktivitätsfluktuationen, während laterale Hemmung die räumliche Ausbreitung dieser erhöhten Aktivität verhindert. Auf diese Weise entstehen benachbarte aktive Domänen mit einem typischen Domänenabstand. Während es experimentelle Evidenz für diese Art von rekurrenter Verschaltung gibt, deuten andere Studien darauf hin, dass die laterale Reichweite inhibitorischer Verbindungen tendenziell kürzer ist als die der exzitatorischen Verbindungen[280,281,279,278,265].
Die Entstehung der langreichweitigen Korrelationsstruktur vor der vollständigen Entwicklung anatomischer langreichweitiger Verbindungen wird in der vorliegenden Arbeit beschrieben[389]. Aus diesem Grund liegen noch keine theoretische Arbeiten vor, die beschreiben, wie rein lokale Schaltkreise langreichweitig korrelierte Netzwerkaktivität erzeugen können.
In dieser Arbeit versuche ich die oben genannten Lücken zu füllen und untersuche die Entstehung von modularer und langreichweitig korrelierter spontaner Aktivität in kortikalen Netzwerken. Im Einzelnen addressiere ich die folgenden drei Fragen:

- Wie kann ein Netzwerk mit einer biologisch plausiblen Architektur modulare Aktivität erzeugen?
- Wie entsteht zu Beginn der Entwicklung eine weitreichende, langreichweitig korrelierte Netzwerkaktivität?
- In welcher Beziehung stehen die weitreichenden Netzwerke im ausgereiften visuellen Kortex zu seiner funktionalen Organisation?

Um diese Fragen zu beantworten, kombiniere ich mathematische Netzwerkanalyse und die Analyse experimenteller Daten von neuronaler Aktivität im sich entwickelnden Kortex. Die neuronalen Aktivitätsdaten wurden im Labor von David Fitzpatrick am Max Planck Florida Institute aufgenommen. Gordon B. Smith und David E. Whitney führten die Experimente unter der Betreuung von David Fitzpatrick durch. Um die Entstehung und Ausreifung der weitreichenden funktionalen kortikalen Netzwerke zu untersuchen, wurde ein experimenteller Aufbau benutzt, der die chronische Bildgebung von Populationsaktivität im visuellen Kortex von Frettchen *in vivo* ermöglicht. Mit Hilfe des hochsensitiven Kalziumindikator GCaMP6s konnte zuverlässig die spontane und visuell evozierte Aktivität in der kortikalen Schicht 2/3 aufgenommen werden. Frettchen erlauben, dank ihrer Geburt relativ früh in ihrer Entwicklung, kortikale Aktivität im reifenden Kortex zu erfassen. Motiviert durch die Ähnlichkeit zwischen spontaner und evozierter Aktivität im reifen Kortex, wird versucht mittels spontaner Aktivität, die schon während der frühen kortikalen Entwicklung zu beobachten ist bevor zuverlässige kortikale Antworten evoziert werden können, den Zustand von Netzwerkinteraktionen im unreifen Kortex zu ermitteln. Dies erlaubt es auch die kortikale Netzwerkaktivität zu untersuchen, ohne der Aktivität eine Struktur aufzuerlegen, die hauptsächlich durch Stimuli dominiert ist. Um die reife funktionale Organisation ausgedehnter Netzwerke im Kortex zu untersuchen, wird die Orientierungsselektivität aufgenommen.
In dieser Arbeit analysiere ich quantitativ die räumlich-zeitlichen Eigenschaften spontaner und visuell hervorgerufener neuronaler Aktivität während der frühen Entwicklung des Kortex. Basierend

auf dieser Quantifizierung entwickle ich dynamische und statistische Modelle, die mittels einfacher Mechanismen Schlüsseleigenschaften der beobachteten kortikalen Aktivität reproduzieren können.
Zuerst zeige ich, dass spontane Aktivität im reifen Kortex aus räumlich ausgedehnten und modularen Aktivitätsmustern besteht. Kortikale Elemente sind in ihrer spontanen Aktivität über mehrere Millimeter hinweg miteinander korreliert. Meine Analysen zeigen, dass diese langreichweitige Korrelationsstruktur dem Layout der Orientierungsdomänen über das komplette Sichtfeld bis hin zu räumlich feinen Strukturen sehr ähnlich ist. Diese hohe Ähnlichkeit unterstützt unsere Annahme spontane Aktivität stellvertretend für die Netzwerkinteraktionen zu verwenden. Mittels der langreichweitigen Korrelationsstruktur ist es sogar möglich die lokale funktionale Organisation über mehrere Millimeter hinweg genau vorhersagen. Selbst die feinsten topografischen Merkmale von Orientierungskarten - Frakturen oder Pinwheels - spiegeln sich genau in den langreichweitigen Netzwerkwechselwirkungen wider, die sich aus der korrelierten spontanen Aktivität ergeben. Diese Ergebnisse zeigen zusammen mit der Stabilität von Korrelationsmustern über Wach- und Narkosezustände hinweg einen außergewöhnlichen Grad an funktionaler Kohärenz in kortikalen Netzwerken.
Die Prinzipien, die der funktionalen Organisation und Entwicklung von weitreichenden Netzwerkinteraktionen im Neokortex zugrunde liegen, sind nach wie vor wenig verstanden. Zudem ist noch wenig über die räumlich-zeitliche Struktur spontaner Aktivität in der frühen Entwicklung bekannt. Diese Arbeit zeigt zum ersten Mal, dass es bereits im unreifen Kortex modulare Netzwerkkorrelationen gibt, die sich über Entfernungen erstrecken, die mit denen im reifen Kortex vergleichbar sind. Die Möglichkeit, dass derartige langreichweitige Korrelationen in diesem frühen Entwicklungsstadium vorliegen, wurde noch nicht in Betracht gezogen. Angesichts der starken Assoziation modularer Aktivitätsmuster mit der modularen Anordnung horizontaler, langreichweitiger Verbindungen im reifen Kortex[154,285,48] erscheint es überraschend, bereits 10 Tage vor Augenöffnung, einem Zeitpunkt an dem sich die horizontalen Verbindungen noch nicht vollständig entwickelt haben[46,122,364], robuste modulare Aktivitätsmuster mit großer Reichweite zu finden. Das Vorhandensein derartiger langreichweitiger modularer Korrelationsmuster in Abwesenheit eines gut entwickelten horizontalen Netzwerks in Schicht 2/3 stellt damit die Notwendigkeit monosynaptischer langreichweitiger Verbindungen zur Erzeugung ausgedehnter modularer Netzwerkaktivität in Frage.
Die korrelierten Aktivitätsmuster in diesem frühen Entwicklungsstadium sind nicht identisch mit den Mustern im reifen Kortex, sondern werden über einen Zeitraum von mehreren Tagen vor Augenöffnung erheblich verfeinert. Tatsächlich spiegeln Veränderungen in den Mustern der korrelierten Aktivität während der Entwicklung wahrscheinlich die fortschreitende Reifung mehrerer Merkmale der Netzwerkorganisation wider, einschließlich der Entstehung langreichweitiger, horizontaler Verbindungen[439].
Obwohl Netzwerkkorrelationen während der Entwicklung erheblich verfeinert werden, weisen sie zu Beginn der Entwicklung ein modulares Muster auf, das die reife funktionale Organisation vorhersagen kann. Bis zu 10 Tage vor Augenöffnung zeigt die spontane Aktivität schon einige Signaturen der funktionalen Organisation des reifen Kortex. Die modularen Muster spontaner Aktivität zu Beginn der Entwicklung und ihre Beziehung zur reifen Schaltkreisorganisation wurden zuvor nicht beschrieben. Die Ähnlichkeit früher Netzwerkkorrelationen mit dem ausgereiften funktionalen Layout ist konsistent mit der Vorstellung einer selbstorganisierten kortikalen Aktivität.
Es ist unklar, ob die langreichweitig korrelierten und modularen Aktivitätsmuster hauptsächlich durch Feedforward-Input, über einen intrakortikalen Mechanismus oder durch Feed-Back-Input erzeugt werden. Die von unserer Kollaboration im Labor von David Fitzpatrick durchgeführten Inaktivierungsexperimente der Retina und des Thalamus zeigen, dass in der frühen Entwicklung korrelierte spontane Aktivität vom visuellen Kortex erzeugt werden kann, selbst dann wenn

kein Input von der Retina oder vom LGN vorliegt. Der beobachtete Rückgang in der Frequenz spontaner Events nach der Inaktivierung vom LGN lässt darauf schließen, dass der LGN intrinsische kortikale spontane Events auslöst. Das Vorhandensein modularer Korrelationsmuster, die sich über ähnliche Distanzen, wie diejenigen mit intakten Feedforward-Inputs erstrecken, zeigt, dass bereits unreife kortikale Schaltkreise die Fähigkeit haben, modulare ausgedehnte Muster zu erzeugen. Es ist wichtig zu betonen, dass diese Beobachtungen eine kausale Rolle für den Feedforward-Input beim Aufbau einer modularen kortikalen Netzwerkstruktur nicht ausschließen. Muster der retinalen und genikulo-kortikalen Aktivität könnten eine kritische Rolle bei der Steuerung der Entwicklung dieser kortikalen Aktivitätsmuster spielen (z.B.[311,69,75,201]), aber sie sind eindeutig nicht für ihre Ausbildung erforderlich. Diese Ergebnisse zeigen, dass frühe kortikale Schaltkreise strukturierte Korrelationen mit großer Reichweite erzeugen können. Diese werden im Laufe der Entwicklung verfeinert, um reife, ausgedehnte funktionale Netzwerke zu bilden, wodurch die funktionale Architektur auf kleiner räumlicher Skala mit der entfernten Netzwerkorganisation gekoppelt wird.

Diese Ergebnisse werfen jedoch das Problem auf, wie langreichweitige Aktivität im frühen Kortex durch intrakortikale Schaltkreise ohne langreichweitige horizontale Konnektivität erzeugt werden kann. Ich addressiere dieses Problem, indem ich ein statistisches Modell untersuche, welches ein Ensemble von räumlich ausgedehnten spontanen Aktivitätsmustern beschreibt. Ich zeige, dass eine Reduzierung der Dimensionalität dieses Ensembles von Aktivitätsmustern zu einer größeren Reichweite führt, über die die Domänen korreliert sind. Dies legt nahe, dass ein Mechanismus im frühen kortikalen Netzwerk implementiert ist, der die Dimensionalität von Aktivitätsmustern einschränkt, wodurch der frühe Kortex in der Lage ist, ausgedehnte Netzwerkaktivität ohne anatomische langreichweitige Verbindungen zu erzeugen.

Aufbauend auf dieser Hypothese, studiere ich ein dynamisches Netzwerkmodell in welchem ein Mechanismus implementiert ist, der die Dimensionalität der Aktivitätsmuster reduziert. Mit Hilfe diesen Modells zeige ich, dass langreichweitige Korrelationen in heterogenen Schaltkreisen durch multisynaptische lokale Wechselwirkungen entstehen können, indem sie bestimmte räumlich ausgedehnte Aktivitätsmuster auf Kosten anderer begünstigen.

Da die spontane Aktivität schon im frühen visuellen Kortex modular ist, werden in diesem Netzwerkmodell die lateralen Verbindungen so angenommen, dass sie die Bildung aktiver Domänen unterstützen. Der dynamische Mechanismus, der zur Erzeugung modularer Aktivitätsmuster angenommen wird, ist als Turing-Mechanismus bekannt: modulare Muster entstehen aus einem räumlich homogenen Zustand, indem räumlich heterogene Störungen durch dynamische rekurrente Netzwerke verstärkt werden[130]. Da der Fokus dieses Modells auf den Mechanismen liegt, Domänen über große Distanzen zu korrelieren, wurde eine generische lokale Verschaltung gewählt, um den Turing-Mechanismus zu implementieren: die sogenannte Mexican Hat Konnektivität (lokale Exzitation mit lateraler Inhibition). In einigen Studien wurde Evidenz für ein solches Motiv gefunden[108], wohingegen andere Studien[265] nahelegen, dass die Reichweite der inhibitorischen Interaktion der Inhibition tatsächlich kleiner ist als die Reichweite der Exzitation. Aus diesem Grund habe ich ein zweites dynamisches Netzwerkmodell untersucht, das aus zwei Populationen besteht, die so verschaltet sind, dass ihre Konnektivität mit den aktuellen experimentellen Daten übereinstimmt[265].

Basierend auf früheren Arbeiten[428,464,353], die gezeigt haben, dass Heterogenität im Netzwerk die Dimensionalität des Ensembles der möglichen Aktivitätsmuster reduziert, habe ich in beiden Netzwerkmodellen eine heterogene Konnektivität angenommen. Mit dem Grad an Heterogenität konnte in beiden Netzwerkmodellen die Dimensionalität der Aktivitätsmuster kontrolliert werden. Konsistent mit dem statistischen Modell, führt eine reduzierte Dimensionalität zu einer langreichweitigen Korrelationsstruktur, die quantitativ mit derjenigen übereinstimmt, die in experimentellen Daten beobachtet worden ist. Die Beziehung zwischen der Dimensionalität des Ensembles von Aktivitätsmustern und weiteren Eigenschaften spontaner Korrelationen legt nahe,

dass eine niedrige Dimensionalität als Organisationsprinzip der kortikalen Aktivität fungieren könnte. Das Modell sagt voraus, dass eine Zunahme der Heterogenität in den lokalen Verschaltungen die räumliche Ausdehnung der spontanen Korrelation erhöht. Zukünftige Experimente könnten diese Vorhersage testen, indem die Heterogenität innerhalb des kortikalen Netzwerks experimentell manipuliert wird. Durch die optogenetische Aktivierung weniger, zufällig ausgewählter Neuronen könnte die lokale Struktur der funktionalen lateralen Wechselwirkungen heterogener werden. Die Idee, dass die langreichweitige Ordnung in kortikalen Netzen ihren Ursprung in kurzreichweitigen Wechselwirkungen hat, wurde nach Kenntnis des Autors in früheren Studien noch nicht vorgeschlagen.
Insbesondere erzeugt das dynamische Netzwerk mit lokaler Inhibition und räumlich ausgedehnter Exzitation, welches im vorigen Absatz zur Beschreibung der Bildung langreichweitiger Korrelationen verwendet wurde, modulare Aktivitätsmuster. Im Gegensatz dazu haben frühere klassische Netzwerkmodelle, die basierend auf einem intrakortikalen Mechanismus modulare Aktivität ausbilden, entweder langreichweitige Inhibition[129] oder Inhibition mit schneller Zeitkonstante[346,226] benötigt. Diese Annahmen scheinen jedoch im Widerspruch zu aktuellen experimentellen Daten zu stehen[265,329]. Überdies wurden diese früheren Modelle noch kaum experimentell getestet. Ich zeige, dass eine räumlich lokalisierte Selbstinhibierung die Einschränkungen in der genannten Modellklasse lockert, so dass biologisch plausible Netzwerkmotive, insbesondere solche mit lokaler Inhibition, robust modulare Aktivität generieren. Ich wende eine lineare Stabilitätsanalyse auf das Netzwerkmodell an, um die Grenzen des Parameterregimes für die Bildung modularer Aktivität zu bestimmen. Darüberhinaus stelle ich mehrere Modellvorhersagen vor, die im Hinblick auf neuartige Entwicklungen experimenteller Methoden die Modellklasse experimentell testbar machen. Eine kritische Vorhersage unseres Modells ist, dass der typische Abstand aktiver Domänen abnimmt, wenn die Gesamtstärke der Inhibition zunimmt. Dieses Modell stellt damit einen neuartigen Mechanismus bereit, mit Hilfe dessen kortikale Netzwerke mit kurzreichweitiger Inhibition modulare Aktivität formen können.
Zusammengenommen zeigen diese Ergebnisse, dass die experimentell beobachteten Merkmale der kortikalen Aktivität schon während der frühen Entwicklung des Kortex vorhanden sind und durch einfache Prinzipien in frühen kortikalen Netzwerken entstehen können.

Abstract

Cortical circuits exhibit highly dynamic and complex neural activity. Intriguingly, cortical activity exhibits consistently two key features across observed species and brain areas. First, individual neurons tend to be co-active in spatially localized domains forming orderly arranged, modular layouts with a typical spatial scale. Second, cortical elements are correlated in their activity over large distances reflecting long-range network interactions distributed over several millimeters. Currently, it is unclear how these two fundamental properties emerge in the early developing cortical activity.

Here, I aim to fill this gap by combining analyses of chronic imaging data and network models of developing cortical activity. Neural recordings of spontaneous and visually evoked activity in primary visual cortex of ferrets during their early cortical development were obtained using *in vivo* 2-photon and widefield epi-fluorescence calcium imaging. Spontaneous activity was used to probe the early state of cortical networks as its spatiotemporal organization is independent of a stimulus-imposed structure, and it is already present early in cortical development prior to reliably evoked responses. To assess the mature functional organization of distributed networks in cortex, the tuning of neural responses to stimulus features, in particular to the orientation of an edge-like stimulus, was assessed. Cortical responses to moving gratings of varying orientations form an orderly arranged layout of orientation domains extending over several millimeters.

To begin with, I showed that spontaneous activity correlations extend over several millimeters, supporting the assumption of using spontaneous activity to assess distributed networks in cortex. Next, I asked how distributed networks in the mature visual cortex - assessed by spontaneous activity correlations - are related to its fine-scale functional organization. I found that the spatially extended and modular spontaneous correlation patterns accurately predict the fine spatial structure of visually evoked orientation domains several millimeters away. These results suggest a close relation between spontaneous correlations and visually evoked responses on a fine spatial scale and across large spatial distances.

As the principles governing the functional organization and development of distributed network interactions in the neocortex remain poorly understood, I next asked how long-range correlated activity arises early in development. I found that key features of mature spontaneous activity introduced in this work, including long-range spontaneous correlations, were present already early in cortical development prior to the maturation of long-range, horizontal connections, and the predicted mature orientation preference layout. Even after silencing feed-forward input drive by inactivating retina or thalamus, long-range correlated and modular activity robustly emerged in early cortex. These results suggest that local recurrent connections in early cortical circuits can generate structured long-range network correlations that guide the formation of visually-evoked distributed functional networks.

To investigate how these large-scale cortical networks emerge prior to the maturation and elab-

oration of long-range horizontal connectivity, I examined a statistical network model describing an ensemble of spatially extended spontaneous activity patterns. I found a direct relationship between the dimensionality of this ensemble of activity patterns and the decay of its correlation structure. Specifically, reducing the dimensionality of the ensemble leads to an increase in the spatial range of the correlation structure.
To test whether this mechanism could generate a long-range correlation structure in cortical circuits, I studied a dynamical network model implementing a dimensionality reduction mechanism. Based on previous work demonstrating that network heterogeneity reduces the dimensionality of activity patterns, I showed that by increasing the degree of heterogeneity in the network, the dimensionality of the ensemble of activity patterns decreases and in turn their correlations extend over a greater range. A comparison to experimental data revealed a quantitative match between the network model and the observations *in vivo* in several of the key features of the early cortex including the spatial scale of correlations. Low dimensionality of spontaneous activity thus might provide an organizational principle explaining the observed long-range correlation structure in the early cortex.
Finally, I asked whether a network with a biologically plausible architecture can generate modular activity. Several classical models showed that modular activity patterns can emerge via an intracortical mechanism involving lateral inhibition. However, this assumption appears to be in conflict with current experimental evidence. Moreover, these network models were not experimentally tested, so far. Here, I showed by using linear stability analysis that spatially localized self-inhibition relaxes the constraints on the connectivity structure in a network model, such that biologically more plausible network motifs with shorter ranging inhibition than excitation can robustly generate modular activity. Importantly, I also provided several model predictions to make the class of network models experimentally testable in view of recent technological advancements in imaging and manipulation of cortical circuits. A critical prediction of the model is the decrease in spacing of active domains when the total amount of inhibition increases. These results provide a novel mechanism of how cortical circuits with short-range inhibition can form modular activity.
Taken together, this thesis provides evidence that the two described fundamental features of neural activity are already present in the early cortex and shows that activity with those features can be generated in network models with an architecture consistent with the early cortex using basic principles.

Author contributions

The core results presented in Chapter 3, Chapter 4 and the second part of Chapter 5 are published in: Gordon B. Smith, Bettina Hein, David E. Whitney, David Fitzpatrick, and Matthias Kaschube: *"Distributed network interactions and their emergence in developing neocortex"* (2018). Nature Neuroscience.
G.B. Smith and D.E. Whitney recorded all widefield and 2-photon data shown in Chapter 3 and Chapter 4 under the supervision of D. Fitzpatrick. I did the registration of the widefield data together with supervised former Master students Klaus Neuschwander and Philipp Hülsdunk. I analyzed all widefield imaging data presented in Chapter 3 and Chapter 4. I analyzed the 2-photon imaging data with G.B. Smith and D.E. Whitney presented in Chapter 3. I generated the figures presented in Chapter 3 and Chapter 4 with G.B. Smith and D.E. Whitney. G.B. Smith and D.E. Whitney provided the analysis of the retina silencing experiments shown in Chapter 4. I analyzed the LGN silencing data together with G.B. Smith and D.E. Whitney in Chapter 4. I did the analytical and numerical computations of the dynamical network model and generated all the figures presented in Chapter 5. I wrote the manuscript together with all authors.
Chapter 6 is part of the publication: Bettina Hein, Dmitry Bibichkov, and Matthias Kaschube: *"A mechanism for generating modular activity in the cerebral cortex"* (2019) in preparation.
I performed all analytical and numerical calculations in this study and generated all figures.
As the bulk of this work presented in this thesis was in collaboration with experimental neurobiologists mentioned above I will change from "I" to "we" in the following.

Chapter 1

Introduction

In many physical systems, internal order develops from an initially disordered state through local interactions between the system's components. This *self-organization* is not externally guided but happens spontaneously, and it is robust against changes or perturbations in the system. Self-organization is thus an elegant mechanism to form order in a complex system based only on elementary rules.

A formidable example of a complex system is the brain which consists of hierarchically arranged cortical areas that process sensory information to translate into behavioural motor output. A cortical area consists of up to several hundred million neuronal cells interacting with each other via an intricate wiring scheme. Intriguingly, neuronal activity across many different brain areas and even species of carnivores and primates seems well-ordered on a mesoscopic scale consistently exhibiting two prominent features.

First, in cortical activity individual neurons tend to be co-active in spatially localized domains and these active domains form orderly patterns across the cortical surface with a typical spacing between adjacent domains of roughly 1 mm[164,43,45,331,154,285,48,231,389]. As shown in this thesis, spatially modulated activity is observed in different states of the animal (anesthetized and awake[389]), in neural activity that is either evoked by external stimuli[43,389] or emerges spontaneously in the absence of experimental external stimuli[235,327,389], and from an early stage in development to adulthood[389]. The consistent and robust presence of modular activity throughout various conditions implies that it is a fundamental property of the underlying cortical circuit. Although several hypotheses have been put forward, it is still unclear by which mechanism brain circuits generate modular activity. Understanding how patterns of cortical activity arise remains therefore a key problem of current computational and systems neuroscience.

Second, cortical domains are correlated in their spontaneous[389] and evoked[231] activity over large cortical distances of several millimeters. In mature cortical circuits the presence of long-range lateral, anatomical connections provides the substrate for this long-range correlation structure. However, as shown by the author long-range correlations are already present at an early stage of cortical development, in particular prior to the maturation of long-range anatomical connections[389]. This naturally raises the question of how long-range correlations form in the presence of purely local network interactions. A potential solution to this problem is that modular and long-range correlated activity emerge via an intracortical mechanism consistent with the idea of self-organisation. This hypothesis builds the core of this thesis.

Understanding how cortical circuits shape neural activity is a key problem in computational neuroscience[287,19,434,433,57,307,182]. Gaining a deeper understanding of how network units interact via their activity can potentially illuminate how information from the environment is transmitted in the form of neural activity between brain areas. A direct application of such an intuition could possibly lie in stimulating new approaches to treatment for e.g. neurological disorders

that exhibit in deviations from normal brain activity.
The recent advancement of novel experimental tools has created new opportunities to study the development and maturation of neuronal activity in cortical circuits. Highly sensitive genetically encoded calcium indicators have been developed[81] that make it possible to reliably image single trial responses and spontaneous activity in cortex. This new family of calcium indicators allows to image large populations of neurons[390,388,375] chronically over several weeks to months[81,375,389]. In combination with the use of ferrets which are born at a relatively early stage in their development[267], these calcium indicators are well suited to record cortical activity early in life. The possibility to obtain those large-scale recordings of neuronal population activity requires us to develop new analysis and modelling approaches in this thesis. Together with recent experimental techniques, these novel analytical tools might enable us to elucidate the principles underlying the emergence and maturation of cortical activity.
To study the development of cortical activity, the mammalian visual cortex is a particularly well-suited system processing visual information entering the brain through the retina. The functional organization in the mature visual cortex has been extensively studied and characterized. In primary visual cortex, oriented edge-like stimuli robustly evoke strong neuronal responses[196]. In carnivores and primates these cortical responses exhibit a modular layout[285,86,344,389]. Systematically varying the orientation of visual edge-like stimuli reveals an orderly arranged map of orientation domains that are distributed across the visual cortex[231]. Within one orientation domain nearby neurons preferably respond to the same orientation. These orientation domains repetitively cover the entire primary visual cortex exhibiting a typical domain spacing. This global organization of orientation domains reflects the long-range correlation structure in cortical activity, e.g. distant neurons sharing a similar orientation preference are correlated in their activity, and is a prime example for long-range correlated and modular activity. Still, little is known about how the layout of orientation domains emerges during development.
Mature spontaneously co-active domains often coincide with those functional modules[344,235,327,389]. In mature visual cortex instantaneous spontaneous activity patterns have been shown to resemble to a certain degree stimulus evoked activity patterns[235,327]. The authors[235] suggested that spontaneous and evoked activity patterns are similar over a large cortical range. Subsequent theoretical work investigated whether the properties of spontaneous activity are consistent with a long-range similarity, but did not come to a conclusive result[159]. It also remains unclear up to which fine spatial scale the similarity between spontaneous and evoked activity holds. As spontaneous activity is already present prior to reliable evoked responses, together with its similarity to the layout of evoked responses, makes it potentially well-suited to assess the state of the functional organization of cortical circuits during development.
A tremendous amount of theoretical and experimental work has shed light on how brain circuits form cortical activity. In particular, many studies investigated whether cortical activity is mainly driven by feed-forward inputs or whether its origin lies within cortex itself. Theoretical studies have introduced different modeling frameworks to study the ability and scope of feed-forward input and intracortical mechanisms in shaping the spatiotemporal properties of neuronal network activity[218,224,241,420]. Similarly, experimental work has aimed towards dissecting the contribution from feed-forward inputs compared to intracortical mechanisms in shaping network activity[303,352,389]. Yet, the contribution from these different input sources to the formation of the local and distributed organization of cortical activity remains elusive. Intriguingly, experiments motivated by and described in this thesis show that the modular and long-range correlated organization of spontaneous cortical activity remains intact after inactivation of the upstream brain area[389], demonstrating that this fundamental property is not imposed to the cortex by feed-forward circuits.
In fact, there has been extensive theoretical work on modelling the emergence of modular activity based on an intracortical mechanism within the framework of dynamical network mod-

els[287,411,28,226,71,44,163]. Such a neural network consists of a population of neurons that interact via recurrent connections. Typically, the intracortical mechanism relies on local facilitation and lateral suppression of activity which is in a broader context known as the Turing mechanism[430,152,296]. A straightforward way to implement this mechanism is through a specific from of recurrent circuitry consisting of local excitation and spatially more extended inhibition (sometimes called a 'Mexican hat' connectivity profile)[287,411,28,71,44]. Local excitation amplifies locally elevated activity fluctuations whereas lateral inhibition suppresses activity nearby, such that adjacent active domains can arise with a typical domain spacing. However, while there is some experimental evidence for this type of organization[108,80], other studies indicate that the lateral extent of inhibitory connections tends to be shorter than excitatory connections[280,281,279,278,265]. The emergence of the long-range correlation structure prior to the maturation of anatomical, long-range connections has for the first time been described by the author[389]. For this reason there is a lack of theoretical work describing how purely local circuits can generate distributed network activity that is correlated between distant cortical areas.
In this thesis I aim to fill this gap and investigate the emergence of modular and long-range correlated spontaneous activity in cortical circuits. Specifically, I address the following three questions:

- How can a network with a biologically plausible architecture generate modular activity?
- How does distributed, long-range correlated network activity arise early in development?
- How are the distributed networks in the mature visual cortex related to its fine-scale functional organization?

To approach these questions I use a combination of computational modelling and analysis of experimental recordings of cortical activity. The neural recordings were obtained in the laboratory of David Fitzpatrick at the Max Planck Florida Institute. Gordon B Smith and David E Whitney performed the imaging experiments. To assess the emergence and maturation of distributed functional cortical circuits, neural population activity in ferret primary visual cortex was recorded in a chronic imaging setup using the highly sensitive calcium indicator GCaMP6[81]. Ferrets are used as the model system as their cortex maturates largely after their birth. To examine the emergence of distributed networks and their state in the mature animal, spontaneous and visually evoked activity is imaged prior to after eye-opening. As spontaneous activity is already present early in development, it is used to probe the state of neural activity during early cortical development. Furthermore, spontaneous activity allows to probe cortical activity without imposing an organization that is driven mainly by stimuli. So far, only little is known about its spatiotemporal structure early in development.
In this thesis, I quantitatively characterize the spatiotemporal properties of spontaneous and visually evoked activity during the early development. I find that mature spontaneous activity shows a long-range correlation behaviour. Those long-range spontaneous correlations are tightly related to the functional organization of visual cortex over several millimeters and on a fine spatial scale much more than previously anticipated. Based on this close relationship I assess the early state of cortical circuits using spontaneous correlations. Already at the earliest observed stages in development prior to the elaboration of long-range anatomical connections the spontaneous correlations extend over a distance similar to the one in mature animals. To address how cortical circuits with local connectivity generate long-range correlated activity, I develop a heterogeneous network model based on elementary rules that is able to quantitatively match key properties of the experimentally observed spontaneous activity. Consistent with the idea of self-organizing network activity our network model shows that features of long-range network behaviour can emerge from purely local lateral connections. Extending this network model I

show that by introducing weak local self-inhibition modular activity can be generated with a network architecture that appears consistent with current experimental data, in particular when the excitatory interaction range exceeds the one of inhibition. Importantly, combining the two network mechanisms I propose leads to long-range correlated and modular activity consistent with experimental data. Together, these results suggest that the two key features of neural activity - modularity and long-range correlations - emerge already early in cortical development and can be generated by basic network mechanisms.
The organization of this thesis is as follows. Chapter 2 outlines the functional and anatomical properties of the visual system and its maturation during early development highlighting spontaneous cortical activity. It further introduces previous relevant theoretical work on modelling cortical activity and describes the main analysis methods used. In Chapter 3 I describe the experimental setup used for recording the imaging data that is analyzed in this thesis, followed by an overview about the basic analysis steps used in the signal processing. The chapter ends by showing that spontaneous activity in the mature visual cortex exhibits a long-range correlation structure and resembles locally and over extended distances the visually evoked activity. In Chapter 4 I demonstrate that already early in development spontaneous activity is correlated over large distances prior to the maturation of anatomical, long-range connections and I present evidence that this activity can be intracortically generated. The properties of spontaneous activity necessary for the emergence of this long-range correlation structure is investigated in Chapter 5, followed by introducing a mechanism that quantitatively captures core aspects of the experimentally observed spontaneous activity resulting in distributed network activity. Finally, in Chapter 6 I propose a mechanism that allows networks with a biologically plausible architecture to generate modular activity patterns. A discussion of the main results is given in Chapter 7.

Chapter 2

Foundations

In this thesis we investigate how modular and long-range spontaneous activity in cortex emerges during early development using data analysis and modeling approaches of cortical activity. The experiments providing the data are performed in mammalian primary visual cortex which has been extensively studied in the previous decades[198,65,135]. To help the reader to put this work into context and to distinguish this thesis' findings from previous research, we give in the following a comprehensive overview about (1) the neuroanatomical and functional structure of the visual system, (2) its development together with how spontaneous and evoked activity is organized in the developing visual system, (3) previous approaches to model cortical activity and (4) the main analysis tools used in this thesis.

2.1 Anatomical and functional organization of the visual system

Visual information is transmitted to the mammalian brain via three major pathways. In the first pathway information from the retina is relayed via the thalamus to the visual cortex where information is processed for further visual perception (**Fig. 2.1a**). In the second pathway information from the retina is sent to the pretectum. This pathway is mainly responsible for the pupillary light reflex and the optokinetic reflex. In the third pathway information from the retina is relayed to the superior colliculus, which is among others responsible for directing eye movement. In the following we will elaborate on the anatomical and functional organization of the first pathway. we will specifically focus on the primate and carnivoran visual system, as these are most relevant to this thesis.

2.1.1 Retina

Visual information from the environment enters the eye through the lens and strikes the light-sensitive retina at the back of the eye. The retina exhibits an orderly layered organization of a small number of main cell types with stereotypical morphology[120,404] (**Fig. 2.1b**). The deepest layer furthest away from the incoming light consists of two types of light-sensitive photo receptors, so-called *rods* and *cones*, that are arranged in a mosaic. They are responsible for night and day time vision, respectively. Rods function in an environment with little light and they are extremely light-sensitive in darkness. A single photon is already sufficient to evoke a measurable signal in one of them[371]. Activating about seven rods suffices to evoke a conscious sensation[178]. Cones on the other hand are responsible for day time vision and exhibit a large dynamic range and detect subtle changes in contrast and color. There are about 100 Mio. rods and 5 Mio. cones in the adult human retina[106].

The photoreceptors transmit information to *bipolar* cells which in turn are connected to *Retinal*

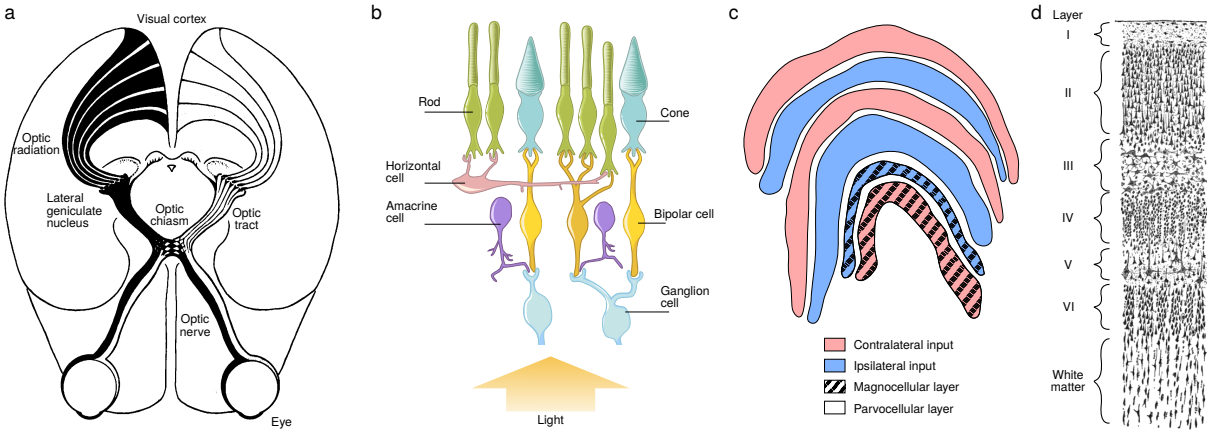

Figure 2.1: Visual pathway and its three main stages. **a** Information is carried from the retina (**b**) via the LGN (**c**) to the primary visual cortex (**d**), adapted from[198]. The brain is viewed from below. The left part of each retina (indicated in black) projects via the LGN to the left hemisphere of the visual cortex at the back of the brain (top of schematic). **b** The schematic shows the five main cell types and their connections in the mammalian retina. Adapted from[334]. **c** In primates, the LGN consists of 6 layers which receive eye-segregated input (ipsilateral input: blue, contralateral input: red) and are divided into the magnocellular (striped area) and the parvocellular pathway. **d** In mammals, the primary visual cortex consists of six layers of varying neuron types and density. Adapted from[64].

Ganglion Cells (RGCs) (**Fig. 2.1b**). Their bundled axons form the optic nerve fibers which transmit signals from the retina to the next processing station which is the thalamus (**Fig. 2.1a**). Two other main cell types are *horizontal* and *amacrine* cells which exhibit predominantly lateral connections to RGCs and bipolar cells (**Fig. 2.1b**). Their lateral wiring scheme suggests that they transmit and modify signals traveling through the retina. Amacrine cells and RGCs can generate action potentials whereas the other three cell types produce only graded potentials. These five major cell classes can be further subdivided according to differences in function and structure.

In darkness the photoreceptors are depolarized and release the neurotransmitter glutamate. Incoming photons can be absorbed by the molecules inside of the photoreceptor. These molecules convert the energy of the photon into an electrochemical signal by changing their configuration and in turn hyperpolarizing the photoreceptor. After hyperpolarization, the photoreceptor stops releasing glutamate. This decrease in glutamate depolarizes (excites) *ON* bipolar cells, whereas it hyperpolarizes (inhibits) *OFF* bipolar cells.

Incoming light only evokes a response in a bipolar cell if the light is confined to a small spot in visual space that lies within the cell's *receptive field*[172,250]. OFF bipolar cells have an *off-center* receptive field, i.e. if the incoming light is confined to the center of the receptive field an OFF bipolar cell is being hyperpolarized, whereas if the light has the form of a broader ring the OFF bipolar cells is being depolarized. In contrast, ON bipolar cells exhibit an *on-center* receptive field (hyperpolarization for ring-like illumination, depolarization for spot-like illumination)[462]. RGCs connected to OFF bipolar cells (ON bipolar cells) similarly show an off-center (on-center) receptive field. In *ON-type* RGCs the increase in light in the center of the receptive field or the decrease of light in the surround of the receptive field causes an increase in the cell's firing rate. In *OFF-type* RGCs an increase (decrease) in light in the surround (center) of the receptive field increases the cell's firing rate. Diffuse, homogeneous light evokes only a weak response in RGCs;

thus, RGCs encode the difference in the light level between the center and surround of their receptive field. There are several types of RGCs. *Parasol-type* RGCs typically exhibit larger receptive fields and respond well to motion[379]. *Midget-type* RGCs have smaller receptive fields. They are color-sensitive and respond preferably to fine spatial details[263,95].
At every stage in the visual system neuronal signals converge and diverge extensively. The human eye contains approximately 100 Mio. photoreceptors, but only 1 Mio. optic nerve fibers are connecting the retina to the thalamus[435]. This bottleneck indicates that the visual input is already processed in the retina by compressing its information using in parts the specific form of the center surround structure of the receptive fields implemented by bipolar cells and RGCs. As an example, the receptive field structure decorrelates the incoming image of the visual world and can approximately be thought of as applying an edge-detection filter.
The processed information from the retina is carried along the retinofugal optic fibers. The optic fibers divide into two pathways at the optic chiasm (**Fig. 2.1a**). The left side of each retina corresponds to the right part of the visual world due to the optical reversal by the lens, and projects to the left cerebral hemisphere (pathway shaded in black in **Fig. 2.1a**). Information from the left (right) visual field is carried by the right (left) optic tract to the *lateral geniculate nucleus* (LGN) in the thalamus[49].

2.1.2 Lateral geniculate nucleus

The LGN receives the major part of the output of the retina and is the main and direct relay station between retina and visual cortex (**Fig. 2.1a**). The number of optic nerve fibers equals roughly the number of geniculate cells. Nevertheless, geniculate cells receive convergent input from several optic nerve fibers, and optic nerve fibers diverge to several geniculate cells.
The LGN is one of the nuclei of the thalamus. In primates including humans it is arranged into six layers (**Fig. 2.1c**). Each layer receives information from only one eye. Layers 1, 4 and 6 receive information from the contralateral eye, whereas layers 2, 3 and 5 receive input from the ipsilateral eye[191]. Layers 1 and 2 contain *magnocellular* cells which receive input from the parasol-type RGCs in retina[263,95], and thus form the magnocellular pathway. This pathway contributes motion and depth information[379], is sensitive to light/dark contrast[348] and, thus, helpful when detecting edges[83] (see Section 2.1.3). Layers 3 to 6 contain *parvocellular* cells which receive input from the midget-type RGCs, and form the parvocellular pathway. In this pathway information about the fine detail of objects and color is carried[263,95]. Inbetween each layer lies a zone of very small *interlaminar* or *koniocellular* cells[95,181,72]. They receive signals from a heterogeneous group of RGCs in the retina and from neurons in the superior colliculus. They are thought to relay short-wavelength visual information, and appear to be binocularly driven[461] in contrast to magnocellular and parvocellular cells.
The incoming optic fibers are ordered to form a *retinotopic* map in LGN. Neighbouring RGCs in the retina project to neighbouring geniculate cells such that the receptive fields of neighbouring neurons strongly overlap[181,72]. Thus, neigbouring geniculate cells receive inputs from a similar region of the visual field, but from notably diverse classes of RGCs[25]. A general rule of thalamic organization seems to be that neurons that are close to each other process similar information. This orderly, anatomical architecture suggests a massively parallel processing of information in the early visual system.
LGN receives strong feedback connections from visual cortex that are necessary for synchronized firing in LGN[384,147,437]. Due to these feedback connections LGN is thought to be not only a relay station in the visual system but capable of contextualizing incoming signals[437].
In primates the major part of the output of LGN is being transmitted via the optic radiations to primary visual cortex[33,60] (**Fig. 2.1a**). This is unlike to carnivores where LGN also relays information directly to higher cortical areas[33,60].

2.1.3 Visual cortex

LGN relays its output to visual cortex. The visual cortex is dedicated to process visual information and is located in the occipital lobe of the brain (**Fig. 2.1a**). Information from LGN first arrives in the primary visual cortex (V1) and is then sent to higher cortical areas where it is thought to follow two different paths depending on its content[161]. Information about object identification and recognition is sent along the *ventral* stream (also called the "what pathway"), whereas information about an object's spatial location follows the *dorsal* stream ("where pathway")[161]. V1 is the largest cortical area in the adult human brain with a surface area of $\sim$25 cm^2 and about 140 Mio. neurons in each hemisphere[261]. In many species area V1 is located at least partially close to the surface making it particularly accessible for various imaging methods, and one of the most extensively studied areas in the brain.

Anatomical architecture

Similarly to LGN, V1 shows a very orderly and structured organization. Within the gray matter (containing cell bodies, dendrites, few myelinated axons and glial cells) it consists of six layers (**Fig. 2.1d**) which vary in thickness and cell density[64]. In most large brained mammals, primates and carnivorans, V1 (and the higher visual areas) is *retinotopically* organized which means adjacent cortical cells have overlapping receptive fields. The positions of the receptive fields form an orderly arranged map in visual cortex[111,286]. Moreover, nearby neurons share similar functional properties, e.g. they respond similarly to specific visual features[145,414].
Geniculate fibers projecting to visual cortex are excitatory[15,305] and mostly project to layer IV[191,255,198]. In primates, layer IV is further subdivided into the sublayers IVA, IVB, IVCα and IVCβ[72]. IVCα receives most input from the magnocellular pathway, whereas IVCβ typically receives input from the parvocellular pathway[191,180,42]. Thalamic input only provides a small fraction of all synapses in layer IV of about 6% (in cat[98,107]). The majority of synapses is provided by other cortical neurons[292,138,119]. Thalamic synapses are comparable in their properties (e.g. strength) to synapses coming from other cortical neurons[9,37]. Taken together these observations led to the hypothesis that thalamic input is "just enough"[119,290] to drive activity in the cortex and is then amplified by cortical circuits[107,405,26,266,352].
In addition to this orderly feed-forward organization V1 exhibits a remarkably organized vertical structure. First, neurons connect vertically different layers. Especially, layers II, III and V receive input from other layers within cortex. Layer IV transmits signals to layers II/III which in turn relay information to layers V and VI[162].
The vertical organization is complemented by extensive long-range connections within the layers[155,357,153,154,232,68]. These extend up to 6-8 mm and reciprocally connect discrete and periodically organized clusters of neurons[357,356,270,243]. These clustered long-range connections are not only found in primary visual cortex but throughout the brain, i.e. in higher visual areas, the motor cortex, the prefrontal cortex, and the inferotemporal cortex[315]. The modular structure of vertically organized cortical columns[313,194] interconnected via long-range horizontal connections suggests that neuronal columns might serve as computational units, i.e. process certain features of the visual scene and then pass information on to other cortical regions.

Functional architecture

Neurons in V1 are typically characterized by their functional properties towards topological relations inherited from retina and LGN, and towards specific features of the visual stimulus[440]. In V1 the eye-segregated pathways from retina to LGN merge, and cortical neurons receive input from both eyes simultaneously. Most neurons show a strong preference, *ocular dominance*, for

the input of either one of the eyes[272,20].
In a remarkable experiment Hubel and Wiesel revealed that neurons in V1 respond preferably to edge-like stimuli[194]. The neurons exhibit either a *simple* or a *complex* receptive field. The simple receptive field consists either of an extended narrow, oriented central area flanked by two antagonistic regions, either excitatory or inhibitory, or is approximately rectangular with one side being excitatory and the other being inhibitory. The optimal stimulus to drive a simple cell is of a certain orientation and width. In contrast, a complex receptive field implements the abstract concept of orientation preference without the strict reference to a spatial position. Most of the simple cells are located in layers VI[194,156,59] and IV, whereas most complex cells are located in layers II,III and V. This layering is consistent with anatomical studies showing that many complex cells lie within the range of axons from layer IV simple cells, but outside the range of most thalamic axons[18]. Besides orientation selectivity and ocular dominance, neurons in V1 show preference to direction[413,382,436], spatial frequency[415,414] and further stimulus properties[415,414].
Measuring the response of an orientation selective neuron as a function of stimulus orientation shows that its firing rate increases as the oriented stimulus matches the neuron's preferred orientation (**Fig. 2.2a**). This is visualized by a tuning curve (**Fig. 2.2b**). The narrower the tuning curve and the higher the response to the preferred orientation relative to the baseline response, the more selective the neuron is to this particular orientation.
Initially, it was hypothesized that orientation selectivity is caused by thalamic inputs converging onto a cortical neuron such that their superimposed center-surround receptive fields form an elongated receptive field as exhibited by a simple cell[194]. Several experiments are consistent with this model, e.g. silencing cortical circuits either pharmacologically[78] or by cooling[139,78] while leaving the thalamocortical inputs intact, leaves the tuning of cortical neurons stable indicating that thalamic input contributes substantially to cortical tuning. Similarly, optogenetically silencing visual cortex demonstrated that the tuning of cortical neurons could be predicted by the receptive field structure of their thalamic inputs[217,266]. This is remarkable considering that only 6% of the synaptic connections to V1 neurons come from thalamocortical axons. However, another series of experiments demonstrated the presence of certain properties of orientation selectivity that cannot sufficiently be explained by thalamic inputs, such as contrast invariance[374,386,427], extraclassical receptive fields[392,441,183], e.g. surround suppression[192,40,246,326] and contextual modulation[438,154,467,112], and state-dependent modulation[325,366]. Further factors besides thalamocortical projections that might potentially contribute to orientation selectivity include spike threshold or nonlinearity, gain control and intracortical excitation and inhibition.
The organization of the neuron's functional properties within V1 reflects its underlying precise and orderly anatomical architecture. Recordings with electrodes placed orthogonal to the cortical surface revealed that neurons with similar functional properties are placed close to each other in a vertical, columnar organization[195,199]. Electrode recordings tangential to the cortical surface demonstrated that preferred orientation and ocular dominance change smoothly across cortex (in macaque monkey[199]). Follow-up experiments using the uptake of 2-deoxyglucose by active cells visualized for the first time bands of highly active regions, *ocular dominance* columns, as well as orientation columns in macaque monkey[197] going through all layers (except for layers IVc, and possibly I; in rhesus monkey[236,391]). Eventually, experiments using optical imaging methods in living animals demonstrated that orientation columns are orderly arranged across the cortical surface only interrupted by pinwheel centers. Pinwheel centers are discontinuities in the otherwise smooth organization of orientation domains at which all orientations are represented[43,164,45] (see also **Fig. 2.2c,d**). The spatial layout of orientation domains is precise and almost continuous (except for pinhweels) on a single cell level[331] (**Fig. 2.2d**). Although their spatial layout has been described as "complex" and "unpredictable"[43], the preferred orientation varies on a typical spatial scale across cortex[48,45,164,43,231,373] and the layouts of all examined

species of the orders of carnivora and primates follow a common organizing principle[231], termed common design. As orientation selectivity is a well-studied, prominent and robust feature of V1, we will use the orientation preference map to assess the functional organization of V1.

This robust and very orderly architecture of preferred orientation in the primary visual cor-

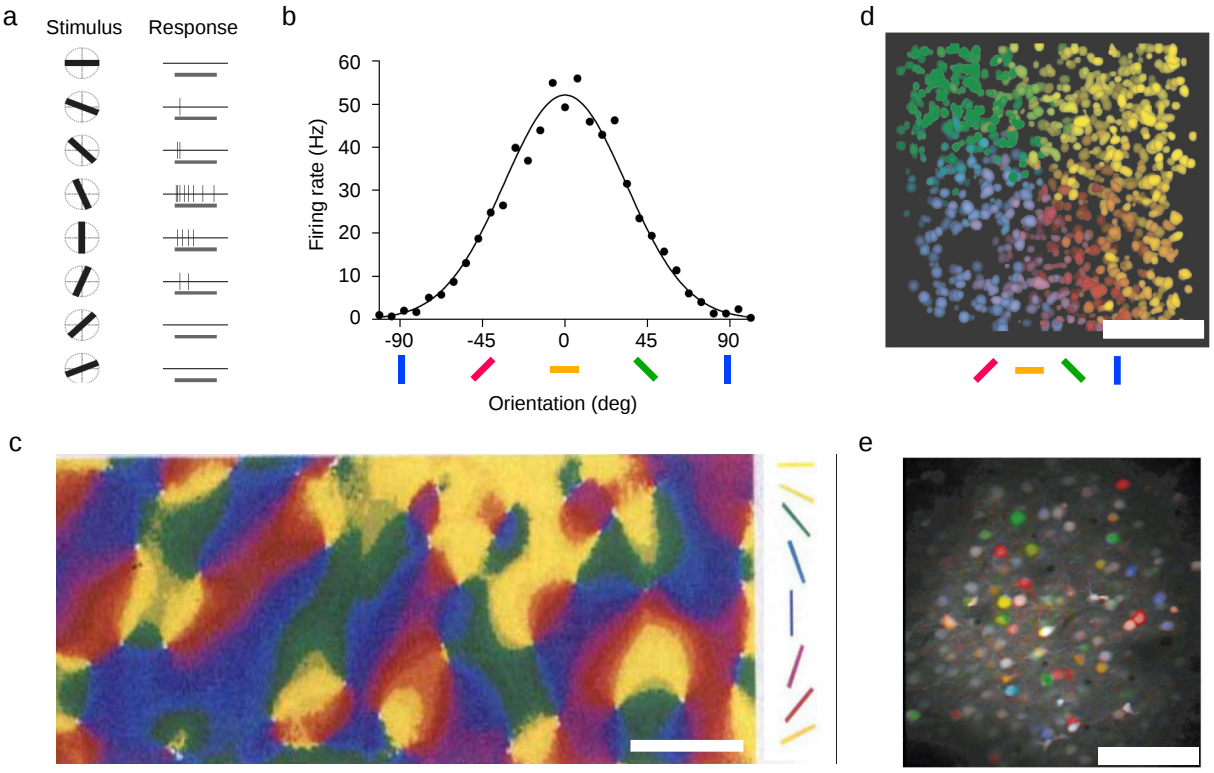

Figure 2.2: Orientation selectivity and its layout. **a** Schematic of firing rate response of simple cell in V1 to differently oriented stimuli. **b** The tuning curve shows an increase in firing rate for the preferred orientation. A narrow (broad) tuning curve indicates a highly (weakly) selective neuron. ((a) and (b) adopted from[193]) **c** Color-coded layout of smoothly changing orientation preference domains with pinwheel centers in cat area 18 obtained by *in vivo* intrinsic signal optical imaging (adapted from[45]). **d** Orientation preference in single neurons arranged around an individual pinwheel center in cat visual cortex reveals a precise functional architecture[331]. **e** The visual cortex in rat shows an interspersed layout[331]. Scale bar: 1 mm (**c**), 100 µm (**d**,**e**).

tex of carnivores and primates stands in stark contrast to the observed dispersed organization of orientation preference in V1 of rodents and lagomorphs. Although neurons in primary visual cortex of rodents and lagomorphs can be highly orientation selective, electrode recordings suggest an apparently disorganized layout of orientation preference (in rabbits[318], mouse[301,324], rat[157,337,331], gray squirrel[432]). Follow-up experiments using 2-photon imaging revealed an interspersed, spatially irregular, salt-and-pepper like organization of orientation preference in rodents[331] (**Fig. 2.2e**).

Histological architecture

The visual cortex exhibits not only an orderly anatomical and functional organization, but is also compartmentalized into regions with high and low metabolic demand. These regions can be differentiated by staining with cytochrome oxidase (CO) which is an enzymatic marker for long-term activity in neuronal cells, and is prevalent in cells with high metabolic activity. CO

staining exhibits a distinct pattern of *blobs* (highly active regions) and *interblobs* (low metabolic demand) in cortex. They are most prevalent in the upper cortical layers[270].
Initially, CO blobs were thought to be only found in primate cortex, only later studies indicated that CO blobs are also present in cortex of carnivores (in ferret[103] and cat[319]). The formation of CO blobs and their relationship to the functional cortical organization is still unclear. Differently active regions are hypothesized to serve different functions. Early studies suggested that neurons within blob regions exhibit low orientation selectivity whereas neurons outside are orientation selective (in macaque and squirrel monkey[116,190]). However, following studies did not confirm this relationship (in macaque monkey[263]). Other studies proposed that neurons within CO blobs are unselective for orientations and instead selective for color[270,271], but since CO blobs are also found in colorblind nocturnal primates[94,456,455] and cats[319], it seems unlikely that CO blobs are purely concerned with color signals.

2.2 Visually evoked and spontaneous activity during the development of the visual system

The functional domains in the visual cortex are organized with single-cell precision over an extended spatial scale ranging up to several millimeters. Naturally, the question arises how this exquisite architecture emerges and maturates during development. Extensive research has shown that the development of the visual system takes place over an extended period in time in a stereotypical set of hierarchically ordered steps. The formation and maturation of the visual system is driven by both activity independent as well as activity dependent mechanisms. Activity independent mechanisms involving axon guidance molecules construct a rough topographic map which is then refined by activity dependent mechanisms to provide a precise set of inputs to a target cell. Activity dependent mechanisms rely on spontaneous and evoked activity. Spontaneous or ongoing activity is not related to an external, experimentally given stimulus but is internally generated, whereas evoked activity is a response elicited by a specific external stimulus.
Spontaneous activity seems to play a prominent role in the development of cortical circuits especially early in development. At early stages in development external stimuli often do not reliably or robustly elicit cortical responses as the feed-forward architecture from the sensory periphery to sensory cortices is not established, yet. In cat, ferret and mice the eye-lids are still closed (although pups might experience visual stimuli through closed eye lids[249,439]) and pups are typically reared in a protected environment with limited sensory stimulation. In contrast, spontaneous activity is present throughout the visual system already prior to birth and is therefore assumed to play a role in shaping the maturation of cortical activity and cortical architecture especially early in development. Due to its presence already at early stages in development, spontaneous activity can also be used to probe the state and development of early cortical circuits without additional stimulus specific contributions. In the following an overview about visually evoked and spontaneous activity during the development of the anatomical and functional organization of the visual system is given. In the main part of this thesis we will analyze imaging data of spontaneous activity to read out the state of cortical activity throughout development and to compare it to the mature functional organization assessed by visually evoked activity.

2.2.1 Early development of the visual pathway

The development of the visual system has been extensively studied in carnivores, especially in cat and ferret (Mustela putorius furo) whose visual systems strongly resemble each other[252]. The ferret belongs to the genus Mustela of the family Mustelidae (**Fig. 2.3a**). They are small

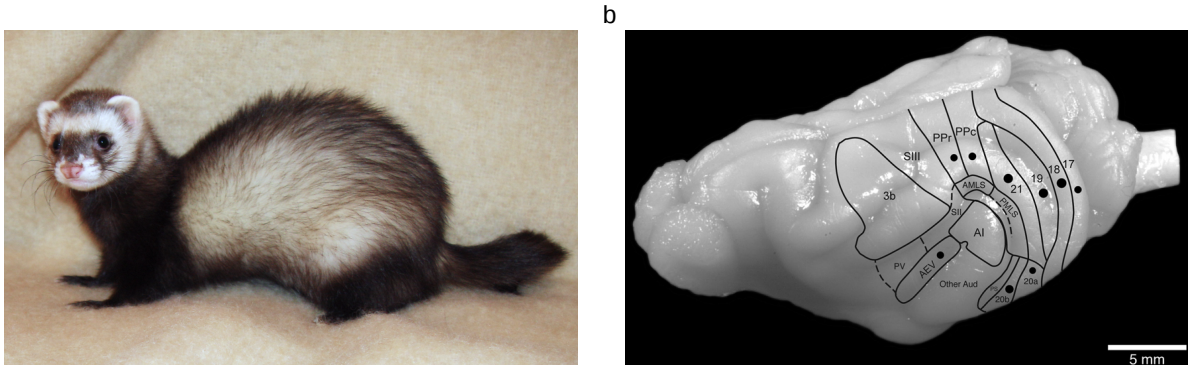

Figure 2.3: Ferret and its brain structure. **a** Ferret, photograph adapted by Alfredo Gutierrez, distributed under a CC BY-SA 4.0 license. **b** Lateral view of the ferret brain (*left*: frontal lobe; *right*: occipital lobe and brain stem) with the boundaries of the areas of the visual system where areas A17 to A21 correspond to V1 to V4, respectively. Image taken from[339].

carnivorous predators that are mostly active around dawn and dusk (crepuscular behaviour). Their average gestation period is 41-42 days[214] and they open their eyes only at around 30 days after birth. Their litter consists of usually between 3 and 7 kits which are weaned after 3 to 6 weeks. They become sexually mature after around 6 months with an average life span of 7 to 10 years.

The ferret's short gestation period and its birth relatively early during its cortical development - it is born three weeks earlier in its development than the cat[267] - makes it a superb animal model for developmental studies. The ferret shows vigorous cortical responses and is physiologically robust compared to the cat at the equivalent developmental stage. Cortical responses can be evoked as early as P23 in ferret which is equivalent to the day of birth in cats whereas neuronal activity in kittens is hard to elicit at this age[76].

The visual system of ferrets develops over an extended period from before birth until after eye-opening (**Fig. 2.4**). Most processes relying on intrinsic mechanisms (activity-independent mechanims or spontaneous activity) have maturated prior to eye-opening, whereas processes depending on visual experience start to become more prevalent briefly after eye-opening (**Fig. 2.4**). Similar to other species, in ferret the retina is maturating prior to the LGN which in turn maturates before V1[450,233]. The number of RGCs in the retina has reached its mature level by postnatal day 6 (P6)[179]. In the developing LGN the inputs from the two eyes are intermixed and at birth the LGN is not laminated, yet[381,396]. Segregation of ipsilateral and contralateral inputs within LGN emerges between embryonic day 39 (E39) and P4. The cellular lamination in LGN begins to appear at around P13[262,254,376]. By P21 the retinogeniculate connections are specific for eye, on/off contrast and layer[396], and by P22 the LGN attains an essentially adult architecture[267], although the receptive fields in LGN still undergo refinement[422,12]. In contrast to primates ferret LGN consists of two major layers A and A1 in between which are four *C laminae*[267] (comparable to those of cats[355] and mink[369]).

Cortical neurons are generated within the ventricular zone (close to the brain's ventricles) from progenitor cells which divide to produce glial cells (non-neuronal brain cells) and neurons[227] which later form the six cortical layers. During early development the transient fetal *subplate* is located below the cortical plate[248,220,221,227] and is responsible for the emergence and maturation of thalamocortical projections[228,276]. The subplate consists of a heterogeneous population of neurons and changes throughout development in size and cellular composition[228,276] until after birth the majority of subplate neurons disappear[227].

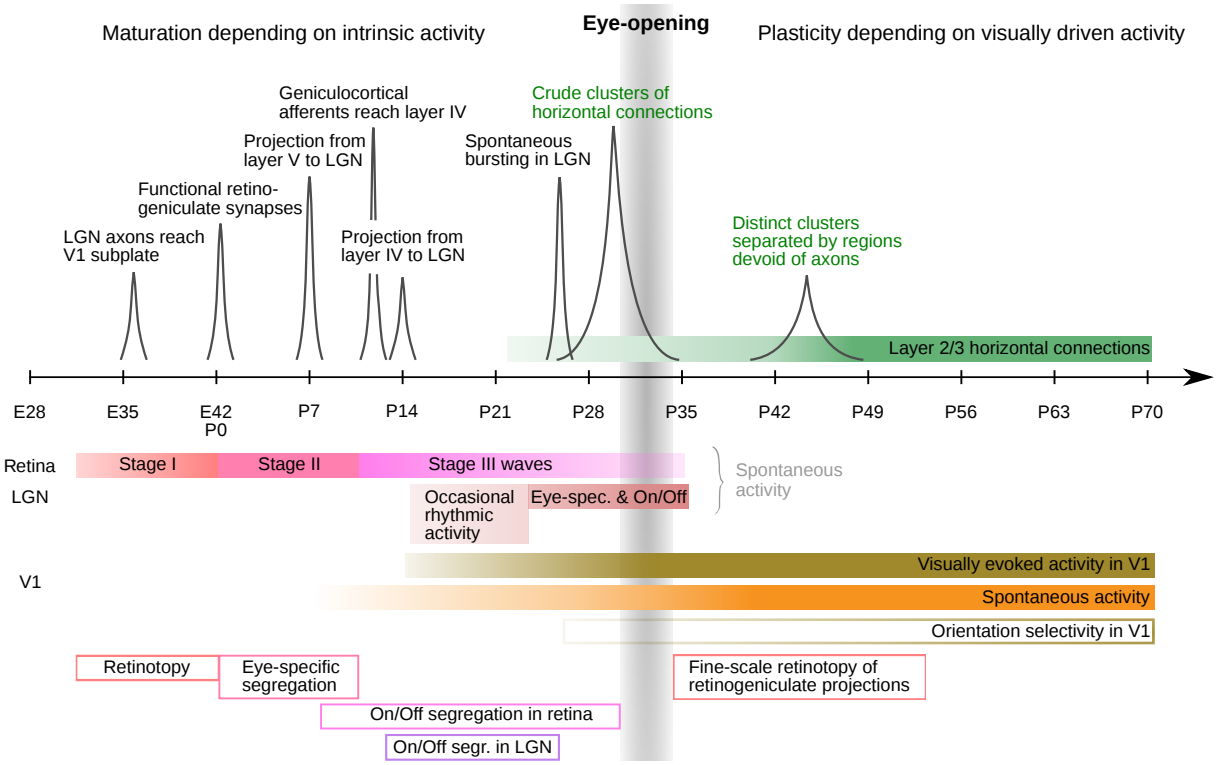

Figure 2.4: Schematic of the development of the ferret visual system. Top part indicates important stages during the development of the anatomical architecture. The colored bars below the timeline indicate periods in time when spontaneous (and visually evoked activity in V1) occurs in different components of the visual system. The open bars (*bottom*) show the development of functional properties of the visual system. Adapted from[376,200].

Already at around E35 LGN axons reach the V1 subplate to establish a temporary link[376]. They reach their final target layer IV at around P16[410]. The neurogenesis in visual cortex starts at around E20 and continues until two weeks after birth[214]. The primary visual cortex can first be discerned at around P14. Its neurogenesis follows an inside-out radial gradient, as observed in primates and other mammals, where neurons of the deeper cortical layers are generated before those of the superficial layers (except for layer I)[214]. Neurons of one layer are typically generated over a period of several days, and migrate to their specific layer within one week[214]. Neurons of layer II/III are mostly produced between P1 and P8 and by P21 most of them have completed their migration[214]. At P33 the laminar distribution of V1 resembles the distribution of the mature animal[214]. The imaging data used in this thesis was obtained between P21 to P37, so after the establishment of layer II/III.

2.2.2 Spontaneous activity in the visual system during early development

Retinal waves

Spontaneous activity has been observed throughout the visual system already at early stages in development. Most studies examined the properties of spontaneous activity and its influence on the development of neuronal networks in the retina. RGCs generate bursts of spontaneous action potentials that are spatially correlated and that spread across the retina in a wave-like manner. These retinal waves start before the photo receptors are capable to react to incoming

light, and they disappear at around eye-opening[200]. Retinal waves can be separated into three stages occuring one after each other and differing in wave velocity, domain size and frequency (**Fig. 2.4**). Waves of stage I start to appear prior to birth in ferrets[297,200], are rather infrequent (occur every 1-2 min) and require gap junctions to mediate activity[416].
Stage II retinal waves start to appear at around birth[402,416] and occur at a similar frequency every 1-2 min at a time when eye-specific input is segregated in LGN (**Fig. 2.4**). These waves do not travel across the entire retina, but are several 100 µm wide[297]. Since they occur relatively infrequent, it is unlikely that RGCs in different eyes but at a similar position within the visual field are active at the same time. This makes stage II waves suitable to relay instructive, eye-specific information to higher brain regions[297,126,62,63].
After about two weeks after birth stage III retinal waves appear and are present until around eye-opening. These activity waves are correlated between RGCs with the same polarity, and are, thus, capable of relaying information about ON vs OFF cells to areas in the brain[449,320].

Spontaneous activity in LGN

Experiments studying the spontaneous activity in the developing LGN *in vivo* are limited. Multi-electrode recordings in ferrets as early as one week prior to eye-opening (coinciding with stage III retinal waves) showed that spontaneous activity in LGN is generated from interactions between retina, thalamus and visual cortex[437]. Its spatiotemporal properties are modulated by corticogeniculate feedback connections and retinogeniculate feedforward input[437]. Neurons of the same polarity (on-center or off-center) are more correlated in their spontaneous activity than neurons of different polarity. Spontaneous activity shows significant binocular correlations if the corticogeniculate feedback connections are intact. The contralateral eye mainly drives spontaneous activity in LGN. Cutting the optic nerve to the contralateral eye changes the spontaneous activity patterns to shorter, more coherent and more frequent bursts[437].

Spontaneous activity in V1

Only little is known about the spatiotemporal properties of spontaneous activity in the developing visual cortex of ferret. Electrode experiments in awake ferrets suggest that the spatial layout of spontaneous activity in primary visual cortex prior to eye-opening (P22 to P28) is patchy with a typical spatial scale of about 1 mm. This spatial pattern remains after LGN is transiently blocked suggesting that spontaneous activity is generated intrinsically in cortex[86].
Large parts of cortex in immature kittens at around birth are silent[206,207]. Only after a few days after birth brief, synchronized and infrequent spontaneous activity is observed. With age its frequency increases whereas its synchronicity decreases[206,207]. From the third week after birth sustained spontaneous activity is observed which is inhibited by the animal's arousal reactions[206,207]. In the anaesthetized, adult cat spontaneous activity in V1 comprises dynamically switching spatial activity layouts that resemble its evoked orientation preference map. These spontaneous activity states extend over several millimeters[429,235,327] and are coordinated between hemispheres[327]. It remains unclear from this work on which fine spatial scale and over which distance the similarity between spontaneous and evoked activity holds. It is also unresolved how this similarity emerges during development.
In rodent neocortex different stages of spontaneous activity have been extensively studied. Already several days prior to birth spontaneous Calcium transients are observed in neocortical slices of mice on a single cell and network level[97]. In neocortical slices from newborn rats large scale network events - termed cortical early network oscillations (cENOs) - propagate over the entire cortex ($\sim 2\frac{mm}{s}$)[150]. These activity patterns are similar to spontaneous Calcium waves observed *in vivo* in awake mice[7]. Several days after birth spontaneous activity is dominated by

cortical giant depolarizing potentials (cGDP) with a higher frequency, faster kinetics and only partially affected by AMPA/NMDA receptor antagonists[17]. These cGDPs are hypothesized to synchronize local neural assemblies[277]. At around P10-11 prior to eye-opening slow activity transients (SATs) are observed in visual cortex of rats produced by the summation of rapid oscillatory bursts[93]. In addition to these large-scale spontaneous patterns, spatially confined gamma oscillations (30-40 Hz) are observed in cortex of neonatal rats[458,309]. Another type of short and local network oscillation are spindle bursts (10-20 Hz) observed in primary visual and somatosensory cortex of rats[239,170,308,458,459] and similar to the spontaneous activity observed in immature ferret visual cortex[86,85]. This spindle burst activity is synchronized across neuronal populations and correlated with spontaneous musculuar twitches which are typically evoked from bursts of activity in the spinal cord[239].

2.2.3 The role of spontaneous activity in the development of neuronal networks

In this thesis we use spontaneous activity as a read out for the state of cortical circuits early in development. However, extensive research has shown that spontaneous activity together with other mechanisms intrinsic to the brain, i.e. axon guidance molecules, and mechanisms that involve externally driven activity plays an essential role in the development of the anatomical and functional architecture of the visual system. We therefore give a brief overview about the current state of the research on how spontaneous activity is generated in cortical circuits and how it is involved in the development and maturation of the organization of the visual system by giving specific examples.
It is still unresolved to which extent each one of these activity dependent and independent mechanisms contributes to the formation of cortical circuits and how they interact. Neuronal networks are formed by generating and refining correct connections between cells. Synaptic connections are typically formed in three steps. First, during pathway selection, the growth cones of neurons form and navigate through the cortex to find their target. Second, at the target region growth cones contact a localized group of target neurons and establish an initial layout of connections[370]. In the third step, this initial layout is refined to a precision on the level of individual synapses by selectively removing and expanding connections[162,245].
Activity-dependent mechanisms underlying the formation of neuronal networks can play an *instructive*, *permissive* or *selective* role[376]. Activity is instructive if it is not only required for the establishment of a neuronal structure, but when its level or its pattern can be directly related to the shape of the structure. Activity is permissive if a certain level of activity is required for establishing a structure, but higher levels or patterns of activity do not influence the structure of the neuronal networks. Activity is selective if it is required for the maintenance of a neuronal structure, and a loss of activity would lead to a deterioriation of said structure.

Mechanisms underlying spontaneous network activity

Spontaneous activity is ubiquitously observed throughout the developing nervous system of all species examined, so far. It consists of bursts of activity coordinated across space and time which makes it a well-suited candidate for restructuring the developing brain circuits. The underlying mechanisms of spontaneous activity within the different brain areas are highly similar.
Synchronized, spontaneous activity may be triggered by a specific brain area, or a group of pacemaker neurons[238]. So far, it is unclear which neurons could function as pacemaker cells[277]. At early stages of development most neurons are electrically coupled via gap junctions[127]. Experiments *in vivo* and *in vitro* have shown that gap junctions mediate spontaneous activity

around the time of birth[460,225,73]. This spontaneous activity is synchronized between a small number of neurons. Together gap junctions and synchronized spontaneous activity can regulate the formation of excitatory synapses[238]. Specifically, gap junctions contribute to the emergence of stage I and III retinal waves[73,451,416,13].
It is thought that in early development GABA and glycine act as excitatory neurotransmitters because of an initially higher intracellular chloride concentration[31,39]. Since GABA and glycine transmitters are typically present before glutamatergic synapses are established, early spontaneous activity in cortical circuits largely relies on them. During later stages of development these two transmitters are thought to become inhibitory[39], while simultaneously the spatial pattern of spontaneous activity changes. In the retina, local inhibitory circuits desynchronize the spontaneous activity between neurons with dissimilar functional properties[13]. In addition, the formation of excitatory and inhibitory synapses seems to depend on GABA acting either excitatory or inhibitory[258,259,79,144,338,11]. This indicates that the switch of GABA and glycine plays an important role for forming balanced excitatory and inhibitory circuits. However, it has recently been suggested that depolarizing GABAergic potentials are an effect of the conditions of the *in vitro* experimental setup[187,123] (and see[127] and references therein). To fully understand the complex chloride dynamics underlying the GABAergic potentials further experiments are necessary.
Extrasynaptic neurotransmission such as the nonsynaptic release of transmitter or the escape of transmitters from the synaptic cleft (termed *spill-over*) contributes to the formation of spontaneous activity, especially in networks with immature synaptic connections. Extrasynaptic communication underlies the formation of stage II[452,466] and stage III[13,41,141] retinal waves, and is observed in the brain stem[380], hippocampus[115,74] and neocortex[17,238]. A considerable amount of the influence of excitatory GABA and glycine stems from the extrasynaptic transmission of neurotransmitters.
The formation of transient cells and transient connections contributes to a large degree to generating and propagating early spontaneous activity. Specifically in the neocortex of placental mammals, neurons within the subplate of the cortical, ventricular zone are among the first neurons being generated[16]. They play a major role in the formation of thalamocortical connections, and receive input mostly from LGN and from cortex[121], while relaying signals to layer IV and via feedback connections to LGN[113]. Subplate neurons are highly spontaneously active. Excitatory feed-forward connections from retina relay retinal waves to them[5], and due to strong feedback loops and strong lateral connectivity they intrinsically generate spontaneous activity bursts[121]. These neurons are eliminated when direct connections from thalamus to layer IV of V1 maturate[16]. Transient excitatory connections are observed in the retina where they contribute to stage II retinal waves[143,465].
Remarkably, spontaneous activity is present throughout development, although its underlying cortical substrate is constantly changing during this period of time. To compensate for these changes caused by neuronal development, synapse formation and elimination and maturation of synaptic connections, a homeostatic mechanism is expected to underly the formation of spontaneous activity not only on a single cell level, but on a network level[41,238]. Such a homeostatic mechanism has been directly observed in the retina. The retina of transgenic mice that were constructed to not exhibit cholinergic retinal waves generated after a few days compensatory waves[397,398,409]. Similar experiments in spinal cord and hippocampus showed that perturbing the mechanism that generates spontaneous activity leads to compensatory activity together with a potential restructuration of the circuit[88,102,385].

Activity-dependent plasticity mechanisms

So far, a complete understanding of the mechanisms that can alter the wiring diagram driven by neuronal activity is missing[257]. It has classically been assumed that neuronal activity affects the wiring in a Hebbian-like way[403,297,289,287,306]. The Hebbian plasticity rule strengthens connections between neurons that are correlated in their activity and weakens connections between neurons that fire uncorrelated[177]. Indeed, experiments in the visual system have found evidence for Hebbian plasticity in the maturation of retinogeniculate projections where synapses are strengthened via Long-Term Potentiation (LTP), and weakened via Long-Term Depression (LTD)[63]. Subsequent experiments could relate developmental synapse pruning to balanced learning rules enabling both Long-Term Potentiation and Long-Term Depression at retinogeniculate synapses[256]. It has recently been shown that spontaneous activity influences the connectivity structure on a sub-cellular level at individual synapses[245,448]. Recent experiments revealed that synapses that are not synchronized with their neighbours become depressed[245,448]. This local plasticity mechanism requires precise pre- and postsynaptic firing and appears to be an appropriate candidate to restructure connectivity according to highly correlated spontaneous activity. Although there is experimental evidence for competitive and activity-dependent mechanisms underlying the development of cortical circuits in the visual system, it has been also shown that several developmental processes require non-Hebbian learning rules which rely on the activation of either the pre- or the post-synaptic cell but not both[247,350]. Indeed, theoretical studies have shown that generic plasticity rules including Hebbian-like plasticity and homeostatic mechanisms in a network model are sufficient to generate network activity with several key properties of spontaneous activity observed in experimental data[253,173]. In summary, a combination of Hebbian and non-Hebbian plasticity mechanisms potentially varying between brain regions appears to translate neuronal activity into changes in the anatomical wiring[242].

Influence of spontaneous activity on the development of components of the visual system

Retinotopic maps in LGN Initially, coarse retinotopic maps are instructed by molecular guidance cues such as ephrin/Eph which guide projections from the LGN to V1 independently of activity related mechanisms (in ferret[69], in mouse and chick[34]). The refinement of the retinotopic map depends on spatially correlated retinal activity (reviewed in[91,162,200]). Retinal waves are capable of transmitting information about neighbouring cells to higher brain regions and, thus, can refine the retinotopic maps. Blocking retinal waves or perturbing their correlated, spatiotemporal pattern results in a reduced refinement (in ferret[341], in mouse[61,454]; reviewed in[242,257]) indicating an instructive role of spontaneous retinal activity.

Eye-specific segregation in LGN Eye-specific segregation in LGN develops in two main steps. Early in development inputs from the two eyes to LGN are intermixed and neurons in LGN obtain binocular input. At the time when stage II retinal waves occur[267], the retinal connections from the neuron's less preferred eye are eliminated whereas the connections from the preferred eye are strengthened and maintained until the characteristic left and right-eye laminae have developed (**Fig. 2.4**).
Since stage II retinal waves occur independently in the two eyes, they are thought to segregate the retinogeniculate axons. Experiments showed that by increasing retinal wave activity in one eye, this eye's ipsilateral projections strongly extend (in ferret[341]). When elevating retinal wave activity in both eyes, the areas occupied by the two eyes in LGN remain normal (in ferret[401]). These results suggest that eye-specific segregation is based on binocular competition.
Subsequent experiments demonstrated that perturbing the spatiotemporal properties of stage

II waves does not impair the development of eye-specific segregation (ferret[203,394], but see mouse[453]), but an increase in the fraction of asynchronous RGCs spiking occurring outside of burst activity perturbs normal eye-specific segregation. Similarly, optogenetically stimulating both eyes synchronously disrupts the refinement of eye-specific segregation (in mouse[463]). These results indicate, that normal eye-specific segregation requires only certain features of stage II wave propagation as well as asynchronous bursty firing patterns between the two eyes (reviewed in[242]).
Blocking stage II retinal waves in both eyes still yields eye-specific areas in LGN since stage III retinal waves which occur later during development seem to compensate for the missing stage II waves (mice[314], ferret[202]). The eye-specific areas that are occuring under these conditions are randomly distributed and vary strongly between individuals indicating that not only the presence but also the timing of long-range stage II retinal waves is essential for the normal development of eye-specific segregation. Other factors that are only present early in development, i.e. the axon guidance cue Ephrin-As, may be required for the normal development[200]. This suggests that spontaneous activity acts in concert with activity-independent mechanisms to induce eye-specific segregation.

Horizontal long-range connectivity during early development Lateral excitatory and inhibitory synaptic connections undergo substantial remodeling during development (see also **Fig. 2.4**). Prior to eye-opening at around P21, but after the thalamocortical loop has been established, uniformly distributed and few unbranched horizontal connections that extend up to 1 mm have formed in V1[364,122,46]. Although such axons can extend up to 1 mm, neurons exchange functional inputs mainly with their local neighbours[109,322]. Basal dendrites are short and weakly branched prior to P22[46]. By P27-28 crudely clustered horizontal connections which extend 1-2 mm are established (ferret[122,364,46], cat[275,67,66,174,149]). At around P28 to P35 these crude clusters are being refined and exhibit more elaborate branches with unbranched axons in between them. Between P42 to P49 distinct clustered connections separated by areas free from axons were visible[122,364]. At this age an adult-like level of specificity was attained by selectivitely eliminating long-range horizontal connections that initially project to incorrect columns, and by adding long-range lateral connections to correct columns[122]. Inhibitory connections appear to become refined on a faster time scale than excitatory connections[108].
After bilateral enucleation clustered horizontal connections in V1 still appear, whereas continuously silencing V1 (TTX applied at P21 for two weeks) results in randomly, not-clustered distributed axon collaterals (in ferret[364]). These results strongly indicate that the initial emergence of clustered connections requires cortical activity, but not retinal activity. Potentially, correlated spontaneous cortical activity drives the emergence of clustered long-range connections. Evidence for this was found at a later stage in development by inducing strabismus in kittens and thus eliminating correlation in the activity between the two eyes[273]. This leads to a perturbed distribution of horizontal connections which segregate based on ocular dominance and indicates that normal patterns of visual activity are necessary for normal circuit formation and refinement[273].
Dark rearing and binocular deprivation permit the initial development of lateral connections, but prevent their normal refinement since incorrect axons are not eliminated (in cat[275,66]). This suggests that the pruning process depends on visual experience. Similarly, other studies showed that lateral connections in mature cortex in dark reared and in lid-sutured animals is spatially more constricted and shows less clustering than in normal animals (in ferret[439]).

Ocular dominance It is still unclear how ocular dominance bands are initially emerging. In cats they are thought to form within one week after eye-opening[99,100], but are refined further in

development[234]. Experiments showed that these early ocular dominance patterns are not affected by inducing an imbalance in retinal activity between the two eyes[105]. However, blocking stage II retinal waves severely perturbs their formation (in ferret[201]). This suggests that stage II retinal waves potentially shape the segregation of LGN axons at an early stage in development when they are still connected to the subplate (in ferret[200]).

Orientation selectivity It is currently still unclear when and how the layout of orientation domains in visual cortex of primates and carnivores develops. Already prior to eye-opening individual neurons show orientation selectivity (in ferret[76,249]). Cortical domains start to become selective for certain orientations at around eye-opening and maturate over the following days into orientation preference maps as seen in adults (in ferret[77,439]). Animals reared in a dark environment (*dark-rearing*, that means animals are without any form of visual experience) still show an orientation preference map but with a lower level of selectivity than normally reared animals (in ferret[439]). In both normal and dark-reared animals the selectivity increases during two weeks following eye-opening eventually plateauing. However, orientation selectivity in dark reared animals remains lower than in normally reared animals. Nevertheless, this suggests that experience independent mechanisms play a significant role in the emergence and maturation of orientation selectivity. Moreover, applying binocular lid-suture leads to only rudimentary levels of orientation selectivity in ferret visual cortex[439] (but see in cat[99,158]). This indicates, that not the presence of visually evoked responses alone but specific spatiotemporal properties of activity are necessary for the maturation of orientation preference.
Blocking all cortical activity early in development disables the formation of orientation selectivity (in ferret[76], but see mouse[167]). Experiments in which an animal was reared in an environment with only one orientation present (*stripe-rearing*) revealed that the experienced orientation occupied a larger area within the layout of orientation domains than other orientations (in cat[377,419]). Nevertheless, some regions still preferred orientations that the animal had never seen arguing for the contribution of an experience-independent mechanism for determining the tuning of neurons. Together, these results suggest that intrinsic, spontaneous activity either from retina, LGN or from cortical sources plays a role in the emergence of orientation preference maps.

2.2.4 Summary

Spontaneous activity is observed throughout the nervous system already at early stages in development. It acts together with activity-independent mechanisms such as guidance molecules and evoked activity to drive and maintain the anatomical and functional organization of the visual system. The development of the visual system consists of multiple stages; the initial stage seems to require a combination of spontaneous activity and activity-independent mechanisms, whereas later stages of refinement typically rely more on visual experience. The presence of spontaneous activity already early in development makes it a suitable tool for assessing the state of cortical activity and its changes throughout development.

2.3 Theoretical background

Cortical activity in primates and carnivores exhibits a modular and distributed correlation structure. The goal of this thesis is to shed light on key mechanisms responsible for the formation of these two observed properties by studying models of cortical circuits. However, cortical circuits *in vivo* are highly complex and intricate. Dynamics on many different temporal and spatial scales contribute to give rise to correlated activity within and even across different brain regions. It is computationally highly demanding to capture these multi-level dynamics of cortical circuits. To reduce the complexity in their description, we take advantage of the fact that the two observed features of cortical activity emerge on the mesoscopic level. Therefore, we can consider simplified descriptions of the full circuits, modelling cortical activity on the population level. In the following, we will give an overview about neural network models and their limitations in the descriptions of cortical activity. In the first part we will briefly describe classical network models[447,446,159,317,130,226,148,14] on which the models presented in Chapter 5 and Chapter 6 in this thesis are based. In the second part we will provide an overview about concepts and tools used in this thesis to analyze datasets of activity patterns obtained either from network models or in imaging experiments.

2.3.1 Modelling dynamics of cortical activity

We aim towards describing the modular and long-range correlated structure of cortical activity at early stages in development as described in the main part of this thesis. A well used approach to describe this kind of population activity is by a network model consisting of simplified firing rate units that are active if their integrated input crosses a certain threshold and interconnected. One of the most influential firing rate network models is the *Wilson-Cowan* model[447,446]. This model yields a coarse-grained desciption of the mean activities of two interacting, homogeneous populations of excitatory (E) and inhibitory (I) neurons in a large-scale network. In the following, we will briefly summarize how its network dynamics can be derived.
To derive the dynamics of the Wilson-Cowan model several simplifying assumptions are made. The variety of neuron types observed *in vivo* is generalized to one excitatory and one inhibitory population of units, neglecting differences in morphology, connectivity schemes, signal transmission dynamics, etc. The model describes the time coarse-grained activity of excitatory and inhibitory units. Therefore changes in activity on a time scale which is larger than the units' membrane time constant τ can be investigated. To describe the refractory period of neurons after an action potential, the fraction of units within the refractory period r_E (excitatory units) and r_I (inhibitory units) is introduced. The network units are homogeneously distributed within a two-dimensional plane with density ρ_E for excitatory and ρ_I for inhibitory units motivated by the layer structure of cortex[64], and by the two-dimensional receptive fields structure in which sensory information is received in visual cortex[172,250,181,72]. In the network model the units typically interact via recurrent lateral connections that only depend on distance. Thus, their interaction is isotropic and homogeneous across the two-dimensional plane. Each unit's output activity is weighted by an interaction weight to yield the input to the postsynaptic unit. The dynamics of the spatially structured population activity are then given by[446]

$$\tau \frac{\partial}{\partial t} u_E(\mathbf{x},t) = -u_E(\mathbf{x},t) + (1 - r_E u_E(\mathbf{x},t)) S_E \left[\alpha(t)\tau \left(\rho_E u_E(\mathbf{x},t) * M_{EE}(\mathbf{x},t) - \right.\right. \tag{2.1}$$

$$\left.\left. \rho_I u_I(\mathbf{x},t) * M_{EI}(\mathbf{x},t) + P(\mathbf{x},t)\right)\right] \tag{2.2}$$

$$\tau \frac{\partial}{\partial t} u_I(t) = -u_I(\mathbf{x},t) + (1 - r_I u_I(\mathbf{x},t)) S_I \left[\alpha(t)\tau \left(\rho_E u_E(\mathbf{x},t) * M_{IE}(\mathbf{x},t) - \right.\right. \tag{2.3}$$

$$\left.\left. \rho_I u_I(\mathbf{x},t) * M_{II}(\mathbf{x},t) + Q(\mathbf{x},t)\right)\right]. \tag{2.4}$$

where $*$ denotes the convolution operator. Here $u_E(\mathbf{x},t)$ and $u_I(\mathbf{x},t)$ describe the time coarse-grained activity of excitatory and inhibitory cells at time point t and location $\mathbf{x}$. $P(\mathbf{x},t)$ and $Q(\mathbf{x},t)$ denote the external input to excitation and inhibition, respectively, combining inputs to cortex from feed-forward and feed-back sources. S_E and S_I denote nonlinear functions which are typically chosen to be a sigmoidal function modeling the nonlinear threshold response of neurons. $\alpha(t)$ is the membrane impulse response describing the response to a unit excitation. M_{KL} (with $K,L \in E,I$) denote the connectivity weights between units in population K and L only depending on their distance.
Applying a phase-plane analysis reveals that the system provides three modes of behaviour that can be related to activity in sensory cortex, thalamic nuclei and prefrontal cortex[446]. The dynamical mode corresponding to sensory cortex involves transient responses. The dynamical mode appropriate for thalamus shows non-linear oscillatory behaviour, whereas the mode for prefrontal cortex exhibits spatially inhomogeneous stable steady states. Variants of this model have been widely used when modeling neural networks to describe the activity of a population of neurons[32,226,8,14,389].

Ring model

One specific type of the Wilson-Cowan model is the *ring model* where the network units are arranged on a one dimensional line with periodic boundary conditions[32]. Each unit is described by its preferred orientation θ which is determined by its position on the ring. In the limit of a large network, the mean activity $m(\theta,t)$ of excitatory and inhibitory units obeys the following dynamics

$$\tau_0 \frac{dm(\theta,t)}{dt} = -m(\theta,t) + g[h(\theta,t)] \tag{2.5}$$

$$\text{with} \quad h(\theta,t) = \int_{-\pi/2}^{\pi/2} \frac{d\theta'}{\pi}\, J(\theta-\theta')m(\theta',t) + h^{\text{ext}}(\theta-\theta_0) \tag{2.6}$$

with the characteristic time constant τ_0, a nonlinear function g and the total synaptic input $h(\theta,t)$. $J(\theta-\theta')$ denotes the interaction between units θ and θ' which is chosen such that units with similar preferred orientations excite each other whereas units that are orthogonally tuned inhibit each other. The external input $h^{\text{ext}}(\theta-\theta_0)$ models the input evoked by a bar of a certain orientation θ_0 and contrast c to a unit with preferred orientation θ. The input is modulated such that for nonzero contrast it drives most strongly units with a preferred orientation close to θ_0. For zero contrast the input is homogeneous across units. This simple network model allows to study the emergence of orientation selectivity via different mechanisms and is used for modeling spontaneous activity (see below). In the case that orientation selectivity is shaped by the recurrent connectivity in the presence of homogeneous external input, the model reproduces characteristic properties of experimentally observed visually evoked cortical responses, such as contrast invariant responses[32]. In the following we will give an overview about an extension of the ring model aiming towards describing the dynamics of spontaneous activity.

Network model of spontaneous activity

Previous experimental studies in cat visual cortex have shown that spontaneous activity fluctuates on a time scale of several tens of milliseconds[235]. During these fluctuations the spatial layout of spontaneous activity changes such that a different layout of domains becomes active. These layouts often resemble visually evoked response patterns[235]. The underlying mechanism generating spontaneous activity with these properties has not been resolved, yet. Two mutually exclusive scenarios of a network model have been proposed that both reproduce the similarity

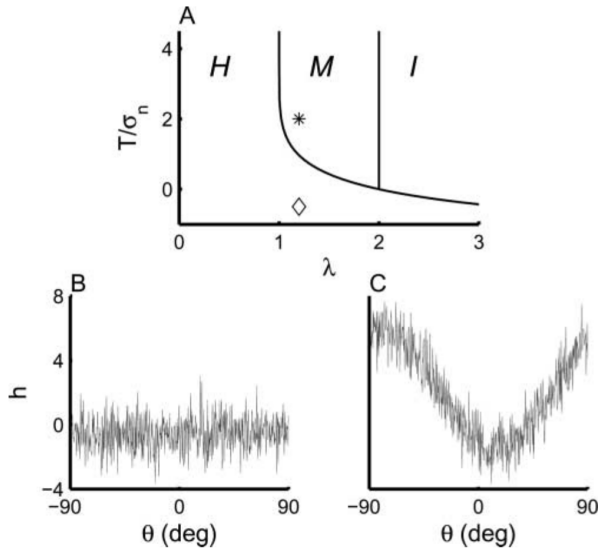

Figure 2.5: Phase diagram of network states in the ring model. **a** Phase diagram of the ring model as a function of the strength of cortical interactions λ and the ratio of the mean feedforward drive T to its standard deviation σ_n. H denotes the homogeneous phase, M denotes the marginal phase and I denotes the instability phase. **b** Example of network input h in the homogeneous (H) phase as a function of the preferred orientation θ. Network settings of simulation are marked by diamond in (**a**; $\lambda = 1.2$, $T/\sigma_n = -0.5$). **c** Example input h in the marginal (M) phase. Simulated for network settings marked by asterisk in (**a**; $\lambda = 1.2$, $T/\sigma_n = 2$). Reproduced from[159].

between the spatial layout of spontaneous activity and evoked responses[159]. To experimentally test these two scenarios the authors[159] provided several model predictions. In the following we will describe both scenarios and how they can be distinguished based on the model predictions. In their paper Goldberg and colleagues[159] studied several scenarios of a dynamic network model and determined statistics to experimentally test their models. To model spontaneous and stimulus evoked activity in the mature visual cortex, the authors used an extension of the one-dimensional ring model[32]. In their model they considered correlations in the feed-forward input, cortical interactions that are spatially restricted and used a layout of orientation domains that was experimentally obtained[159]. In addition, they considered a network representing several stimulus features instead of only orientation selectivity as done in the ring model[159].
The network model is based on the ring model as explained above. Each firing rate unit (corresponding to a mini-column in visual cortex) presents a particular preferred orientation. In the absence of visual stimuli the network is driven by Gaussian white noise to model spontaneous activity.
To experimentally test the different scenarios of the network model, the authors investigated two quantities measuring the similarity in the spatial layout of spontaneous activity and evoked response. The similarity index (SI) is the correlation coefficient between an instantaneous spontaneous activity pattern and the response pattern evoked by a moving grating. The spike-triggered SI measures the correlation between the spiking of an individual neuron and the global SI.
In the network model the evoked states correspond to activity bumps localized around one of the orientation domains. The ensemble of evoked responses forms a circle embedded within a two-dimensional subspace. In contrast, the spontaneous activity can be in either one of three regimes depending on the strength of recurrent connections and the ratio between the mean of

the spontaneous LGN drive and its standard deviation (**Fig. 2.5a**). The H regime (*homogeneous* phase; weak recurrent connectivity; **Fig. 2.5b**), also termed the single state scenario, is dominated by the noisy feed-forward input and the activity fluctuates around a spatially uncorrelated solution corresponding to a resting or background state. The time constant of the fluctuations is fast and on the order of the time constants of the synaptic currents. The single state scenario generates high-dimensional (noise-driven) activity patterns that generally do not resemble the orientation preference map and therefore lead to a low SI and a small bias in the spike-triggered SI. The SI distribution is narrow and Gaussian shaped. In the M regime (*marginal* phase; moderate levels of recurrency; **Fig. 2.5c**), also termed the multiple states scenario, the solution is a localized bump in orientation space. Assuming that the underlying connectivity structure shapes spontaneous activity such that it resembles the layout of evoked cortical responses, the noisy cosine-shaped profile of spontaneous activity is very similar to the evoked state. In this regime the network selectively amplifies certain patterns via its recurrent connectivity, such that co-active units tend to excite themselves whereas units that are anti-correlated in their activity tend to inhibit each other. The noise in the input causes the localization of the bump to slowly move. In this regime spontaneous activity is described by dynamic transitions between different attractor states intrinsic to the network. The fluctuations of spontaneous activity are slower than the time constants of the synaptic currents due to the slow transitions. Spontaneous activity patterns are confined to a low-dimensional manifold and resemble to a high degree the evoked response patterns, resulting in a high SI and a high bias in the spike-triggered SI. Due to being constrained to a low-dimensional manifold, the SI distribution can be highly non-Gaussian. Lastly, in the I (*instable*) regime at high recurrency strengths the activity diverges.
Several model scenarios have been found to be consistent with previous experimental data of spontaneous activity[235], and could not be invalidated by the established measures. In this data the SI distribution is Gaussian-like and the spike-triggered SI exhibits a positive bias[235,159]. Both the H regime (corresponding to the single state scenario) and the M regime encoding multiple stimulus features (corresponding to the multiple states scenario) match these experimentally observed properties of spontaneous activity. However, these two network scenarios differ in how the width of the SI distribution changes with the number of orientation columns modeled. In the single state scenario (H regime) the input to the network is dominated by noise which yields Gaussian distributed similarity indices. Moreover, the width of the SI distribution decreases with the network size as $1/\sqrt{N}$ with N the numbers of columns in the network as remote regions are independent from each other. In contrast in the multiple state scenario (M regime) the similarity between spontaneous activity states and the orientation preference map is independent of the number of orientation columns modeled due to the slow transitions from one global state to another.
To experimentally distinguish these two scenarios, the width of the SI distribution as a function of the observed region size should be analyzed. A recent study[327] in anesthetized cat reported that the width of the distribution of the similarity indices between spontaneous activity states and the orientation preference map changes only little when comparing the distribution based on a single hemisphere to the distribution based on both hemispheres. In Chapter 3 in this thesis, we will test both proposed scenarious by systematically varying the region size over which the SI is calculated to quantitatively assess the dependency of the width of the distributed similarity indices as a function of the area size in the awake animal.
In the ring model the activity patterns emerge through selective amplification via recurrent connectivity. Co-varying units excite each other and anti-correlated units inhibit each other, and in turn the activity pattern is iterated and its decay rate is slowed down. In experimental data only a limited slowing of the dynamics has been observed[235] and instead spontaneous activity appears to exhibit fast temporal fluctuations[235,317]. In the next section we briefly discuss an alternative method termed balanced amplification that allows to amplify activity states without

a slowing of the dynamics.
The ring model relies on being homogeneous and isotropic, e.g. it requires a uniform and homogeneous distribution of preferred orientations across the network units. In the case that the stimulus features are heterogeneously distributed, the network's line attractor disappears and a low number of discrete attractor states remains. However, experiments have demonstrated that cortex is highly heterogeneous in its distribution of represented stimulus features and also in the properties across neurons. In the next section we briefly discuss consequences of taking into account network heterogeneity. In Chapter 5 we will use network heterogeneity as a potential mechanism to generate long-range correlation structure within activity patterns.
In summary, in this extension of the ring model spontaneous activity is described by activity patterns that are driven by unstructured input and selectively amplified via the underlying connectivity structure. This network model is able to reproduce experimentally observed features of spontaneous activity, such as its similarity to the visually evoked response map, the timescale of its fluctuations and the shape of the SI distribution.

Balanced amplification

The ring model selectively amplifies certain activity patterns via its recurrent connectivity by covarying units exciting each other and anti-correlated units inhibiting each other. In the absence of the recurrent circuitry an activity state would decay on a time scale determined by cellular and synaptic time constants. The recurrent circuitry slows the decay rate by iterating activity states. The amplification can overcompensate the intrinsic decay rate and lead to the growth of the activity states. However, in experimental data only a limited slowing of the dynamics has been observed[235].
An alternative mechanism which is termed *balanced amplification* for the selective amplification of activity patterns from unstructured input noise relies on the balance between strong recurrent excitation and strong feed-back inhibition[317]. Such a balance is theoretically hypothesized to be present in cerebral cortex[434,433] and experimental signatures of it have been observed[168,27,444].
It is assumed that both excitation and inhibition are strong, and thus small spatially dependent fluctuations in the net input drive to excitation and inhibition drive large, spatially modulated fluctuations in the total activity of excitation and inhibition[434,433,317]. The key assumption in this model is that the connectivity matrix is non-normal due to the characteristic structure of neurons exhibiting either purely excitatory or inhibitory connections which leads to a hidden feed-forward connectivity between activity patterns. Specifically, a sum pattern (of excitation and inhibition) is amplified from a differentially driven excitation and inhibition pattern (difference pattern)[317]. Due to this feedforward structure the dynamics of neither the sum nor the difference pattern are slowed down. This mechanism can enhance certain network states while maintaining fast network dynamics as observed in the experimental data of spontaneous activity[235].

2.3.2 Influence of network heterogeneity on network activity

The network models[32,159] described previously rely on the assumption that the interactions are homogeneous and isotropic and each unit shares identical properties. An isotropic and homogeneous network exhibits a line attractor where it is possible to shift an activity pattern in space and the result is a new stable pattern of the same shape but at a new location. Using this mechanism, a particular network location can encode e.g. a particularly oriented stimulus in a one to one relation as shifting the orientation of the edge-like stimulus in visual space corresponds to shifting the cortical response pattern in cortical space. However, in general cortical circuits are

not homogeneous and isotropic and neurons differ in their properties. Cortical circuits are highly heterogeneous, e.g. in their distribution of anatomical connections[51], their single cell properties[293,283] and their distribution of preferred orientation[159]. The brain consists of a large variety of different cell types of inhibitory interneurons with potentially different electrophysiological and anatomical properties[140,426]. Similarly, excitatory pyramidal cells show heterogeneous electrophysiological properties[293].
Previous studies have investigated the consequences of introducing heterogeneity into network models. Already in the presence of small network heterogeneity the line attractor disappears[353] and the activity patterns within the network cluster into a small number of discrete states[464,428,408,353] with a relative large basin of attraction[428]. Network heterogeneity breaks the network's translation and rotation symmetry and constrains the set of continuous attractors such that only a lower dimensional set of possible attractor states is reached. The speed with which the activity state drifts away from the formerly stable state increases with the amount in heterogeneity[353]. Heterogeneity in more than one network property further increases the drift rate whereas increasing the system size diminishes the drifting[353].
External input further changes the attractor landscape. Driving the network with non-uniform input splits up the remaining few clustered states as the input drive potentially reaches attractor states with a more confined basin of attraction[428].
Based on the property of heterogeneity to reduce the dimensionality of the set of network activity patterns, we will formulate a network model that quantitatively reproduces features of the experimentally observed spontaneous activity (see Chapter 5).

2.3.3 Modelling modular cortical activity

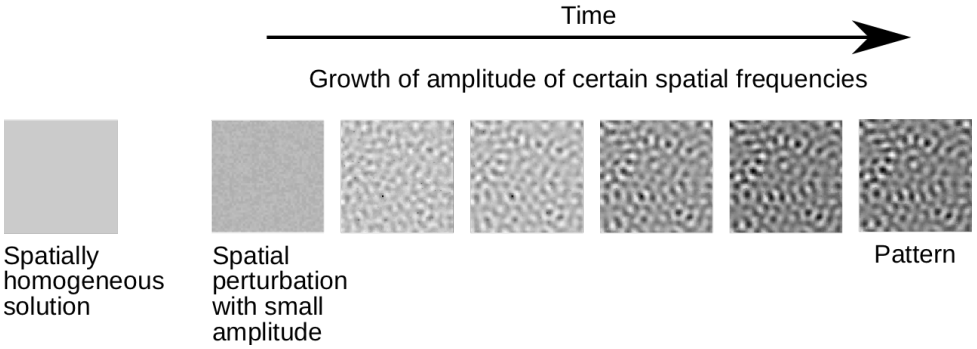

Figure 2.6: Growth of spatially heterogeneous modes of a typical domain spacing. From *left* to *right*: A spatially heterogeneous perturbation to a network with Mexican hat connectivity in a spatially homogeneous state (leftmost) leads to the growth of a pattern consisting of modes of a finite spatial frequency.

In primates and carnivores spatially modulated cortical activity is often varying on a spatial scale of approximately 1 mm. In visual cortex evoked responses and spontaneous activity form a near regular pattern of active domains with a typical spacing of 0.5 to 2 mm[86,231,373,389]. This *modular* activity is present in many species (cat[194,45,330], macaque[198,43], ferret[389], tree shrew[48], marmoset[358,294], owl monkey[328,456], galago[455], sheep[89] and human[457]), in excitatory as well as inhibitory cells[444] and already at early stages in development[389], but is not observed in all cortical areas[160,2], not for all response properties and generally not in rodents[301,157,337,331,432,324]. The underlying mechanism that leads to this modular activity is at present unclear.
A hypothesis put forward by many different theoretical studies[287,321,417,223,268,304] is that mod-

ular activity is intracortically generated which is consistent with recent experimental evidence provided in this thesis[389]. However, due to experimental limitations this model class has hardly been experimentally tested, so far.
Classical models generating such activity patterns are based on competition between excitatory and inhibitory population activity. The dynamical mechanism typically assumed for generating modular patterns of activity is known as the Turing-mechanism[430,152,296]: modular patterns arise from a spatially homogeneous state by amplifying spatially heterogeneous perturbations through dynamical feedback loops mediated by the recurrent connections[130] (**Fig. 2.6**). In this case the network exhibits a finite wavelength instability such that the spatially homogeneous fixed point state becomes unstable to spatially modulated fluctuations in a frequency band around a finite frequency. A detailed derivation of the Turing mechanism is given in Chapter 6.
A generic local circuit motive known to implement the Turing-mechanism, is the so-called Mexican hat connectivity (local excitation with lateral inhibition). With this kind of connectivity excitation amplifies locally elevated activity fluctuations whereas lateral inhibition suppresses activity at an intermediate distance (**Fig. 2.6**). For simplicity, this connectivity scheme is often studied in a network with one population of units that can act both excitatory and inhibitory on its neighbouring units[55]. In this thesis we use this simplified version as the basis for a network model to describe the emergence of long-range correlations in the absence of anatomical long-range connections (see Chapter 5). Variants of this mechanism have been used to describe the emergence of the functional organization of various stimulus features represented in cortex, such as the formation of ocular dominance stripes[411,134] and the emergence of orientation preference maps in visual cortex of carnivores and primates[287,302], as well as the generation of visual hallucination patterns[130] and the formation of modular spontaneous activity[148,389]. Yet, evidence for a Mexican hat like connectivity profile is limited and has only been observed in cortical areas early in development[108]. Other studies using electrode recordings in mature mouse cortex[265] suggest that the spatial range of inhibition is in fact more constrained than the range of excitation. Thus, although this model type has been successfully applied to various activity layouts, it relies on the assumption of lateral inhibition which still needs to be experimentally shown. Given this biological constraint effort has been put into investigating network architectures whose connectivity does not require a connectivity motif with local excitation and long-range inhibition but still leads to modular activity patterns[346,14,226,21].
Modular activity can form in a network where inhibition is spatially more constrained than excitation if inhibition acts with a faster time constant than excitation[346,14,226,21]. This can intuitively be understood assuming instantaneous inhibition. In this case the range of the effective inhibitory influence consists of the summed excitatory and inhibitory range via the disynaptic path from the excitatory to the inhibitory unit and back to the excitatory unit. Experimental evidence for fast inhibition is, however, limited[329]. Rather the typical decay time constant of the most abundant receptor in cortex $GABA_A$ is larger than the timescale of AMPA receptors[335,136,90,219,47]. Extending the two-population model by introducing an additional slow excitatory population (potentially corresponding to neurons with slow NMDA receptors) into the network resolves this issue, but at the cost of higher complexity within the network[226].
Another recent study[14] examined the formation of modular activity patterns around a spatially homogeneous but temporally oscillating activity state. Again, the formation of modular network activity either requires lateral inhibition or inhibition with a faster time constant than excitation.
Other work studied the effect of dendritic structure on the formation of activity patterns and demonstrated that the passive membrane properties of the dendritic tree can induce spatial activity patterns in networks with local inhibition and long-range excitation[53,54,56]. This model relies on the assumption that the average distance of a synapse from the soma increases with increasing separation between the two connected neurons. However, experimental evidence rather

suggests that the distance between synapse and soma is largely determined by neuron type[140,426]. In summary, it is typically assumed that modular activity is intracortically generated through a Mexican hat like connectivity profile with local excitation and lateral inhibition. An effective Mexican hat connectivity can be obtained when assuming a fast inhibitory time constant. Experimental studies showing evidence for both of these two assumptions are limited[265,335,136,90,219,47,329]. Increasing the complexity of the network model, either by introducing a third population of units or by specifically modeling the neurons morphology relaxes the constraints on the lateral connectivity such that wiring schemes that are biologically plausible may lead to the formation of modular activity. In Chapter 6 we investigate in a network model alternative connectivity schemes that are consistent with current biological observations and allow the network to form modular activity without adding further complexity to the network model. In particular, we show that local self-inhibition is sufficient to robustly lead to the formation of modular activity even in the absence of fast and lateral inhibition.
All in all, a key advantage of network models is that they can be analytically and numerically analyzed potentially leading to new insights into the underlying principles that generate the described properties of cortical activity whereas more complex models might obscure these principles.

2.3.4 Dimensionality of cortical activity

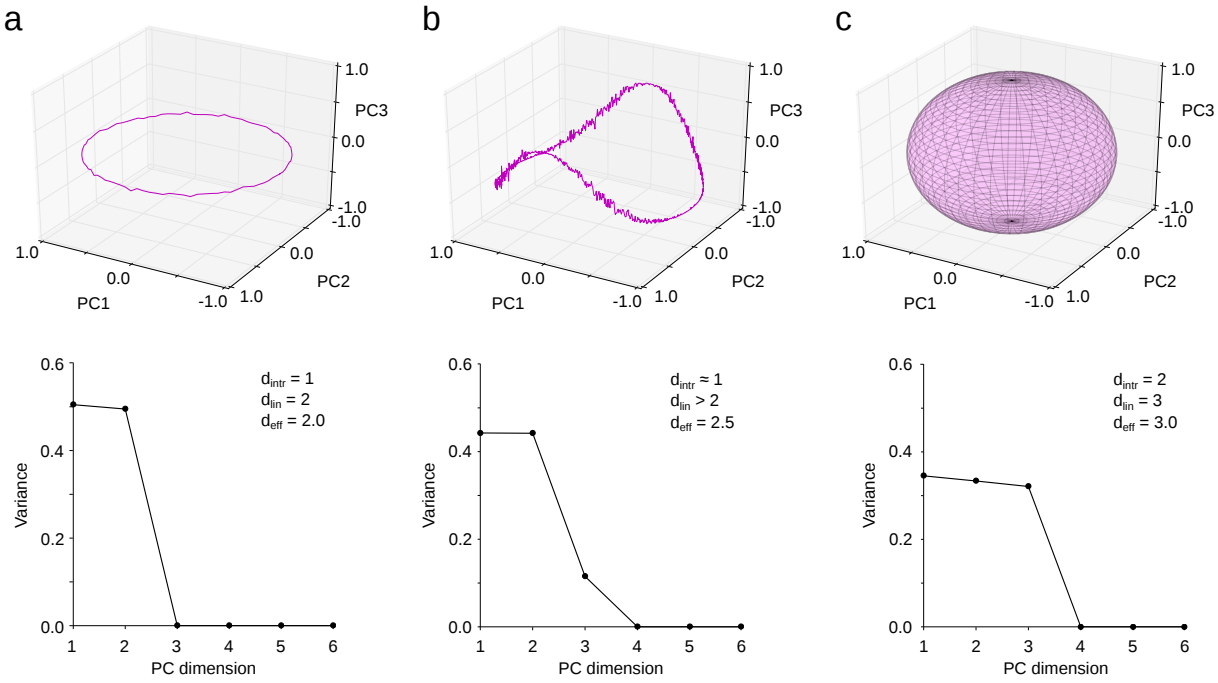

Figure 2.7: Intrinsic and embedded dimensionality of simulated neural activity can differ. **a-c** *Top*: 3d projection of simulated neural activity onto the first three principal components (see following Section 2.3.5). *Bottom*: Explained variance of simulated activity for first six components. Intrinsic (d_{intr}) and embedded (d_{lin}) dimensionality are varied and for comparison the effective dimensionality d_{eff} (see Section 2.3.6) is determined for each case. Values are $d_{\text{intr}} = 1, d_{\text{lin}} = 2$ (**a**), $d_{\text{intr}} \approx 1, d_{\text{lin}} > 2$ (**b**) and $d_{\text{intr}} = 2, d_{\text{lin}} = 3$ (**c**).

With the advancement of large-scale imaging techniques allowing to record the activity of a large population of neurons simultaneously, it becomes ever more important to develop

methods to assess the complexity of neural activity and to potentially find an interpretable low-dimensional structure in large datasets. Previous work has shed light on the complexity of neural activity by investigating the dimensionality of spontaneous and evoked activity. In a previous study spontaneous activity has been observed to outline the space of possible activity patterns of evoked activity, thus, indicating that spontaneous activity is more high-dimensional than evoked activity in sensory areas[274]. This is in line with other work showing that spontaneous activity explores a substantial part of state space[407]. Recently, a study showed that visually evoked activity in mice V1 is high-dimensional with its correlation structure following a power-law. This power-law decay suggests a smooth population code meaning that similar stimuli are encoded by similar activity patterns[406]. All these experiments were performed in mature animals. However, it is still an unresolved question of how the dimensionality of cortical activity develops during development. In this thesis, we therefore assess the dimensionality of visually evoked and spontaneous activity during development (see Chapter 4).
The activity of a population of neurons can be thought of as a trajectory in a high-dimensional space (state space) where each axis represents the activity of an individual observed neuron. The goal is then to describe the structure of the trajectory in this high-dimensional space. A straightforward quantification is to determine the dimension of the manifold in which the activity is embedded termed *linear* dimension (d_{lin} in **Fig. 2.7**). A complex trajectory might explore a great part of the state space corresponding to activity with a high linear dimensionality. In contrast, a trajectory that is confined to a subspace in state space corresponds to activity with low linear dimensionality. Potentially, the dimensionality of the activity trajectory itself termed *intrinsic* dimension can be smaller than the dimension of the subspace in which the trajectory is embedded (**Fig. 2.7**; see also Fig. 4 in[406]).
High dimensional activity potentially allows for general and complex computations[351,137]. In contrast low-dimensional activity represented by trajectories confined to a low-dimensional manifold in state space might be a signature of data compression or denoising[351,137]. In low-dimensional activity individual neurons are more coordinated in their activity exhibiting higher correlations between them.
The dimensionality and the components that span the manifold in which the cortical activity is embedded can be determined by various methods. In this thesis we use methods based on the covariance of neural activity between cortical locations. Intuitively, high dimensional activity corresponds to little co-variance between individual neurons which in turn corresponds to an almost diagonal covariance matrix with eigenvalues that are of similar magnitude. In contrast, in the case of low dimensional activity, individual neurons co-vary leading to a block structure in the covariance matrix, and to many of its eigenvalues being zero. To determine the dimensionality, it is possible to quantify the shape of the eigenvalue distribution (see Section 2.3.6). Another possibility is to use *Principal Component Analysis* to assess the dimensionality and to obtain the principal components that explain the most variance of the data (see Section 2.3.5).

2.3.5 Principal Component Analysis

In principal component analysis (PCA) a dataset consisting of n observations of p variables is decomposed into a set of uncorrelated variables - its *principal components*. The first component is found by maximizing the dataset's variance along this component, thus explaining the highest amount of variance in the data. PCA is essentially a coordinate transformation from the original coordinate system into a coordinate system where the first coordinate accounts for the greatest variance along one direction, the second coordinate explains the second largest variance under the constraint that it is orthogonal to the first coordinate and so on. It is therefore a suitable and widely used tool to assess the complexity of neural activity by determining how many principal

components are needed to sufficiently describe the original data. Moreover, it is used to reduce the dimensionality of a dataset by only keeping the first l components that explain the largest part of the dataset's variance.

To describe the procedure of PCA, we consider a dataset X (centered around zero and with stan-

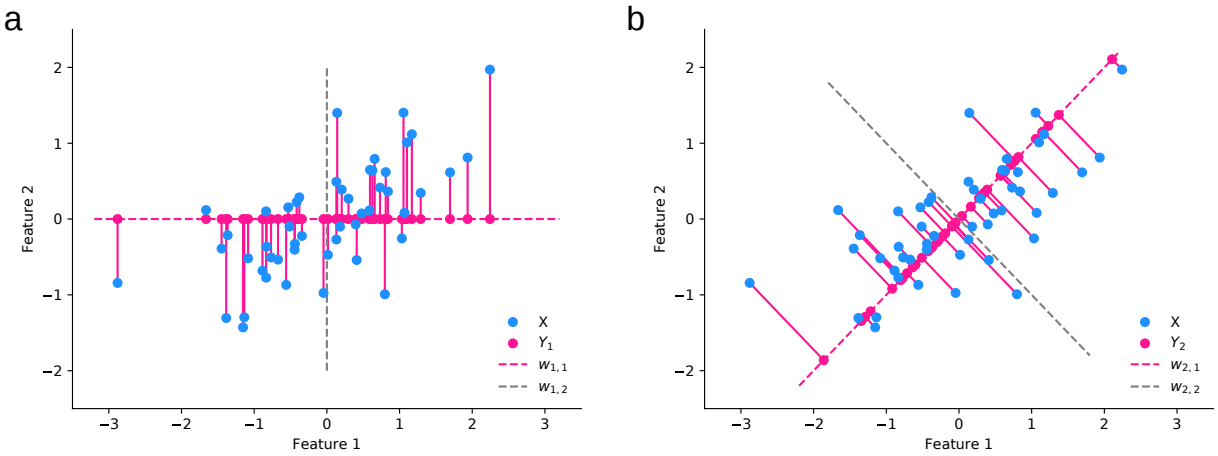

Figure 2.8: Dimensionality reduction based on Principal component analysis explains larger variance of dataset than naive transformation. **a** Data points (blue) are transformed naively onto first coordinate ($\vec{w}_{1,1} = (0,1)^T$, pink dashed line; second component is given by $\vec{w}_{1,2} = (1,0)^T$, gray dashed line). **b** Same data points as in (**a**) are transformed onto eigenvector with largest eigenvalue of the covariance matrix ($\vec{w}_{2,1} = \frac{1}{\sqrt{2}}(1,1)^T$, pink dashed line; second component is given by $\vec{w}_{2,2} = \frac{1}{\sqrt{2}}(1,-1)^T$, gray dashed line). Reconstruction error (pink solid line) for transformation in (**a**) is larger compared to the one in (**b**). Similarly, the spread of the data points along the principal component (explained variance) is smaller in (**a**) compared to (**b**).

dard deviation of 1) consisting of $n = 50$ observations in rows and $p = 2$ variables (**Fig. 2.8**). We want to reduce its dimensionality and describe this two-dimensional dataset by a one-dimensional representation. We apply two different transformations to the dataset - one of them the PCA transformation - and compare which transformation represents the dataset better. In the first transformation, we project X onto the first feature coordinate (**Fig. 2.8a**)

$$Y_1 = X\vec{w}_{1,1}\,\vec{w}_{1,1}^T \tag{2.7}$$

with the principle component $\vec{w}_{1,1} = (0,1)^T$. Each transformed data point Y_1 is now represented by only one number.

In the second transformation, we want to maximize the variance that we explain when we project X onto a second vector $\vec{w}_{2,1}$

$$\vec{w}_{2,1} = \underset{|\vec{w}_{2,1}|=1}{\operatorname{argmax}} \left(\operatorname{Var}(Y_2)\right) = \underset{|\vec{w}_{2,1}|=1}{\operatorname{argmax}} \left(|Y_2|^2\right) \tag{2.8}$$

$$= \underset{|\vec{w}_{2,1}|=1}{\operatorname{argmax}} \left(|X\vec{w}_{2,1}|^2\right) \tag{2.9}$$

$$= \underset{|\vec{w}_{2,1}|=1}{\operatorname{argmax}} \left(\vec{w}_{2,1}^T X^T X \vec{w}_{2,1}\right) \tag{2.10}$$

$$= \underset{|\vec{w}_{2,1}|=1}{\operatorname{argmax}} \left(n\vec{w}_{2,1}^T C \vec{w}_{2,1}\right) \tag{2.11}$$

where $C = \frac{1}{n}X^T X$ is the covariance matrix. The last expression is maximal if $\vec{w}_{2,1}$ is the eigenvector with the maximal eigenvalue of C. Therefore, to find the principal component of

the second transformation, we diagonalize C

$$C = \frac{1}{n} X^T X = U D U^{-1} \tag{2.12}$$

where D is the diagonalized matrix and the rows of U contain the eigenvectors $\vec{v}_i$ ($i \in \{1, 2\}$) of C. The eigenvector $\vec{v}_1$ with the maximal eigenvalue describes the principal component $\vec{w}_{2,1}$ which captures the maximal variance of the data in one dimension (**Fig. 2.8b**).
Comparing the two projections in **Fig. 2.8** we note that the data transformed by PCA captures more of the total variance than the naive transformation. Further we note that the projection based on PCA exhibits a smaller reconstruction error r which is measured by the sum of the squared difference between the original dataset X and the dataset projected onto the principal component. In the following we show that maximizing the explained variance of the data corresponds to minimizing the reconstruction error

$$\begin{aligned}
r &= \mathrm{tr}|X - Y_2|^2 = \mathrm{tr}|X - X\vec{w}\vec{w}^T|^2 && (2.13)\\
&= \mathrm{tr}\left((X^T - \vec{w}\vec{w}^T X^T)(X - X\vec{w}\vec{w}^T)\right) && (2.14)\\
&= \mathrm{tr}\left(X^T X - X^T X\vec{w}\vec{w}^T - \vec{w}\vec{w}^T X^T X + \vec{w}\vec{w}^T X^T X\vec{w}\vec{w}^T\right) && (2.15)\\
&= n\ \mathrm{tr}\,(C) - \mathrm{tr}\left(X^T X\vec{w}\vec{w}^T\right) - \mathrm{tr}\left(\vec{w}\vec{w}^T X^T X\right) + \mathrm{tr}\left(\vec{w}\vec{w}^T X^T X\vec{w}\vec{w}^T\right) && (2.16)\\
&= n\ \mathrm{tr}\,(C) - 2\mathrm{tr}\left(X^T X\vec{w}\vec{w}^T\right) + \mathrm{tr}\left(X^T X\vec{w}\vec{w}^T\right) && (2.17)\\
&= n\ \mathrm{tr}\,(C) - \mathrm{tr}\left(\vec{w}^T X^T X\vec{w}\right) && (2.18)\\
&= n\sum_i \lambda_i - n\ \vec{w}^T C\vec{w}. && (2.19)
\end{aligned}$$

For brevity we used here $\vec{w}$ instead of $\vec{w}_{2,1}$ to denote the principal component. In the derivation we used that the eigenvectors are normalized such that $\vec{w}^T\vec{w} = 1$. In the last line the expression for the eigenvector from Eq. (2.11) appears with a minus sign. Thus, minimizing r corresponds to maximizing the explained variance.
The remaining components are given by the remaining eigenvectors of C sorted by their eigenvalues, respectively. That is the second principal component is given by the eigenvector with the second largest eigenvalue and so on. The eigenvalues describe the relative amount of the explained variance per component. To reduce the dimensionality of a given dataset to k dimensions the data is projected onto its k largest principal components. Typically k is chosen such that the variance explained by all k components crosses a defined threshold. PCA determines the linear dimensionality of the dataset (see **Fig. 2.7**).

2.3.6 Linear estimate of dimensionality based on eigenvalues of covariance matrix

To estimate the linear dimensionality of neural activity, the eigenvalue distribution of its covariance matrix can be examined. In particular, the following measure of the effective dimensionality d_{eff} has been established[30,347,1]:

$$d_{\mathrm{eff}} = \frac{\left(\sum_{a=1}^{N} \lambda_a\right)^2}{\sum_{a=1}^{N} (\lambda_a^2)} \tag{2.20}$$

where λ_a are the eigenvalues of the covariance matrix for the N locations (pixels) within the ROI. This measure is maximal ($d_{\mathrm{eff}} = N$) if all eigenvalues are equal whereas it becomes minimal ($d_{\mathrm{eff}} = 1$) if one eigenvalue is much larger than the rest.
This measure is not only used to assess the dimensionality of the subspace spanned by activity

patterns[1], but has been introduced in physical systems[30] and also been widely used in economical research[347]. In this thesis, we estimate the dimensionality d_{eff} of the subspace spanned by spontaneous activity patterns (see also **Fig. 2.7**).

Chapter 3

Organization of distributed networks and their link to visual response properties in mature cortex

The layout of spontaneous activity patterns has been shown to resemble to a degree the layout of visually evoked responses. However, the cortical distance and fine spatial scale over which this relationship holds remain unclear. Using *in vivo* wide-field and 2-photon calcium imaging of spontaneous and visually evoked activity patterns in mature ferret visual cortex, we found spatially extended and modulated spontaneous correlation patterns that accurately predicted the fine spatial structure of visually evoked orientation domains several millimeters away. These results suggest a tight relation between spontaneous correlations and visually evoked responses on a fine spatial scale and across large spatial distances.
Gordon B. Smith and David E. Whitney performed all experiments under supervision of David Fitzpatrick in this chapter and did the analysis of the 2-photon imaging data (**Fig. 3.17**).

3.1 Introduction

Spontaneous activity patterns have been shown to resemble to some degree the spatial layout of visually evoked responses (in mice[310,303], zebrafish[215,361] and cat[429,235,327]). In particular, spontaneous activity patterns in the visual cortex of mature, anesthetized cats are significantly correlated to the average responses evoked by moving gratings[235], and these patterns are synchronized between hemispheres[327]. It has been argued that the resemblance in the layout between spontaneous and visually evoked activity patterns extends over large distances[235]. A subsequent theoretical study investigated in a network model whether the properties of the observed spontaneous activity are consistent with a long-range similarity to the orientation preference map layout. However their results remained inconclusive[159].
Here, we characterize mature spontaneous activity in ferret visual cortex and study its relationship to visually evoked responses. We take advantage of a newly developed and highly sensitive calcium sensor[81] allowing to robustly image neuronal activity on a single trial level *in vivo*. Using *in vivo* wide-field and 2-photon calcium imaging of spontaneous and visually evoked activity patterns in awake and anesthetized, mature ferret visual cortex, we find spatially extended and modulated spontaneous correlation patterns that resemble the layout of orientation domains over large cortical distances of several millimeters. These correlation patterns accurately predict the fine spatial scale of selectivity to visual stimulus features of distant cortical domains demonstrating a tight relation between spontaneous correlations and visually evoked responses

on larger and finer spatial scales than previously shown. Finally, we test the predictions made by the previously suggested network model[159]. We show that the suggested scenarios[159] do not capture properties of the similarity between our observed spontaneous activity patterns and visually evoked responses. In particular, the scenarios fail to account for the observed long-range correlation structure in spontaneous activity decaying over several millimeters. We conclude that in the mature visual cortex the layout of spontaneous activity correlations resembles the layout of orientation domains to a very fine spatial scale and over large cortical distances.

3.2 Experimental setup

3.2.1 Animals

All experimental procedures were approved by the Max Planck Florida Institute for Neuroscience Institutional Animal Care and Use Committee and were performed in accordance with guidelines from the US National Institutes of Health. 24 female ferret kits were obtained from Marshall Farms and housed with jills on a 16 h light/8 h dark cycle. These sample sizes were similar to those reported in previous publications[77,388,390].

3.2.2 Viral injections

Viral injections were performed as described in[388,390,387]. Two weeks after birth (P13-14) after neurons from layer 2/3 have largely finished migrating GCaMP6s was expressed in visual cortex by injecting AAV2/1.hSyn.GCaMP6s.WPRE.SV40 (obtained from University of Pennsylvania Vector Core). Animals were anaesthetized with ketamine (50 mg/kg), and then maintained with isoflurane (1-2 %). The animals were given atropine (0.2 mg/kg) and bupivacaine, and animal temperature was maintained at approximately 37 °C with a homeothermic heating blanket. Animals were also mechanically ventilated and both heart rate and end-tidal CO_2 were monitored throughout the surgery. Using aseptic surgical technique, skin and muscle overlying visual cortex were reflected and a small burr hole was made with a hand-held drill (Fordom Electric Co.). The virus (≈1 µL) was injected over 20 min at 200 and 400 µm below the cortical surface. After 6-8 days GCaMP6s was expressed in a patch of around 3 mm x 3 mm around the injection site in layer 2/3 (**Fig. 3.1**).

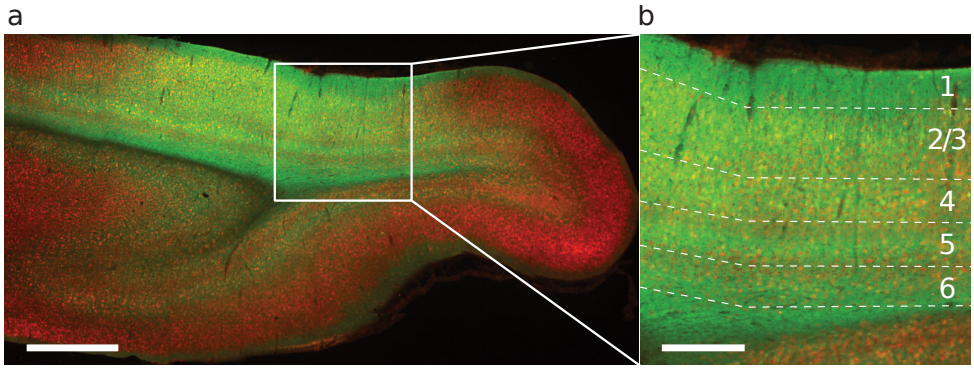

Figure 3.1: Virally-mediated labelling of visual cortex with GCaMP6s. **a** Coronal section showing widespread GCAMP6 expression in layer 2/3 neurons of primary visual cortex (Green - GCAMP6s / Red - NeuN). **b** Expanded view of region indicated in (**a**) with GCaMP6s. Scale bars were 1 mm (**a**) and 0.5 mm (**b**).

3.2.3 Cranial window surgery

To allow repeated access to the same imaging field, a chronic cranial window was implanted in each animal 0-2 days prior to the first imaging session. Animals were anesthetized and prepared for surgery as described above. Using aseptic surgical technique, skin and muscle overlying visual cortex were reflected and a custom-designed metal headplate was implanted over the injected region with MetaBond (Parkell Inc.). Then both a craniotomy (∼5 mm) and a subsequent durotomy were performed, and the underlying brain stabilized with a 2 % agarose plug and a 8 mm glass coverslip. In some animals, the agarose plug was substituted, and instead a clear Kwik-Sil plug (World Precision Instruments, 3-4 mm diameter, ≈1 mm thickness) or a custom glass coverslip (3 mm diameter, 1.4 mm thickness) was adhered to the 8 mm glass coverslip. The headplate was hermetically sealed with a stainless steel retaining ring (5/1" internal retaining ring, McMaster-Carr) and glue (VetBond, 3M). Unless the animal was immediately imaged after a cranial window surgery, the imaging headplate was filled with a silicone polymer (Kwik-kast, World Precision Instruments) to protect it between imaging experiments.

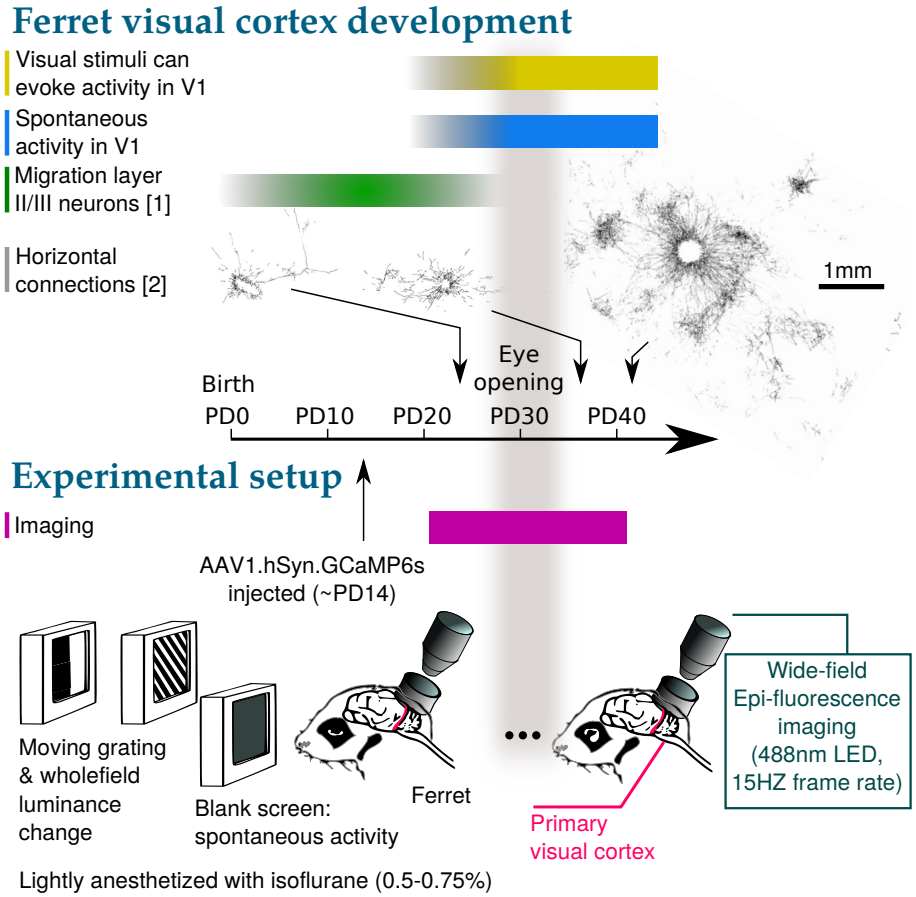

Figure 3.2: Experimental setup and overview of developmental timeline of ferret. *Top*: Overview of stages in development of ferret in relation to imaging (purple) time line. *Bottom*: Sketch of imaging setup. Ferret pups were injected with AAV1.hSyn.GCaMP6s at around 14 days after birth (P14). Chronic imaging of primary visual cortex was performed starting at around P21 until around P45. Spontaneous activity and responses visually evoked by fullfield moving gratings and fullfield luminance changes were imaged using wide-field epi-fluorescence microscopy and single cell 2-photon microscopy.

3.3 Wide-field epifluorescence and two-photon imaging

Wide-field epifluoresence imaging was achieved using a Zyla 5.5 sCMOS camera (Andor) controlled by µManager39[124]. Images were acquired at 15 Hz with 4 x 4 binning to yield 640 x 540 pixels. Two-photon imaging was performed with a B-Scope microscope (ThorLabs) driven by a Mai-Tai DeepSee laser (Spectra Physics) at 910 nm. The B-Scope microscope was controlled by ScanImage (Vidreo Technologies) in a resonant-galvo configuration with single-plane images (512 x 512 pixels) being collected at 30 Hz.
In animals imaged after eye opening, we applied phenylephrine (1.25-5 %) and tropicamide (0.5 %) to the eyes to retract the nictitating membrane and dilate the pupil. The cornea was protected with regular application of eye drops (Systane Ultra, Alcon Laboratories). Then the silicon polymer plug overlying the sealed imaging chamber was gently peeled off. Whenever the imaging quality of the chronic cranial window was find to be suboptimal, the chamber was opened under aseptic conditions, regrown tissue or neomembrane was removed and a new coverslip was inserted. In some cases, prior to imaging, animals were paralyzed with either vecuronium or pancuronium bromide (2 mg/kg/h in lactated Ringer's, delivered IV). This anesthetic regimen produced highly stable heart rates of 280-330 b.p.m. for the duration of imaging, with end-tidal CO_2 levels stably maintained between 35-45 mmHg.
For imaging experiments in awake animals, animals were habituated to head fixation beginning at least 2 days before imaging. During habituation animals were exposed to the fixation apparatus for brief periods after which they were returned to their home cage. For imaging, animals were head fixed and wide-field and two-photon imaging was performed as above. In experiments where both awake and anesthetized imaging were performed, awake imaging was always performed first, followed by anesthesia induction as described above.
For anesthetized, longitudinal imaging experiments, anesthesia was induced with either ketamine (12.5 mg/kg) or isoflurane (4-5 %), and atropine (0.2 mg/kg) was administered. Animals were intubated and ventilated, and an IV catheter was placed in the cephalic vein. In some imaging sessions, it was not possible to catheterize the cephalic vein; in these cases, an IP catheter was inserted. Anesthesia was then maintained with isoflurane (0.5-0.75 %).
Following imaging, animals were recovered from anesthesia and returned to their home cages. During recovery, neostigmine was occasionally administered to animals that were paralyzed (0.01-0.1 µL/kg per dose).

3.4 Visual stimulation

Visual stimuli were delivered on a LCD screen placed approximately 25-30 cm in front of the eyes of the animals using PsychoPy[340]. For evoking orientation responses, stimuli were full-field sinusoidal gratings at 100 % contrast, at 0.015-0.06 cycles per degree, drifting at 1 or 4 Hz, and presented at one of eight directions of motion. Stimuli were randomly interleaved and were presented for 5 s followed by a 5-10 s gray screen. Imaging experiments were performed every 1 to 3 days for each animal. At the beginning of the imaging session spontaneous activity (5 to 30 min) was recorded while the animal was sitting in a dark room looking at a black screen. Following the recording of spontaneous activity visual stimuli (moving gratings, flash stimuli) were shown to the animal to record visually evoked activity for about 1 to 3 hours.

3.5 Signal preprocessing

Imaging neuronal activity, especially *in vivo* is typically contaminated by noise from various sources such as light scattering and absorption by tissue, movement artefacts, uneven expression of the activity indicator that is recorded, or photon shot noise. To increase signal to noise ratio and reduce these imaging artefacts, we preprocessed the data prior to analyzing. In the following the preprocessing pipeline consisting of image alignment to reduce motion artefacts, baseline subtraction to reduce uneven expression of the calcium indicator and spatial filtering to remove activity artefacts caused by neuropil is described. These steps were then followed by detecting events in ongoing spontaneous activity, calculating the spontaneous correlation structure, the orientation preference and ocular dominance maps, and registrating the imaging data across days. Lastly, methods to generate surrogate datasets used for significance tests are described.

3.5.1 Signal extraction for wide-field epifluorescence imaging

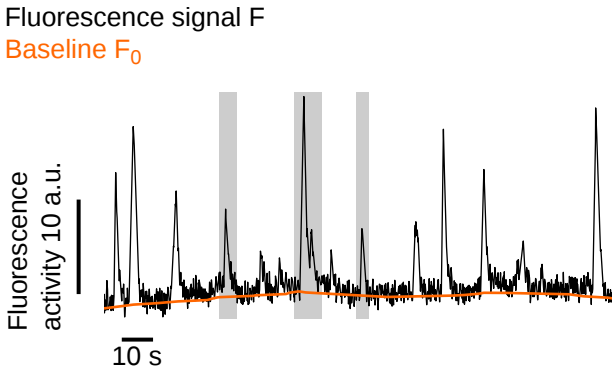

Figure 3.3: Applying a rank filter to the fluorescence trace F of spontaneous activity yields the baseline F_0. We obtain F_0 for each pixel independently by applying the rank filter to each pixel's fluorescence trace. The parameters of the rank filter - the window size and the rank - depend on the frequency of high activity events (highlighted by gray background; for clarity three randomly chosen events are marked) and are chosen such that the baseline captures the slowly (slow compared to the time scale of events) changing underlying trend of the activity.

To correct for mild brain movement during imaging (especially in the awake state), we registered each imaging frame by maximizing its phase correlation to a common reference frame which was typically the first frame[204]. Following this alignment all imaging data acquired on the same day were registered into one reference frame. The region of interest (ROI) was manually drawn around the cortical region with high and robust visually evoked activity. The baseline F_0 for spontaneous activity for each pixel was obtained by applying a rank-order filter to the raw fluorescence trace with the rank between 15 to 70 and the time window between 10 and 30 s (values chosen for each imaging session individually, depending on the strength and frequency of spontaneous activity). The rank and time window were chosen manually such that the baseline F_0 followed faithfully the slow trend of the fluorescence activity. Following the standard procedure the baseline corrected calcium signal was calculated as

$$\Delta F/F = \frac{F - F_0}{F_0}. \tag{3.1}$$

For the visually evoked activity the baseline $F_{0,k}$ for each pixel and stimulus k was obtained by taking the last 1 s activity of the inter-stimulus interval immediately before stimulus onset $t_{\text{onset},k}$ averaged across the ROI. The evoked response to a moving grating was then calculated as the average of the baseline corrected fluorescence $F(t)$ over the full stimulus period (5 s) as

$$w_k(\vec{x}) = \sum_{t=t_{\text{onset},k}}^{t_{\text{onset},k}+5s} \frac{F(t) - F_{0,k}}{F_{0,k}} \tag{3.2}$$

$$\text{with} \quad F_{0,k} = \sum_{t=t_{\text{onset},k}-1s}^{t_{\text{onset},k}} F(t). \tag{3.3}$$

Here $\vec{x} = (x, y)^T$ is the location within the ROI, index k denotes the stimulus orientation, and the sum runs over time frames from either before or after stimulus onset.
To decrease the computing time and the amount of memory required for the data analysis the imaging frames were scaled down by a factor of 2 from 640 x 540 pixels to 320 x 270 pixels.

3.5.2 Denoising of wide-field epifluorescence imaging data

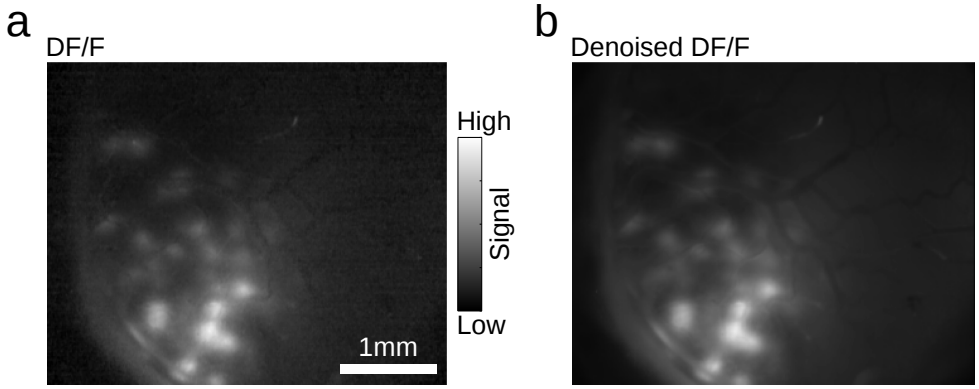

Figure 3.4: Denoising algorithm removes spatiotemporal high-frequency noise components in neural dataset. **a** Example DF/F activity pattern at eye-opening (P31) showing high frequency noise especially in background of image. **b** Denoised variant of activity pattern shown in (**a**). Spatial component of high frequency noise is considerably reduced.

In Chapter 4 we determined the dimensionality of spontaneous and evoked activity. To test how high-frequency components affect the estimation of the dimensionality, we applied a novel denoising algorithm[58] to the dataset and compared the dimensionality of the denoised data to the original data. In contrast to the previous state of the art denoising methods this new empirical approach takes advantage of the locality of the neuronal signal. It assumes that the neuronal signal is localized in space and time, and that the noise components are spatially and temporally uncorrelated. The method only depends on a low number of parameters, and the authors claimed that its results are robust against changes in the parameter settings. In sequential steps the method first separates the original baseline corrected signal Y into its denoised part $\hat{Y}$ and the noise component E ($V \approx \hat{Y} + E$) and then compresses $\hat{Y} \approx UV$ into lower rank spatial and temporal components U, V. To this end, the original data matrix Y is split into (possibly overlapping) local patches which are subsequently decomposed using a factorization method that enforces smoothness in the spatial and temporal domains of the estimated signal. Applying this

method to the DF/F signal, it extracted the high-frequent noise across development (**Fig. 3.4**). The bloodvessels were still clearly visible after denoising.
By removing high frequency noise from the imaging data, we expected the dimensionality of the data to decrease. To estimate how strongly the estimate of the dimensionality is influenced by the high-frequency components, we compared the dimensionality between data that were only spatially filtered and data that were additionally denoised. We found that the dimensionality changes only little after the denoising algorithm was applied to the spontaneous activity. In the following we therefore used only spatially bandpass and highpass filtering (see following section) to remove high frequency noise for the analysis shown in Chapter 3 and Chapter 4.

3.5.3 Spatial filtering of wide-field epifluorescence imaging

High-pass filtering

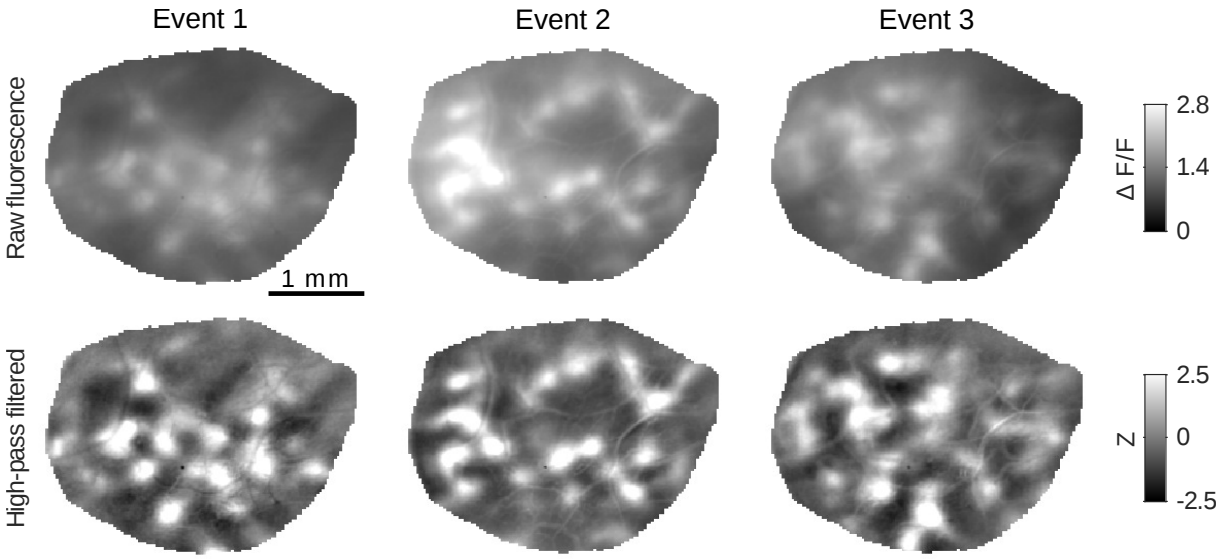

Figure 3.5: Spatial high-pass filtering of modular spontaneous activity. Representative spontaneous events shown as ΔF/F (*top*) and after high-pass filtering (*bottom*). The modular nature of spontaneous events is clearly evident already prior to filtering.

The spatial structure of spontaneous activity shown as Δ F/F exhibited active domains with a typical spatial scale which we termed in the following *modular* activity layout (**Fig. 3.5a**(top)). To eliminate the neuropil signal inbetween active domains, we applied a spatial high-pass filter on each frame. To minimize the influence of activity from the boundary region outside the ROI, we first applied the ROI and afterwards the high-pass filter. We implemented the high-pass filter as the difference between the image $f(\vec{x})$ of Δ F/F and the image filtered by a Gaussian kernel. To eliminate edge effects caused by applying the ROI, we normalized the filtered image by the filtered image of the ROI. The high-pass filtered image is then given by

$$f_{\mathrm{hp}}(\vec{x}) = f(\vec{x}) - \frac{\sum_{\vec{y}} \left(f(\vec{y})\, e^{-\frac{(\vec{x}-\vec{y})^2}{2\sigma^2_{\mathrm{high}}}} \right)}{\sum_{\vec{y}} \left(f_{\mathrm{ROI}}(\vec{y})\, e^{-\frac{(\vec{x}-\vec{y})^2}{2\sigma^2_{\mathrm{high}}}} \right)} \tag{3.4}$$

where f_{ROI} is the image of the ROI (being 1 within the ROI and 0 outside), and the sum goes over all locations $\vec{y} = (y_1, y_2)^T$ within the ROI. Throughout the study we used σ_{high}=200 µm (corresponding to 15 pixels within the 320x270 frame) except noted otherwise.

Band-pass filtering

To remove the fine line artefacts caused by bloodvessels, we applied a spatial band-pass filter. We implemented the band-pass filter as the difference between the low-pass filtered image $f_{lp}(\vec{x})$ of Δ F/F and the low-pass filtered image convolved with the high-pass Gaussian kernel. Additionally, we normalized each filtered image by the filtered ROI to eliminate edge effects caused by the ROI. The bandpass filtered image is given by

$$f_{\mathrm{bp}}(\vec{x}) = f_{\mathrm{lp}}(\vec{x}) - \frac{\sum_{\vec{y}} \left(f_{\mathrm{lp}}(\vec{y})\ e^{-\frac{(\vec{x}-\vec{y})^2}{2\sigma^2_{\mathrm{high}}}} \right)}{\sum_{\vec{y}} \left(f_{\mathrm{ROI}}(\vec{y})\ e^{-\frac{(\vec{x}-\vec{y})^2}{2\sigma^2_{\mathrm{high}}}} \right)} \tag{3.5}$$

$$\text{with} \quad f_{\mathrm{lp}}(\vec{x}) = \frac{\sum_{\vec{y}} \left(f(\vec{y})\ e^{-\frac{(\vec{x}-\vec{y})^2}{2\sigma_{\mathrm{low}}}} \right)}{\sum_{\vec{y}} \left(f_{\mathrm{ROI}}(\vec{y})\ e^{-\frac{(\vec{x}-\vec{y})^2}{2\sigma^2_{\mathrm{low}}}} \right)} \tag{3.6}$$

$$\tag{3.7}$$

Throughout the study we used σ_{low}=26 µm and σ_{high}=200 µm (corresponding to 2 pixels and 15 pixels in the 320x270 frame), respectively, except noted otherwise.

3.5.4 Signal extraction for 2-photon imaging

2-Photon images were corrected for in plane motion via a 2D cross correlation-based approach. For awake imaging, periods of excessive motion were discarded and excluded from further analysis. Cellular regions of interest (ROIs) were drawn using custom software (Cell Magic Wand[445]) in ImageJ. Fluorescence was averaged over all pixels within one ROI and imported into Matlab. Traces were converted to ΔF/F[388] where the baseline fluorescence F_0 was computed from a filtered fluorescence trace. The raw fluorescence trace was filtered by applying a 60 s median filter, followed by a first-order Butterworth high-pass filter with a cut-off time of 60 s.

3.6 Event detection

Spontaneous activity showed periods of high activity followed by periods of low activity (**Fig. 3.3**). We called periods of high activity spontaneous activity events. In anesthetized animals events could be well separated. To assess the frequency and size of events of high spontaneous activity, we first applied a threshold to each pixel individually which was set to 5 times the standard deviation of the pixel's fluctuations around its baseline (**Fig. 3.6a,b**). If a pixel's activity crossed this threshold we termed this an *active* pixel. A frame with high activity was detected when at least 0.01 mm^2 of connected pixels were active (**Fig. 3.6c**). Consecutive frames with high activity were called an event. Start and end of an event were defined as the time points when the region of active pixels falls below the threshold of 0.01mm^2. Moreover, we defined a spatially extended activity pattern for which at least 80% of the pixels in the ROI showed activity above their threshold.

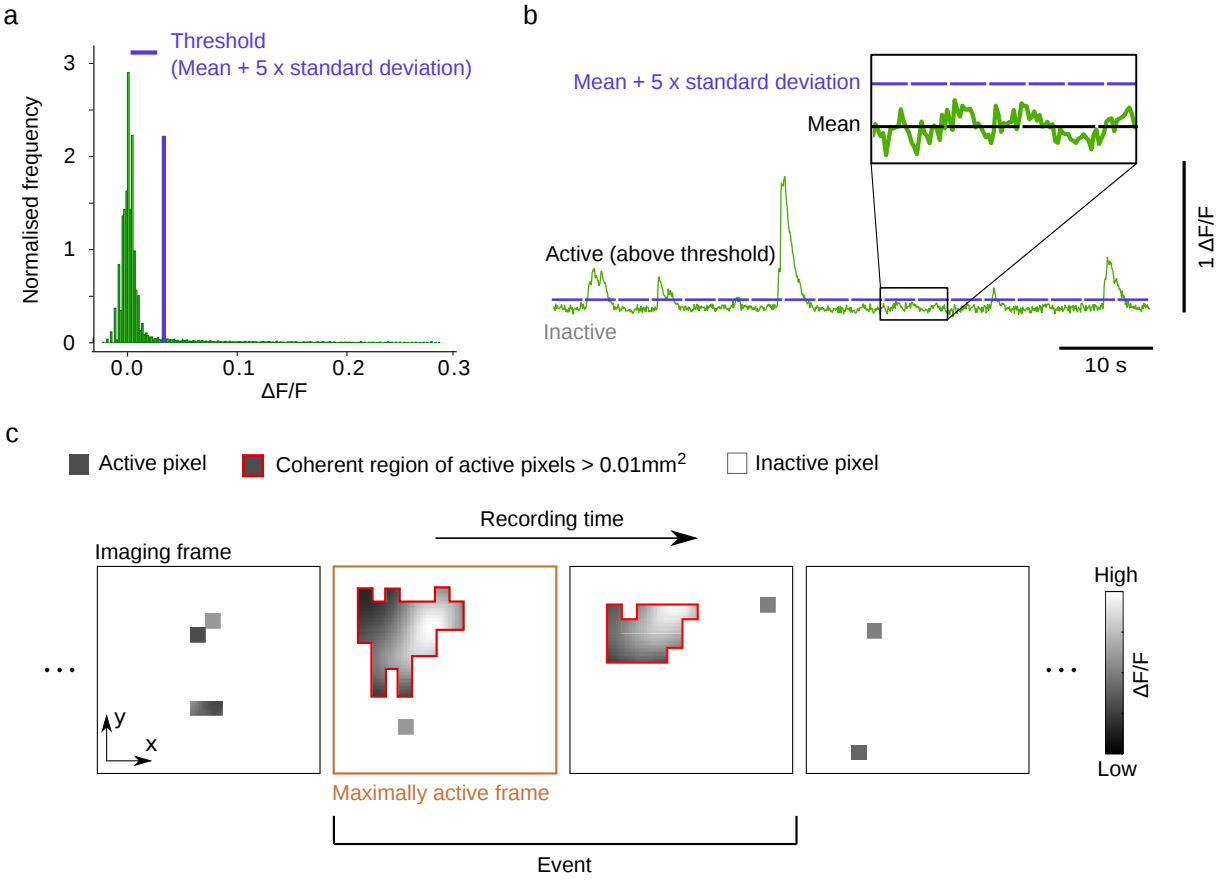

Figure 3.6: Detecting events in spontaneous activity. **a** Distribution of DF/F values of one pixel. Mean and standard devation (SD) of its fluctuations are determined from the Gaussian-like distribution around zero neglecting the long tail. **b** Pixels are defined as *active* during the period of time their DF/F value is above threshold (mean + 5 x SD), and inactive when DF/F is below threshold. **c** An event consists of the series of successive frames which show a coherent region of active pixels larger than 0.01mm^2. Start and end of an event are defined when the region of active pixels falls below the threshold of 0.01mm^2.

Especially in awake animals, but also in anaesthetized more mature animals events defined like this often did not decay back to low activity (below 0.01 mm^2 of active pixels) but were quickly followed by another high activity period with a different spatial layout. To differentiate these different activity patterns, we further divided these long events containing different patterns into shorter events separated by a valley in the average activity trace (**Fig. 3.7**).

The spatial layout during one event changed little (see Chapter 4). Generally, the spatial layout of the activity pattern appeared within the first 0.1 to 0.3 s of the event and then increased in intensity. Eventually, the pattern then decayed by decreasing intensity of the layout. Spatially separated blobs of high activity might decay with different time scales. Thus, in order to assess the extended spatial layout of each spontaneous activity event, we extracted the maximally active frame for each event which is the frame with the highest activity averaged across the ROI during the event.

Typically, the frequency of spontaneous events increased during development. In early development, at around 10 days prior to eye-opening, animals exhibited at the order of 10 events per 10 to 20 min of imaging. The frequency increased to the order of 100 events per 10 to 20 min

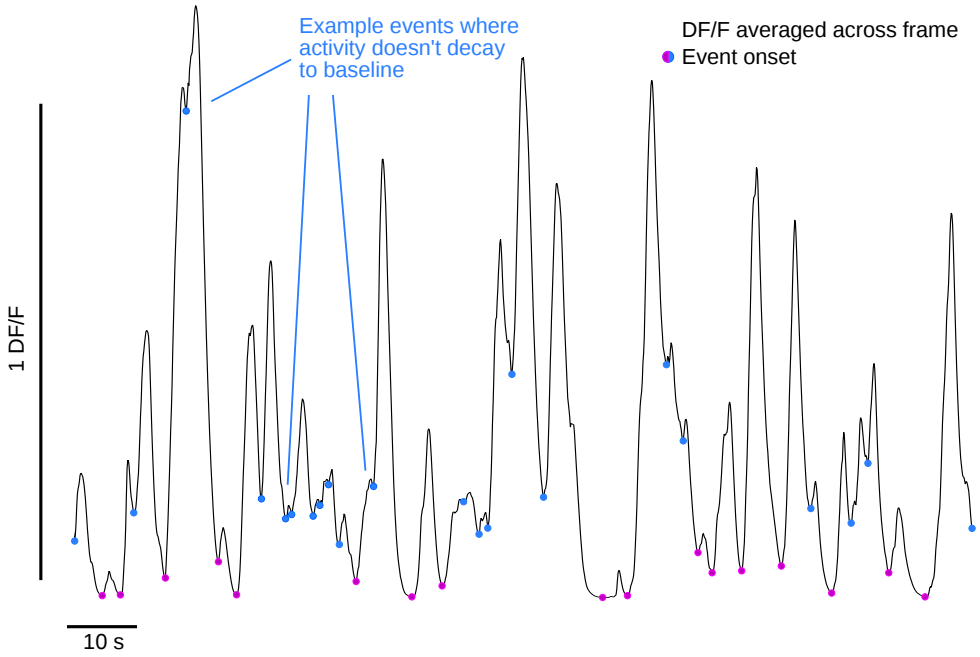

Figure 3.7: Timecourse of DF/F averaged across imaging frame to detect spontaneous events. A new event starts (indicated by marker) either from an inactive state when the increasing size of a coherent region of active pixels reaches the threshold of 0.01 mm^2 (purple), or at the minimum of the activity averaged across the ROI when the size of active regions has not fallen below threshold between two successive peaks in the averaged activity (blue). Two subsequent events separated by the latter method typically display different spatial patterns.

at around eye-opening (**Fig. 3.8**). This could be a consequence of anesthesia acting differently at different age.

3.7 Registration for longitudinal imaging

The experiments were performed over a period in development of the animal when the cortex was still growing. In addition changes, e.g. in bloodvessels were easily visible by eye between experiments performed on successive days. In order to be able to compare cortical responses between experiments performed on different days, we transformed the coordinate system of each stack of imaging frames to align it to the reference coordinate system of an imaging experiment performed at eye-opening[204] (compare **Fig. 4.12** in Chapter 4). We chose eye-opening as reference day since the days on which experiments were performed varied among animals, but for each animal imaging was done on the day of eye-opening. We described the cortical growth by an affine transformation, thereby taking into account rotation, scaling, translation and shear mapping of the cortex:

$$\vec{x}' = M\vec{x} + \vec{h} \tag{3.8}$$

$$\text{with} \quad \vec{x} = (x, y)^T, \tag{3.9}$$

$$M = \begin{pmatrix} a & b \\ c & d \end{pmatrix} \tag{3.10}$$

$$\text{and} \quad \vec{h} = (e, f)^T \tag{3.11}$$

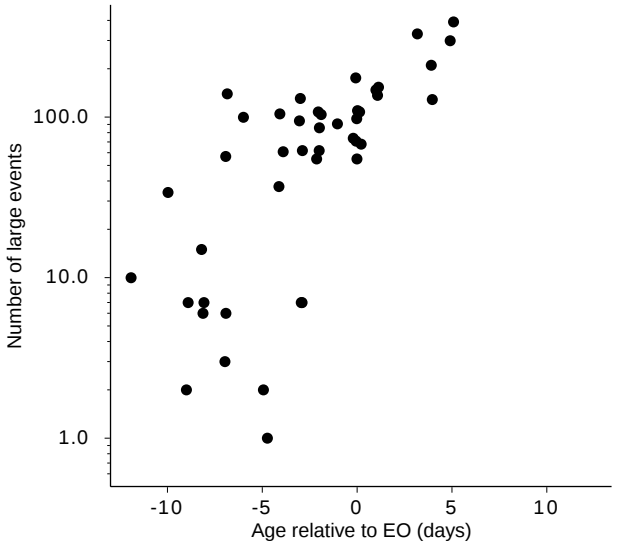

Figure 3.8: Frequency of spontaneous activity events during development. The number of events per 10 min recordings increases consistently over several orders of magnitude from prior to after eye-opening (n=12 animals). One marker corresponds to a 10 minute recording of spontaneous activity.

where e, f are parameters related to translation, and a, b, c, d describe rotation, scale and shear. This transformation corrected for small displacements of the imaging field and expansions of cortical tissue over the imaging period. Appropriate morphing parameters M and $\vec{h}$ were found by minimizing the distance between landmarks determined for each day of experiment. Landmarks were found by marking vertical bloodvessels, meaning bloodvessels which are oriented orthogonally to the imaging plane by visual inspection (compare **Fig. 4.11a** in Chapter 4). We used vertical bloodvessels as markers since they are assumed to remain fixed inside the tissue during growth. The following expression was minimized to find the transformation parameters from day t to the reference day t_{ref} (eye-opening)

$$\sum_{a=1}^{N}(\vec{x}_{t_{\mathrm{ref}},a} - \vec{x}'_{t,a})^2 = \sum_{a=1}^{N}(\vec{x}_{t_{\mathrm{ref}},a} - M\vec{x}_{t,a} - \vec{h})^2. \tag{3.12}$$

with N landmarks in both coordinate systems at coordinates $\vec{x}_{t_{\mathrm{ref}},a}$ in the reference coordinate system, and the coordinates $\vec{x}_{t,a}$ at day t. The number of landmarks N ranged between 10 to 30.
Constraining the affine transformation and only allowing rotation, scaling and translation to describe cortical growth leads to similar results for the morphing parameters[204]. Similarly, morphing parameters that were obtained by optimizing the similarity between either the spontaneous correlation structure (see Section 3.8) or orientation preference maps (see Section 3.10.2) of successive days lead to quantitatively similar results in the statistical properties of spontaneous and evoked activity.

3.8 Spontaneous correlation patterns

To determine how spontaneous activity is correlated across space, we computed its spatial correlation structure across spontaneous events. In other words, we computed spontaneous activity correlation patterns from detected events by choosing a given seed point and computing its

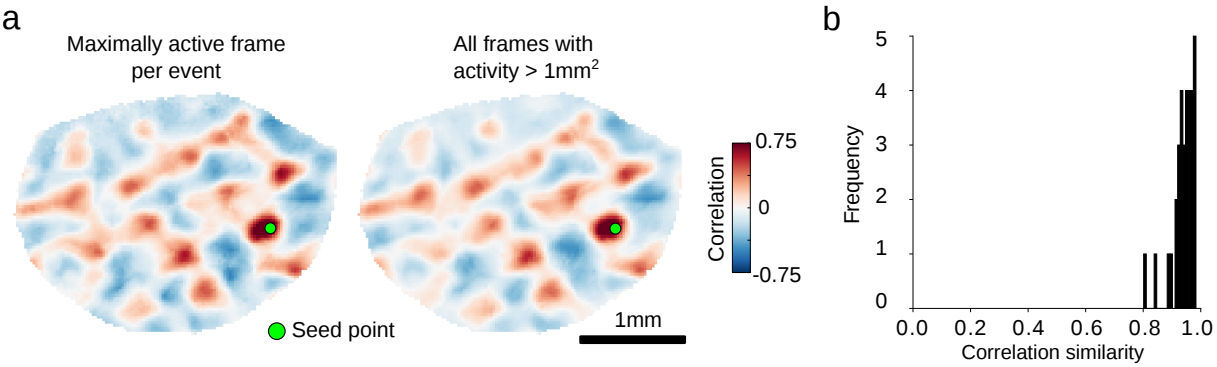

Figure 3.9: Correlation patterns based on all events are highly similar to those computed from large events only. **a** Example correlation pattern calculated over only the maximally active frames of large events (*left*) strongly resembles the correlation pattern from the same seed point calculated over all frames of all events larger than 1 mm^2 (*right*). **b** The average similarity between all correlation patterns within the ROI are shown for n=12 animals, N=33 experiments throughout development.

correlation in spontaneous activity with the remaining locations within the field of view. To this end, we first applied a Gaussian spatial high-pass filter (with SD of Gaussian filter kernel s_{high}=200 µm) to the maximally active frame in each event (see Section 3.6) and down-sampled it by a factor of 2 to 160 x 135 pixels. The resulting activity patterns A were used to compute the spontaneous correlation patterns as the pairwise Pearson's correlation coefficient between all locations $\vec{x}$ within the ROI to the seed point $\vec{s}$ (**Fig. 3.9**)

$$C(\vec{s},\vec{x}) = \frac{1}{N}\sum_{i=1}^{N}\frac{(A_i(\vec{s})-\langle A(\vec{s})\rangle)(A_i(\vec{x})-\langle A(\vec{x})\rangle)}{\sigma_{\vec{s}}\,\sigma_{\vec{x}}}. \tag{3.13}$$

Here the brackets $\langle\cdot\rangle$ denote the average over all events and $\sigma_{\vec{x}}$ ($\sigma_{\vec{s}}$) denotes the standard deviation of A over all events i at location $\vec{x}$ ($\vec{s}$). Throughout this work we used Pearson's correlation coefficient to calculate correlations.

High-pass filtering allowed us to extract the modular spatial structure of correlated domains, but the results did not sensitively depend on the filtering. For instance, weaker high-pass filtering using a kernel with s_{high}=520 µm resulted in a highly similar correlation structure. Note that calculating the spontaneous correlation patterns over all frames of all events larger than 1 mm^2 instead of selecting only the maximally active frame per large event preserves their spatial structure (**Fig. 3.9**).

To properly estimate correlations across spontaneous events a minimum number of events is required. To determine how many events are sufficient to still capture the correlation structure we determined the correlation structure across a subsampled set of events, and compared it to the correlation structure obtained across the full set of events. Subsampled correlation structures based on only 10 events still resembled the original correlation structure (**Fig. 3.10a,b**). In order to quantify the similarity between the correlation structure, we calculated their (second-order) correlation coefficient for different numbers of subsampled patterns (**Fig. 3.10c**). Subsampling only 10 events of >100 spontaneous events still resulted in a correlation similarity of 0.5 (**Fig. 3.10c**). Plotting the correlation similarity as a function of the fraction of events sampled showed that subsamples of 10 events asymptote at a similarity of approximately 0.5, even for cases with a large number of events (in which the fraction of events sampled is very low), indicating that 10 events is sufficient to capture major features of correlation structure.

In the following, imaging sessions in which less than 10 spontaneous events were detected were excluded from further analysis unless noted otherwise.

The ten-event threshold for inclusion was not applied to the LGN inactivation experiments

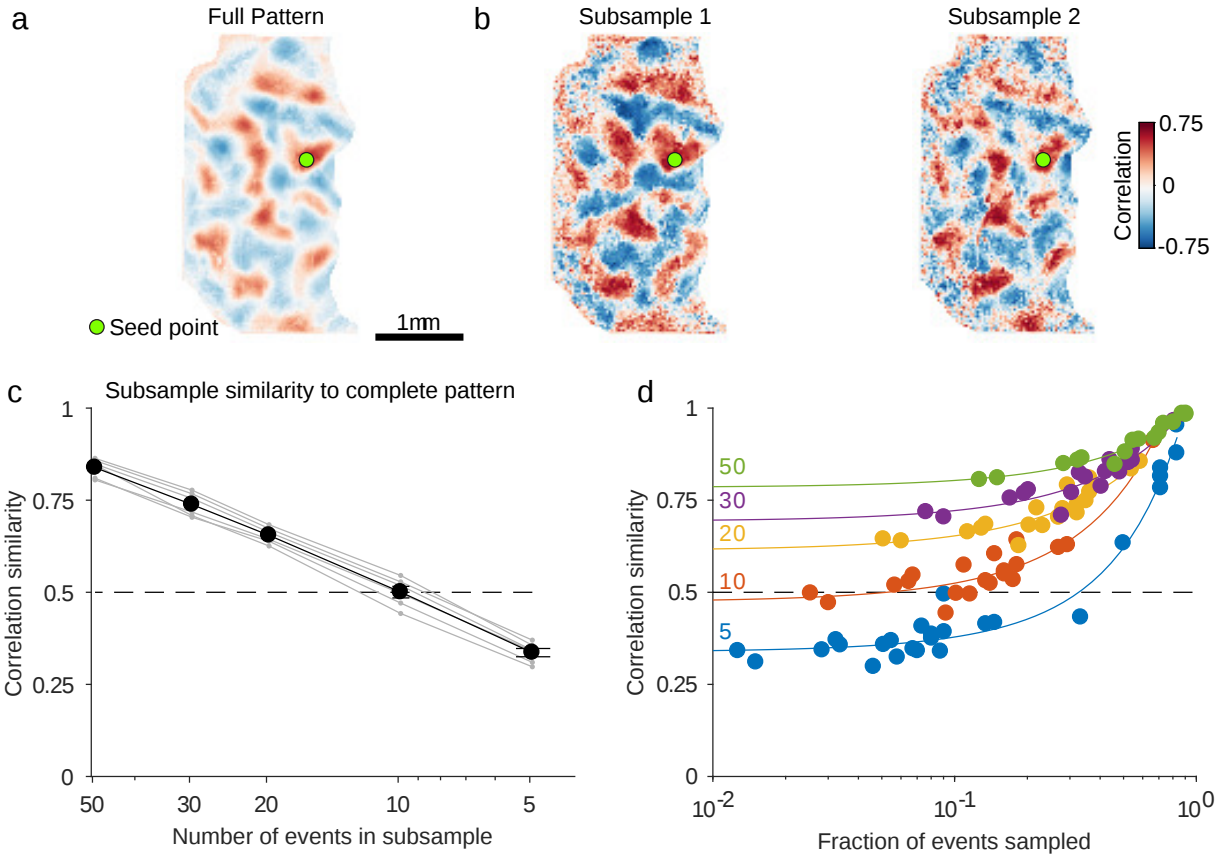

Figure 3.10: Minimum number of spontaneous events required to estimate correlations. **a** Correlation pattern from all events (393 events) for a seed point indicated in green. **b** Two example correlation patterns produced by randomly subsampling 10 of 393 events. **c** Similarity (second order correlation) of subsampled correlation structure to the correlation structure computed from all events (n=6 experiments with >100 spontaneous events). Correlation similarity of 0.5 is reached with approximately 10 events. **d** Similarity of subsampled correlation structure to complete correlation structure as a function of the fraction of events sampled for 5, 10, 20, 30, or 50 events (blue, orange, yellow, purple, and green curves respectively). Subsamples of 10 events asymptote at a similarity of approximately 0.5, even for cases with a large number of events (in which the fraction of events sampled is very low).

as, in 1 of 3 cases, fewer than ten events were recorded after LGN inactivation (see Chapter 4). We compared pre- and postinactivation activity patterns using second-order correlations as described for comparisons of awake and anesthetized activity in Section 3.10.1.

To compute spontaneous correlations of the 2-photon imaging data, we first identified frames containing spontaneous events, which were defined as frames in which >10 % of imaged neurons exhibited activity >2 standard deviations above their mean. Cellular activity on these frames was then Z-scored using the mean and standard deviation of each frame. We then computed the pairwise Pearson's correlation coefficient across the event frames between all pairs of cells.

3.9 Bootstrapping and surrogate data for statistical testing

3.9.1 Surrogate orientation preference map

To statistically test the similarity between orientation preference map and spontaneous correlations, we obtained surrogate maps as similar as possible to the original maps, but lacking any relation to the spontaneous activity patterns. Surrogate orientation preference maps were generated by phase shuffling the original maps in the Fourier domain but keeping their spectrum[231] yielding surrogate maps of the same two point statistics, but with domains distributed in cortical space without relation to the original map.

3.9.2 Surrogate datasets of spontaneous activity

To statistically test properties of spontaneous activity and the similarity of their spatial layout to orientation preference maps, we generated surrogate datasets of spontaneous activity patterns. We used two different approaches to generate surrogate datasets. In the first approach, all spontaneous activity patterns were randomly rotated (rotation angle drawn from a uniform distribution between 0° and 360° with a step size of 10°), translated (shifts drawn from a uniform distribution between ±450 µm in increments of 26 µm, independently for x- and y-direction) and reflected (with probability 0.5, independently at the x- and y-axis at the center of the ROI), resulting in an equally large control ensemble with similar statistical properties of individual patterns, but little systematic interrelation between patterns.
In the second method, spontaneous activity patterns were phase shuffled in the Fourier domain but kept their spectrum[231] yielding surrogate activity patterns of the same two point statistics, as in the method above with domains distributed in cortical space without relation to the original activity pattern.
We then computed surrogate correlation patterns from these ensembles as for the original activity patterns described in Section 3.8. Both methods resulted in qualitatively similar results.

3.9.3 Bootstrapping tests

Bootstrapping is a method to resample a distribution, enabling to repeatedly calculate a statistic of the resampled distributions and by this to assess the uncertainty of this statistic[125]. Bootstrapping is typically used if the underlying distribution of the data is unknown. The theoretical distribution can be replaced by the empirical distribution obtained from the bootstrapping method.
In this work we used the bootstrap test to assess if two datasets are drawn from the same distribution function or from different distributions. The two datasets were either a set of measured data points and a surrogate dataset, or two groups of data points (e.g. grouped by age). Typically, we compared the two distributions by comparing their mean or their median. Bootstrapping one of the datasets gives an error estimate of this dataset's mean (or median) which allowed us to reject or accept the null hypothesis that both datasets are drawn from the same distribution function.
In the following the bootstrap method we used is briefly outlined. Suppose we have a parameter P (in our case either mean or median) and an empirical estimate P_h for P. To obtain a non-parametric bootstrap estimate P_B of P, we generated a bootstrap sample by sampling with replacement from the first dataset. We typically generated an ensemble of N=10000 bootstrap estimates. To find the percentiles of P_h, we approximated the two-sided $100(1-2\alpha)$ confidence interval for P with the interval $[P_{B,(1-\alpha)}, P_{B,(\alpha)}]$, where $P_{B,(1-\alpha)}$ is the $100(1-\alpha)$ percentile of the P_B values, and similarly $P_{B,(\alpha)}$ is the 100α percentile. We then tested the null hypothesis H_0 that the parameter estimate of the second dataset R_h coincides with the estimate of the first

dataset P_h against the hypothesis that R_h and P_h differ. Since by bootstrapping we generated a confidence interval for P, we constructed an α level hypothesis test by simply accepting the null hypothesis H_0 if R_h is contained within the confidence interval $[P_{B,(1-\alpha)}, P_{B,(\alpha)}]$ for P, and rejecting H_0 if it is outside of this interval.

3.9.4 Statistical analysis

Throughout this thesis non-parametric statistical analyses were used. All tests were two-sided unless noted otherwise. Bootstrapping and surrogate approaches were used to estimate null distributions for test statistics as described above. Sample sizes were chosen to be similar to prior studies using similar methodologies in non-murine species[388,76,77,46,265]. All animals in each experiment were treated equivalently. No randomization or blinding was performed.

3.10 How does the long-range and fine-scale correlation structure of spontaneous network activity relate to evoked patterns of activity in the mature cortex?

3.10.1 Spatiotemporal properties of spontaneous activity at and after eye-opening

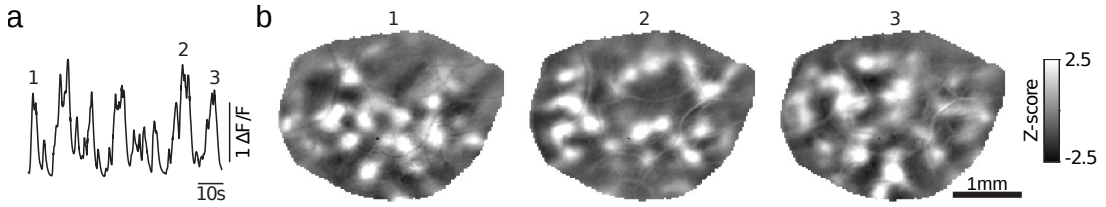

Figure 3.11: Spontaneous activity in awake ferret visual cortex is widespread and modular. **a** Timecourse of spontaneous activity measured with wide-field epifluorescence in an awake ferret (mean across locations in ROI). **b** Representative z-scored images of spontaneous events at times indicated in (**a**). Scale bar is 1 mm (**b**).

In the awake visual cortex of ferrets around the time of eye-opening, wide-field epifluorescence imaging revealed highly dynamic and spatially modulated patterns of spontaneous activity that cover millimeters of cortical surface area (**Fig. 3.11**). Spontaneous activity was spatially patterned such that active domains were arranged in a modular fashion which we will call modular activity in the following. Typically, spontaneous activity showed periods of prominent activity across the whole field of view intermitted by periods of low activity (**Fig. 3.11a**). High activity domains became active either almost simultaneously or in a spatiotemporal sequence of a few hundred milliseconds. This behaviour allowed to define periods of high activity as spontaneous *events*, and subsequently, to determine individual large-scale spontaneous patterns within ongoing spontaneous activity (**Fig. 3.11b**; see Section 3.6), which occurred frequently in the awake cortex.

Cortical locations co-vary in their spontaneous activity

Spontaneous activity patterns exhibited a remarkably regular modular structure extending over several millimeters. This might indicate a high degree of correlation in the activity of a specific

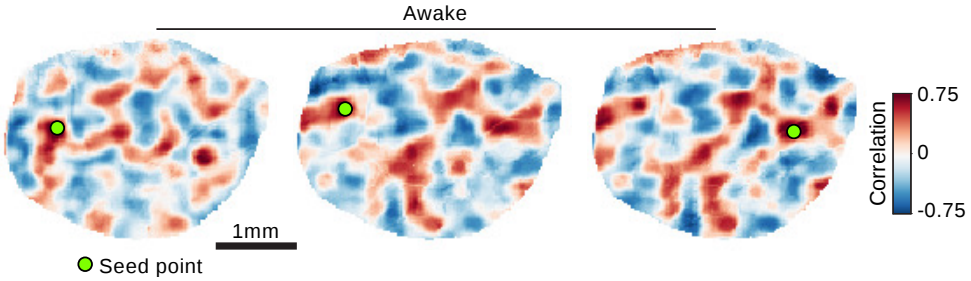

Figure 3.12: Correlated spontaneous activity in awake ferret visual cortex reveals large-scale modular distributed functional networks. Spontaneous activity patterns from around eye-opening shown for three different seed points (green circle). Red shaded areas are positively correlated with the seed point, whereas blue shaded areas are negatively correlated with the seed point. Correlation patterns span millimeters; they show both rapid changes between nearby seed points (*left* and *middle*) and long-range similarity for distant seed points (*middle* and *right*). Scale bar is 1 mm.

subset of neurons that are part of this distributed network. To determine if active domains co-vary, we computed the correlation structure across detected events in the spontaneous activity by choosing a given seed point and calculating its correlation in spontaneous activity with the remaining locations within the field of view (see Section 3.8). The correlation coefficients showed a widespread and modular structure with patches of positively correlated domains being interweaved with patches of negatively correlated activity (**Fig. 3.12**). The correlation patterns were self-consistent such that seed points placed in regions that were negatively correlated exhibit highly different spatial correlation patterns (**Fig. 3.12**, left and middle), while seed points placed millimeters away in regions that were positively correlated showed quite similar spatial correlation patterns (**Fig. 3.12**, middle and right). Systematically determining the correlation pattern for each seed point across the cortical surface revealed a large diversity of patterns. This impression was consistent with Principal component analysis (see Section 2.3.5 in Chapter 2) showing that the overall number of relevant global variance components in spontaneous activity patterns was typically larger than ten (**Fig. 3.13**; 13±3 PCs required to explain 75% variance, mean±SD, n=10 animals).

Spatial correlations show long-range organization

Distributed networks might display a long-range correlation structure not only in their stimulus evoked responses but also in their spontaneous activity. This notion seemed to be confirmed visually as the correlation patterns for a given seed point showed a striking widespread modular organization, with patches of positively correlated activity separated by patches of negatively correlated activity (**Fig. 3.12**). To quantify the impression of long-range correlations within spontaneous activity, we assessed the spatial scale over which the correlations decay. To this end, we first determined the envelope of the spontaneous correlations decaying over the distance to the seed point by identifying the local maxima (minimum separation between maxima 800 µm) in the correlation pattern for each seed point (**Fig. 3.14b**). Second, to properly assess the spatial range of spontaneous correlations we took care of spurious correlations caused by the finite sample size and compare the correlation structure of the real ensemble of spontaneous activity patterns from a given experiment with the correlation structure obtained from a control ensemble in which most of the spatial relationship between the patterns was eliminated (see

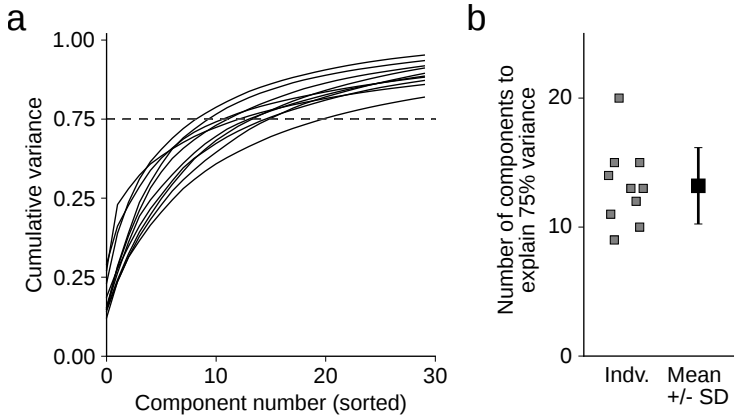

Figure 3.13: Principal component analysis of spontaneous activity. **a** The spontaneous activity events contain a moderate number of relevant principal components as shown by the cumulative explained variance. Gray dashed line indicates 75% variance. **b** The number of components needed to explain 75% variance is shown for 10 individual animals (gray) and the group mean±SD (black; 13±3, n=10 animals after eye-opening) is shown.

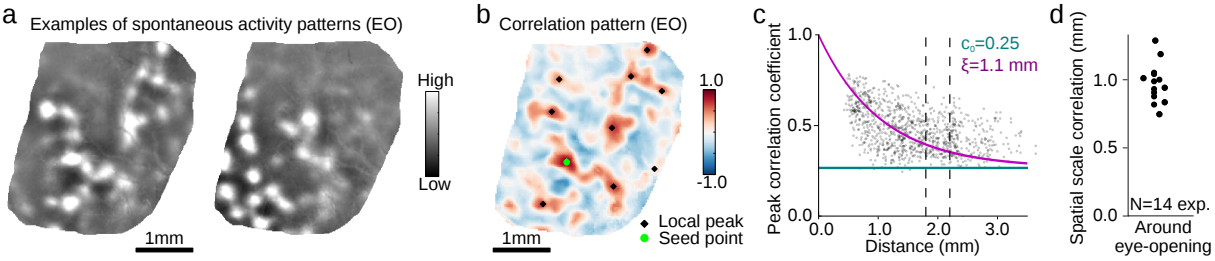

Figure 3.14: Spatial structure of spontaneous correlations extends over large distances. **a** Two representative spontaneous activity patterns at eye-opening (EO). **b** Correlation pattern calculated across all large events from EO for seed point shown in green. Local maxima (black markers) of correlation patterns are used to assess the envelope of the decaying correlations and plotted as a function of their distance to the seed point in (**c**). **c** Correlation values at the maxima as a function of distance from the seed point show that the correlation amplitude remains strong over long distances. Exponential fit (purple) with decay constant $\xi = 1.1$ mm and baseline correlation c_0 (cyan). **d** Spatial scale of correlations from N=14 experiments in n=10 animals at and after eye-opening. Scale bar is 1 mm (**a**,**b**).

Section 3.9). We then fitted an exponential decay function

$$f(x) = e^{-\frac{x}{\xi}}(1 - c_0) + c_0 \tag{3.14}$$

to the correlation maxima as a function of distance x to the seed point (**Fig. 3.14c**; see also **Fig. 5.12a**). Here ξ is the decay constant, named "spatial scale correlation" in **Fig. 3.14c**. The baseline c_0 accounts for the spurious correlations and was estimated as the average value of maxima at least 2 mm away from the seed point in the surrogate correlation patterns. This was the maximal distance for which we could robustly estimate the baseline value for most animals. We found that spontaneous correlations decay over a distance of ξ=(0.9±0.1) mm (mean±SD) (n=10 animals).

However, correlations extended significantly over more than 1 mm. To assess the statistical significance of long-range correlations at ∼2 mm from the seed point, we compared the median

correlation strength for maxima located (1.8-2.2) mm away against a distribution obtained from the correlation structure of 100 ensembles of surrogate spontaneous activity patterns (see Section 3.9). For individual animals, the p-value was taken as the fraction of median correlation strength values from surrogate data greater than or equal to the median correlation strength for real correlation patterns (bootstrap test). For 1 of 11 animals, the statistical significance of long-range correlations could not be assessed, due to insufficient coverage in rotated and translated surrogate activity patterns caused by a highly asymmetrically shaped ROI. This animal was excluded from the analysis of long-range correlation strength. Correlation patterns exhibited a significant long-range structure, with statistically significant correlations persisting for more than 2 mm (**Fig. 3.14c,d**; p <0.01 vs. surrogate for example shown, p <0.01 for 10 of 10 animals imaged following eye-opening). The peak correlation values showed a large variability as a function of distance and other functions such as a power law also captured its decay over several millimeters. Therefore, the result of long-range correlation did not sensitively depend on the fitting function.

Influence of brain state on correlation

To determine the impact of brain state and anesthesia on the spatial patterns of correlated spontaneous activity, we imaged spontaneous activity in awake animals and animals under light anesthesia (0.5-1% isoflurane). Although spontaneous activity in the awake cortex displayed a shorter mean inter event interval than under anesthesia (inter-event interval in awake cortex: 2.1 (1.3 - 6.5) s; median and IQR; n=5 animals; in anesthetized cortex: 4.3 (2.6 - 7.1) s; $p < 0.0001$ bootstrap test; **Fig. 3.15a,c**, **Fig. 3.16b**), the event duration did not show a significant difference between awake (event duration: 0.9 (0.5-1.3) s; median and IQR) and anesthetized animals (1.1 (0.7-1.6) s; **Fig. 3.16a**). Similarly, the spatial patterns of spontaneous activity, both in extent, modularity, and correlation structure were remarkably similar across states (**Fig. 3.15e,f**). To quantify this resemblance, the correlation similarity across awake and anesthetized states was computed for each seed-point as the Pearson's correlation coefficient of the spontaneous correlations for that seed point across states. For each seed-point, correlations within 400 µm were excluded from analysis in order to eliminate the local peak around the seed point which would bias the correlation similarity towards positive values. These "second-order correlations" (shown for each seed point in **Fig. 3.15f**) were then averaged across all seed points within the ROI. To determine the significance of these second-order correlations across state, we shuffled corresponding seed points across states 1000 times, and again computed correlation similarity. Likewise, to obtain an estimate of the expected similarity for a well-matched correlation structure, we computed the similarity of each state to itself. To this end, correlation patterns were first separately computed for half of the detected events, and then the two patterns were compared as above. The correlation similarity was high between the correlation structures in the awake and anesthetized states (**Fig. 3.15i**; p=0.031 one-sided Wilcoxon signed-rank test, with 5 of 5 experiments from 3 animals individually significant at p <0.001 vs. shuffle). Given this strong similarity, we pooled across awake and anesthetized recordings in the analyses presented in this thesis. In some experiments only anesthetized recordings were performed. The stability of the large-scale correlation patterns across awake and anesthetized states was consistent with previous work demonstrating that properties of spontaneous activity are similar across states[383].

Wide-field and cellular correlations are consistent

To test whether the modular structure of spontaneous activity observed with wide-field imaging is also found on a single cell level, we performed 2-photon imaging with cellular resolution

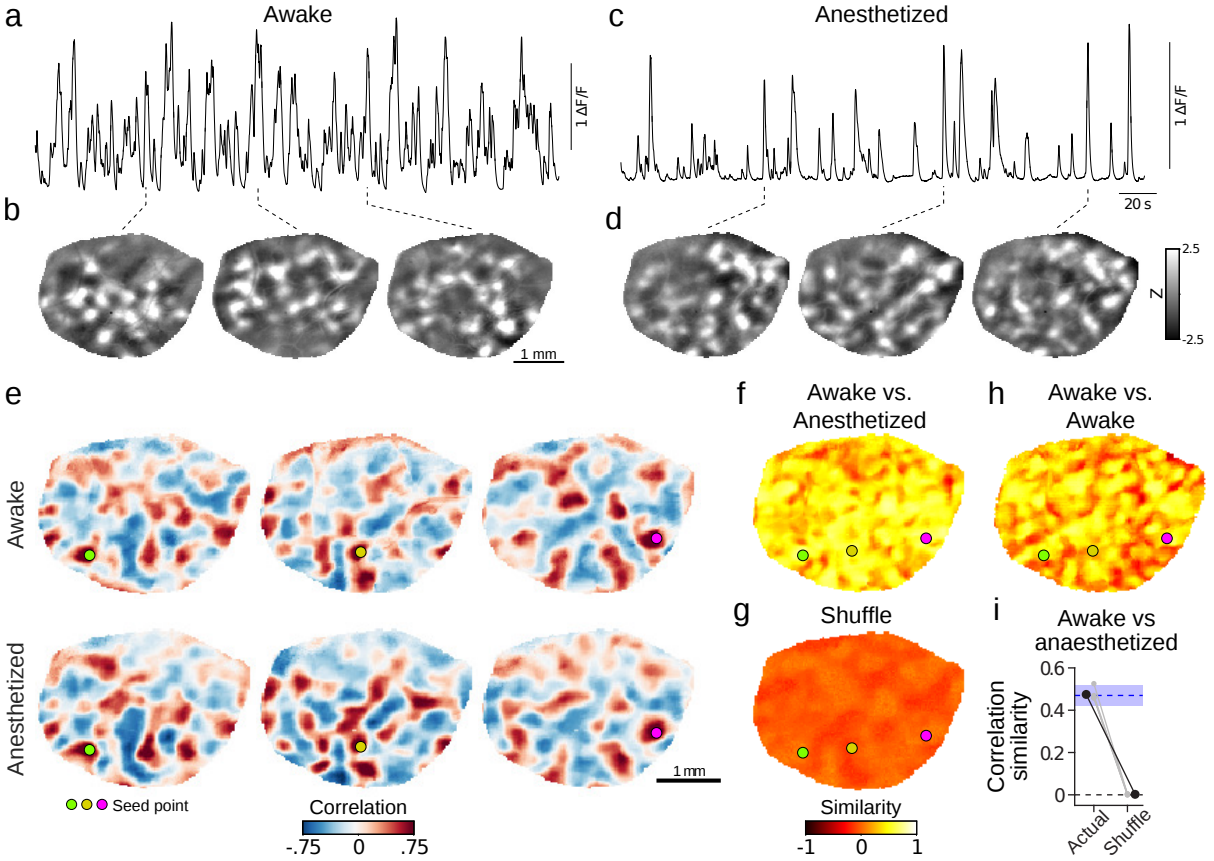

Figure 3.15: Spatial structure of spontaneous correlations is not affected by anesthesia. **a** Timecourse of spontaneous activity (mean frame $\Delta F/F$) for awake animal. **b** Three representative events at times indicated. **c** Timecourse of spontaneous activity in same animal under anesthesia (0.5-1% isoflurane) **d** Representative events. **e** Three spontaneous activity correlation patterns for awake activity (*top*) and under anesthesia (*bottom*). **f** Similarity of awake vs. anesthetized correlation patterns evaluated at each location in ROI. **g** Similarity for shuffled patterns. **h** Similarity of awake patterns calculated from 50% of spontaneous events to patterns calculated from remaining 50% of events. **i** Correlations measured under anaesthesia are statistically similar to those in the awake cortex (number of animals n=5, grey: individual animals, black: mean ± standard error of the mean (SEM=SD/$\sqrt{n}$)). Blue shaded region indicates within-state similarity (mean±SEM).

in conjunction with wide-field imaging in the same animal. In the 2-photon imaging data we found robust and spatially organized spontaneous activity at the cellular level. The duration of events was similar to that observed with wide-field imaging (0.88 (0.54-1.32) s, median and IQR; compare **Fig. 4.2** in Chapter 4), and within an event the pattern of active cells was largely consistent across time (frame-to-frame correlations >0.5 for one second around the peak frame within an event, p <0.01 vs. random epochs, bootstrap test).

To compare the correlation structure obtained at the cellular level with that obtained via wide-field imaging (**Fig. 3.17**), we first computed the correlation patterns for each cell as the pairwise Pearson's correlation coefficient, using the activity of all neurons on all active frames (see Section 3.6).

Next, we corrected 2-photon images for in plane motion via a 2D cross correlation-based approach. We then aligned the 2-photon field of view (FOV) to the wide-field image using blood

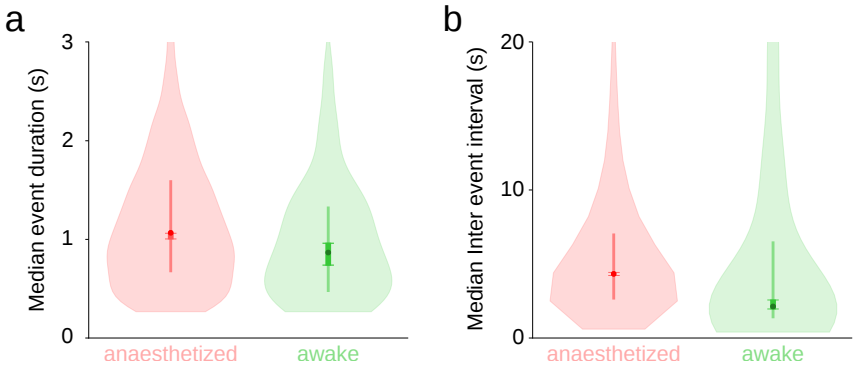

Figure 3.16: Distribution of event duration and inter event interval of spontaneous events in anesthetized and awake animals after eye-opening. **a** The distribution of median event duration is similar between awake and anesthetized animals. **b** The median inter event interval is significantly smaller in the awake animals compared to the comparable age group in anesthetized animals ($p < 0.0001$, bootstrap test). Shaded area shows histogram of distribution with median denoted by circular marker. Vertical lines show errorbars of median from bootstrapping. Horizontal lines mark interquartile range (25 to 75 percentile) of distribution.

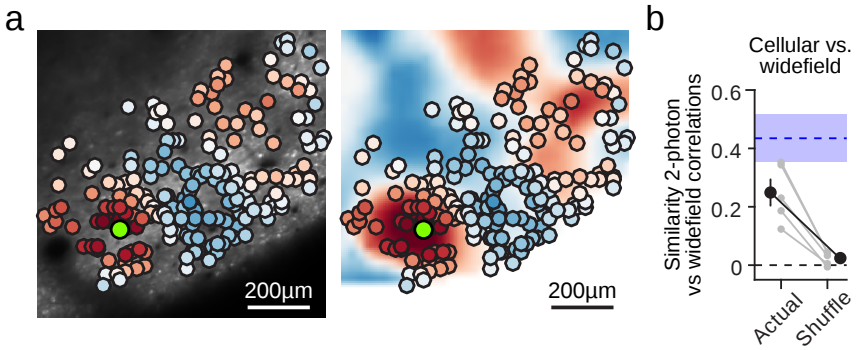

Figure 3.17: Spontaneous activity is modular at the cellular level. **a** Spontaneous activity is modular and correlated at the cellular level (*left*) and shows good correspondence to spontaneous correlations obtained with wide-field imaging (*right*). **b** Cellular correlations are signifcantly similar to wide-field correlations (n=5 animals, gray: individual animals, black: mean±SEM). Blue region indicates within-modality similarity (mean±SEM; similarity of 2-photon correlation structure between subsampled sets of detected events).

vessel landmarks and applied an affine transformation to obtain the pixel coordinates of each imaged neuron in the wide-field frame of reference. Correlation similarity was obtained as above by computing the second-order correlation between the cellular correlation structure and that of the corresponding wide-field pixels, using all cells >200 µm from the seed point. Shuffled second-order correlations were obtained by randomly rotating and translating the 2-photon FOV within the full wide-field ROI, 1000 times. To estimate the maximum expected degree of similarity, we computed a second-order correlation within the cellular correlation structure itself by determining the similarity of correlation structures computed using only 50% of detected events (dashed line and blue bar in **Fig. 3.17b**). The modular organization of spontaneous activity and the spatial correlation patterns observed in populations of individual layer 2/3 neurons was well-matched to those found with wide-field imaging, demonstrating that the network structures revealed with wide-field epifluorescence imaging reflect the spatial activity patterns of individual

neurons in superficial cortex (**Fig. 3.17b**; p=0.031 one-sided Wilcoxon signed-rank test, with 4 of 5 experiments from 3 animals individually significant at p <0.05 vs. shuffle).

Summary

At around eye-opening ferret primary visual cortex exhibited strong, on-going spontaneous activity. Spontaneous activity consisted of periods of high activity (events) intermitted by periods of low activity without any apparent spatial structure. Spatial activity patterns during events were modular exhibiting an orderly layout of active domains. This modular layout was also visible with single cell resolution. Active domains co-varied; their correlation structure was spatially modulated and extended up to at least 2 mm in cortex. These properties of spontaneous activity were conserved across states when comparing anesthetized and awake animals. Taken together, these results indicate that neurons in layer 2/3 of visual cortex participate in long-range modular networks.

3.10.2 Spontaneous activity resembles fine-scale structure of functional cortical layout on a global range

Layout of spontaneous activity resembles functional maps

Previous experimental studies have shown that the arrangement of active domains in individual spontaneous events in anesthetized, mature animals can resemble activity patterns evoked by oriented stimuli[235,327]. We therefore sought to determine whether the correlated spontaneous activity representing an average over many events and potentially revealing the underlying network architecture, accurately reflects the structure of the visually evoked modular network that represents stimulus orientation. In particular, we investigated if the similarity between spontaneous correlations and evoked responses holds also on a fine spatial scale and over an extended range.

First, we calculated the orientation preference map (**Fig. 3.18a**, **Fig. 3.20a**, **Fig. 4.10a** (right)) based on the trial-averaged responses to moving grating stimuli of eight directions equally spaced between 0° and 360°. Responses were Gaussian band-pass filtered (see Section 3.5.3) and the orientation preference $z(\vec{x}) = r(\vec{x})e^{2i\phi(\vec{x})}$ with selectivity $r(\vec{x})$ and preferred orientation $\phi(\vec{x})$ was computed by vector summation for each location $\vec{x}$ as

$$z(\vec{x}) = \sum_{k=1}^{8} w_k(\vec{x})e^{2i\phi_k} \tag{3.15}$$

$$\text{with} \quad \vec{x} = (x, y)^T \tag{3.16}$$

where $w_k(\vec{x})$ is the tuning curve at location $\vec{x}$ (see Section 3.5), i.e. the trial-averaged response to a moving grating with direction ϕ_k at location $\vec{x}$. ϕ_k is expressed in radians. The factor 2 in the argument of the exponential function takes into account that orientation tuning is periodic over 180° instead of 360° (stimuli whose directions are 180° apart share the same orientation). The preferred orientation at $\vec{x}$ is then 0.5 arg($z(x)$). Orientation contour lines in **Fig. 3.18a,c**, **Fig. 3.19b**, **Fig. 3.20b** are the zero-levels of the 0° -90° difference map, obtained by using the matplotlib.pyplot.contours routine.

Next, we compared the patterns of spontaneous correlations assessed after eye-opening to the spatial layout of visually-evoked orientation domains in animals imaged five or more days after eye-opening, when orientation selectivity was robust (**Fig. 3.20a**). To quantify how similar patterns of correlated spontaneous activity were to the orientation preference map in visual cortex, we computed the average pairwise magnitude of the Pearson's correlation coefficient

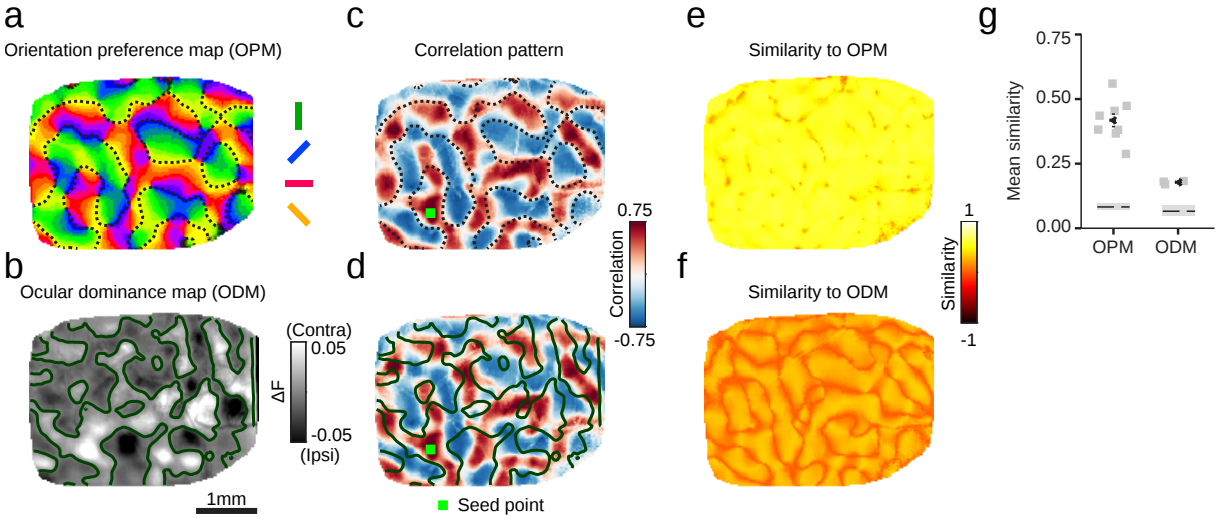

Figure 3.18: The correlation structure of spontaneous activity more closely resembles the functional layout of iso-orientation domains than ocular dominance domains. **a** An orientation preference map (OPM). The black-dotted line represents 0°-90° zero contours. **b** An ocular dominance map (ODM). The dark green line represents zero-contours separating contralateral and ipsilateral domains. **c,d** The contours from the OPM in (**c**) better match the correlation structure of spontaneous activity than the contours from the ODM in (**d**). The seed point in (c) and (d) corresponds to a region preferentially driven by a contralaterally presented horizontal grating. **e,f** For the example animal shown in (**a-d**), most spontaneous correlation patterns show higher similarity to the layout of the OPM (**e**) than to the ODM (**f**). **g** On average, spontaneous correlation patterns show significantly higher pairwise similarity to the OPM than the ODM (p=0.02, Mann-Whitney U test, n=8 animals for orientation map and n=3 animals for ocular dominance map; gray: individual animal; black: mean±SEM), but the mean pairwise similarity to both the orientation preference and ocular dominance maps is significantly higher than to control shuffled maps (p <0.0001, bootstrap test; dashed line with gray shaded area indicates mean±SEM).

between the correlation pattern of each seed point in the ROI to the real (cardinal difference map) and imaginary (oblique difference map) components of the orientation preference map z:

$$r_{\mathrm{OP}}(\vec{x}) = \sqrt{\left(\frac{\mathrm{cov}(\mathrm{Re}(z(\vec{y})), C(\vec{x},\vec{y}))}{\sigma_{\mathrm{Re}\,z}\ \sigma_{C_x}}\right)^2 + \left(\frac{\mathrm{cov}(\mathrm{Im}(z(\vec{y})), C(\vec{x},\vec{y}))}{\sigma_{\mathrm{Im}(z)}\ \sigma_{C_x}}\right)^2} \tag{3.17}$$

where $C(\vec{x},\vec{y})$ is the spontaneous correlation pattern between seed location $\vec{x}$ and location $\vec{y}$, and cov denotes the covariance. $\sigma_{C_x}, \sigma_{\mathrm{Re}(z)}, \sigma_{\mathrm{Im}(z)}$ denote the standard deviation of the correlation pattern and the difference maps, respectively. We observed individual spontaneous correlation patterns that closely matched the layout of orientation domains up to several millimeters from the seed point across the entire field of view (**Fig. 3.18**, **Fig. 3.20b**; average across seed points of similarity of orientation vs. spontaneous: r_{OP}=0.42±0.03; mean±SEM; n=8 animals). To determine statistical significance, we obtained control datasets by phase shuffling the original orientation preference map in the Fourier domain[231] (see Section 3.9.1) and calculating the pairwise correlation coefficient between them and each spontaneous correlation pattern (**Fig. 3.18g**) (see Section 3.9.3).

The resemblance was particularly high between correlation patterns of orientation selective seed

points and the response to their respective preferred orientation. The correlation patterns of seed points which were selective for cardinal orientations (0° and 90°) strongly resemble the cardinal difference map (**Fig. 3.19a,b,e**) whereas correlation patterns of low-selective seed points did not show this strong resemblance (**Fig. 3.19b,e**, *right*). For this reason, the second order correlation between the cardinal difference map and the spontaneous correlation patterns resembled the cardinal map (**Fig. 3.19c**). In **Fig. 3.19** the similarity with the cardinal difference map is shown and quantified, but quantitatively similar results were obtained when considering the oblique difference map. To determine statistical significance, surrogate datasets were obtained by phase shuffling the orientation preference map in the Fourier domain[231], calculating the pairwise correlation coefficient between their real part and each spontaneous correlation pattern (**Fig. 3.19d**; see Section 3.9), and then comparing the resemblance to the surrogate cardinal map.

To test if spontaneous activity encompassed more than only the orientation preference map,

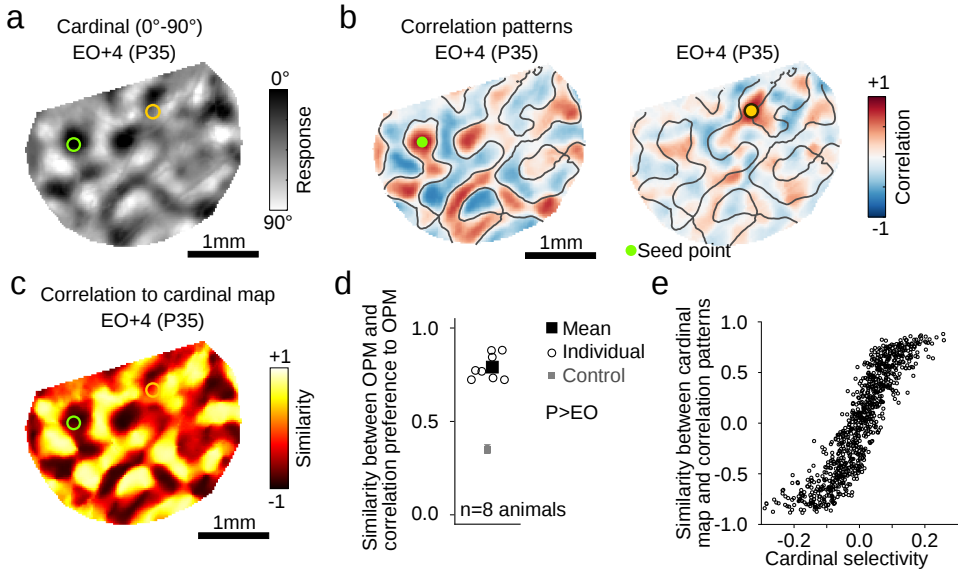

Figure 3.19: The correlation patterns of highly orientation selective seed points are particularly similar to the layout of orientation domains. **a** Cardinal difference map from four days after eye-opening (EO+4). White shaded regions prefer 90° , and black regions 0° oriented moving gratings. **b** Examples of spontaneous correlation patterns from EO+4. *Left:* Seed point is selective for 90° oriented stimuli and its correlation pattern resembles the layout of the cardinal difference map shown in (**a**). *Right*: Seed point is not selective for cardinal orientations, and the correlation pattern shows low similarity to the cardinal map. Gray contour lines denote the zero level of the cardinal difference map shown in (**a**). For comparison seed points are also shown in (**a**,**c**). **c** The correlation between the spontaneous correlation patterns and the mature cardinal difference map is highest for patterns from seed points that are selective for cardinal orientations. **d**. Each individual data point (open circle) shows significant higher correlation between the cardinal map and the 2nd order correlation between each correlation pattern and the cardinal map ($p < 0.01$, boostrap test, n=8 animals) than control (gray; Mean±SD). Average across individual data points is indicated by black rectangle. **e** The cardinal selectivity (positive values correspond to prefering 0° oriented stimuli) is correlated to the similarity between cardinal map and correlation patterns. Same example as shown in (**a-c**). Scale bar: 1 mm (**a-c**).

we next assessed the similarity between the spontaneous correlation patterns and the ocular dominance map m_{OD} (**Fig. 3.18b**). Ocular dominance maps were calculated based on the trial-

averaged responses evoked by presenting moving grating stimuli of eight directions Φ_k equally spaced between 0° and 360° either to the contralateral or ipsilateral eye. The trial averaged response to each stimulus condition was Gaussian band-pass filtered as described above for the orientation map. Contralateral and ipsilateral response maps were computed by respectively averaging together the trial-average responses to the stimuli presented either to the contralateral or ipsilateral eye as described for the orientation map. The ocular dominance map m_{OD} was computed as the difference of the contralateral w_{contra} and ipsilateral (w_{ipsi}) response maps

$$m_{\mathrm{OD}}(\vec{x}) = w_{\mathrm{contra}}(\vec{x}) - w_{\mathrm{ipsi}}(\vec{x}) \tag{3.18}$$

$$\text{with} \quad w_{\mathrm{contra/ipsi}}(\vec{x}) = \sum_k w_{k,\mathrm{contra/ipsi}}(\vec{x}) \tag{3.19}$$

where k denotes the index of the direction of the moving grating (see Eq. (3.15)). The similarity of each spontaneous correlation pattern to the ocular dominance map was quantified by the magnitude of the pairwise Pearson's correlation coefficient (**Fig. 3.18f**)

$$r_{\mathrm{OD}}(\vec{x}) = |\frac{\mathrm{cov}(m_{\mathrm{OD}}(\vec{y}), C(\vec{x},\vec{y}))}{\sigma_m \sigma_{C_x}}|. \tag{3.20}$$

Contour lines of ocular dominance map in **Fig. 3.18b**, are the map's zero-levels and obtained by using the matplotlib.pyplot.contours routine.
We found a significantly weaker but above chance (p=0.02, Mann-Whitney test comparing similarity of spontaneous activity to ODM and to OPM, n=3 animals) similarity of spontaneous correlations to the ocular dominance map than to orientation preference maps (**Fig. 3.18g**, mean similarity of ocular dominance vs. spontaneous: r_{OD}=0.18±0.04; mean±SEM; n=3 animals; p <0.0001 vs. surrogate for 3 of 3 animals tested). This limited similarity between spontaneous correlations and ocular dominance map was consistent with previous multielectrode recordings in developing ferret[85]. To determine statistical significance control datasets were obtained by phase shuffling the contralateral and ipsilateral orientation preference map in the Fourier domain[231] and calculating the pairwise correlation coefficient between the resulting control ocular dominance map and each spontaneous correlation pattern (**Fig. 3.18g**) (see Section 3.9). Thus, this analysis indicates that spontaneous activity does not only contain information about the orientation preference map but also to a weaker degree resembles the layout of the ocular dominance map.

Similarity between spontaneous activity and evoked response extends over large spatial range

Notably, the correlation patterns of certain seed points at around eye-opening showed a strong similarity to the orientation preference across the whole field of view and not only localized around the seed point (**Fig. 3.20a,b**). This robust long-range similarity suggests that the orientation tuning at such seed points can be predicted from the tuning at remote locations that are correlated in spontaneous activity. To test this idea, we predicted the tuning at a seed point by computing the sum over tuning curves at distant locations weighted by their spontaneous correlation with the seed point and compared this prediction w_k^{pred} to the seed point's actual tuning curve w_k (**Fig. 3.20c**, *top left*)

$$w_k^{\mathrm{pred}}(\vec{s}) = \sum_{\vec{x}} w_k(\vec{x}) C(\vec{s},\vec{x}) \tag{3.21}$$

where $\vec{s}$ denotes the location of the seed point, the tuning curve $w_k(\vec{x})$ gives the response of location $\vec{x}$ for a moving grating of orientation k, and $C(\vec{s},\vec{x})$ is the correlation coefficient between $\vec{s}$ and $\vec{x}$. The sum was taken over locations $\vec{x}$ outside a circular area centered at the seed

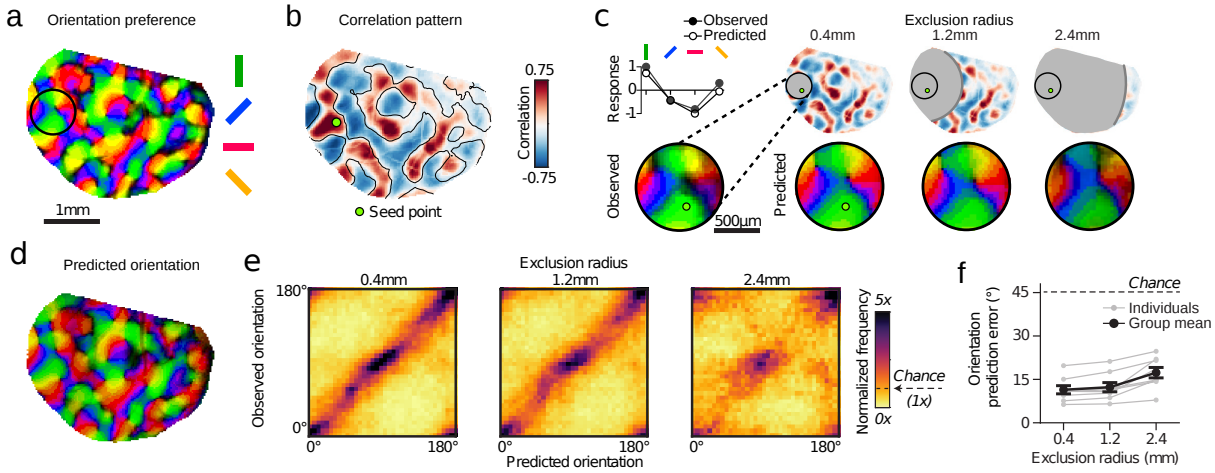

Figure 3.20: Spontaneous correlation resembles orientation preference on a long-range scale after eye-opening. **a** Orientation preference map from five days after eye-opening (EO+5). **b** Spontaneous correlation pattern for indicated seed point (EO+5). Contour lines from vertical selective domains from (**a**) reveal that spontaneous correlations globally resemble the layout of orientation preference map. **c** Local orientation tuning for region within black circle in (**a**) can be accurately predicted from the aggregate orientation tuning of distant cortical locations, weighted by long-range correlations. *Top left*: Observed and predicted tuning for single pixel shown below. *Bottom left*: Observed orientation tuning. *Right*: Accurate orientation predictions based on increasingly distant regions of spontaneous correlations (excluding pixels within either 0.4, 1.2, or 2.4 mm from the seed point). **d** The prediction based on correlations >1.2 mm away (excluding all correlations >1.2 mm from seed point) matches the actual preferred orientation within the entire field of view (see (**a**)). **e** Across animals, the precision of predicted orientation tuning remains high, even when based on restricted regions more than 2.4 mm away from the site of prediction (see (**c**)) **f** Prediction error as function of exclusion radius (45° is chance level). For (**e,f**): n=8 animal experiments with 5 days or more of visual experience; group data in (**f**) is shown as mean±SEM.

point with radius 0.4, 1.2 or 2.4 mm. To assess the goodness of the prediction, we calculated the angular difference between the predicted and the actual preferred orientation (**Fig. 3.20f**). Low values indicate a high match, whereas 45° indicates chance level.

Correlated spontaneous activity predicted the preferred orientation in a small circular patch of radius 0.4 mm highly accurately (**Fig. 3.20c**). Remarkably, the orientation predictions remained precise even if only correlations were considered in regions more than 2.4 mm from the circle's center point (**Fig. 3.20c,f**, $p < 0.0001$ vs. surrogate for all exclusion radii, with 8 of 8 individual animals significant at $p < 0.05$ across all exclusion radii). This demonstrates a high degree of long-range fidelity in the structure of spontaneously active networks and those evoked by oriented visual stimuli. An accurate prediction was achieved for the most part of the imaged region (**Fig. 3.20d,e**) and remained fairly precise even when excluding all locations up to 2.4 mm from the predicted site (**Fig. 3.20e**), as demonstrated by the group data (**Fig. 3.20f**). Both the predicted and the observed orientations showed a peak in their distribution around the cardinal orientations 0 and 90° . This is consistent with the overrepresentation of cardinal orientations in the field of view found in the majority of the animals.

Statistical significance (**Fig. 3.20f**) was determined by repeating this analysis for 100 surrogate orientation preference maps, obtained by phase shuffling in the Fourier domain[231] (see Section 3.9). For individual animals, the p-value was taken as the fraction of values equal or

smaller than the value for the real orientation map. To pool across animals within an exclusion radius (**Fig. 3.20f**), we then generated 10.000 surrogate group medians by randomly drawing from the distributions of surrogate data points (one per animal), and the p-value was taken as the fraction of group medians equal or smaller than the median value for the actual data (see Section 3.9).

Spontaneous activity reflects fine-scale structure of layout of orientation domains

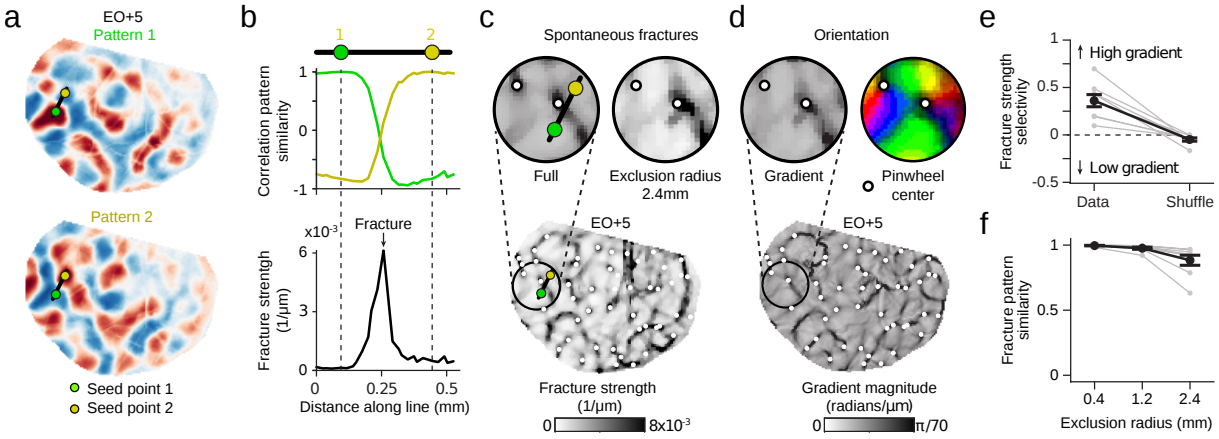

Figure 3.21: Tight interrelation between long-range spontaneous correlation and the fine-scale structure of orientation columns after eye-opening. **a-b** Fractures in correlated networks. Advancing the seed-point along the black line in (**a**) reveals a punctuated rapid transition in global correlation structure (EO+5) expressed by a high rate of change in the correlation pattern between adjacent pixels (**b**, *bottom*). **c** Locations with high rate of change form a set of lines across the cortical surface, which we termed spontaneous fractures. **d** The layout of spontaneous fractures (EO+5) precisely coincides with the high-rate of change regions in the orientation preference map (EO+5). **e** Correlation fractures show selectivity for regions of high orientation gradient. **f** Fracture location is independent of local correlation structure and remains stable when only long-range correlations are included. For (**e**, **f**): n=8 animal experiments with 5 days or more of visual experience; group data in (**f**) is shown as mean±SEM. For (**c**, **f**) same exclusion radii as in **Fig. 3.20c**).

Orientation preference changed with a highly heterogeneous rate across the cortical surface, most notably at pinwheel centers[43,45,332]. Determining the magnitude of the gradient of the orientation preference map revealed that orientation preference changes relatively little within large domains, but strongly between domains. Thus the iso-orientation domains were surrounded by narrow, elongated areas of high rate of change. Therefore an even more stringent test of the relationship between the spontaneous activity and the fine spatial structure of the layout of orientation domains is to assess whether spontaneous correlation patterns exhibit an analogous heterogeneity in their rate of change that correlates with the orientation preference map. By visual inspecting the correlation patterns of neighbouring seed points we found regions with gradual changes in the correlation patterns that were interrupted by areas with abrupt shifts in the large-scale pattern. We quantified this rate of change R of the correlation pattern when moving the seed point a small distance by

$$R(\vec{s}) = \sqrt{R_{dx}(\vec{s})^2 + R_{dy}(\vec{s})^2} \tag{3.22}$$

where R_{dx} (R_{dy}) denotes the $x(y)$-component of the rate of change of the correlation pattern at seed point $\vec{s}$. We approximated this rate of change by the (second-order) correlation between two correlation patterns with seed points at adjacent pixels a distance d apart:

$$R_{di}(\vec{s}) = \frac{|1 - C_i(\vec{s})|}{d} \tag{3.23}$$

$$C_i(\vec{s}) = \frac{\mathrm{cov}\left(C(\vec{s},\vec{x}), C(\vec{s} + d\ \vec{e}_i, \vec{x})\right)}{\sigma_{C_s}\ \sigma_{C_{s+d\vec{e}_i}}} \quad \text{with} \quad i \in \{x, y\} \tag{3.24}$$

where cov denotes the covariance calculated over all locations $\vec{x}$ normalized by the standard deviation across the correlation pattern $\sigma_{C_s}, \sigma_{C_{s+d\vec{e}_i}}$. $\vec{e}_x$ ($\vec{e}_y$) is a unit vector in x (y)-direction. The subtraction from 1 in the numerator ensures $R = 0$ at seed point locations, around which the correlation pattern does not change, whereas high values of R indicate high changes. We used d=26 µm, the spatial resolution of the correlation patterns.

By computing the rate of change of the correlation pattern as the seed point is moved, we observed peaks of large change over relative small distances (**Fig. 3.21a-b**). Systematically computing the two-dimensional gradient across the cortical surface revealed a set of lines with high gradient magnitude, which we termed *spontaneous fractures* (**Fig. 3.21c**). Moving the seed point across any of these fractures led to changes in the global correlation pattern, whereas the correlations changed relatively little when the seed point is moved within the regions between the fractures.

To test whether spontaneous fractures reflected the correlation structure over remote distances and not only in their local neighborhood, we computed R as described in Eqs. (3.22)-(3.24), but excluding a circular region with radius 0.4, 1.2 or 2.4 mm, centered at the seed point $\vec{s}$ (**Fig. 3.21c,f**). Notably, the layout of spontaneous fractures was stable even when only correlations with remote locations (>2.4 mm from seed point) were used to determine the local rate of change, demonstrating again the long-range correlation structure in spontaneous activity (**Fig. 3.21f**; correlation between fracture patterns for radius >0 mm vs. >2.4 mm: r=0.88±0.04, mean±SEM, n=8 animals).

Strikingly, the spontaneous fractures followed closely the layout of heterogeneous rate of change in the orientation preference map (**Fig. 3.21c,d**). To quantify the co-alignment between spontaneous fractures and high orientation gradient regions, we measured the fracture selectivity as the difference between $R(\vec{x})$ at high orientation gradient locations ($\vec{x}_{\mathrm{high}}$, $|\vec{\nabla} z(\vec{x})| > \pi/5$ radians/pixel) and locations far from high orientation gradients ($\vec{x}_{\mathrm{low}}$, $|\vec{x}_{\mathrm{low}} - \vec{x}_{\mathrm{high}}| >$150 µm from $\vec{x}_{\mathrm{high}}$):

$$FS = \frac{\langle R(\vec{x}_{\mathrm{high}})\rangle - \langle R(\vec{x}_{\mathrm{low}})\rangle}{\langle R(\vec{x}_{\mathrm{high}})\rangle + \langle R(\vec{x}_{\mathrm{low}})\rangle} \tag{3.25}$$

where the brackets denote average over locations $\vec{x}_{\mathrm{high}}$ and $\vec{x}_{\mathrm{low}}$, respectively. A value of FS of 1 indicates co-alignment between the spontaneous fractures and the orientation gradient, whereas a value near 0 indicates a lack of such an alignment. To assess significance we repeated this analysis for 1000 surrogate orientation preference maps that were obtained by phase shuffling in the Fourier domain[231] (**Fig. 3.21e**). The p-value was the fraction of values equal or larger than the value for the orientation map (see Section 3.9). The layout of spontaneous fractures in the mature animal followed closely the heterogeneity in the rate of change in preferred orientation (**Fig. 3.21d**), and often they appeared in tight register with one another (**Fig. 3.21e**; p=0.0078, Wilcoxon signed-rank test, with 8 of 8 individual animals significant at p<0.001, bootstrap test).

To further test the relation between spontaneous fractures and changes in the orientation preference map, we compared the fractures to the position of pinwheel centers. Pinwheels mark points in the orientation preference map where all preferred orientations converge and mark

singularities in the otherwise smooth map. Their layout and density follow a common design[231]. The positions of the pinwheel centers lied mostly on top of the spontaneous fracture lines which further highlights the close relationship between the spontaneous correlation structure and the evoked functional organization (**Fig. 3.21c,d**). Orientation pinwheel centers were estimated as described in Refs.[231,373]. The Matlab routine provided by Schottdorf et al.[373] was used (**Fig. 3.21c,d**).

Summary

Around eye-opening the spatially modulated layout of the spontaneous correlation structure resembled the orientation preference map and to a degree also the ocular dominance map. This similarity held not only locally but over several millimters across the entire field of view. The correlation structure exhibited a variety of different correlation patterns. The transition from one pattern to another could occur over a relatively small cortical distance accompanied by large-scale changes in the pattern. These large-scale changes were organized in the intricate layout of spontaneous fractures. Its similarity to the gradient of the orientation preference map revealed that both the fine- and large-scale organizations of correlated spontaneous activity were closely aligned with the structure of the visually evoked orientation network.

3.10.3 Trial-to-trial variability in visually evoked responses in mature cortex

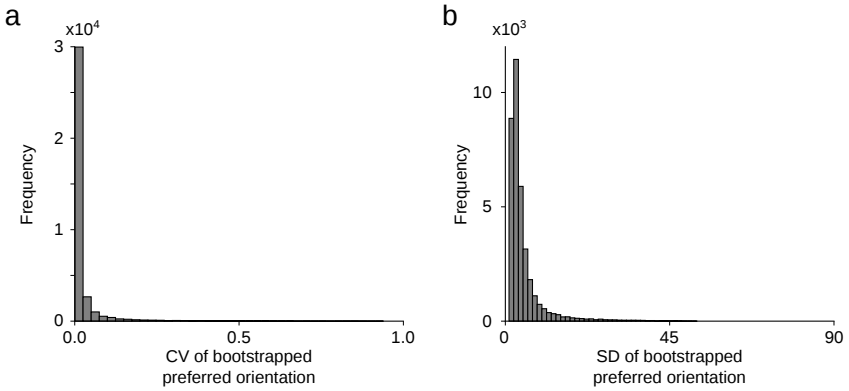

Figure 3.22: Low trial-to-trial variability in mature cortical responses to moving gratings. Circular variance (**a**) and standard deviation (**b**) of preferred orientations bootstrapped (1000 bootstrap sampling ensembles) over 12 trials for all locations (n=36188 locations) within the ROI is strongly biased towards low values indicating a low variability in responses between different trials of the same stimulus. Responses from representative animal after eye-opening.

Previous studies have argued that naively comparing trial averaged responses with the layout of spontaneous activity is compromised by a bias due to covariance in the trial-to-trial fluctuations of the evoked responses[406,407]. In particular, the authors of these studies argued that by naively estimating the signal correlation of evoked responses it contains a positive bias due to the noise covariance between trials[406,407]. If strong enough this bias can impose its structure on the signal correlation and subsequently distort analyses of said signal correlation. The authors especially described the case when trial-to-trial variability in neural responses is caused by ongoing, spontaneous activity as they observed in mouse visual cortex[407]. In this case the naively calculated signal correlation contained components from the noise covariance that

trivially resembled the spontaneous correlations. Therefore, a comparison between signal and spontaneous correlations will show a high overlap although the actual signal correlations might be unrelated to spontaneous correlations, as the bias due to noise covariance hides the actual relationship between signal and spontaneous correlations. Here we test whether our observed similarity between spontaneous correlations and orientation preference map is compromised by covariance in the trial-to-trial fluctuations.

First, we show that after eye-opening moving grating evoked responses in ferret visual cortex are highly reliable and exhibit low trial-to-trial variability on the mescoscopic scale. The spatial layout of evoked responses showed only little change inbetween trials to the same stimulus. To assess the variability in the orientation tuning, we determined for each location within the field of view the uncertainty in its preferred orientation by bootstrapping from the observed responses in different trials. We found that the preferred orientation can typically be assessed with a high fidelity of a few degrees (see **Fig. 3.22**).

We further observed that the trial-to-trial variability in the visually evoked responses was correlated to the average responses. In other words the stronger the average response of a location is to a certain stimulus the higher its response variability (**Fig. 3.23a,b**). We assess the trial-to-trial variability by calculating the standard deviation (SD) of the responses across trials of the same stimulus (**Fig. 3.23b**). The SD was correlated to the average response to the stimulus (**Fig. 3.23c**). This finding is consistent with results based on networks consisting of Poisson neurons[342]. In these networks the variability originates either from shared input, common gain fluctuations or from recurrent connectivity. For the recurrent network the authors[342] derived analytical expressions for the noise and signal correlation revealing a close relationship which they corroborated with numerical simulations (shown in their Figure 3[342]). Interestingly, the similarity between average response and response variability was also observed in mouse auditory cortex[29,342].

Another way to assess the trial-to-trial varibility in cortical responses is to calculate their signal

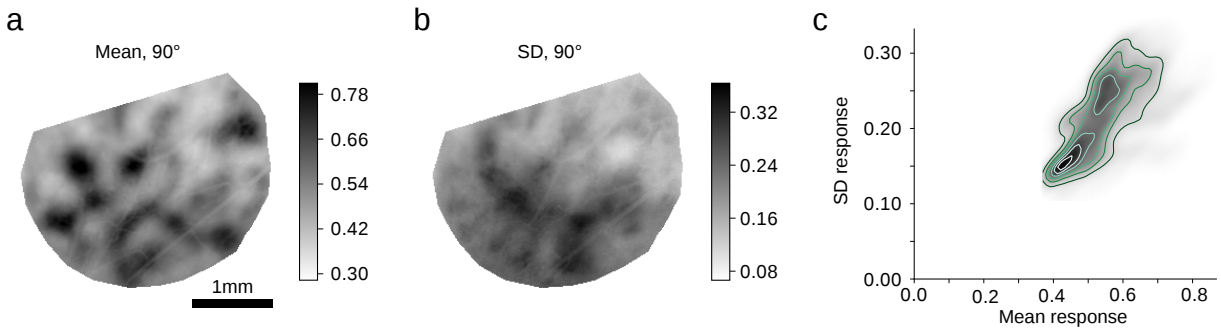

Figure 3.23: Similarity between average visually evoked response and variability in response. **a** Response averaged across trials to 90° moving grating after eye-opening. **b** Standard deviation of response over trials of same dataset as shown in (**a**). **c** Mean and standard deviation of visually evoked response are correlated. Scale bar: 1 mm (**a**,**b**).

and noise correlation which are often defined as[92]

$$C_{\text{signal}}(\vec{x},\vec{y}) = \frac{1}{N_k}\frac{\sum_{k=1}^{N_k} r_k(\vec{x})r_k(\vec{y})}{\sigma_x\sigma_y}, \tag{3.26}$$

$$C_{\text{noise}}(\vec{x},\vec{y}) = \frac{1}{TN_k}\frac{\sum_{t=1}^{T}\sum_{k=1}^{N_k}(r_{t,k}(\vec{x})-r_k(\vec{x}))(r_{t,k}(\vec{y})-r_k(\vec{y}))}{\sigma_x\sigma_y} \tag{3.27}$$

where $r_k(\vec{x})$ is the centered, i.e. has zero mean across all trials, trial averaged response to a stimulus of orientation k at location $\vec{x}$ and $r_{t,k}(\vec{x})$ is the response to stimulus k in trial t. σ_x, σ_y

denote the standard deviation of the responses at locations $\vec{x}, \vec{y}$ across all stimuli k (and trials t for the noise correlation). N_k denotes the number of different stimuli, and T denotes the number of trials. C_{signal} measures how two locations co-vary in their average response across different stimuli. In contrast, C_{noise} quantifies how two locations co-vary in their fluctuations around the average responses to different stimuli.
The bias in the signal correlation due to correlations in the trial-to-trial fluctuations can be reduced by averaging across many trials, but cannot be eliminated. To eliminate this bias, the signal correlation must be calculated between responses from different trials[406]. Assuming that the noise in the observed neural responses has zero mean and is uncorrelated between trials, shuffling the trials between all pairwise locations when computing the signal correlation averages out the bias. We term this definition "shuffle signal correlation" in **Fig. 3.24** and the following. Consistent with our previous analyses, we found that spontaneous correlations were similar in their structure to the naively estimated signal correlations (**Fig. 3.24a**, *center left* and *right*). To test whether this similarity is caused by the noise covariance, we calculated the shuffle signal correlation. We found that the shuffle signal correlations were highly correlated to the naive signal correlations (**Fig. 3.24a,b,f**). Consistent with this result, we observed that the shuffle signal correlations strongly resembled the noise and spontaneous correlation structure (**Fig. 3.24a,c,d**) demonstrating that the similarity we observed between signal and spontaneous correlations was not caused by noise correlations alone. This also indicates that our observed visually evoked responses were only weakly affected by trial-to-trial variability (see also **Fig. 3.22**). Interestingly, the spontaneous correlation structure resembled the signal and the noise correlations to a similar degree (**Fig. 3.24d,e**). Together, these results indicate that the similarity between signal and spontaneous correlations is not due to a bias due to the noise covariance. Instead computing the revised shuffle signal correlations resembled the spontaneous correlations to a similar degree.

3.10.4 Network model of spontaneous activity fails to capture long-range correlations

Previous experiments indicated that cortical spontaneous activity dynamically switches between global spatial patterns that resemble the layout of functional properties of cortex[235] suggesting that these spontaneous activity patterns reflect intrinsic states of the underlying cortical circuit. Motivated by this hypothesis a network model has been suggested describing spontaneous activity by spatial patterns generated by amplifying weakly modulated input via the network's recurrent connectivity[159] (see also Section 2.3.1 in Chapter 2). Two different network scenarios[159] were consistent with previous experimental data of spontaneous activity[235]. In the first scenario spontaneous activity was modelled by fluctuations about a single "background" state reflecting the idea that cortical activity in the absence of external stimuli relaxes to this background state (the "single state scenario"). In the second scenario spontaneous activity was described by wandering activity among multiple intrinsic "attractor" states representing different stimulus features (the "combinatorial multiple features scenario"; see also Section 2.3.1 in Chapter 2). Although the network model provided predictions to experimentally test these two scenarios, it remains unclear if one of the two cases appropriately describes spontaneous cortical activity.
Here we critically test the model predictions based on spontaneous and visual evoked activity in mature ferret visual cortex. To distinguish both scenarios we first determine how the similarity in the layout between spontaneous and evoked activity depends on the observed region size by computing the distribution of the correlation coefficients between the orientation preference map and the spontaneous activity patterns for varying region sizes (similarity index; see Section 2.3.1 in Chapter 2). Second, we determine the dimensionality of the spontaneous activity patterns

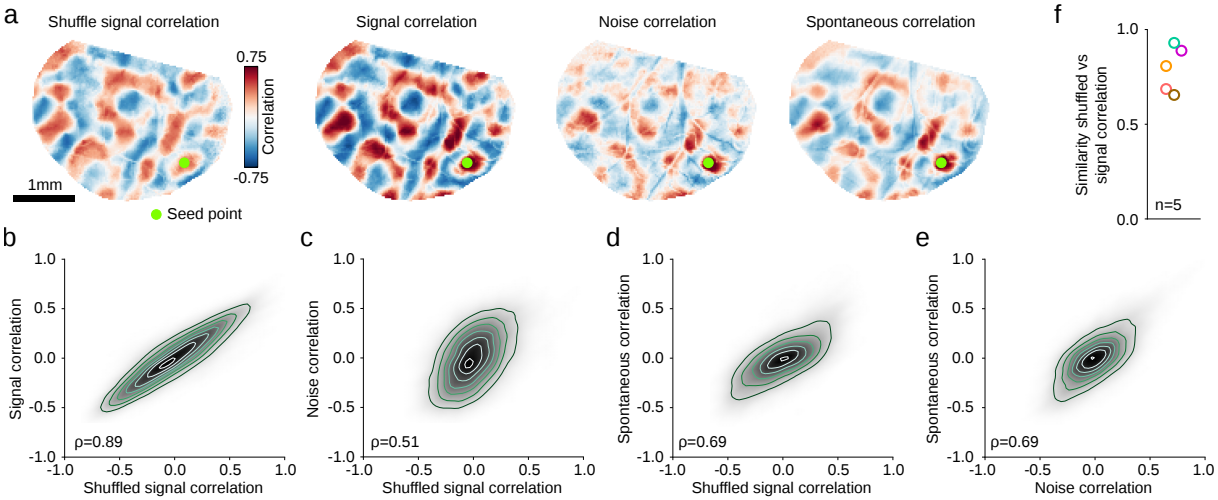

Figure 3.24: Both noise and shuffle signal correlations are highly similar to spontaneous correlations. **a** From *left* to *right*: Example pattern of shuffle signal correlations, (naive) signal correlations, noise correlations and spontaneous correlations from five days after eye-opening (EO+5). **b** Shuffle signal correlation is highly correlated with (naive) signal correlation with a correlation coefficient $\rho = 0.89$ at EO+5. Shown is the Gaussian kernel density estimation of the distribution of 20000 randomly sampled pairwise correlation coefficients. Shuffle signal correlation is also correlated to **c** noise correlations and **d** spontaneous correlations. **e** Spontaneous and noise correlations are similarly correlated. **f** The second order correlation between (naive) and shuffle signal correlations is high for all tested animals (n=5 animals after eye-opening). The example in (**b**) is shown in purple. Scale bar: 1 mm (**a**).

compared to a surrogate dataset. In the scenario increasing the size of the field of view increases the number of independent degrees of freedom (since regions far away are expected to be only weakly correlated) and thus, reduce the width of the SI distribution. In this case the width of the model SI distribution decreases with $\sim 1/\sqrt{N}$ with N being the number of independent degrees of freedom (number of observed domains). Network activity is dominated by fluctuations leading to a high dimensional spontaneous activity. In contrast, in the second scenario spontaneous activity switches between different global attractor states and, thus, globally resembles the orientation preference map. Therefore the SI distribution is expected to be invariant against changes in region size. In this scenario spontaneous activity wanders only between a limited number of attractor states, therefore its dimensionality is low.

Width of distribution of the similarity index

We systematically varied the region size from the size of a cortical column ($\sim$0.2 mm^2) to the full region of interest ($\sim$4 mm^2). We found that the SI distribution obtained from the experimental data became narrower for increasing region size (**Fig. 3.25b**). This decrease in width (assessed by the SD of each distribution) could be approximated by a power law a^b + const. where a denotes the region size and b is the fitted exponent. The exponent b of the experimental data was significantly smaller than the exponents obtained from a surrogate dataset demonstrating that spontaneous and evoked responses show a similarity over significantly longer distances than expected by chance ($p < 0.01$, N=100 control datasets; **Fig. 3.25c**; see also Section 3.9). The surrogate dataset was obtained by rotating and reflecting the original spontaneous activity patterns (see Section 3.9). Quantitatively similar results were obtained

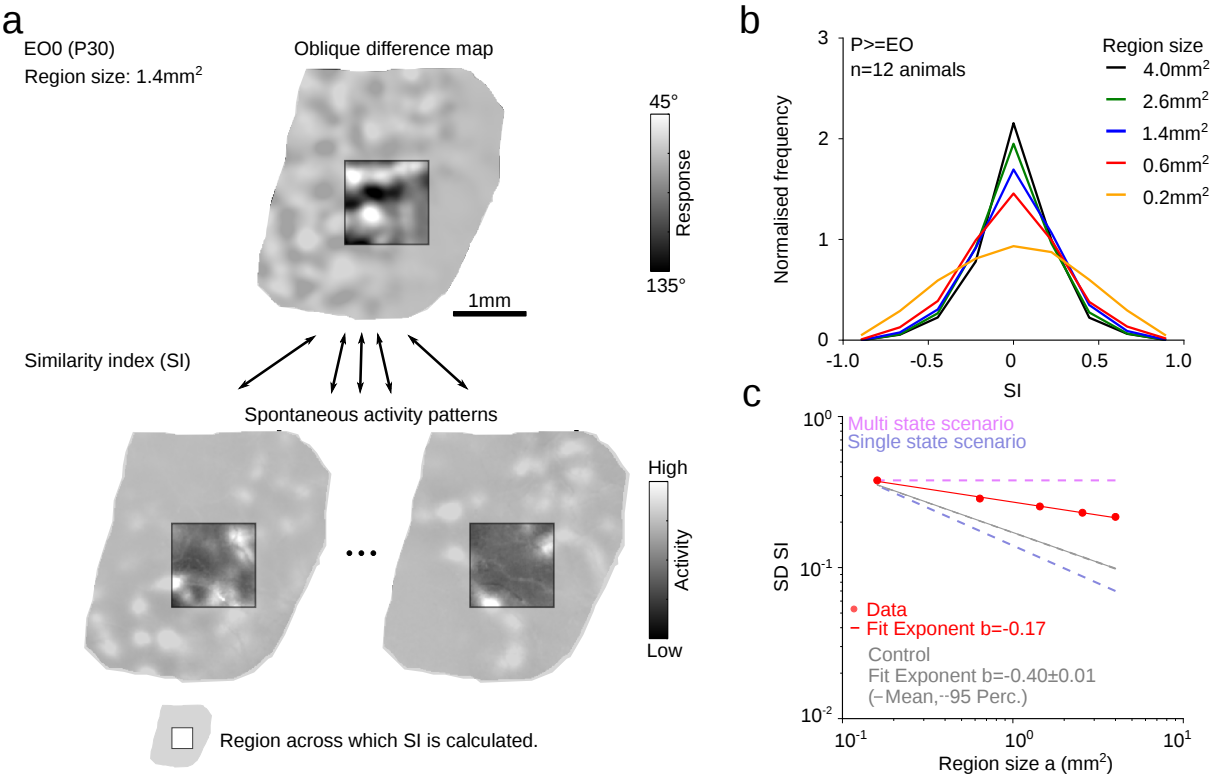

Figure 3.25: Single and multiple state scenario are both inconsistent with experimental data. **a** *Top*: Typical example of an oblique map (45° -135°) from the day of eye-opening (EO0). *Bottom*: Two typical examples of spontaneous activity patterns from EO0. The non-shaded area indicates the parcellation of the ROI into smaller regions (here, region size is 1.4mm^2) across which the SI between difference map and spontaneous activity patterns are calculated. **b** The histogram of the SI pooled across n=12 animals for all experiments after eye-opening (P>EO) is shown for systematically varied region size. **c** The widths of the histograms shown in (**b**), assessed by taking the SD of the distribution, decrease with increasing region size (red markers). This decrease is fitted by a power law a^b + const. yielding the exponent $b = -0.17$ (solid red) compared to SI width invariant against change in region size (light purple), and decay in SI width proportional to $1/\sqrt{N}$ with N being the region size (proportional to number of observed domains; dark purple). Gray lines show decay of SI width of control dataset (mean and 95% percentile; N=100 control datasets).

when generating surrogate datasets by phase shuffling the spontaneous activity patterns in the Fourier domain. The decay of the original data lied inbetween the decay expected by the single state scenario and a constant expected by the multiple state scenario. This result demonstrates that spontaneous activity patterns and evoked responses do not globally resemble each other, but their similarity decreases on average with region size. Still, the similarity remained higher with increasing region size than expected when remote domains are independent consistent with our result that spontaneous activity patterns exhibit a long-range correlation structure of a certain spatial extension (see Section 3.8 and Section 4.2.4 in Chapter 4) . In contrast, in the multiple state scenario the correlations would be global. Thus, the experimental data were neither consistent with a pure single-state scenario nor with the pure multiple states scenario and instead we found that the similarity decays weakly with the observed region size as a powerlaw.

Dimensionality of mature spontaneous activity patterns

Intimately related to the question of whether the similarity in the layout between spontaneous activity and the orientation preference map is local or global is how high-dimensional spontaneous activity patterns are. In the first scenario the fluctuations around the background state lead to high dimensional spontaneous activity. In contrast, the second scenario yields spontaneous activity of fewer dimensions with its variance contained within a low-dimensional subspace which coincides with the subspace of evoked maps (assuming the network is constructed in this way; see Section 2.3.1 in Chapter 2).
To assess whether the dimensionality of observed spontaneous activity agrees with one of these two scenarious, we compared the dimensionality of the original dataset to those of surrogate datasets and of visually evoked responses in mature cortex. The surrogate datasets were obtained by phase shuffling the spontaneous activity patterns in the Fourier domain[231] generating activity patterns with the same domain spacing as the original patterns but without any relation between the layout of active domains between patterns (see Section 3.9). Therefore, the dimensionality of the surrogate dataset should correspond to the one in the first scenario for a given number of activity patterns and a given Fourier spectrum (see also Section 5.2 in Chapter 5). In the case that spontaneous activity represents global states corresponding to the orientation preference maps and other features, its dimensionality should correspond to the one of relevant features.
Computing the dimensionality based on the distribution of the eigenvalues of the activity's covariance matrix[30,347,1] (see also Section 2.3.6 in Chapter 2), we found that the original activity patterns were notably lower dimensional than the surrogate dataset (see figure **Fig. 4.14a** in Chapter 4). Thus, the observed spontaneous activity was constrained to a smaller subspace than expected by random fluctuations around a single state. Moreover, spontaneous activity showed a signifcantly higher dimensionality than visually evoked responses. Applying Principal component analysis (see Section 2.3.5 in Chapter 2) to assess the dimensionality of the spontaneous activity yielded similar results. 75% of the variance were distributed onto 13 ± 3 (mean±SD, n=10 animals) components. These are more components than expected if spontaneous activity would only replay grating evoked response patterns, but less than expected by spontaneous activity fluctuating around one state. Still, the subset of principal components partially coincided with the space spanned by the evoked orientation preference maps. It seems unlikely that noise in the measurement led to the high dimensionality in spontaneous activity compared to evoked responses. In fact, the dimensionality of the evoked responses was calculated over the single trial responses and consistently yielded a dimensionality of four at a similar signal to noise ratio than spontaneous activity. Even when removing high frequency temporal and spatial components by denoising the neural data (see Section 3.5.2) the dimensionality changed only little. Together these results demonstrate that spontaneous activity is higher dimensional than expected if only representing grating evoked responses, but also lower dimensional than expected by the noise-driven scenario. This is consistent with the previous result where the width of the SI distribution changed weakly with region size inconsistent with either one of the two scenarios. All in all, both scenarios fall short in describing the long-range correlation structure observed in spontaneous activity.

3.11 Discussion

In this work we have been able to identify the precise local and large-scale organization of cortical networks revealed through correlated spontaneous activity in the mature visual cortex. Evidence supporting a fundamental modular structure for distributed network interactions in visual cortex has been demonstrated in previous anatomical studies documenting clustered

long-range horizontal connections specific to orientation[154,285,48], and in studies using voltage sensitive dyes to reveal the similarity of spontaneous activity to the modular patterns of responses evoked by grating stimuli[235,327]. Here the analysis of spontaneous activity in mature visual cortex of ferrets extends these observations by showing the remarkable degree of precision evident in the long-range spontaneous correlation structure, such that the correlation patterns of a local cortical area accurately predict the structure of local functional architecture over broad regions of cortex covering millimeters of surface area. The long-range network interactions evident from correlated spontaneous activity even reflect the finest-scale topographic features of orientation maps: the fractures and pinwheel centers. A tight relation between spontaneous and evoked activity is also found on a single cell resolution via 2-photon imaging. These results, together with the stability of large-scale correlation patterns across awake and anesthetized states, demonstrate an exceptional degree of functional coherence in cortical networks and potentially ensure reliable distributed neural representations of sensory input.

Here we focused on the analysis of spontaneous and evoked activity within layer 2/3 of visual cortex in ferrets. Other work compared spontaneous and evoked activity across the laminar structure in rat auditory cortex and find similar patterns in spontaneous and evoked activity in layer 2/3 and 5[365]. In this study the authors also observed differences in the propagation of activity. Spontaneous activity mostly spread upwards from deep layers (see also[368]), whereas sensory responses are initialized in presumptive thalamorecipient layers. The authors argued that this indicates a similarity in the local processing of activity but a difference in the flow of information through cortex. It would be interesting to expand our analysis to deeper layers such as layer 4. Layer 4 receives input from thalamus and analyzing its responses might also shed light on the emergence of orientation selectivity.

In accordance with previous work in other cortical areas and different species[186,235,169,274,35,327], we observed that spontaneous events resemble sensory driven responses in their spatial structure. This stands in contrast to recent work in mouse visual cortex and areas of the forebrain reporting that spontaneous activity was strongly correlated to behavioural motor output and only shows similarity to sensory driven responses in one dimension[407]. In this study the authors argued that this discrepancy in results might come from signal correlations that are distorted by noise correlations and resemble the spontaneous correlations only due to this noise artefact. In their data the authors observed strong ongoing sponanteous activity during visual stimulation. Subsequently, their signal correlations were biased by noise correlations and seemingly trivially resembled spontaneous correlations. Eliminating these noise correlations by computing a shuffle signal correlation also removed its similarity to the spontaneous correlation structure. Spontaneous and visually evoked activity overlapped in one dimension corresponding to a global change in the mean firing rate. However, in our experimental data we observed little trial-to-trial variability. Instead we observed highly consistent layouts in the grating evoked responses after eye-opening for different trials of the same stimulus. Even when computing the shuffle signal correlations they still resembled the layout of spontaneous correlations. We further demonstrated that the structure of the noise correlations is in fact similar to the structure of the signal correlations consistent with previous experimental and modeling work[342]. The difference in results might stem from different experimental conditions. The previous study analyzed single cell resolved and deconvolved neuronal activity traces obtained using 2-photon microscopy in mouse visual cortex. In our work we analyzed mesoscopic (and not deconvolved) imaging data from ferret V1 exhibiting robust and reliable responses across different trials to the same stimulus. To test whether differences in the temporal or spatial resolution of the recordings explain the apparent discrepancies, it would be instructive to analyze deconvolved, single cell resolved cortical activity in ferret visual cortex.

Previous work showed that spontaneous activity in anesthetized cats roughly resembled functional maps[235] but it remained unclear over which spatial distance this similarity holds. Subse-

quently, a theoretical study suggested two model scenarios predicting either a global similarity between spontaneous and evoked activity in the case that spontaneous activity wanders between different global attractor states, or a local similarity in the case when spontaneous activity fluctuates around one attractor state. To distinguish between both scenarious, we determined how the width of the SI distribution depends on the observed region size. We find that the SI distribution decreases weakly in its width for increasing region size following a power law whose exponent is neither consistent with a pure single-state scenario nor with the pure multiple states scenario. Consistent with this the dimensionality of spontaneous activity lies inbetween the expected values for both scenarios. Together, these results are consistent with the observation of a long-range correlation structure in spontaneous activity which is not explained by either of the two scenarios.

Our analysis is based on calcium imaging data using wide-field microscopy. We studied a cortical area of several mm^2 and observed a distinct spatially modulated structure within the cortical activity reflecting the underlying columnar structure of primary visual cortex in carnivores and primates[231,373]. Since the wide-field imaging setup did not resolve individual neurons, we complemented our recordings with single cell resolution 2-photon microscopy. These additional recordings corroborated the observed modular activity and correlation structure of spontaneous activity on a single cell level. Solely relying on 2-photon microscopy, however, would not have enabled us to assess the long-range correlation structure of spontaneous activity due to the notably smaller field of view of the recordings.

We used GCaMP6s as calcium indicator which in combination with wide-field microscopy allowed us to assess the averaged activity of a local pool of neurons. GCaMP6s enabled us to record single trial responses and spontaneous activity with high signal to noise ratio[81]. The high signal to noise ratio and the ability to reliably record the cortical activity without the need to average across several trials allowed us to assess spontaneous activity. Typically, calcium indicators exhibit a fast rise in activity but a relative slow decay of several hundreds of milliseconds[81]. This slow decay in the activity limits the temporal resolution and constrains our analyses to timescales of a few hundreds of milliseconds. To potentially circumvent this limitation, other work has investigated the application of a deconvolutional algorithm on the calcium imaging data to eliminate the slow decay in the signal[399]. Following these deconvolution analyses it might be possible to expand the data analysis to those analyses that require a finer temporal resolution such as investigating state transitions from one layout of spontaneous activity to the next, or comparing the temporal behaviour of spontaneous events and visually evoked responses. However, deconvolving the mesoscopic imaging data might be a complex task and requires a careful choice of parameters and comparison to ground truth data.

Although our data neither exhibited single cell resolution nor resolved distinct action potentials, we observed a striking degree of spatial organization over several spatial scales within the cortical circuit which might indicate that the cortical code encompasses also large spatial scales.

Here we focused on the properties of spontaneous activity and its resemblance to visually evoked responses in the mature animal after eye-opening. However, currently, it is unclear how the spontaneous long-range correlation structure develops during the maturation of cortex, and how the similarity to the orientation preference map on local and long-range scales evolves. Using a longitudinal imaging setup we will address these two points in the next chapter.

Chapter 4

Emergence of distributed cortical networks

The principles governing the functional organization and development of long-range network interactions in the neocortex remain poorly understood. We used *in vivo* wide-field and 2-photon longitudinal calcium imaging to demonstrate that long-range spontaneous correlations were present early in cortical development prior to the maturation of horizontal connections, and predicted mature network structure. Early long-range correlated activity remained stable even after silencing feed-forward input drive by inactivating retina or thalamus. These results suggest that short-range recurrent connections in early cortical circuits can generate structured long-range network correlations that may guide the formation of visually-evoked distributed functional networks. Gordon B. Smith and David E. Whitney performed all experiments under supervision of David Fitzpatrick in this chapter and analyzed the data for the retina and LGN inactivation data (**Fig. 4.16** and **Fig. 4.17**).

4.1 Introduction

Cortical networks in many brain areas exhibit an exquisitely ordered and coherent functional organization. In mammalian auditory cortex such as humans[360,205], non-human primates[299,312], carnivores[10,349,38] and rats[367] the dominant organizational feature is the gradient of frequency selectivity (*tonotopy*) where neurons are ordered by their preferred frequency. Likewise, the functional organization of the primary taste cortex in mice is topographically separated into cortical fields for the basic taste qualities sweet, bitter, umami and salty, revealing a *gustotopic map*[82]. In visual cortex the receptive fields of neighbouring neurons in visual cortex are orderly arranged such that they are overlapping and sample the visual field in an orderly way (*visuotopic* or *retinotopic* map). Moreover, in visual cortex of carnivores and primates orientation preference maps show an almost continuous distribution of preferred orientations on a single cell level[331]. Neighboring columns of neurons occupying a millimeter of cortical surface area represent the full range of stimulus orientations at a specific visual field location and are anatomically linked into distributed networks spanning several millimeters that share similar functional properties and are arranged in a modular fashion[43,45,331,154,285,48]. In Chapter 3 we established that the spontaneous correlation structure reliably captures key aspects of the distributed networks evoked by visual stimulation, namely long-range correlations and their similarity on a fine spatial scale (20 µm) across a large field of view (several mm^2). However, the emergence of these network interactions that bridge the fine-scale functional architecture and distant network elements during development remains unexplored.

Here we used spontaneous correlations to shed light on the nature of these networks at earlier stages of development and assessed how they evolve to their mature state. We took advantage of spontaneous activity being observed already early in the development of primary visual cortex prior to coherent visual responses[86,437,395] and well before orientation tuning has fully matured (compare **Fig. 2.4** in Chapter 2; and see[76]). Using a chronic widefield imaging setup (see Section 3.2 in Chapter 3) that allows us to record spontaneous activity from up to 10 days prior to several days after eye-opening in primary visual cortex of awake and anesthetized ferret, we show that already at the earliest observed time points spontaneous activity exhibits long-range correlations over cortical distances comparable to those in mature animals. These early spontaneous correlation patterns are predictive of the mature layout of orientation domains, but also reorganize their spatial layout during development and become more similar to the mature layout of orientation preference maps. Moreover, we find that throughout development spontaneous activity is confined to a subset of possible patterns demonstrating that active domains are not randomly distributed across cortex consistent with the finding of long-range correlations. Intriguingly, we observe modular and long-range spontaneous correlations even after inactivation of feed-forward input to cortex suggesting an intracortical mechanism for the emergence of these correlations. Together these results suggest that local recurrent connections in early cortical circuits can generate modular long-range network correlations that appear able to guide the formation of visually-evoked distributed functional networks.

4.2 Statistical analysis of spontaneous activity in early cortex

In the following chapter we analyzed longitudinally imaged activity recordings starting at around postnatal day 21 (P21), 10 days prior to eye opening, and mapped all imaging data onto a common reference frame for each individual animal via an affine transformation (see Section 3.7 in Chapter 3). This allowed us to track the development of the spatiotemporal structure of spontaneous correlations. In order to make it simpler to detect potential trends in the analyses, we grouped the datasets across all animals and experimental days into four age bins relative to eye-opening (EO): EO-10≤P<EO-5, EO-5≤P≤EO-1, P=EO, P>EO where P denotes the animal's age relative to eye-opening. We chose the age groups such that they are approximately equidistantly distributed across the observed developmental period, and that each age group contains a similar number of experiments.

4.2.1 Duration of spontaneous events

From the earliest experimental time point on (at P21, 10 days prior to eye-opening) we observed robust spontaneous activity exhibiting periods of high activity which we termed 'events' and intermitted by intervals of low activity (see Section 3.6 in Chapter 3). We determined the event duration as the time between event onset when the size of an area with high activity crosses the threshold of 0.01 mm^2 to event offset (see Section 3.6 in Chapter 3). To quantify the frequency of spontaneous events, we calculated the inter-event interval as the time interval between successive large events in spontaneous activity. We found that spontaneous activity prior to eye-opening displayed on average events with longer durations than after eye-opening (event duration at -10<P<-5: 1.53 (0.9, 2.4) s; P>EO: 3.7 (2.3, 5.9) s; median and IQR; p=0.0001 based on bootstrap test; **Fig. 4.1**).
Fig. 4.2d). In the mature cortex the median duration of all large events from event onset to end lied at 1 s (duration 1.0 [0.7, 1.5] s; median and inter-quartile range (IQR); n=12 animals, widefield imaging; **Fig. 4.2c**) and the inter-event interval at around 4 s (inter-event interval: 4.3 [2.5, 7.0] s; median and IQR; n=12 animals; **Fig. 4.2d**). The frequency and duration of spontaneous events was similar between widefield and 2-photon imaging data again bolstering

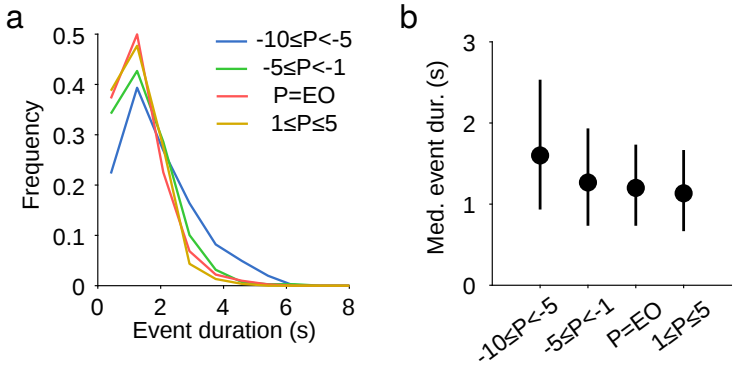

Figure 4.1: Median event duration decreases during development. **a** The distribution of event duration becomes narrower at shorter event duration. The data points are binned into four age groups (from EO-10 to EO-6, EO-5 to EO-1, EO, and >EO). **b** The median of the event duration distribution decreases from before eye-opening to after eye-opening. Circles denote median of distribution of event duration (*left*) and errorbars denote their IQR.

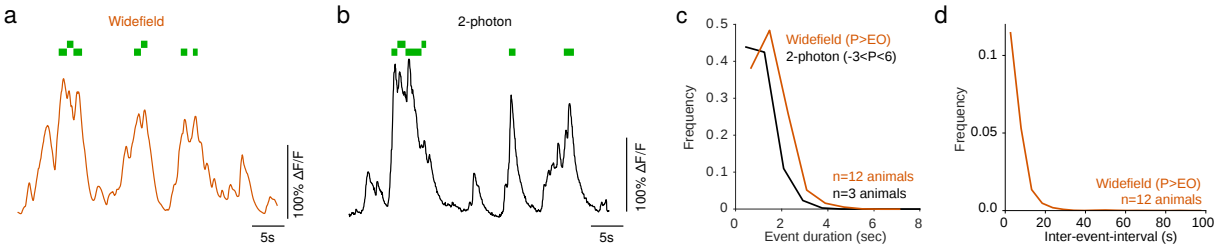

Figure 4.2: Distribution of duration of spontaneous events is similar between widefield and 2-photon imaging data. **a** Timecourse of spontaneous activity (mean frame $\Delta F/F$) measured during widefield imaging. Green bars above trace indicate event epochs (see Section 3.6 in Chapter 3). Scale bars: 5 s, 100% $\Delta F/F$. **b** Timecourse of spontaneous activity measured at the single cell level with 2-photon imaging, plotted as mean $\Delta F/F$ across all cells. Green bars above trace indicate event epochs. Scale bars: 5 s, 100% $\Delta F/F$. **c** Event durations measured at the cellular level (orange; n=12 animals) are similar to those observed at a columnar scale with widefield imaging (orange; n=3 animals). **d** Inter-event interval of widefield data (n=12 animals).

the fact that widefield epifluorescence imaging captured the combined activity of individual neurons (see also Section 3.10.1 in Chapter 3). The frequency and duration of spontaneous events is reminiscent of synchronous states observed in LFP recordings from awake animals, appearing distinct from both the desynchronized activity often observed during active attention, as well as the oscillatory activity seen in slow-wave sleep and with certain types of anesthesia[171].

4.2.2 High variability in how fast spontaneous activity spreads across cortex

During these spontaneous events the spontaneous activity patterns consist of a distributed set of active domains which become active either near simultaneously or in a spatial-temporal sequence spreading across the field of view within a few hundred milliseconds (**Fig. 4.3**, **Fig. 4.4**). In order to quantify the temporal sequence of spontaneous activity, we made use of the fast rise of the GCaMP6s signal rise (rise time of 0.18 s in Supplementary table 3 of[81]) and we estimated

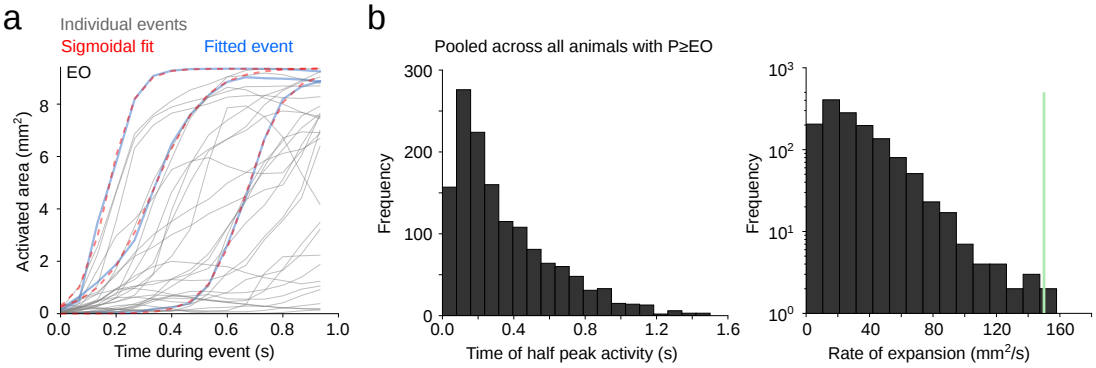

Figure 4.3: Spread of activity during an event after eye-opening (EO) differs broadly across events. **a** Activated cortical area (gray; threshold=80% of total size of ROI) as a function of time from event onset for sets of representative events (gray lines) from an animal at EO. A sigmoidal function $s(t)$ (red; see (4.1)) was used to fit the traces (blue). All traces were fitted, but only randomly selected examples are shown. **b** Distributions of time of half peak (t_0; *left*) and rate of activity spread $\frac{s_0 a}{4}$ (*right*). Rates >100-150 mm^2/s (green line) can hardly be distinguished from instantaneous/uniform rise of activity in our field of view. Events were pooled across all animals with imaging days on and after EO (n=12 animals).

the velocity with which spontaneous activity expands across cortex after the onset of an event. To this end, we determined the increase in size of the activated region (locations with activity higher than threshold; see Section 3.6 in Chapter 3) as a function of time during an event. Typically, this rise was well fitted by a sigmoidal function

$$s(t) = \frac{s_0}{1 + e^{-(t-t_0)\,a}} \tag{4.1}$$

where s_0 is the maximal average activity of each event, t is the time starting at event onset, t_0 denotes the time when the activity reaches half of the maximum activity, and a denotes the rate of increase in activity. The slope $\frac{s_0 a}{4}$ at half maximum value gives an estimate of the rate of activity expansion. Both the rate of activity expansion and the time when half of the cortex is activated varied broadly across events. The median velocity was ~1 mm^2/50 ms but expansion rates faster than 1 mm^2/10 ms were observed (**Fig. 4.3b**, right). Thus, while we cannot resolve expansion rates larger than these, given that typically the field of view is roughly 10 mm^2 large and the frame rate is 15 Hz, this analysis shows that for two sites several millimeters apart from each other often the rise of activity during a spontaneous event was not simultaneous, but showed a lag that may vary from several tens to a few hundred ms.

Similar to after eye-opening, spontaneous activity prior to eye-opening varied widely in how fast it spread across cortex (compare **Fig. 4.3** after eye-opening and **Fig. 4.4** during development). Again, we captured the rate of expansion by fitting a sigmoid (Eq. (4.1)) to the cortical area above an activity threshold during the time course of each spontaneous event (**Fig. 4.4a**) and took the slope of the sigmoid at half maximum as an estimate for the velocity of activity expansion across cortex. We observed that the velocity varied considerably across events over one order of magnitude between 10 to 100 mm^2 per second (**Fig. 4.4b**, right). The average rate of activity expansion per mm^2, meaning the time needed for the spontaneous activity to activate 1 mm^2 of cortex, changed little during development (**Fig. 4.4c**). Together, these results show that throughout development two sites several millimeters apart from each other exhibit a lagged rise of spontaneous activity varying from several tens to a few hundred ms during cortical

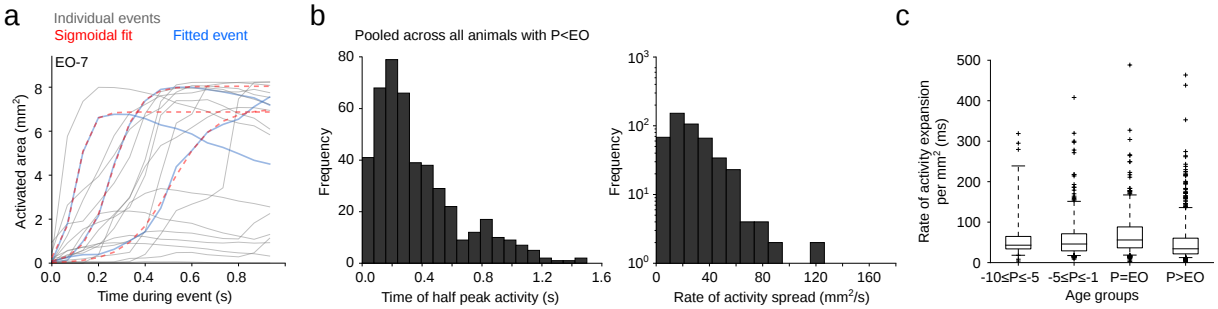

Figure 4.4: Spread of activity during an event prior to eye-opening differs broadly across events similar to spontaneous activity after eye-opening. **a** Activated cortical area (gray; threshold=80% of total size of ROI) as a function of time from event onset for sets of representative events (gray lines) from an animal 7 days prior to EO. A sigmoidal function (red; see (4.1)) was used to fit the traces (blue). All traces were fitted, but only randomly selected examples are shown. **b** Distributions of time of half peak (t_0; *left*) and rate of activity spread $\frac{s_0 a}{4}$ (*right*). Rates >100 mm^2/s can hardly be distinguished from instantaneous/uniform rise of activity in our field of view. Events were pooled across all animals and imaging days prior to EO (n=12 animals). **c** Throughout development the median rate of activity expansion per mm^2 changes little and is skewed towards values of several hundred ms. Shown are distributions across four age groups (EO-10≤P<EO-5, EO-5≤P≤EO-1, P=EO, P>EO). Median of distribution is denoted by horizontal line, quartiles are denoted by box. Whiskers show 5 and 95 percentile of distribution. Markers show outliers.

development.

4.2.3 Early spontaneous activity is widespread across cortex

From the earliest experimental time point on we observed robust spontaneous activity exhibiting modular patterns that extend over long distances across the cortical surface. Furthermore we note that in immature animals the activation of domains across cortical surface is heterogeneous over events but covers the whole field of view. Certain cortical regions are on average more often active than other regions. We quantify the average activation within the field of view by computing the mean of activity patterns over all observed spontaneous events (**Fig. 4.5a**). To assess the variability in the average activity, we determine the standard deviation (SD) of the mean activity across cortical surface (**Fig. 4.5c**). To quantify the variability in the activity for an individual cortical location, we compute the SD across events for each location within the field of view (**Fig. 4.5b**). We find that the average activity over all spontaneous events becomes more homogeneous within the field of view (**Fig. 4.5a,c**) suggesting that the layout of active domains becomes more evenly distributed over all events. Similarly, the SD of the activation in different spontaneous events decreases for cortical locations demonstrating a decrease in variability across events (**Fig. 4.5b,d**). The SD itself also becomes more homogeneous across cortex (**Fig. 4.5e**).

The observed increase in the homogeneity of the average activity and the decrease of its SD during development cannot be trivially explained by the increase in the frequency of spontaneous events during development (see **Fig. 3.8** in Chapter 3). Alternatively, the change could either be explained by (1) an increase in the number of activity patterns with different layouts of active domains corresponding to an increase in the dimensionality of spontaneous activity,

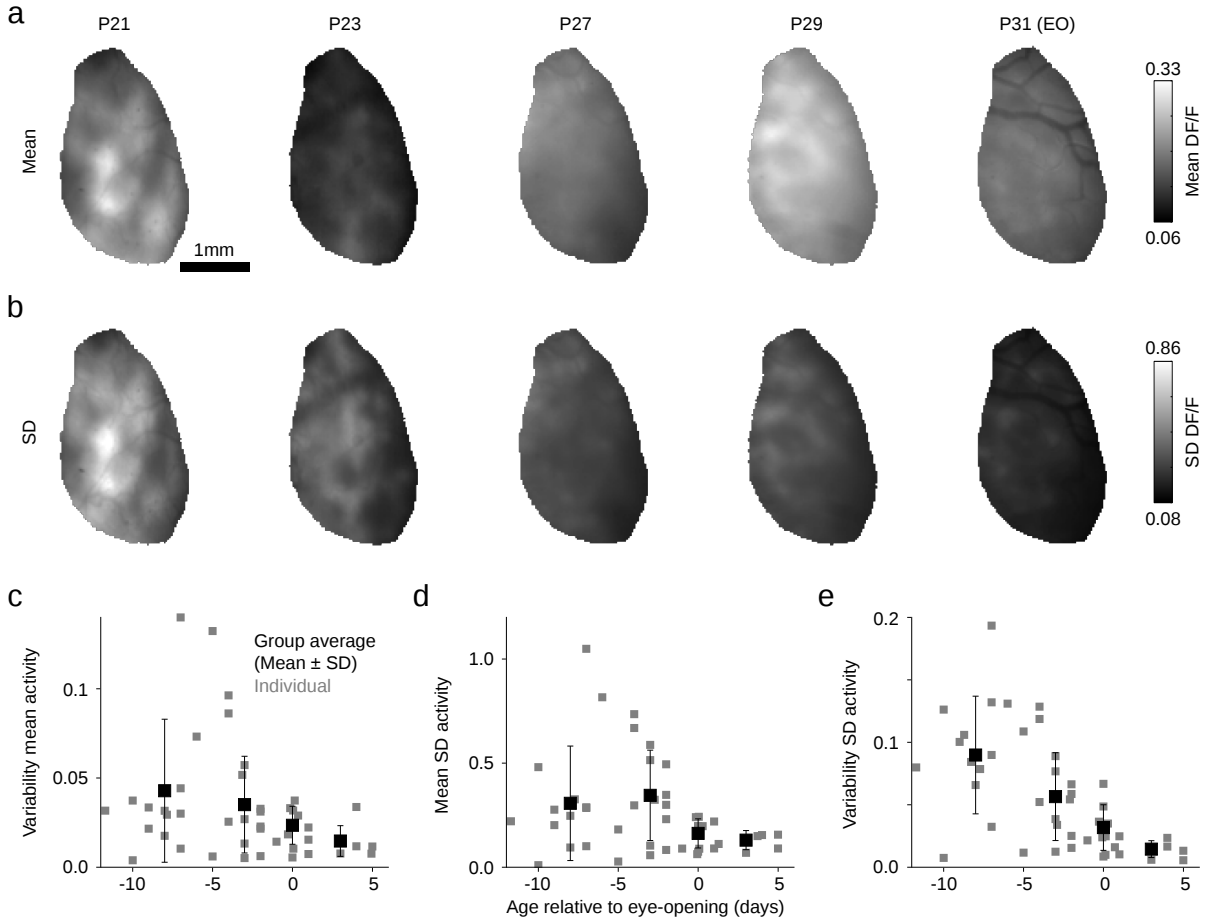

Figure 4.5: Spontaneous activity becomes more homogeneously distributed across cortical space during development. **a** Mean activity over spontaneous events during development. Average activity becomes more homogeneously distributed across field of view. **b** Standard deviation over all spontaneous events decreases and becomes more homogeneously distributed in cortical space with age. **c** Mean activity over all events becomes less variable across ROI with age. **d** Average variability over the ROI measured by calculating the standard deviation (SD) decreases with age. **e** The variability of the SD over spontaneous events across cortical space decreases during development. Scale bar is 1 mm (**a**,**b**).

or by (2) a rearrangement of the layout of activity patterns such that the active domains are more evenly distributed across cortical surface but the dimensionality remains stable. In fact in Section 4.2.7 we find that the dimensionality of spontaneous activity changes only little with age consistent with the latter hypothesis.

4.2.4 Distant network elements co-vary already prior to eye-opening

Importantly, we observed spatially extended, modular spontaneous activity patterns (**Fig. 4.6a**) already at early stages in development reflected by correlation patterns that displayed pronounced peaks even several millimeters away from the seed point (**Fig. 4.6b**), consistent with electrophysiological recordings[86]. To assess the statistical significance of long-range correlation strength at large distances (analogous to Chapter 3 we use a distance of 2 mm) across development, we compared maxima of correlation patterns to those of surrogate correlation patterns as

described in Chapter 3 and Chapter 3. To pool across animal experiments within an age group, we generated 10.000 surrogate group medians by randomly drawing from the distributions of surrogate data points (one per animal experiment), and the p-value was taken as the fraction of group medians greater than the median value for the actual data. Indeed, the spatial scale of spontaneous correlations remained stable during development and already 10 days prior to eye-opening the correlations were nearly as extended as 5 days after eye opening (**Fig. 4.6d,e**; correlation spatial scale: p=0.86, Kruskal Wallis H-test; correlation strength at 2 mm: p <0.0001 vs. surrogate for all groups; across groups: p=0.42, Kruskal Wallis H-test). Furthermore, pronounced spontaneous fractures were already present at the earliest time points, indicating that the early cortex already exhibits precisely organized long-range functional networks (**Fig. 4.6c**). These observations seemed unexpected given the limited development of long-range horizontal connections at this early stage in cortical development. Anatomical studies in ferret visual cortex demonstrate that axons of layer 2/3 pyramidal cells exhibit only about two branch points at P22[46], extend only up to 1 mm[122], and are still missing spatially clustered synaptic terminals, which are distributed across several millimeters in the mature cortex[439], but only start to become evident at about P26-27[122,364] (see Section 2.2.1 in Chapter 2).

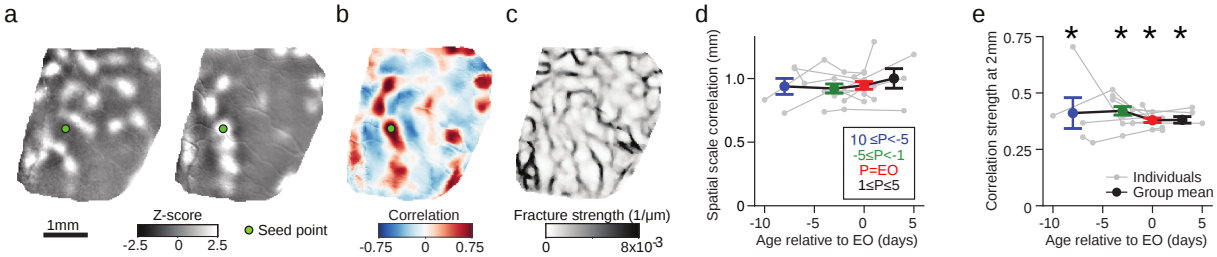

Figure 4.6: Early spontaneous activity exhibits long-range correlations similar in range to after eye-opening. **a** Representative z-scored images of early spontaneous activity at P23, seven days prior to eye-opening (EO). **b-c**. Early spontaneous activity shows hallmarks of mature spontaneous activity, including long-range correlated activity (**b**) and pronounced spontaneous fractures (**c**). **d** The spatial scale of correlations in spontaneous activity (decay constant ξ of correlation maxima) does not change across ages. **e** The magnitude of long-range correlations for maxima 2 mm from the seed point is statistically significant at all ages examined. For **d,e**: n=10 chronically recorded animals; **e**: Asterisks indicate p <0.0001, actual vs surrogate data; **d,e**: Group data is shown as mean±SEM.

4.2.5 Signatures of the mature evoked map are evident in early spontaneous activity

We found that features of the modular distributed network, namely modular activity, long-range correlations, and fractures, were already evident at the earliest time points. This suggests that the basic structure of the early network might be similar to the network's mature state. If this is the case, then signatures of the mature orientation preference map might already be apparent in the early spontaneous correlation structure. These signatures might then allow us to predict the structure of the mature visually evoked network using early spontaneous correlations. To test this, we first examined whether signatures of the mature orientation preference map are present in early spontaneous correlations by determining their similarity in their layout. Next, we assessed the quality of the prediction of the layout of orientation domains analogous to Chapter 3. As shown in Chapter 3 especially spontaneous correlation patterns of orientation selective seed

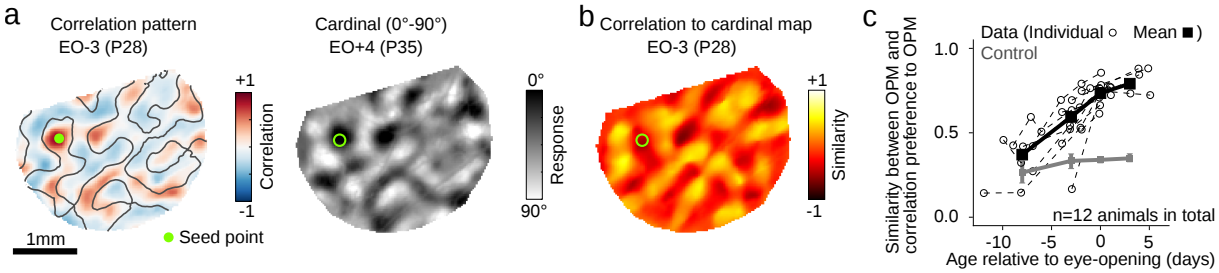

Figure 4.7: Similarity between correlation patterns and layout of orientation domains is particularly evident for highly selective seed points and increases during development. **a** *Left:* Example of spontaneous correlation pattern (3 days prior to eye-opening (EO-3)), *right*: cardinal difference map (four days after EO) with reference point from left. Gray contour lines on left denote the zero level of the cardinal difference map. **b** The similarity between the spontaneous correlation patterns and the mature cardinal difference map is highest for patterns of seed points that are selective for cardinal orientations. **c**. Already early in development the spontaneous correlation patterns of selective seed points resemble most strongly the layout of orientation domains. Individual data points (open), group average (solid black; EO-10≤P<EO-5, EO-5≤P≤EO-1, P=EO, P>EO) across n=12 animal vs shuffle control (gray). Scale bar: 1 mm (**a**).

points resemble the layout of orientation domains. Here we tested whether we see a similar behaviour already in the early correlation patterns. To this end, we quantified the second order correlation of the similarity between spontaneous correlations and cardinal difference map and the cardinal difference map (example shown in **Fig. 4.7b**). We found that the correlation patterns of seed points that were selective for cardinal orientations (0° and 90°) strongly resembled the cardinal difference map (**Fig. 4.7a,b**) whereas correlation patterns of low orientation selective seed points did not show such a strong resemblance (**Fig. 4.7b**). The similarity between spontaneous correlations and orientation preference map increased with age but was already present early on (**Fig. 4.7c**). **Fig. 4.7** shows the similarity of the correlation patterns to the cardinal difference map, but we obtained quantitatively similar results when considering the oblique difference map instead. To determine statistical significance, we obtained control datasets by phase shuffling the orientation preference map in the Fourier domain[231], calculating the pairwise correlation coefficient between the maps' real part and each spontaneous correlation pattern (**Fig. 4.7c**) (see Section 3.9 in Chapter 3), and then comparing the resemblance to the surrogate cardinal map. Thus, signatures of mature visually evoked responses were already evident in early spontaneous correlated activity.

Having established that already prior to eye-opening the spontaneous correlations contained information about the mature layout of orientation domains, we visualized this trend by sorting the spontaneous correlation structure according to the mature preferred orientation of the seed points (**Fig. 4.8a**). Indeed after sorting the correlation matrices in this way a clear structure appeared consisting of a stripe of positive correlations along the major diagonal and a stripe of negative correlations on the minor diagonal. This structure demonstrates that cortical locations with similar orientation tuning are likely positively correlated, whereas orthogonally tuned locations are on average negatively correlated. The structure became even more apparent when only considering the most selective cortical locations (**Fig. 4.8a**,*bottom*), consistent with our finding above that especially correlation patterns of highly selective seed points resemble the layout of visually evoked responses. Considering only the correlations between the most selective locations revealed that already up to 10 days prior to eye-opening the early spontaneous correlation structure showed signatures of this structure dependent on the mature orientation

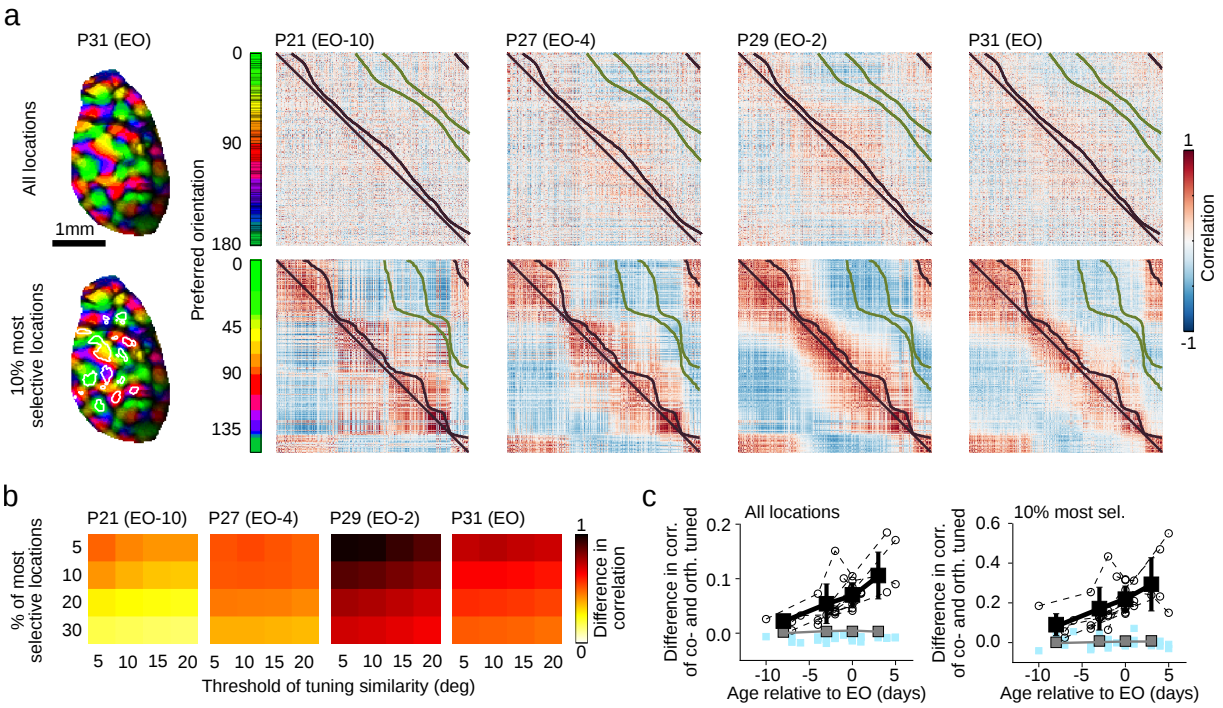

Figure 4.8: Alignment between spontaneous correlations and the mature layout of orientation tuning is already evident in early development and for all locations and increases further with age and selecting only most selective locations. **a** Spontaneous correlations (*right*) are ordered according to the seed point's orientation tuning after eye-opening (EO; *left*). *Top*: All locations within field of view. *Bottom*: 10% most selective locations outlined by white contour lines on *left*. With age and for subset of most selective locations the spontaneous correlations improve their resemblance to the layout of orientation tuning. The contour lines denote correlation coefficients between pairs with similar (black) and orthogonal (green) orientation tuning ($\pm 10°$). **b** Average difference between correlations of similarly and orthogonally tuned locations of subset of most selective locations. The average difference increases with (1) increasing the threshold of selectivity for the subset of most selective locations (y-axis) and with (2) increasing the threshold for tuning similarity throughout development (same animal as in (**a**)). **c** The average difference in correlations between locations with similar vs orthogonal tuning increases with age and selectivity of locations. Individual data points (open), group average (solid black; EO-10≤P<EO-5, EO-5≤P≤EO-1, P=EO, P>EO; mean±SD) across n=12 animals vs shuffle control (gray) and average correlations across all locations (light blue).

tuning (**Fig. 4.8**,*bottom*), demonstrating that spontaneous correlations at the earliest observed time points resembled to a degree the future evoked distributed networks. We quantified the structure of the correlations along the diagonals by calculating the average difference between the correlation coefficients between similarly tuned locations (major diagonal) and the correlations between orthogonally tuned locations (minor diagonal) (**Fig. 4.8b**). With age the ordering became more prominent (**Fig. 4.8b,c**). This effect was robust against changes in the definition of tuning similarity when systematically varying the threshold of similarly tuned locations from 5 to 20° and the threshold for selectivity from the 5 to 30% most selective locations (**Fig. 4.8b**). Note that in the example shown in **Fig. 4.8b**, the average difference in correlations does not increase monotonically with age, but is highest for two days prior to eye-opening. This might be due to a general increase in the magnitude of the correlation coefficients at this day (see **Fig. 4.8a**,*right*). The magnitude of the correlation coefficients depend among others on the number of events going into the correlations (see Section 3.8 in Chapter 3). Importantly, for the selection of the 10% most selective locations the signature of the ordering was already significant in the earliest age group (**Fig. 4.8c**, *right*; $p < 0.01$, bootstrap test). Note further that the increase in the difference in the correlation is due to both an increase in the positive correlations between similarly tuned locations and a decrease in correlations between orthogonally tuned locations, since on average the correlation coefficients remain centered around zero (light blue markers in **Fig. 4.8c**).

To show that the results above are robust, we extended the comparison between early spontaneous and mature evoked activity beyond comparing the layout of the map and the correlation structure by determining the pairwise tuning similarity between all locations within the field of view in the mature cortex. Using a pairwise measure to describe the layout of tuning properties allowed us to compare objects of the same dimensionality. To measure the tuning similarity d_{tuning}, we used the Euclidean distance between the values of the complex field at each two locations $\vec{x}$ and $\vec{y}$

$$d_{\text{tuning}}(\vec{x}, \vec{y}) = 1 - |\tilde{z}(\vec{x}) - \tilde{z}(\vec{y})|, \tag{4.2}$$

$$\text{with} \quad \tilde{z}(\vec{x}) = \frac{z(\vec{x})}{r_{\max}} \tag{4.3}$$

where $r_{\max}$ denotes the maximal selectivity of a location within the field of view. If the tuning similarity is close to 1, two locations $\vec{x}, \vec{y}$ either have a similar selectivity and preferred orientation or they are both unselective. Two locations $\vec{x}, \vec{y}$ that differ either in their selectivity or in their tuning share a low tuning similarity. Using this definition, we compared the complete pairwise organization of the mature tuning similarity and the developing correlation structure by computing the correlation coefficient between the correlation patterns and the patterns of tuning similarity for each seed point. We found that early in development spontaneous correlations loosely resemble the evoked tuning similarity (**Fig. 4.9a**,*top*). After eye-opening spontaneous correlations seemed to be more tightly related to the tuning similarity (**Fig. 4.9a**,*bottom*). Already prior to eye-opening a large number of correlation patterns resembled the layout of the orientation tuning (**Fig. 4.9b**,*top*). Several days after eye-opening this distribution shifted notably to high correlation values demonstating that the majority of correlation patterns matched the patterns of tuning similarity. Up to five days prior to eye-opening the resemblance was signifcant but improved further with age (**Fig. 4.9c**), consistent with previous analyses (see **Fig. 4.8** and **Fig. 4.10**).

As shown in **Fig. 3.19** the similarity between the spontaneous correlation patterns and the layout of orientation tuning was especially strong for highly selective locations. Here we showed that the resemblance between tuning similarity and spontaneous correlation structure was increasingly correlated with age with the selectivity of the seed point (**Fig. 4.9d**; summary statistics not shown, but similar behaviour to the example shown was observed in all n=12 animals).

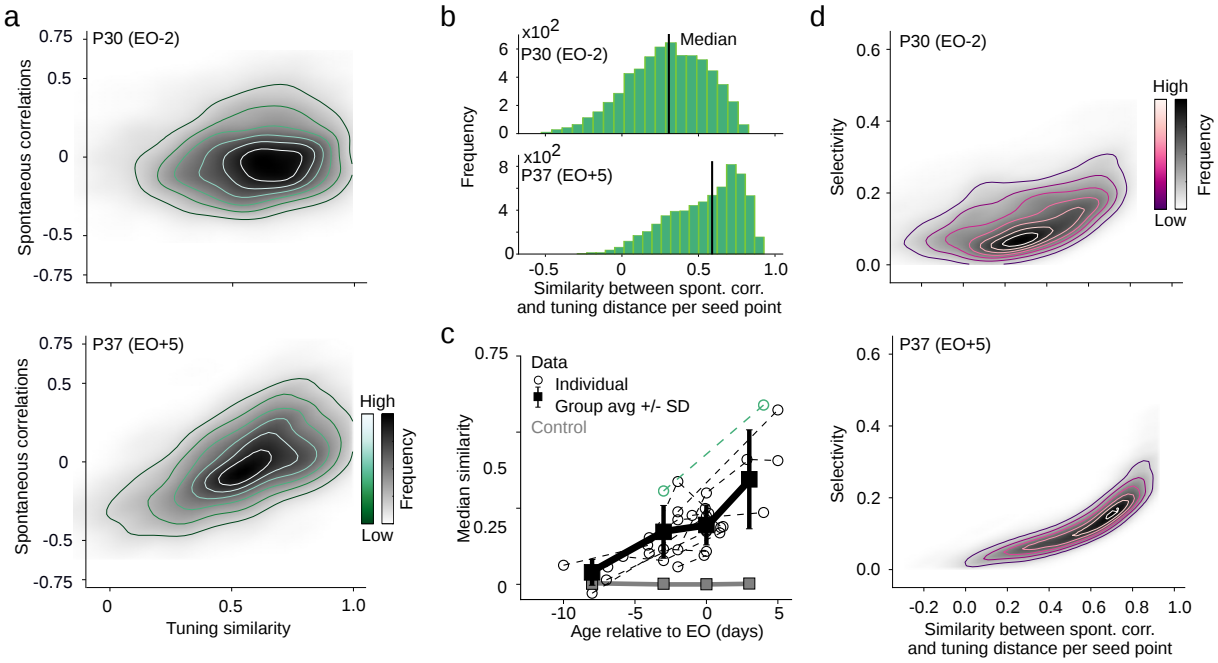

Figure 4.9: Relationship between spontaneous correlations and tuning is evident early on and becomes closer with age. **a** Tuning similarity (Eq. (4.2)) and spontaneous correlations show weak relationship two days prior to eye-opening (*top*) but are tightly correlated after EO (*bottom*). **b** Correlating the layout of spontaneous correlations and tuning similarity for each seed point shows increase in their resemblance during early development (same example as in (**a**)). Line marks median of distribution of correlation coefficients. **c** With age the spontaneous correlations become more correlated to the layout of the tuning similarity. Individual data points (open), group average across n=12 animals (solid black; EO-10≤P<EO-5, EO-5≤P≤EO-1, P=EO, P>EO) vs shuffle control (gray). Example in (**a,b,d**) is highlighted in green. **d** The more selective a seed point, the higher the similarity between its correlation pattern and the layout of its tuning similarity (same example as in (**a**)). (**a,d**) Shown is the Gaussian kernel density estimation of the distribution.

This analysis demonstrates that by selecting a sub-population of all locations based on their selectivity, any measure of similarity between spontaneous and visually evoked activity should always improve compared to when considering all locations within the field of view. This seems reasonable as the preferred orientation of weakly selective locations can only be estimated imprecisely, thus leading to a less accurate estimate of the similarty between evoked and spontaneous activity. All in all, the comparison between the pairwise similarity of orientation tuning and spontaneous correlations was consistent with the analyses above.

Since cortical circuits early in development displayed long-range correlations and a significant similarity to the mature orientation preference map over large distances, we expect to be able to predict the structure of the mature visually evoked network from the spontaneous activity correlation patterns at these early time points. To test this, we obtained the prediction of the mature local tuning from remote correlated locations using early spontaneous activity analogous to the analysis in **Fig. 3.20f** in Chapter 3. We computed the orientation tuning predictions based on the correlation pattern on a given day by weighting tuning curves measured after eye opening using an exclusion radius of 400 µm. The predicted orientation preference map was compared to the actual map (as described in Section 3.10.2 in Chapter 3) for both individual animals and

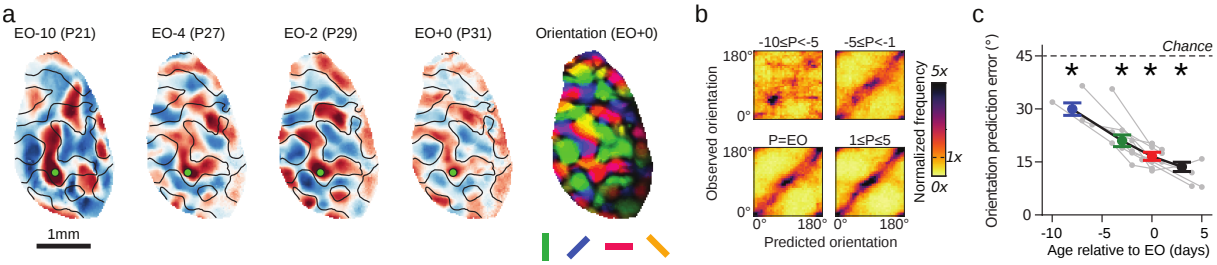

Figure 4.10: Early spontaneous activity predicts future evoked responses. **a** Longitudinal imaging of a chronically-implanted animal reveals that early spontaneous correlation patterns exhibit signatures of the mature orientation map (*right*), despite considerable reorganization in correlation structure. Contour lines indicate horizontal selective domains measured at EO. **b** The structure of spontaneous correlations can predict the future mature orientation preference map organization as early as 10 days before eye opening. **c** Spontaneous correlation structure predicts orientation preference significantly better than chance, even at the youngest ages examined. For **b,c**: n=11 chronically recorded animals; **c**: Asterisks indicate p <0.0001, actual vs surrogate data; **c**: Group data is shown as mean±SEM (colored; from EO-10 to EO-6, EO-5 to EO-1, EO, and >EO) over individual data points (gray).

group medians. The predictions remained accurate up to 5 days prior to eye-opening and were above chance even for the youngest age group. Thus, even at this early developmental stage, signatures of the future visually evoked distributed network are evident and predictive over large distances (**Fig. 4.10b,c**; EO -10 to -5: p <0.0001 vs. surrogate, 4 of 5 individual data points significant vs. surrogate at p <0.05).

4.2.6 Reorganization of spontaneous activity patterns during development

In several analyses we have consistently observed that the similarity between spontaneous correlations and mature visually evoked responses increases with age. By way of example, the ability of the spontaneous correlation patterns to predict the visually evoked layout of orientation domains increased significantly with age (**Fig. 4.10c**; p=0.0004 that data from the four age groups are different, Kruskal Wallis H-test; EO -10 to -5 vs. EO: p=0.004, Wilcoxon rank-sum) indicating that the structure of the distributed network changes over this time period. Indeed, we found extensive reorganization of the correlation structure in all animals (**Fig. 4.10a**; **Fig. 4.11b**) such that their layout became tightly matched to those of evoked responses after eye-opening. The refinement during this period also involved a rearrangement of the spatial organization of spontaneous fractures (**Fig. 4.11c**).

To quantify the degree of reorganization, we compared spontaneous correlation patterns across development and calculated a second-order correlation (**Fig. 4.11d,e**) between the correlation patterns on a given day and the reference day (eye-opening) with the same seed point. Changes in correlation fractures over development were quantified as the second order correlation of fracture patterns (**Fig. 4.11f**). In both cases fluctuations due to the finite number of spontaneous activity patterns might lead to a less than perfect similarity and be interpreted as reorganization. To take this into account, we computed an estimate of the expected degree of similarity by first separately computing correlations and their corresponding fracture patterns for half of the detected events, and then computing the second-order correlations with the other half at the same day as above. Comparing the expected degree of similarity with the observed degree, we found a significant reorganization of spontaneous correlation patterns and fractures from prior

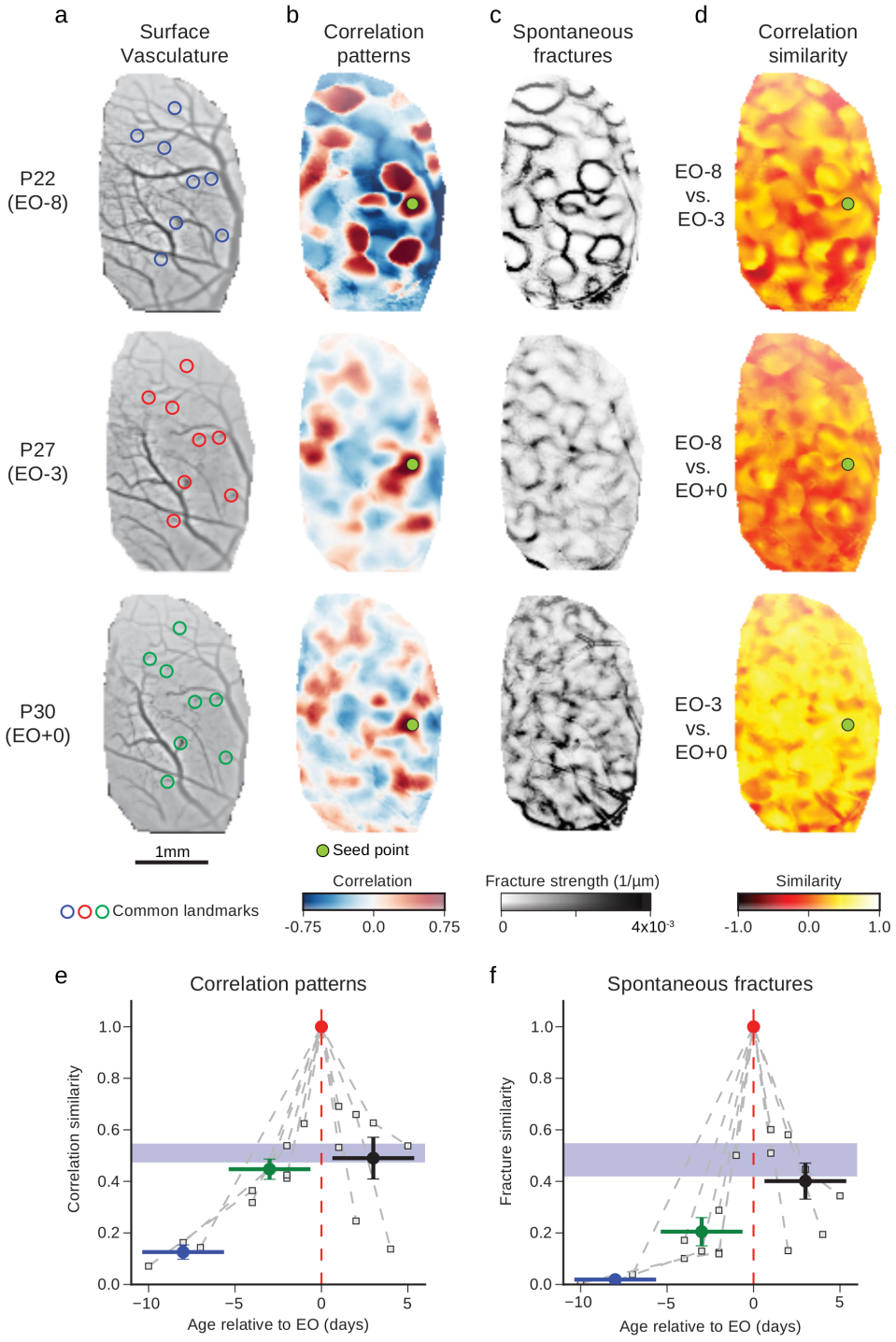

Figure 4.11: Refinement of correlation structure during early development. **a** Registration across days was achieved by matching radial (descending) blood vessels and computing an affine transform. **b** Correlation patterns for same reference point over 8 days prior to eye-opening (EO). **c** Spontaneous fractures. **d** Similarity of correlation patterns to the next imaging session (top) or to final day (*middle* and *bottom*). **e** Similarity of correlation patterns to reference day (eye-opening). Blue region indicates within-day similarity for subsampled reference day correlations. **f** Similarity of spontaneous fracture patterns as a function of relative age. For (**e,f**): n=12 chronically recorded animals; Group data (colored; from EO-10 to EO-6, EO-5 to EO-1, EO, and >EO) is shown as mean±SEM over individual data points (gray). Scale bar is 1 mm (**a-d**).

to after eye-opening.

Potentially, the observed increase in misalignment between spontaneous correlations with

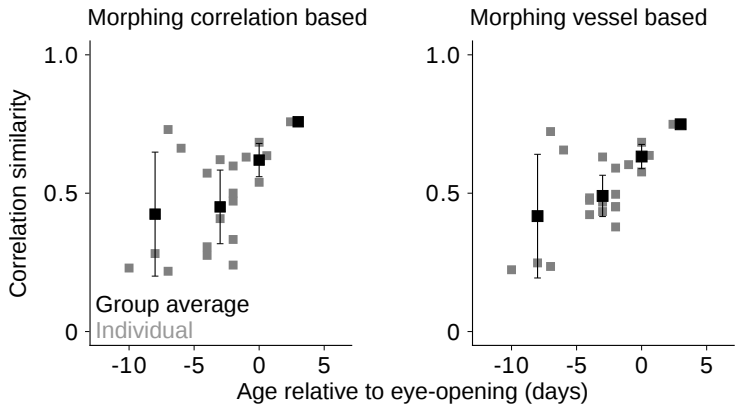

Figure 4.12: Refinement of correlation structure during development cannot be by purely explained by errors due to morphing. *Left*: Similarity based on second order correlations averaged across correlation patterns between successive days confirms refinement of spontaneous correlations especially during early development. Datasets were morphed to reference day with parameters based on maximizing the similarity of the correlation structure between successive days. *Right*: Same plot as shown on *left* but morphing is based on matching radial vessels. Correlation similarity across development is highly similar between the different morphing schemes. Group data (black; from EO-10 to EO-6, EO-5 to EO-1, EO, and >EO) across n=12 animals is shown as mean±SEM over individual data points (gray).

increasing time lag could be caused by an inaccurate morphing of the correlation patterns. The misalignment due to morphing issues might be larger for a longer period of time between spontaneous correlations potentially leading to a similar increase in similarity as observed in **Fig. 4.11e,f**. To test this, we determined an upper limit for the similarity in spontaneous activity during development by computing the transformation parameters of the image registration based on maximizing the correlation coefficient between spontaneous activity patterns of successive days. We found that the similarity based on the average second order correlation of the correlation patterns between successive days changed only little for the datasets that were morphed based on correlation structure compared to the datasets morphed based on radial vessels (**Fig. 4.12**). Thus, the observed reorganization in spontaneous correlation structure during development cannot be purely explained by errors in the registration for longitudinal imaging. As a second check we computed the second-order correlations between spontaneous correlations of successive days enforcing a similar time difference between the compared datasets. We found a similar increase in similarity as shown in **Fig. 4.11e** further demonstrating that the observed reorganization is not due to a morphing artefact.

Fig. 4.10a and **Fig. 4.11b** indicate that the spatial layout of the correlation pattern becomes more detailed and refined during development. Indeed, we found that the domain spacing of spontaneous activity decreased during development (**Fig. 4.13**; from EO≤P<-5 to P>EO p=0.007, Wilcoxon rank-sum). In order to assess the spatial scale of spontaneous activity, we first averaged over all correlation patterns centered around the seed point (**Fig. 4.13a**) and then integrated over the radial dependency of the average correlation pattern, to obtain the correlation coefficients as a function of distance to the seed point. Next, we fitted a Gabor

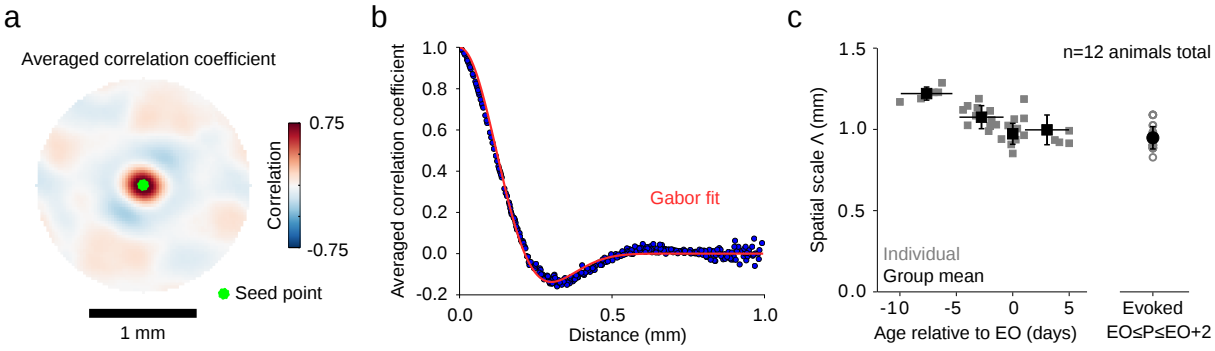

Figure 4.13: Spatial scale of spontaneous activity decreases during development. **a** Correlation pattern centered around seed point averaged across all patterns from day of eye-opening (EO). **b** Correlations averaged across angles decay over distance (blue) fitted by a Gabor function (red). **c** *Left*: The domain spacing Λ of spontaneous activity in the coordinate system of the reference day decreases during development. *Right*: The domain spacing observed in evoked orientation preference map assessed after EO matches the one of spontaneous activity at around EO. For **a**: scale bar is 1 mm; **c**: n=12 chronically recorded animals; Group data (black; from EO-10 to EO-6, EO-5 to EO-1, EO, and >EO) is shown as mean±SEM over individual data points (gray).

function

$$g(x) = e^{-\frac{x^2}{2\sigma^2}} \cos\left(\frac{2\pi}{\Lambda}\, x\right) \tag{4.4}$$

(a Gaussian function modulated by a plane wave) to these correlation coefficients (**Fig. 4.13b**), where σ describes the width of the decay of the envelope of the correlations over the distance x. Λ gives an estimate of the domain spacing of the spontaneous correlations. Note, that we determined the correlation structure in the reference coordinate system of the reference day (typically two days after eye-opening) which means that Λ was determined in the coordinate system of the reference day. We found that the domain spacing decreases throughout development to about 1 mm (**Fig. 4.13c**). Determining the spatial scale in the not-registered data reduced the values for Λ by about 10 to 20% for the earliest age group (data not shown), consistent with what we would expect from the registration parameters (see Section 3.8 in Chapter 3).
Similarly, we assessed the domain spacing of the orientation preference maps at the reference day. First we calculated the auto-correlation function across the map, integrated the correlation function over their radial dependency, and then fitted the Gabor function $g(x)$ (**Fig. 4.13c**, *right*). Alternatively using the signal correlation of the single-trial responses to evaluate the spatial scale of the grating evoked responses analogous to the spontaneous activity, led to quantitatively similar values of Λ. The domain spacing of visually evoked responses and mature spontaneous activity patterns were similar (**Fig. 4.13c**) consistent with their similarity over long distances shown before.

4.2.7 Spontaneous activity patterns are low-dimensional

Given the prominence of distributed patterns of spontaneous activity in the developing and mature cortex, we next asked what we can learn from them about the properties of their underlying cortical circuits. The fact that these activity patterns exhibit such robust long-range correlations suggests that cortical circuits are constrained to express a relatively small, low-dimensional

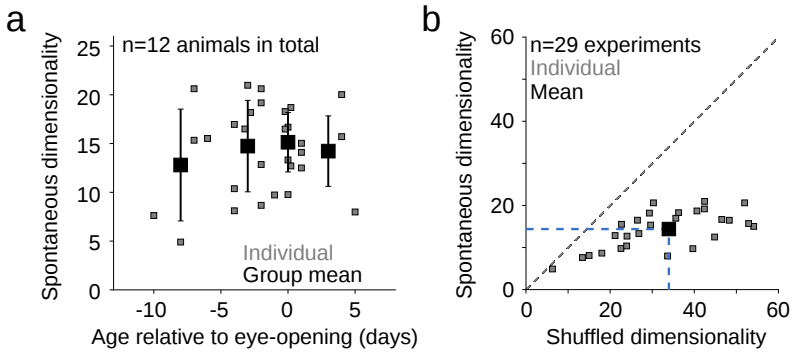

Figure 4.14: Spontaneous activity patterns are low-dimensional with little change throughout development. **a** During development dimensionality of spontaneous activity changes only little. n=12 animals. Individual data points are shown in gray, average group averages are shown in black (mean±SD; from EO-10 to EO-6, EO-5 to EO-1, EO, and >EO). Group data (black; from EO-10 to EO-6, EO-5 to EO-1, EO, and >EO) is shown as mean±SEM over individual data points (gray). **b** Spontaneous activity patterns (individual data points: gray; mean over all experiments: black) are signifcantly lower-dimensional than shuffled controls throughout development (p=1.3x10^{-6}, Wilcoxon signed-rank test, n=29, pooled across animals and ages).

subset of all possible patterns. To test this hypothesis, we employed an empirical estimate of the dimensionality of the spontaneous patterns[30,347,1]

$$d_{\text{eff}} = \frac{\left(\sum_{a=1}^{N} \lambda_a\right)^2}{\sum_{a=1}^{N} (\lambda_a^2)} \tag{4.5}$$

where λ_i are the eigenvalues of the covariance matrix of the N locations within the ROI.

To investigate whether the layout of active domains in spontaneous activity patterns is random or is subject to certain constraints, we compare the dimensionality of the spontaneous activity patterns to the dimensionality of surrogate activity patterns by computing the median value of d_{eff} for 100 surrogate ensembles generated for each animal as described above (see Section 3.9 in Chapter 3). Note that the number of event patterns observed (∼100) is not sufficient to estimate all λ_a. Therefore the sum is truncated, i.e. does not run to N. We found that on average ∼14 dimensions (14 ± 4, mean ± standard deviation) are sufficient to account for all the patterns we observed (**Fig. 4.14**; see also **Fig. 5.1a**). Intriguingly, the dimensionality changed only little during development (**Fig. 4.14**). In other words, any spontaneous activity pattern can be expressed as a linear combination of only ∼14 different "base" patterns, a much smaller number than obtained in sets of surrogate patterns with equal numbers of active domains (**Fig. 4.14**; p=1.3x10^{-6}, Wilcoxon signed-rank test, n=29). In surrogate activity patterns the locations of active domains are randomly distributed across the field of view only constrained by the domain spacing (same power spectrum as in actual data). We therefore conclude that only specific activity patterns are supported by the cortical circuits.

Determining the dimensionality of spontaneous activity by the empirical estimate given in Eq. (4.5), or by applying a Principal Component Analysis (PCA) and taking the number of components necessary to explain a certain amount of variance led to qualitatively very similar results.

To test how the dimensionality depends on the number of spontaneous events used for calculating the covariance matrix, and on the size of the ROI (the number of locations N), we compared the dimensionality of the spontaneous activity and an ensemble of surrogate datasets (see Section

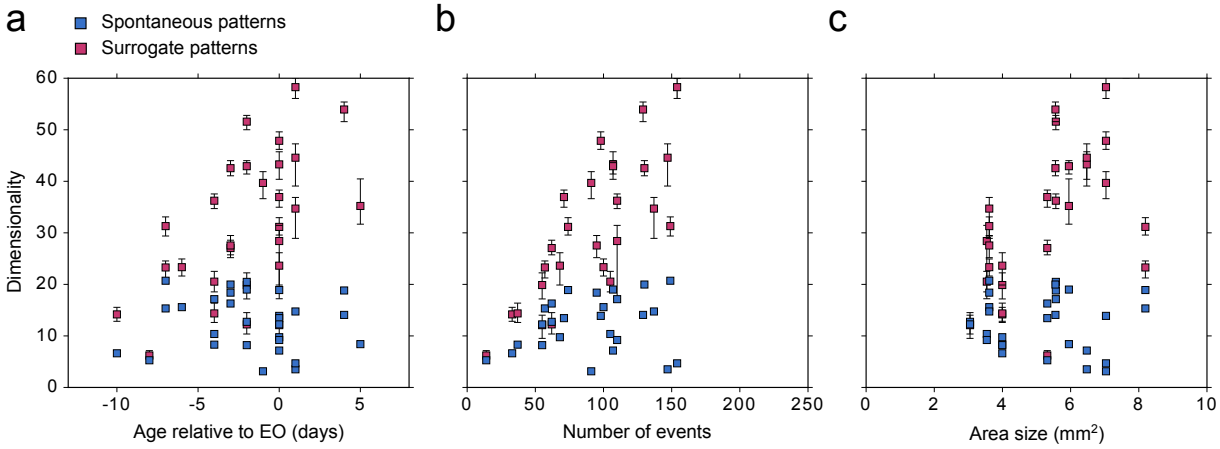

Figure 4.15: Dimensionality of spontaneous activity (blue) varies little during development (**a**), for an increasing number of spontaneous events (**b**) and across animals with differently sized ROIs (**c**). In contrast, dimensionality of surrogate datasets (purple) shows considerable increase (**a-c**).

3.9.2 in Chapter 3) as a function of age, number of spontaneous events and area size of the ROI (**Fig. 4.15**). We found that the dimensionality of spontaneous activity changed only little with age (**Fig. 4.15a**) and with the number of events (**Fig. 4.15b**). In contrast, for the surrogate datasets the dimensionality increased with both (due to the increasing number of spontaneous activity events with age, see **Fig. 3.8**). This indicates that when calculating the dimensionality we did not subsample spontaneous activity. Rather we obtained reliably a very similar dimensionality value on average for very different number of spontaneous events from 10 to 150. This is also consistent with our previous result showing that already a low number of spontaneous activity patterns is sufficient to yield a good approximation of the correlation structure (see Section 3.8 in Chapter 3). This suggests that we can compare the dimensionality values of experiments with different number of spontaneous events and need not compute the dimensionality for the same number of events. The dimensionality of spontaneous activity was similar for animals with different sizes of the ROI varying between 4 to 8 mm^2 whereas the dimensionality of the surrogate datasets slightly increased with area size. This suggests that the dimensionality of animals with ROIs varying in size up to a factor of 2 can be compared consistent with our observation of a long-range correlation structure in spontaneous activity.

4.2.8 Mechanisms generating large-scale distributed networks

Having demonstrated that the cortex exhibits large-scale modular networks (prior to the maturation of horizontal connectivity) which are related to the layout of orientation domains in the mature cortex, we next considered the potential circuit mechanisms capable of generating such large-scale distributed networks in the early cortex. Here we aimed to distinguish between two opposing mechanisms. On the one hand large-scale correlations might be mainly inherited by feed-forward input, on the other hand they might be intrinsically generated by cortical circuits. In the following we address this question by silencing the feed-forward drive to visual cortex and measuring the correlation structure before and after silencing.

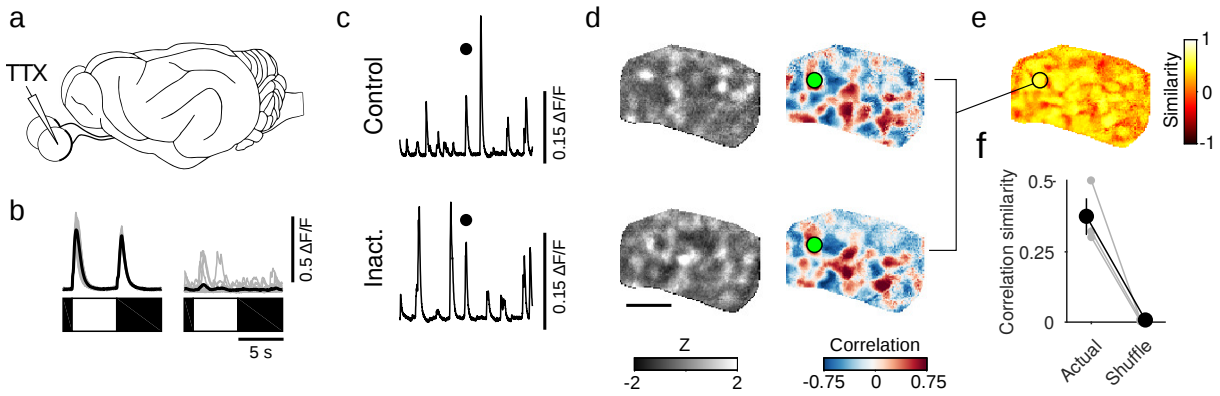

Figure 4.16: Long-range correlations in spontaneous activity persist in the absence of retinal activity. **a** Cortical spontaneous activity was measured before and after retinal inactivation via intraocular injection of TTX. **b** Cortical responses (averaged across field of view) to full-field luminance changes before (*left*) and after (*right*) retinal inactivation. Scale bars: 5 s, 0.5 ΔF/F. **c** Time-course of spontaneous activity (averaged across field of view) before (*top*) and after (*bottom*) inactivation. Scale bars: 30 s, 0.15 ΔF/F. **d** Representative spontaneous events (*left*; indicated by black marker in (**c**)) and correlation patterns (*right*) before (*top*) and after (*bottom*) inactivation. **e** Similarity of correlation structure in representative experiment before and after inactivation for all cortical locations. Scale bar: 1 mm (**d,e**). **f** The spatial structure of spontaneous events following inactivation of retina shows significantly more similarity across events than compared to shuffled data. Group data (black) is shown as mean±SEM over individual data points (gray).

Long-range correlations in early cortex remain stable despite silencing retina

Spontaneous retinal waves are a prominent feature of the developing nervous system[22]. They are highly organized in their spatiotemporal structure and have been shown to propagate into the visual cortex[5]. To assess whether retinal waves contribute to the emergence of long-range correlations, we performed intraocular infusions of TTX, in conjunction with wide-field imaging of spontaneous activity in the early cortex prior to eye-opening (**Fig. 4.16a**). For retinal inactivation experiments, we implanted a cranial window over visual cortex as described in Section 3.2 in Chapter 3. After imaging spontaneous activity under light isoflurane anesthesia (0.5-1 %) (described in Section 3.2 in Chapter 3), visually evoked responses were recorded in response to full-field luminance steps[388]. Isoflurane levels were then increased and intraocular infusions of tetrodoxin (TTX) were performed into each eye. For each intraocular injection, a small incision was made just posterior to the scleral margin using the tip of a 30-gauge needle attached to a Hamilton syringe. Each eye was then injected with 2-2.5 µL of 0.75 mM TTX solution (Tocris Bioscience) to reach an intraocular dose of 21.45 µM that is roughly comparable to the dosage used previously in the ferret[101]. Following infusion of TTX, isoflurane levels were reduced, and the animal returned to a stable light anesthetic plane. The efficacy of TTX was tested by the absence of visually evoked responses to full-field luminance steps. Following confirmation of retinal blockade, spontaneous activity was imaged as above. After the collection of spontaneous activity, retinal blockade was again confirmed through the absence of cortical responses to visual stimuli.

Despite completely abolishing light-evoked responses (**Fig. 4.16b**; response amplitude, preinfusion: 0.357±0.061 ΔF/F, postinfusion: 0.023±0.028 ΔF/F, mean±s.e.m.; bootstrap test versus baseline: preinactivation: $p < 0.008$, postinactivation: $p = 0.365$, n=3 animals, P22-

P25), we continued to observe large-scale spontaneous events of similar frequency (**Fig. 4.16c**) and spatial extension (**Fig. 4.16d**) as before inactivation. The spatial correlation structure was significantly more similar to the structure prior to inactivation than would be expected by chance (**Fig. 4.16e-f**; similarity versus shuffle, $p < 0.001$ for 3 of 3 animals, bootstrap test). Correlation similarity across pre- and post-silencing activity was computed for each seed-point as the Pearson's correlation coefficient of the spontaneous correlations for that seed point across states. For each seed-point, correlations within 400 µm were excluded from the analysis. These second-order correlations (shown for each seed point in **Fig. 4.16e**) were then averaged across all seed points within the ROI. To determine the significance of these second-order correlations across state, we shuffled corresponding seed points across states 1000 times, and again computed correlation similarity. Likewise, to gain an estimate of the expected similarity for a well-matched correlation structure, we computed the similarity of each state to itself. Correlation patterns were first separately computed for half of the detected events, and then the two patterns were compared as above. These results indicate that long-range correlations seem not to be generated by retinal input drive.

Long-range correlations in early cortex remain stable despite silencing LGN

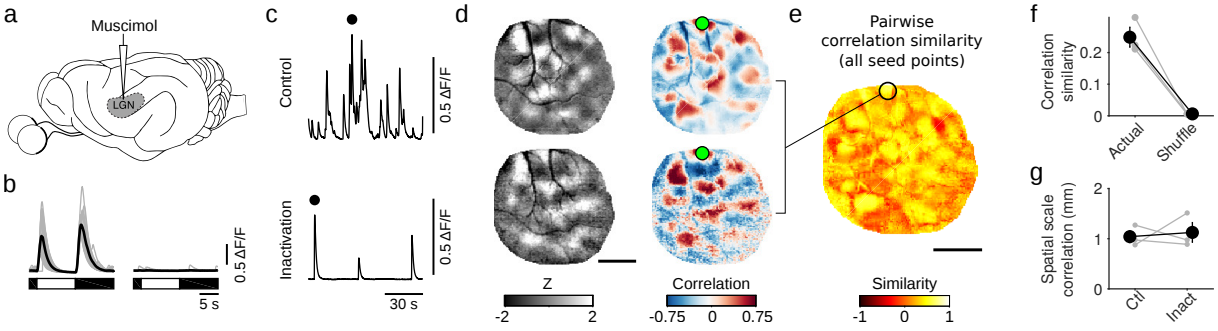

Figure 4.17: Long-range correlations in spontaneous activity persist in the absence of thalamic input. **a** Cortical spontaneous activity was measured before and following LGN inactivation via targeted muscimol infusion. **b** Cortical responses (averaged across field of view) to full-field luminance changes before (*left*) and after (*right*) LGN inactivation. Scale bars: 5 s, 0.5 $\Delta F/F$. **c** Time-course of spontaneous activity for mean of all pixels before (*top*) and after (*bottom*) inactivation. Scale bars: 30 s, 0.5 $\Delta F/F$. **d** Representative spontaneous events (*left*) and correlation patterns (*right*) before (*top*) and after (*bottom*) inactivation. **e** Similarity of correlation structure in representative experiment before and after inactivation for all cortical locations. **f** Correlation structure was significantly more similar before and after inactivation than compared to shuffled data ($p<0.01$, for 3 of 3 individual experiments, bootstrap test). **g** The spatial scale of spontaneous correlations remains long-range following LGN inactivation. For (**d,e**): Scale bar: 1 mm. For (**f,g**): Group data (black) is shown as mean±SEM over individual data points (gray).

To test whether coordinated thalamic activity drives large-scale correlations in the early cortex[459], we infused muscimol into the LGN prior to eye-opening to silence feed-forward inputs to the cortex (**Fig. 4.17a**), while simultaneously imaging cortical spontaneous activity using wide-field microscopy. For LGN inactivation experiments, surgical preparation was as described Section 3.2 in Chapter 3. A head-post was implanted near bregma, a craniotomy was made over visual cortex, and sealed with a coverslip affixed directly to the skull with cyanoacrylate glue and dental cement. A second craniotomy was then made over the approximate location of

the LGN (Horsley-Clarke coordinates: AP -1 mm, LM 6 mm). The LGN was typically located at a depth of 5-8.5 mm, and its spatial position mapped by identifying units responsive to a full-field luminance stimulus through systematic electrode penetrations. Once the LGN position was determined, spontaneous activity in visual cortex was recorded as above, followed by visually-evoked responses to luminance steps. A micropipette filled with muscimol (25-100 mM, Tocris Biosciences) was lowered into the center of the LGN[5], and infusions of ∼0.5 µL were made at three depths along the dorsal-ventral extent of the penetration using a nanoliter injector (Nanoject). The efficacy of thalamic inactivation was confirmed by the abolishment of visually evoked activity prior to and following imaging of spontaneous activity in the cortex. Muscimol completely blocked light-evoked responses (**Fig. 4.17b**; response amplitude, preinfusion: 0.720±0.105 ΔF/F, postinfusion: 0.005±0.006 ΔF/F, mean±s.e.m.; bootstrap test versus baseline: preinactivation: $p = 0.0087$, postinactivation: $p = 0.2584$, n=3 animals), and dramatically decreased the frequency of spontaneous events in the cortex (**Fig. 4.17c**; <1 event per min, with a 713±82% increase in the interevent interval, mean±s.e.m., n=3 animals). However, the events remaining after geniculate inactivation still showed large-scale modular activity patterns spanning several millimeters, and exhibited spatial correlation structures highly similar to those observed prior to inactivation (**Fig. 4.17d-f**, similarity vs. shuffle: p <0.001 for 3 of 3 individual experiments, bootstrap test), consistent with prior experiments where silencing was induced via optic nerve transection[86] (where transection of both optic nerves abolishes all LGN activity for ≈50 min[437]). Spontaneous activity was analyzed as described in Section 3.8 in Chapter 3, with one exception: the 10 event threshold for inclusion was not applied to the LGN inactivation experiments as in 1 of 3 cases <10 events were recorded following LGN inactivation. Comparisons between pre- and post-inactivation patterns were made using second-order correlations as described for comparisons of awake and anesthetized activity in Chapter 3 and for silencing of the retina. Notably, the spatial extent of correlations was unchanged after thalamic inactivation (**Fig. 4.17g**, control: 1.04±0.12 mm; inactivation: 1.13±0.20 mm, mean±SEM). Following inactivation, the spatial layout of correlation fractures was also similar (fracture similarity: 0.164±0.015, $p = 0.04$, bootstrap test, n=3 animals), suggesting that the fine-scale structure of correlation patterns was also generated within cortical circuits. Together, these results demonstrate that feedforward drive cannot account for the spatial structure and extent of the spontaneous correlation structure in the early cortex. They rather suggest that the modular distributed networks are intrinsically generated by early cortical circuits.

Summary

Neither silencing retinal activity nor silencing activity in LGN prevents the formation of distributed, modular, cortical spontaneous activity. The spontaneous activity that is generated in primary visual cortex after inactivation of feed-forward drive still exhibits a long-range correlation structure. These results suggest that rather than being driven by feed-forward pathways, the modular and distributed networks present in the early visual cortex are intrinsically generated by a cortical mechanism. In Chapter 5 we will explore a network model describing the emergence of a long-range correlation structure in the presence of a purely local connectivity.

4.2.9 Local anisotropic correlation structure

In the following Chapter 5 we assess a dynamical network model of early spontaneous activity. This model predicts that the local correlation domain around the seed point of a correlation pattern is anisotropic. Indeed by describing the shape of the peak of a correlation pattern around its seed point (see also **Fig. 5.12g**) by an ellipse, we confirmed this prediction with the experimental data. We fitted an ellipse (least-square fit) with orientation Φ, major axis ζ_1 and

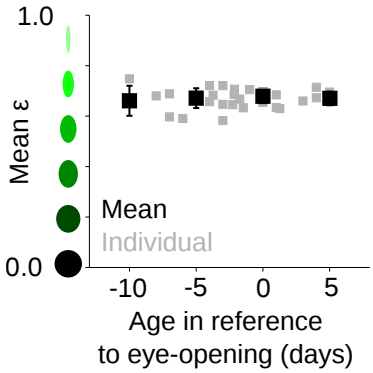

Figure 4.18: Throughout development the average anisotropy of the local correlation domain around the seed point remains stable. Group data (black; EO-10≤P<EO-5, EO-5≤P≤EO-1, P=EO, P>EO;) is shown as mean±SEM over individual data points (gray).

minor axis ζ_2 to the contour line at correlation=0.7 around the seed point. The eccentricity ϵ of the ellipse is defined as

$$\epsilon = \frac{\sqrt{\zeta_1^2 - \zeta_2^2}}{\zeta_1} \tag{4.6}$$

Its value is 0 for a circle, with increasing values indicating greater elongation of the ellipse. The local correlations were already anisotropic early in development and the degree of anisotropy changed only little during development (**Fig. 4.18**). Similarly, the standard deviation of the anisotropy across cortex remained stable during development (data not shown).

We next assessed whether spontaneous fractures - the transition lines from one correlation

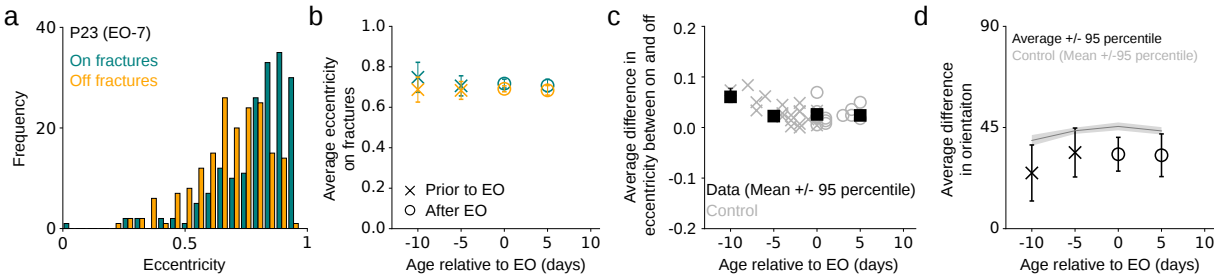

Figure 4.19: The local anisotropy is weakly affected by the organization of spontaneous fractures in the earliest age group but seems to become independent later. **a** Example of eccentricity distributions on fractures (teal) and about 100 µm away from fractures (orange) from 7 days prior to eye-opening (EO-7). **b** Average eccentricity on (teal) and away from (orange) fractures remain largely stable from prior (cross) to after eye-opening (circle) and **c** are only significantly different from each other for the earliest age group. **d** The orientation of the local anisotropy tends to but is not significantly aligned with the underlying fractures. For (**b-d**): Group data (from EO-10 to EO-6, EO-5 to EO-1, EO, and >EO) is shown for individual data points (gray; **c**).

pattern to another - affected the organization of the local anisotropy of the correlation pattern. One might expect that near a fracture the local correlation domain is more elongated and aligned with the direction of the fracture. To this end, we compared the distribution of eccentricity values of seed points on fractures with values of seed points 100 µm away from

fractures (**Fig. 4.19a**). We found that at the earliest stage in development (at around 10 to 7 days prior to eye-opening) the local correlations are significantly more elongated on fractures than away from fractures (**Fig. 4.19b,c**; earliest age group: $p<0.001$, bootstrap test). Similarly, the orientation of the local correlations tended to be weakly but not significantly aligned with the underlying fractures (**Fig. 4.19d**). Thus, we conclude that the organization of spontaneous fractures is weakly reflected in the spatial distribution of orientation and eccentricity of the local correlation domains at the earliest observed stage in development but the eccentricity of the local correlations seems to become nearly independent of the position of orientation fractures with age.

Next, we asked whether spontaneous correlations and the mature tuning similarity also matched

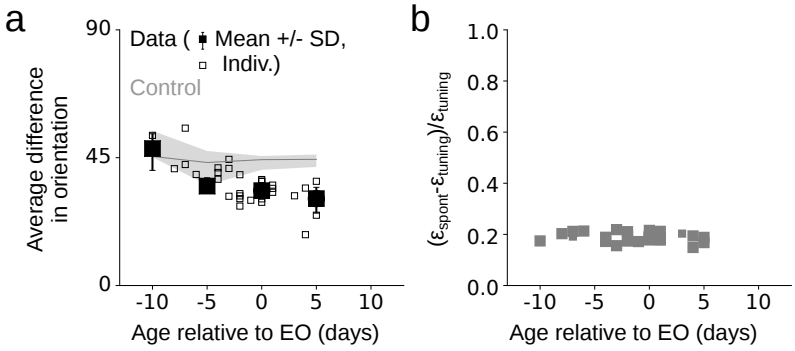

Figure 4.20: Similarity between spontaneous correlations and orientation tuning on local scale increases with age, but is statistically insignificant early on. **a** Shown is the angle difference between the orientation of the fitted ellipses to the local correlation layout and to the local orientation domains after eye-opening (EO) averaged over seed points. Filled marker indicate group average (from EO-10 to EO-6, EO-5 to EO-1, EO, and >EO; Mean ± SD) compared to control datasets (gray; mean ± 95 percentile). **b** Shown is the normalized difference in eccentricity between local correlation structure and orientation domains after eye-opening. The difference remains constant across development, while the tuning eccentricity is only slightly smaller than the eccentricity in the spontaneous correlations (cf. **Fig. 4.18**).

in the anisotropy of the local structure around their seed point. To address this question, we first fitted ellipses to the local correlation structure and the local neighbourhood of the tuning similarity (see Eq. (4.2)) as described above. We then tested whether the local neighbourhoods are similarly oriented by computing the difference in their orientation averaged across all locations (**Fig. 4.20a**). We found that with age the orientation of the local domains of spontaneous correlations and tuning similarity become significantly aligned (**Fig. 4.20a**). To test whether the eccentricity between local correlations and local tuning similarity matches, we calculated their relative difference (**Fig. 4.20b**). The ratio of the eccentricity between spontaneous correlations and orientation tuning remained stable across development (**Fig. 4.20b**) reflecting the stability of the eccentricity of the local correlations with age. Together, these results show that spontaneous correlations and tuning similarity become increasingly matched with age even in their local features.

4.3 Discussion

Patterned spontaneous activity allowed us to characterize the state of distributed network structure early in development. Given the strong association of modular, visually evoked activity patterns with the modular arrangement of long-range horizontal connections in mature cor-

tex[154,285,48], we were surprised to find robust long-range modular patterns of correlated activity as early as 10 days prior to eye opening, when horizontal connections are immature[46,122,364]. The correlated activity patterns at this early stage in development were not identical to the patterns found in the mature cortex, instead they underwent significant refinement prior to eye opening. Indeed, developmental changes in the patterns of correlated activity are likely to reflect ongoing maturation of multiple features of circuit organization including the emergence of long-range horizontal connections. Our retinal and thalamic inactivation experiments bolster previous work[86,284], and establish that early correlated patterns of spontaneous activity cannot be attributed to patterns of activity arising from retina or LGN. The presence of such long-range modular correlation patterns in the absence of a well-developed horizontal network in layer 2/3 and in the absence of feed-forward drive challenges the necessity of long-range monosynaptic connections for generating such distributed modular network activity.

Signatures of the mature orientation preference map were already evident in early spontaneous correlations. However, it remains unclear whether early spontaneous correlations are already similar to early evoked responses or whether their relationship becomes closer during development. To address this question it would be necessary to not only chronically image spontaneous activity but also visually evoked responses.

Similar to previous work[274], we found that the layout of spontaneous activity patterns is confined to a low dimensional manifold. This confinement was expressed in correlated activity between cortical locations (similarly found in other brain areas[151,468,298]) potentially over a large spatial range. Theoretically, it has been shown that already weak correlation coefficients between locations could be sufficient to notably constrain the set of patterns generated by neural circuits[372]. Previous work found that retinal inactivation changed the event size distribution[383]. After enucleation the number of small sized events decreased whereas the number of events in wich more than 80% if neurons participated slightly increased. The authors argued that this might indicate that small events are mainly triggered by retinal input whereas large events are intracortically generated. It would be interesting to investigate whether our data shows a similar reduction in small sized events of spontaneous activity after retinal inactivation compared to before inactivation. Indeed we observed a notable drop in the frequency of spontaneous events after LGN inactivation suggesting that LGN triggers intrinsic cortical spontaneous events[284]. This is also consistent with previous work in cortical slices suggesting that cortical spontaneous activity mainly depends on corticocortical connections[368,423].

The finding of modular correlation patterns distributed over distances comparable to those found with intact feedforward inputs indicates that immature cortical circuits have the capacity to generate long-range correlated modular patterns. It is important to emphasize that these observations do not rule out a causal role for feedforward inputs in establishing modular cortical network structure. Patterns of retinal and geniculocortical activity could play a critical role in guiding the development of these cortical activity patterns (e.g.[311,69,75,201]), but they are clearly not required for their expression.

Taken together, our results suggest that early cortical circuits can intrinsically produce modular long-range correlations that are refined in the course of development to form mature distributed functional networks. This result, however, leads to the challenging puzzle of how the long-range correlation structure in the early cortex is generated through intracortical circuits before the long-range horizontal connectivity maturates. We will address this issue in the next chapter by studying statistical and dynamical network models.

Chapter 5

Modelling long-range correlated spontaneous activity

Key features of spontaneous activity in the mature cortex, such as the modular and long-range correlation structure, are already present in the early cortex prior to eye-opening. Moreover, the presence of these long-range correlation structure in the spontaneous activity even after the inactivation of retina and LGN suggests that long-range correlations are intracortically generated. However, as these large-scale cortical networks are present prior to the maturation and elaboration of long-range horizontal connectivity[364,122,439,46], these results also present a conundrum.
To explore how a developing cortex lacking long-range connectivity could generate long-range correlated patterns of activity, we studied an ensemble of spatially extended activity patterns of a pre-defined dimensionality. We found that reducing the dimensionality of that ensemble led to an increase of the spatial scale of its correlation structure. This could be a potential mechanism generating a long-range correlation structure.
Building on this result, we next studied a dynamical network model of firing rate units[446], variants of which have been used previously to model spontaneous activity in the mature visual cortex[159,44,148,317]. In the model we took advantage of the observation that heterogeneity within a network leads a line attractor to disappear and the activity patterns to cluster into a small number of discrete states[428,464,353]. We assessed how network heterogeneity influences the dimensionality of the ensemble of activity patterns generated by the network and found that with increasing heterogeneity the dimensionality decreases and the range of its correlations increases. The analysis of the model revealed a quantitative match between the network model and the experimental observations *in vivo* in several features of the early cortex including the spatial scale of correlations, the strength of spontaneous fractures and the anisotropy of local correlations. The low dimensionality of the spontaneous activity patterns, thus, might provide an organizational principle in cortex explaining among other things the observed long-range correlation structure.

5.1 Introduction

In Chapter 4 we have shown that spontaneous correlations extend over large distances already at a stage in cortical development when long-range lateral connections have not emerged yet[389]. Inactivating feed-forward drive by silencing either retina or LGN leaves the long-range and modular correlations intact indicating an intracortical mechanism for generating long-range correlations. However, the mechanism generating long-range correlations in the absence of long-

range lateral connections remains elusive. Here, we investigate whether constraining the set of network activity patterns to a lower dimensional manifold might act as such a mechanism. The rationale behind is that if an ensemble of activity patterns is constrained in its dimensionality its active domains are not located randomly within cortical space but are confined in their layout. This might lead to a co-variation in the activity of (distant) cortical elements possibly strong enough to explain the emergence of long-range correlations. To investigate low dimensionality as the underlying principle for long-range correlations, we first study the statistical properties of an ensemble of modular activity patterns of systematically varying dimensionality and compare those to experimental data. We find that for a sufficiently low dimensional ensemble of activity patterns, it agrees quantitatively in the spatial scale of the correlations and in fracture strength. Having established that low dimensionality generates the experimentally observed properties in ensembles of activity patterns, we next study a dynamical network model that constrains the dimensionality of its output activity by assuming a heterogeneously distributed connectivity scheme. The heterogeneity in the network connectivity breaks the translation and rotation symmetry of the network and in turn of its activity patterns confining the network activity to a lower dimensional manifold. An analysis of the model shows that the statistical properties of the network activity and the experimental data are in quantitative agreement. Finally, we show for a simplified model with both excitatory and inhibitory units and a more advanced model consisting of two separate population of excitation and inhibition that introducing network heterogeneity successfully leads to activity patterns with properties as observed in experimental data. In summary, we provide a powerful mechanism and its network implementation of generating a long-range correlation structure in the absence of long-range anatomical connections.

5.2 Statistical model of spontaneous activity patterns

Here we aim towards describing the patterns of spontaneous activity events using a statistical model. We generated in two different variants of the statistical model sets of modular activity patterns with a domain spacing and a pre-defined dimensionality. We assumed a fixed domain spacing which is determined by the experimental data presented in Chapter 3 and Chapter 4. By systematically varying the dimensionality, we examined its influence on the properties of the correlation structure of the activity patterns. We found that for a sufficiently small dimensionality the activity patterns generated by the model are consistent with experimental data in several key properties. In the following, we describe both variants of the model in detail and compare their properties with data of early spontaneous activity.

5.2.1 Key features of spontaneous activity vary with dimensionality

Spontaneous activity patterns exhibit a low dimensionality (14±4, mean±SD; Chapter 4) which is smaller than expected by control datasets with the same domain spacing and the same number of active domains (**Fig. 5.1a**). Thus, active domains in the spontaneous activity are not randomly distributed in cortical space but are constrained in their positions. This raises the possibility that low dimensionality could be an organizing principle that is sufficient to explain the features of spontaneous activity patterns that are observed in the experimental data. To test this idea, we studied the correlation structure in a statistical model of an ensemble of spatially extended, modular activity patterns that were maximally random, but confined to a subspace of predefined dimensionality k. In this model we generated k orthonormal basis patterns v from an ensemble of real-valued Gaussian random fields matching the spectral width in the data[231] (**Fig. 5.1b**). A random field is a generalized stochastic process whose parameter can take values that are multi-dimensional vectors (in our case two-dimensional). A Gaussian random field $G_{\mathbf{m}}$ is then a random field whose joint probability density is described by a multivariate normal

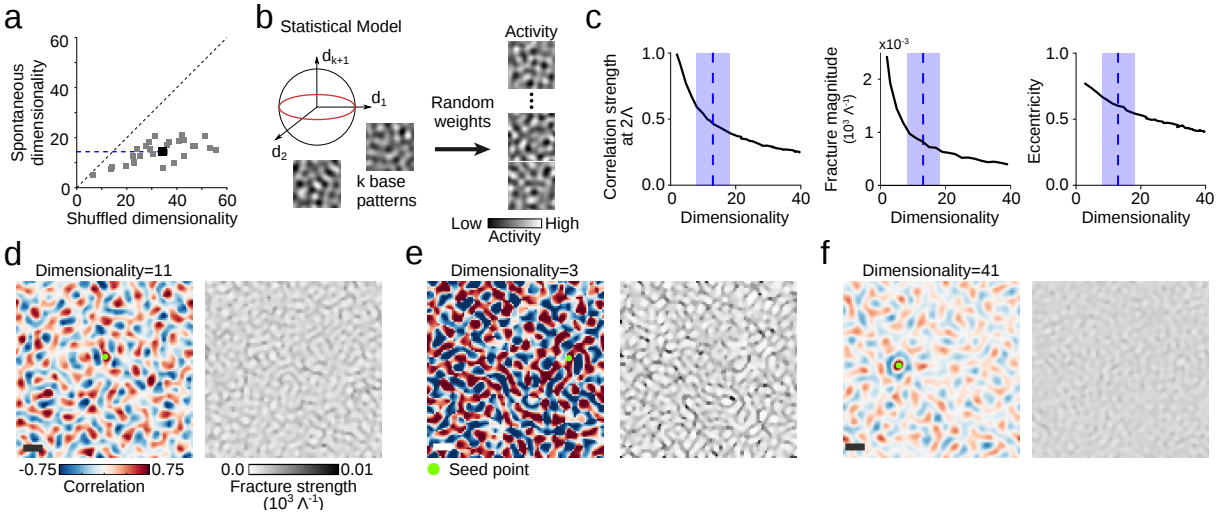

Figure 5.1: Constraining activity patterns to low dimensionality generates long-range correlations and pronounced fractures. **a** Spontaneous activity patterns are significantly more constrained to a low-dimensional subspace than shuffled surrogate patterns (gray: individual experiments; black: population mean, n=29). **b** A statistical model of spontaneous activity generates an ensemble of activity patterns with specified dimensionality k by a randomly weighted superposition of k orthonormal basis patterns. **c** The strength of long-range correlations, fractures, and the eccentricity of the local correlations all increase with decreasing dimensionality. Blue lines (mean±SD) indicate the range of dimensionality in the data (**a**). **d,e,f** The correlation pattern computed over an ensemble of N=10000 patterns and dimensionality $d = 11$ expresses long-range correlations (**d**, *left*) and pronounced fractures (**d**, *right*). Example spontaneous correlation pattern (*left*) and fractures (*right*) for dimensionality $d = 3$ (**e**), and $d = 41$ (**f**). Scale bar is 1 Λ (**d,e,f**).

distribution[3]. Since a normal distribution is fully described by its mean and covariance, it is sufficient to specify the first and second moments of the multivariate normal distribution to determine the Gaussian random field. We assumed the first moment to be

$$\begin{aligned} &\langle v_{\mathbf{m}} \rangle = 0 \\ &\text{with} \quad \mathbf{m} = (m_1, m_2)^T \quad \text{and} \quad m_1, m_2 \in [0, L/M, \ldots L-1]. \end{aligned} \tag{5.1}$$

Here $v_{\mathbf{m}}$ describes a specific realization of the Gaussian random field $G_{\mathbf{m}}$ of size LxL with M lattice points in x and y-direction, respectively. The brackets $\langle\rangle$ denote the integral of the field weighted by its probability density. Due to translational symmetry the second moment depends only on the difference vector $\mathbf{r} = \mathbf{m} - \mathbf{n}$:

$$\langle v_{\mathbf{m}} v_{\mathbf{m}+\mathbf{r}} \rangle = C_{\mathbf{r}} \tag{5.2}$$

Equivalently, we can write the second momentum in Fourier space as

$$\langle v_{\mathbf{m}} v_{\mathbf{m}+\mathbf{r}} \rangle = \frac{1}{M^2} \langle \sum_{\mathbf{k}} \sum_{\mathbf{q}} e^{\frac{2\pi i}{M} \frac{M}{L} \mathbf{m}(\mathbf{k}+\mathbf{q}) + \frac{2\pi i}{M} \mathbf{q}\mathbf{r}} \, \tilde{v}_{\mathbf{k}} \tilde{v}_{\mathbf{q}} \rangle \tag{5.3}$$

$$= \frac{1}{M^2} \sum_{\mathbf{k}} \sum_{\mathbf{q}} e^{\frac{2\pi i}{L} \mathbf{m}(\mathbf{k}+\mathbf{q}) + \frac{2\pi i}{L} \mathbf{q}\mathbf{r}} \langle \tilde{v}_{\mathbf{k}} \tilde{v}_{\mathbf{q}} \rangle \tag{5.4}$$

$$= \frac{1}{M^2} \sum_{\mathbf{k}} \sum_{\mathbf{q}} e^{\frac{2\pi i}{L} \mathbf{m}(\mathbf{k}+\mathbf{q}) + \frac{2\pi i}{L} \mathbf{q}\mathbf{r}} |\tilde{v}_{\mathbf{k}}| \, |\tilde{v}_{-\mathbf{q}}| \langle \, e^{i\phi_{\mathbf{k}}} e^{-i\phi_{-\mathbf{q}}} \rangle \tag{5.5}$$

$$= \frac{1}{M^2} \sum_{\mathbf{k}} \sum_{\mathbf{q}} e^{\frac{2\pi i}{L} \mathbf{m}(\mathbf{k}+\mathbf{q}) + \frac{2\pi i}{L} \mathbf{q}\mathbf{r}} |\tilde{v}_{\mathbf{k}}| \, |\tilde{v}_{-\mathbf{q}}| \delta_{\mathbf{k},-\mathbf{q}} \tag{5.6}$$

$$= \frac{1}{M^2} \sum_{\mathbf{q}} e^{\frac{2\pi i}{L} \mathbf{q}\mathbf{r}} |\tilde{v}_{\mathbf{q}}|^2. \tag{5.7}$$

where $\tilde{v}_{\mathbf{k}}$ denotes the Fourier transform of the Gaussian random field. Here we assumed that the Gaussian random fields are real. This result shows that we can express the second momentum as a function of the power spectrum of the Gaussian random fields $|\tilde{G}_{\mathbf{k}}|^2$ which we assumed to be

$$|\tilde{v}_{\mathbf{q}}|^2 = |\tilde{v}_{qq'}|^2 = e^{-\frac{\left(\frac{2\pi}{L}\sqrt{q^2+q'^2}-\mu\right)^2}{w^2}} \tag{5.8}$$

where μ determines the domain spacing of the Gaussian random field and w denotes its spectral width. Here we used $\vec{q} = (q, q')^T$.
In the model, we then orthogonalized the basis patterns v by applying the Householder reflection and normalized the patterns to zero mean and standard deviation of 1. By forming random superpositions from these (fixed) k patterns using normal-distributed weights ζ (with mean 0, SD $\sigma_\zeta = 1$), we generated an ensemble of N random patterns A_i ($i = 1, 2, \ldots N$) spanning a k-dimensional subspace in the high-dimensional space of all possible spatially extended, modular patterns, thus mimicking the experimentally observed behaviour of spontaneous activity patterns

$$A_j = \frac{1}{k} \sum_{i=1}^{k} \zeta_{ji} v_i. \tag{5.9}$$

Importantly, increasing the ensemble size N does not change its dimensionality as the dimensionality is determined by the number of different base patterns v_i. To study the relationship between the dimensionality of the set of modular activity patterns and the spatial range of their correlation structure, we calculated the cross-correlation between two locations $\mathbf{m}, \mathbf{n}$ across the

N patterns A_j. We used again Pearson's correlation coefficient

$$C_{\mathbf{mn}} = \frac{1}{N}\sum_{j=1}^{N}\frac{(A_{j\mathbf{m}} - \bar{A}_{\mathbf{m}})(A_{j\mathbf{m}} - \bar{A}_{\mathbf{m}})}{\sigma_{A_\mathbf{m}}\sigma_{A_\mathbf{n}}} \tag{5.10}$$

$$\approx \frac{1}{N}\sum_{j=1}^{N}\frac{A_{j\mathbf{m}}\,A_{j\mathbf{n}}}{(\frac{1}{N}\sum_{j=1}^{N}A_{j\mathbf{m}}^2)^{1/2}\,(\frac{1}{N}\sum_{j=1}^{N}A_{j\mathbf{n}}^2)^{1/2}} \tag{5.11}$$

$$= \sum_{j=1}^{N}\frac{\sum_{i=1}^{k}\zeta_{ji}v_{i\mathbf{m}}\sum_{l=1}^{k}\zeta_{jl}v_{l\mathbf{n}}}{(\sum_{j=1}^{N}\sum_{i,l=1}^{k}\zeta_{ji}v_{i\mathbf{m}}\zeta_{jl}v_{l\mathbf{m}})^{1/2}\,(\sum_{j=1}^{N}\sum_{i,l=1}^{k}\zeta_{ji}v_{i\mathbf{n}}\zeta_{jl}v_{l\mathbf{n}})^{1/2}} \tag{5.12}$$

$$= \frac{\sum_{i=1}^{k}\sum_{l=1}^{k}v_{i\mathbf{m}}v_{l\mathbf{n}}\,\sigma_\zeta^2\,\delta_{il}}{\left(\sigma_\zeta^2\sum_{i=1}^{k}v_{i\mathbf{m}}^2\right)^{1/2}\,\left(\sigma_\zeta^2\sum_{i=1}^{k}v_{i\mathbf{n}}^2\right)^{1/2}} \tag{5.13}$$

$$= \frac{\sum_{i=1}^{k}v_{i\mathbf{m}}v_{i\mathbf{n}}}{\left(\sum_{i=1}^{k}v_{i\mathbf{m}}^2\right)^{1/2}\,\left(\sum_{i=1}^{k}v_{i\mathbf{n}}^2\right)^{1/2}} \tag{5.14}$$

where $A_{j\mathbf{m}}$ denotes the value of the j-th realization of the generated patterns at location $\mathbf{m}$, σ_ζ denotes the standard deviation of the coefficients ζ_{ij} and $\sigma_{A_\mathbf{m}}$ denotes the standard deviation at location $\mathbf{m}$ across realizations j of activity patterns A_j. We used here that in the limit of large N the average value $\bar{A}_\mathbf{m}$ vanishes since the coefficients ζ were drawn from a centered Gaussian distribution. Note that for finite dimensions k the standard deviation depends on the specific locations $\mathbf{m}, \mathbf{n}$ as well as on the specific realizations.
This expression shows that for a small number of dimensions k - as observed in experimental data - the correlation coefficient is calculated only over a small set of basis patterns v and is therefore highly seed-point dependent and its spatial structure is dominated by the individual realizations v_l. For low values of dimensionality the correlation coefficients stay high across large distances since a low number of different realizations of Gaussian random fields repeat themselves in the activity patterns. Increasing the number of realizations N does not change the dimensionality, we therefore kept N finite.
To explicitly show the behaviour of the correlation C for low k, we considered the two simplest cases for $k = 1, 2$ (We consider the case $k \to \infty$ below):

$$k = 1: \quad C_{\mathbf{mn}} = \frac{v_{1\mathbf{m}}v_{1\mathbf{n}}}{|v_{1\mathbf{m}}||v_{1\mathbf{n}}|} = (\mathrm{sgn}(v_{1\mathbf{m}})\,\mathrm{sgn}(v_{1\mathbf{n}})) \tag{5.15}$$

$$k = 2: \quad C_{\mathbf{mn}} = \frac{v_{1\mathbf{m}}v_{1\mathbf{n}} + v_{2\mathbf{m}}v_{2\mathbf{n}}}{(v_{1\mathbf{m}}^2 + v_{2\mathbf{m}}^2)^{1/2}\,(v_{1\mathbf{n}}^2 + v_{2\mathbf{n}}^2)^{1/2}} \tag{5.16}$$

For $k = 1$ the correlation coefficient is either ± 1 depending on the sign difference between locations $\mathbf{m}, \mathbf{n}$. In this case, the peaks of the correlation coefficients are equal to 1 even if the distance between $\mathbf{m}$ and $\mathbf{n}$ is large. This means there is a global correlation structure over the set of activity patterns. In the case of $k = 2$ it is possible for certain realizations of v_1, v_2 that the two terms in the numerator (partially) cancel each other such that the peaks of the correlation coefficients become small. However, typically the correlations remain high across the field (compare also **Fig. 5.1e** for $k = 3$). Importantly, in this model the values at the peaks of the correlations do not decay with distance to the seed point for low dimensionality. Instead they quickly drop after about one domain spacing to an average value below 1 where the correlations remain independent of distance (**Fig. 5.2**). Therefore, instead of determining the spatial scale of the correlations, we determined the average value of the correlation peaks at a distance of 2 Λ to the seed point when systematically varying the dimensionality k (see

Chapter 3 and Chapter 4). Linearly increasing the dimensionality k led to a sublinear decrease in the average correlations (**Fig. 5.1c**(*left*)). Similarly, increasing k also led to a decrease in fracture strength and a decrease in the anisotropy of the local correlations around the seed point (**Fig. 5.1c**(*center*, *right*). For increasing dimensionality the ensemble of activity patterns becomes more variable and therefore leads to smaller correlation coefficients. An increase in the dimensionality resulted in correlation patterns that were more symmetric around their seed point due to averaging across a more diverse set of activity patterns (**Fig. 5.1d-f**) and to a stronger drop in the average correlation. Averaging over a more diverse set of patterns also led to correlation patterns that were more similar between neighbouring seed points which in turn decreased the fracture strength (**Fig. 5.1d-f**).

Importantly, we noted above that we did not observe a decay in the correlations for small

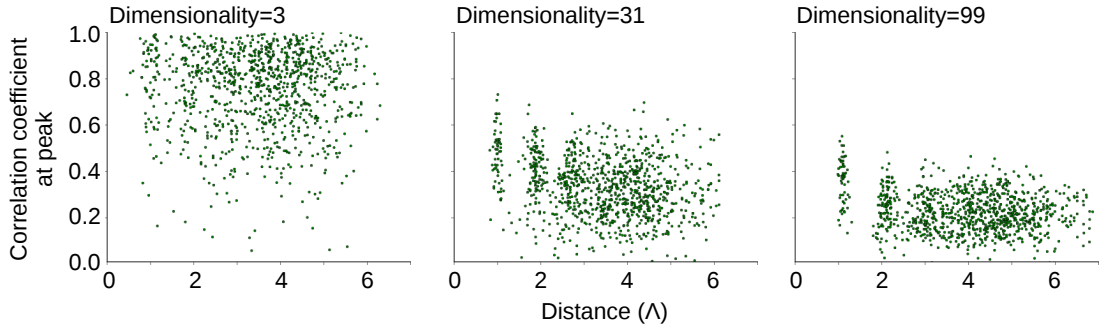

Figure 5.2: Peak values of correlation coefficients start to decay over spatial distance for sufficiently high ensemble dimensionality. From *left* to *right* dimensionality increases. For $d = 3$ (*left*) a spatial decay of the correlations is not apparent. For $d = 31$ (*center*) and even more for $d = 99$ (*right*) the envelope of the correlations tend to decay over the distance over several domain spacings Λ.

dimensionalities. For increasing dimensionalities the correlations started to show a decay over spatial distances similar to those observed in experimental data (**Fig. 5.2**). For low dimensionality the peak correlation coefficients were generally high and showed a high variability occluding a spatial decay. Still for all dimensions the correlations decayed to a finite baseline value and not to zero due to finite size fluctuations. In the next section we will consider another statistical model describing an ensemble of activity patterns with a dimensionality that is sufficiently high to show the experimentally observed decay behaviour and at the same time allows to systematically vary this dimensionality.

In summary, we examined the influence of dimensionality on the experimentally observed features of correlated spontaneous activity. Intriguingly, we found that when the dimensionality is relatively low, this simple statistical model not only produced correlations over large distances and a network of pronounced correlation fractures but also anisotropic local correlations. All these features became more pronounced the smaller the dimensionality in the model (**Fig. 5.1c**). These results raise the possibility that low-dimensionality could be an organizing principle that is sufficient to explain the observed features of correlated spontaneous activity.

5.2.2 For sufficiently high dimensionality correlations decay with spatial distance

The observation that low-dimensional activity yields a long-range correlation structure suggests that any mechanism that reduces the dimensionality of spontaneous activity could have a similar effect on the spatial structure of correlated activity. To test this idea, we simplified the

statistical model presented above such that (1) it allowed us to complement numerical results with analytical calculations and (2) to produce a spatial decay in its correlations. We modeled spontaneous activity patterns by an ensemble of N realizations v_i of two-dimensional Gaussian random fields of a fixed size LxL (with M lattice points in x and y direction as above) that are completely described by their power spectrum (see Eq. (5.8)). These realizations were not orthogonalized, but for large field sizes L are expected to be approximately orthogonal and uncorrelated. For sufficiently large N the ensemble was high dimensional which (1) should result in a spatial decay of the correlations and (2) allowed us to obtain a closed-form expression of the correlation structure of the generated activity patterns. To investigate the influence of the ensemble's dimensionality on the correlation structure, we systematically varied the width w of the power spectrum of the Gaussian random fields. An increase in the spectral width w corresponds to a higher variability in the local domain spacing Λ of the activity patterns in turn leading to a higher dimensionality of the ensemble. In this variant of the statistical model, we tested whether increasing the dimensionality not only lowers the average correlations at large distances as observed in the minimal statistical model but also leads to a decrease in the spatial scale of the correlations.

First, we showed that increasing the spectral width w increases the dimensionality of the en-

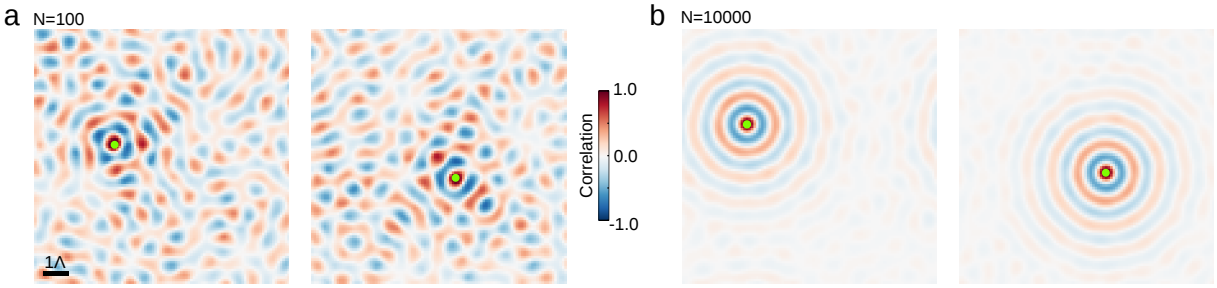

Figure 5.3: Realizations of Gaussian random fields exhibit seed point dependent correlation patterns due to finite size effects. **a** Realizations of correlation patterns across N=100 realizations of Gaussian random fields for two different seed points (green marker). The layout differs between the two seed points. **b** Two correlation patterns across N=10000 realizations of Gaussian random fields with a highly similar radially symmetric layout. Scalebar is 1Λ.

semble of Gaussian random fields. To this end, we used an estimate of the dimensionality of the Gaussian random fields based on the distribution of eigenvalues of their covariance matrix $\hat{C}$ (see Eq. (2.20)[30,347,1]; see also Section 2.3.6 in Chapter 2). In the following, we compared analytical calculations with numerical realizations of Gaussian random fields and therefore considered discretized Gaussian random fields. We first determined the covariance matrix (see Eq. (5.14))

$$\hat{C}_{\mathbf{mn}} = \sum_{i=1}^{N} v_{i\mathbf{m}} v_{i\mathbf{n}} \tag{5.17}$$

where $v_{i\mathbf{m}}$ denotes the value of the realization i at location $\mathbf{m} = (m_x, m_y)^T$. Here we assumed that the Gaussian random fields centered around zero. For a sufficiently large number of realizations N, we can further simplify this expression. In the limit of large N, the covariance becomes identical for all locations (translation invariant) and only dependent on the distance between locations $\mathbf{m}$ and $\mathbf{n}$ (**Fig. 5.3**; covariances are *self-averaging*). We thus replaced the average over realizations i by the average over locations sharing the distance vector $\mathbf{r} = \mathbf{m} - \mathbf{n}$ assuming that

the Gaussian field size L is sufficiently large and boundary effects can be neglected

$$\hat{C}_{\mathbf{mn}} = \sum_{\substack{\mathbf{m}=1 \\ \mathbf{n}=\mathbf{m}+\mathbf{r}}}^{M} v_{\mathbf{m}} v_{\mathbf{n}} \tag{5.18}$$

$$= \mathcal{F}\{\tilde{v}_{qq'}\ \tilde{v}^*_{qq'}\}_{\mathbf{m}-\mathbf{n}} \tag{5.19}$$

where $\tilde{v}_{qq'}$ is the (two-dimensional) Fourier transform of the Gaussian random field v and $\tilde{v}^*_{qq'}$ is its complex conjugate. Here we applied the cross-correlation theorem allowing us to express the covariance as the Fourier transform of the power spectrum of the Gaussian random fields (see also Eq. (5.7)). To take into account the translation invariance of the covariance, we rewrote it as $\hat{C}(\mathbf{m}, \mathbf{n}) = \hat{C}(\mathbf{m} - \mathbf{n})$. By plugging the expression of the power spectrum of the Gaussian random field (Eq. (5.8)) into the equation above, approximating the discrete Fourier transform by its continuous form ($(q, q') \to (q/L, q'/L)$) and transforming the frequency from cartesian to polar coordinates ($(q, q') \to (q_r, \phi)$), we obtained

$$\hat{C}(\mathbf{m} - \mathbf{n}) = \frac{1}{M^2} \sum_{q,q'} e^{\frac{2\pi i}{L}(q\ (m_x - n_x) + q'\ (m_y - n_y))} e^{-\frac{(\frac{2\pi}{L}\sqrt{q^2+q'^2} - \mu)^2}{w^2}} \tag{5.20}$$

$$= \frac{1}{L^2} \int \mathrm{d}q \int \mathrm{d}q' e^{2\pi i (q\ (m_x - n_x) + q'\ (m_y - n_y))} e^{-\frac{(2\pi i\sqrt{q^2+q'^2} - \mu)^2}{w^2}} \tag{5.21}$$

$$= \frac{1}{L^2} \int_0^{2\pi} \mathrm{d}\phi \int_0^{\infty} \mathrm{d}q_r\ q_r\ e^{2\pi i\ q_r(\cos\phi\ (m_x - n_x) + \sin\phi\ (m_y - n_y))} e^{-\frac{(2\pi q_r - \mu)^2}{w^2}} \tag{5.22}$$

$$= \frac{1}{L^2} \int_0^{\infty} \mathrm{d}q_r\ q_r\ J_0(2\pi\ q_r \sqrt{(m_x - n_x)^2 + (m_y - n_y)^2}) e^{-\frac{(2\pi q_r - \mu)^2}{w^2}} \tag{5.23}$$

$$\Rightarrow \hat{C}(r) = \frac{1}{L^2} \int_0^{\infty} \mathrm{d}q_r\ q_r\ J_0(2\pi q_r r) e^{-\frac{(2\pi q_r - \mu)^2}{w^2}} \tag{5.24}$$

where $J_0(x)$ denotes the Bessel function of zeroth order[4] and r denotes the absolute difference $r = \sqrt{(m_x - n_x)^2 + (m_y - n_y)^2}$. To transform the discrete into the continous Fourier series we let $M \to \infty$.

We corroborated this result numerically by generating N realizations of Gaussian random fields and calculated their correlation structure. To show that correlation patterns become independent of the seed point only in the limit of large N, we generated a set of $N = 100$ and $N = 10000$ activity patterns. For $N = 100$ the correlation patterns varied across seed points and were dominated by fluctuations around the mean (**Fig. 5.3a**). For $N = 10000$ the correlation patterns became almost identical for all seed points and their magnitude depended only on the distance to the seed point (**Fig. 5.3b**) consistent with the analytical result in Eq. (5.24). This independence of the covariance pattern on the seed point reflects the homogeneity and isotropy of the averaged realizations.

To determine the eigenvalues of $\hat{C}$, we first rewrote the covariance matrix as a fourth order tensor $\hat{C}_{m_x,m_y,n_x,n_y}$. Since $\hat{C}$ only depends on the distance r (see Eq. (5.24)) it is a circulant tensor and is fully determined by a second order tensor. Without loss of generality we took this matrix to be $c_{m_x,m_y} = \hat{C}_{m_x,m_y,0,0}$. The circulant tensor $\hat{C}$ can be diagonalized by applying the discrete Fourier transform. Its eigenvalues are given by

$$\lambda_{qq'} = \sum_{m_x,n_x=0}^{M-1} c_{M-m_x,M-n_x}\ (\omega_q)^{m_x} (\omega_{q'})^{n_x} = \tilde{c}_{qq'} = |\tilde{v}_{qq'}|^2 \tag{5.25}$$

where $\omega_j = \exp\left(\frac{2\pi i j}{L}\right)$. Note that the eigenvalues correspond to the spectrum of the Gaussian random fields. To determine the dimensionality of the Gaussian random fields, we used Eq.

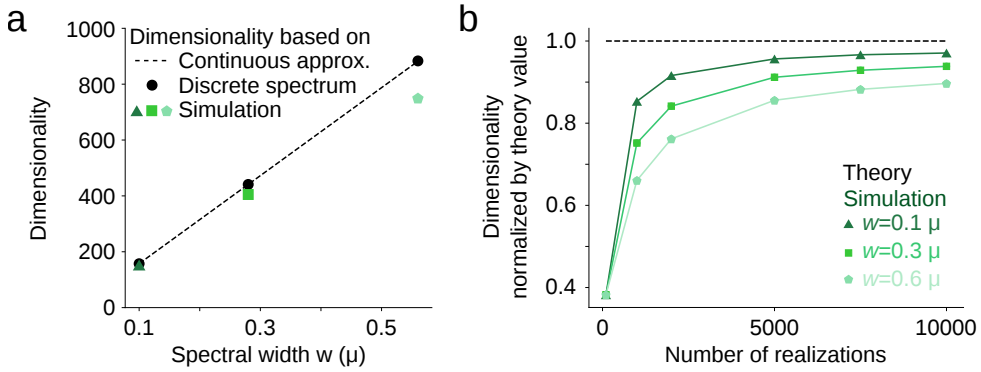

Figure 5.4: Dimensionality increases with spectral width w of Gaussian random fields. **a** Dimensionality of an ensemble of Gaussian random fields increases linearly with w (in units of spatial frequency μ). Dimensionality of $N = 10000$ realizations of Gaussian random fields determined from their covariance matrix (green markers) tends to be smaller than the dimensionality predicted by Eq. (5.30) (dashed line). The dimensionality calculated from the discrete spectrum of the Gaussian random field (Eq. (5.28); black marker) matches the theoretical prediction. **b** Dimensionality (in units of theoretically predicted value) increases with the number of realizations used to calculate the covariance matrix. Increasing w leads to a slower convergence towards the theoretically predicted value (dashed line) indicating that the mismatch in (**a**) stems from limited sample size N.

(2.20)[30,347,1] and by taking the continuous limit we obtained

$$d_{\text{eff}} = \frac{\left(\sum_{q,q'=0}^{M-1} \lambda_{qq'}\right)^2}{\sum_{q,q'=0}^{M-1} (\lambda_{qq'})^2} \tag{5.26}$$

$$= \frac{\left(\sum_{q,q'=0}^{M-1} |\tilde{v}_{qq'}|^2\right)^2}{\sum_{q,q'=0}^{M-1} (|\tilde{v}_{qq'}|^2)^2} \tag{5.27}$$

$$= \frac{\left(\sum_{q,q'=0}^{M-1} \exp\left(-\frac{(2\pi\sqrt{q^2+q'^2}-\mu)^2}{w^2}\right)\right)^2}{\sum_{q,q'=0}^{M-1} \exp\left(-2\frac{(2\pi\sqrt{q^2+q'^2}-\mu)^2}{w^2}\right)} \tag{5.28}$$

$$= \frac{w^2}{8\pi}\left(\frac{M}{L}\right)^2 \frac{\left(\sqrt{\pi}\frac{\mu}{w}\left(1+\text{Erf}\left(\frac{\mu}{w}\right)\right)+e^{-\frac{\mu^2}{w^2}}\right)^2}{\sqrt{2\pi}\frac{\mu}{w}\left(1+\text{Erf}\left(\sqrt{2}\frac{\mu}{w}\right)\right)+e^{-2\frac{\mu^2}{w^2}}} \tag{5.29}$$

$$\overset{\mu/\omega>>1}{=} \sqrt{\frac{2}{\pi}}\frac{\mu w}{8\pi}\left(\frac{M}{L}\right)^2 + h.o.t. \tag{5.30}$$

where Erf denotes the error function[4]. For $\mu/\omega >> 1$, the dimensionality scales linearly with the spectral width w. As before, we corroborated these calculations by simulating $N = 10000$ realizations of Gaussian random fields and found that they match the theoretical prediction of the dimensionality for small values of spectral width w (**Fig. 5.4a**). For large w the dimensionality was affected by the finite size of the ensemble of the realizations and its estimated value was biased towards smaller values (**Fig. 5.4a**). With increasing w more realizations were required to properly assess the ensemble's dimensionality (**Fig. 5.4b**). In summary, increasing w leads

to a nearly linear increase in the dimensionality of an ensemble of activity patterns.

Having demonstrated that increasing the spectral width w leads to a higher dimensionality,

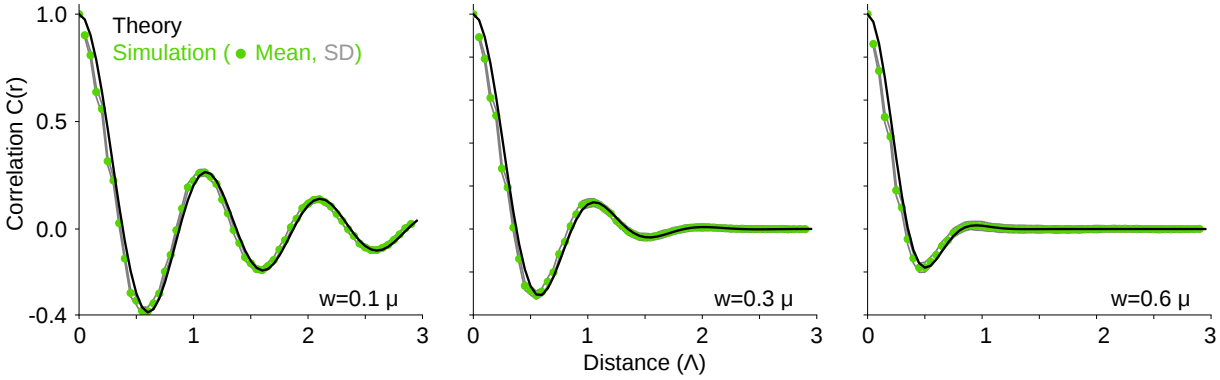

Figure 5.5: Theory and simulation of correlation decay match over range of spectral widths. The correlation coefficients across $N = 10000$ realizations of Gaussian random fields averaged over angle (mean: green markers; SD: gray lines) is in agreement with the theoretical expression (black; Eq. (5.34))

we next tested whether increasing dimensionality decreases the spatial scale of the correlation structure as we would expect from the analysis of the minimal statistical model. To this end, we first determined the correlation structure $C(r)$. Since $C(r)$ (Eq. (5.10)) is the normalized covariance matrix $\hat{C}(r)$ (Eq. (5.24)), we only need to calculate the proper normalization factor C_n such that $C(0) = 1$:

$$1 \stackrel{!}{=} C(0) = \frac{\hat{C}(0)}{C_n} = \frac{1}{C_n L^2} \int_0^\infty \mathrm{d}q \; q \; J_0(0) \; e^{-\frac{(2\pi q - \mu)^2}{w^2}} \tag{5.31}$$

$$= \frac{1}{C_n} \frac{w^2}{L^2 8\pi^2} \left(\sqrt{\pi} \frac{\mu}{w} \left(1 + \mathrm{Erf}\left(\frac{\mu}{w} \right) \right) + e^{-\frac{\mu^2}{w^2}} \right) \tag{5.32}$$

$$\Rightarrow C_n = \frac{w^2}{L^2 8\pi^2} \left(\sqrt{\pi} \frac{\mu}{w} \left(1 + \mathrm{Erf}\left(\frac{\mu}{w} \right) \right) + e^{-\frac{\mu^2}{w^2}} \right). \tag{5.33}$$

Thus, the correlation matrix is given by

$$C(r) = \frac{8\pi^2}{w^2 \left(\sqrt{\pi} \frac{\mu}{w} \left(1 + \mathrm{Erf}\left(\frac{\mu}{w} \right) \right) + e^{-\frac{\mu^2}{w^2}} \right)} \int_0^\infty \mathrm{d}q \; q \; J_0(2\pi q r) \; e^{-\frac{(2\pi q - \mu)^2}{w^2}} \tag{5.34}$$

Using this expression for the correlation coefficients, we next assessed the decay of the correlations as a function of distance to the seed point. We found that consistent with the minimal statistical model studied above with moderate dimensionality k, the correlation coefficients exhibited a spatial decay over a broad range of spectral widths w (**Fig. 5.5**). The analytical result matched the results from numerically obtained realizations (**Fig. 5.5**). Since the Gaussian random fields exhibited a typical spatial scale the correlation coefficients showed an oscillation under the decaying envelope (**Fig. 5.5**). The oscillatory behaviour can be interpreted as an interference such that at the typical domain spacing of 1Λ the activity patterns result in a positive correlations whereas inbetween multiples of the domain spacing the activity patterns yield negative correlations. The envelope of the correlation structure decays faster as the spectral width w becomes broader (**Fig. 5.5**, *left* to *right*) which is also consistent with the results of the minimal statistical model. This further highlights the close relationship between dimensionality

and the spatial scale of the correlations of an ensemble of activity patterns.

To compare whether the decay of the correlations in the model matches those observed in

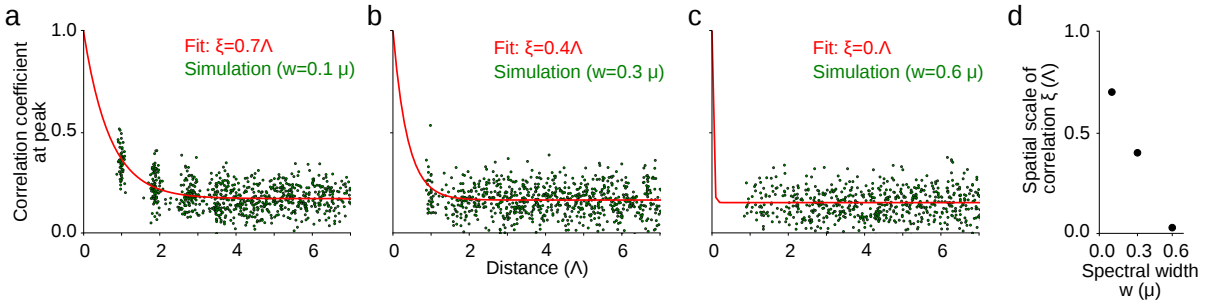

Figure 5.6: Correlation coefficients decay faster over distance to the seed point with increasing spectral width w (**a-c**). The spectral width is varied from $w = 0.1\mu$ (**a**), $w = 0.3\mu$ (**b**) to $w = 0.6\mu$ (**c**). The envelope of the decay of $N = 100$ Gaussian random fields with the same SD of the power spectrum as observed in the data is shown in (**c**). **d** The magnitude of the fitted decay constants ξ decreases with increasing spectral width w.

experimental data, we next examined the spatial scale of the correlations analogous to the analysis of the experimental data (see Section 3.10.1 in Chapter 3). We used $N = 100$ realizations of Gaussian random fields to compute the correlation coefficients to be comparable to the size in the experimental data. The peaks of the correlations decay over shorter spatial distances for increasing w (**Fig. 5.6a-c**) as captured by the spatial scale of correlations (**Fig. 5.6d**). Interestingly, the spatial scales of correlations were relatively large for small spectral widths w and closely approached (but did not match) experimentally observed values (see **Fig. 5.6a** and compare **Fig. 4.6**). Although in **Fig. 5.6**, this relative slow decay was not due to finite size fluctuations as we quantified the decay relative to the baseline correlation at large distances (see Section 3.10.1 in Chapter 3). The baseline was obtained from a surrogate dataset which like the considered activity patterns consists of ensembles of Gaussian random fields.

To quantitatively compare the Gaussian random field model with the experimentally observed spontaneous activity patterns during early development, we first matched their spectral width to the experimental data ($w_{\text{exp}} = (0.62 \pm 0.05)\ \mu$, mean±SD, n=40 experiments of 12 animals). Note that the spectral width is expressed in units of the domain spacing μ. We obtained the experimental spectral width by first calculating the angle averaged spectrum of the individual spontaneous activity patterns. We then computed the average spectrum over all individual spectra and approximated the width of the peak in the average spectrum by the standard deviation of a fitted Gaussian profile (we fitted up to a frequency of 5.7 mm^{-1}).

The dimensionality of an ensemble of Gaussian random fields of comparable spectral width was notably higher than of the spontaneous activity observed in experiment ($d_{\text{GRF}} = 47 \pm 1$, n=3 sets of 100 realizations, vs $d_{\text{exp}} = (13 \pm 6)$, n=5 experiments of 4 animals between 10 to 7 days prior to eye-opening). Similarly, the correlation coefficients decayed significantly faster than observed experimentally (spatial scale ξ_{GRF}=(0.55±0.05) Λ of n=3 sets of 100 realizations vs ξ_{exp}=(0.93±0.14) mm of n=5 experiments of 4 animals; compare also **Fig. 5.7e**, **Fig. 5.9** and **Fig. 5.12b**). In fact, for a spectral width matched to the experimental data the correlation coefficients have decayed to baseline after already one wavelength (**Fig. 5.5**) and no signature of significant correlations was detected in the peak values (**Fig. 5.6**(*right*)). For this comparison we identified 1 Λ with 1 mm, which is roughly the spatial scale of spontaneous patterns observed in experiment. Consistent with the disagreement in spatial scale of the correlations the fractures in the Gaussian random fields were less pronounced (average fracture strength f_{GRF}=(5.0±0.1)

10^{-3} Λ^{-1} of n=3 sets of 100 realizations vs f_{exp}=(14±7) 10^{-3} mm^{-1}, n=5 experiments of 4 animals). The disagreement in all four features between experimental results and values obtained from Gaussian random fields demonstrates that spontaneous activity is not well described by an ensemble of Gaussian random fields. It rather indicates that the location of active domains of the spontaneous activity is more constrained than is achieved by imposing a domain spacing with a certain width. Note that we came to the same conclusion when comparing the dimensionality of the original data to a surrogate dataset consisting of a phase shuffled random ensemble of activity patterns as those surrogate datasets correspond to ensembles of Gaussian random fields Chapter 4.

5.2.3 Summary

In summary, we examined the relationship between the dimensionality and the spatial scale of correlations of an ensemble of activity patterns modeled by Gaussian random fields. Our analytical and numerical analysis revealed a close relationship between those two features. Consistent with the analysis of the minimal statistical model, a decrease in dimensionality due to a decrease in spectral width led to an increase in the spatial scale of correlations. This result further highlights the interrelation between the dimensionality of an ensemble of activity patterns and the spatial scale over which correlations show a decay.
The minimal statistical model (model 1) generated an ensemble of activity patterns whose dimensionality was determined by the underlying number of different base patterns. In particular, increasing the number of activity patterns N in the ensemble did not increase the ensemble's dimensionality. For small dimensionality the peak values of the correlations abruptly dropped to an average value of correlations smaller than 1. Only for a higher ensemble dimensionality the envelope of the correlations with a spatial decay became apparent. In contrast, in the second statistical model (model 2) the ensemble dimensionality was in general sufficiently high to exhibit a decay in its correlations. By systematically varying the ensemble's dimensionality with the spectral width w, we showed that the spatial scale of the correlations increases for decreasing dimensionality indicating that a network mechanism that reduces dimensionality might explain the emergence of long-range correlations in the absence of long-range lateral connections.

5.3 Dynamical network model of early spontaneous activity

The close relationship between a low-dimensional ensemble of activity patterns and their long-range correlation structure suggests that cortical circuits, even if limited to short-range connections as in the early cortex[122,364,439,46], could generate long-range correlations if they act to reduce the dimensionality of the activity patterns supplied by their inputs. To study how a mechanism which constrains the dimensionality of spontaneous activity patterns can be implemented in a neuronal network, we examined dynamical network models of firing rate units[446]. Variants of these network models have been used previously to model spontaneous activity in the mature visual cortex[159,44,148,317]. In these models, modular patterns of activity arise via lateral suppression and local facilitation. Such an interaction is commonly assumed to result from lateral connections that are 1) identical at each position in cortex, 2) circularly symmetric, and 3) follow a *Mexican hat* (MH; local excitation and longer-ranging inhibition) profile. Here, we show explicitly that assuming a connectivity which satisfies these three conditions cannot generate the experimentally observed long-range correlation structure. However, stimulated by previous work[428,464,353] reporting that heterogeneous connectivity can drastically reduce the space of possible activity patterns, we assume an anisotropic Mexican hat function, whose longer axis varies randomly across the cortical surface. Introducing heterogeneity into the network connectivity indeed yields long-range correlations that quantitatively match the experimental data. To the

network, we supply a constant drive, modulated only spatially by a high dimensional Gaussian random field (**Fig. 5.8b**, *left*), as patterns were often fairly static during a spontaneous event in the early cortex (see Chapter 4). For sufficiently strong connections, the network activity evolves towards a modular pattern with alternating patches of active and non-active domains (**Fig. 5.8b**, *right*). While the dimensionality of the input patterns is high, the dimensionality of the produced set of activity patterns can be much smaller and approaches values close to those observed in experiment in a regime of considerably heterogeneous connectivity and moderate input modulation (**Fig. 5.8g**; **Fig. 5.12a,b**). In this regime the model produces pronounced long-range correlations (**Fig. 5.8c,d**; **Fig. 5.12c,d**) and fractures (**Fig. 5.12e,f**) in quantitative agreement with experiment (**Fig. 5.8e**). Moreover, the model predicts that the spatial structure of the correlation peak around the seed point is anisotropic, which is confirmed quantitatively by our data (**Fig. 5.8f**; **Fig. 5.12g,h**). Thus, our dynamical model describes a plausible mechanism for how the early cortex could generate low-dimensional spontaneous activity that is correlated over large distances, even when long-range horizontal connections have only immaturely developed.

5.3.1 Homogeneous Mexican hat network model

In the following, we demonstrate that the homogeneous network model with isotropic Mexican hat connectivity is not sufficient to generate the long-range correlation structure observed in experimental data. We modeled the early spontaneous activity by a two-dimensional firing rate network obeying the following dynamics

$$\tau \frac{\mathrm{d}r(\vec{x},t)}{\mathrm{d}t} = -r(\vec{x},t) + \left[\gamma \sum_{\vec{y}} M(\vec{x},\vec{y}) r(\vec{y},t) + J(\vec{x})\right]_+ \tag{5.35}$$

$$\text{with} \quad [x]_+ = \begin{cases} x & \text{if} \quad x > 0 \\ 0 & \text{else} \end{cases} \tag{5.36}$$

where $r(\vec{x},t)$ is the average firing rate in a local pool of neurons at location $\vec{x} = (x_1, x_2)^T$, τ is the neuronal time constant, $M(\vec{x},\vec{y})$ are the synaptic weights connecting locations $\vec{x}$ and $\vec{y}$, $J(\vec{x})$ is the input to location $\vec{x}$, and γ a factor controlling the overall strength of synaptic weights. The connectivity M was assumed to be short-range and follows a Mexican hat structure

$$\tilde{M}(\vec{x},\vec{y}) = \frac{1}{2\pi\sigma^2} e^{-\frac{(\vec{x}-\vec{y})^2}{2\sigma^2}} - \frac{1}{2\pi(\kappa\sigma)^2} e^{-\frac{(\vec{x}-\vec{y})^2}{2(\kappa\sigma)^2}} \tag{5.37}$$

$$M(\vec{x},\vec{y}) = \frac{\tilde{M}(\vec{x},\vec{y})}{\mathrm{Re}\left(\lambda_{\max}(\tilde{M})\right)}. \tag{5.38}$$

Here σ denotes the SD of the smaller Gaussian. For the larger Gaussian the SD was scaled by a factor $\kappa \geq 1$. M was normalized such that the real part of its maximal eigenvalue is equal to 1. For all simulations we set κ=2, τ=1 and γ=1.02 and used random initial conditions $r(\vec{x}, t = 0)$ drawn from a uniform distribution between -0.1 and 0.1.
In the case of isotropic Mexican hat connectivity the eigenvectors of M are plane waves and the spectrum is peaked at the wavenumber $k = \frac{2\pi}{\Lambda}$, where the spatial period Λ is given by the peak within the spectrum of the Mexican hat which depends on the spatial scales as

$$\Lambda^2 = \frac{4\pi^2\sigma^2(\kappa^2 - 1)}{4\ln(\kappa)}. \tag{5.39}$$

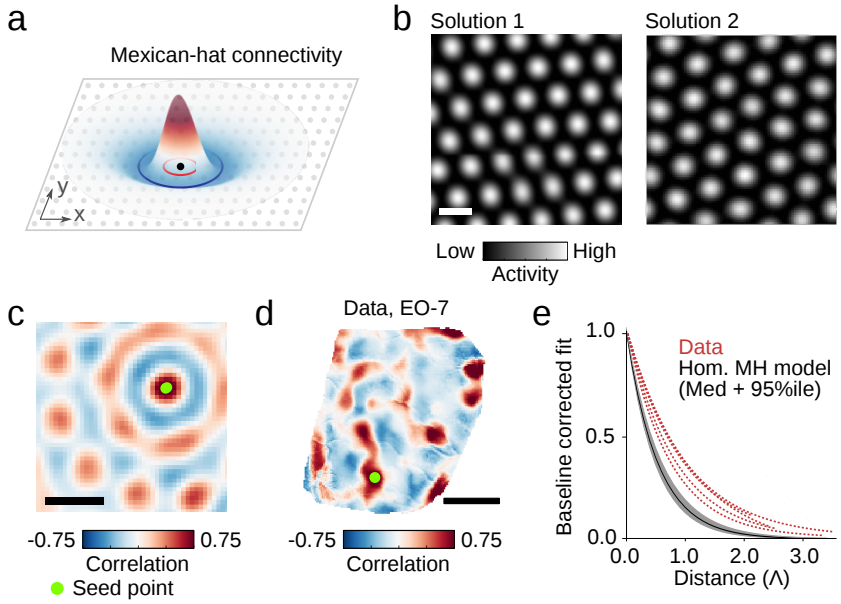

Figure 5.7: Networks with homogeneous and isotropic connections generate modular and regular activity patterns, but do not account for the long-range correlations observed in early visual cortex. **a** The spatial profile of lateral connections follows an isotropic Mexican hat in all neurons. **b** With constant input drive, the activity converges to a regular hexagonal patterns (two representative solutions are shown; simulations performed on a 100x100 grid. **c** Correlations between remote sites are only moderate, owing to the fact that all translated and rotated hexagonal patterns are solutions as well (computed over 100 solutions). **d** Representative example of a correlation pattern observed in ferret visual cortex 7 days prior to eye-opening. **e** For the correlation patterns in the early cortex the peak values decay significantly slower with spatial distance from the seed points (fits, dashed red; N=5) than in the model (104 patterns, $p<0.0097$; black and gray shaded area: mean±95 percentile) and in an ensemble of randomly shifted and rotated ideal hexagonal patterns (100 patterns, $p<0.01$; not shown). To assess significance we used bootstrap tests for all three comparisons see Section 3.9 in Chapter 3. All correlations were baseline corrected, see Section 3.10.1 in Chapter 3. Scale bars: domain spacing 1Λ (**b**,**c**); 1 mm (**d**).

defining the spatial scale Λ used as reference in **Fig. 5.8c-e**. This spatial scale corresponds to the typical spatial scale of activity patterns obtained in the model and, thus, for comparison between model and data we identified 1 Λ with 1 mm, which is roughly the spatial scale of spontaneous patterns observed in experiment.

The input drive J was assumed constant in time for simplicity and modulated in space using a band-pass filtered Gaussian random field G with spatial scale Λ, zero mean and unit SD[231]

$$\tilde{J}(\vec{x}) = 1 + \eta\, G(\vec{x}). \tag{5.40}$$

We varied the input modulation strength η such that the standard deviation of the input matrix J varies systematically between 0 and 0.4.

To model a spontaneous event, we integrated Eq. (5.35) until a near steady state of the dynamics was reached. The results in **Fig. 5.8c-e** were obtained for an integration time of 500τ, but already a much shorter integration over 50τ resulted in similar solutions and nearly the same level of long-range correlations and dimensionality. Different spontaneous events were obtained by using different realizations of input drive J and initial conditions (same connectivity M).

To generate **Fig. 5.7e**, **Fig. 5.8c,d,e**, **Fig. 5.9**, **Fig. 5.12b,d,f,h** and **Fig. 5.13**(*right*) we furthermore averaged over 10 realizations of connectivity M for each parameter setting.
We numerically integrated the dynamics using a 4th order Runge-Kutta method[118] in a square region of size 100 x 100 pixels using periodic boundary conditions. The time step was dt=0.15τ and the spatial resolution 10 pixel per Λ. The simulations were performed on the GPUs GeForce GTX TITAN Black and GeForce GTX TITAN X. The code was implemented in Python (version 2.7) and Theano (version 0.8.1).

5.3.2 Homogeneous network model fails to reproduce the experimentally observed features of spontaneous activity

The homogeneous network leads to the formation of modular activity due to a wavelength instability caused by a Turing bifurcation when the recurrent connectivity is stronger than the exponential decay in the dynamics ($\gamma > 1$)[430]. In such an instability, the spatially homogeneous activity state becomes unstable to the presence of weak, spatially heterogeneous perturbations around a finite spatial frequency. Modular, spatially heterogeneous activity patterns with a finite typical spatial scale Λ can form through dynamical feedback loops mediated by the recurrent connections[130]. The activity bumps of the forming patterns are arranged in a hexagonal lattice structure[130,52].
These hexagonal solutions cannot account for the empirically observed features of the correlation structure of the early spontaneous activity, i.e. long-range correlations (**Fig. 4.6d**), the significant correlation strength above baseline at 2 mm (**Fig. 4.6e**), the dimensionality (**Fig. 5.8a**) and the emergence of fractures (**Fig. 4.6c**). This is due to the translational and rotational invariance of the system which allows a high-dimensional set of continuous solutions. Due to this high variability in the spatial layout between solutions there is only weak covariation between distant locations and therefore their correlation structure decays rapidly as a function of distance from the seed point. The activity patterns generated by the homogeneous network model decay significantly faster than the experimental data (n=104 patterns, p<0.0097; **Fig. 5.7e** and **Fig. 5.9**). In addition, the set of continuous, hexagonal solutions of the homogeneous network results in correlation patterns which are symmetric around the seed point and the same for each seed point, whereas in the experimental data we observed a correlation structure in which the spatial layout of a correlation pattern highly depends on the location of the seed point. The seed-point independent correlation structure leads to weak rates of changes between correlation patterns of neighbouring seed points and therefore fractures do not form (**Fig. 5.9**). Lastly, although the network constrains the dimensionality of the output patterns compared to the dimensionality of the input drive (due to their regular, hexagonal layout), the dimensionality of the network activity patterns is still significantly higher than observed in experiment (**Fig. 5.9**).
As we tested in the previous section activity patterns that were composed of symmetrical hexagonal patterns and noise fields with a typical domain spacing did not reproduce the features of early spontaneous activity patterns. In fact, as shown, the noise patterns further increased the dimensionality of the set of activity patterns, and with this also decreased the spatial scale of the correlation structure. This indicates that the pattern formation mechanism alone cannot account for the widespread and diverse correlation patterns we observe *in vivo*. In addition, the spatial layout of the correlation structure in the experimental data highly depends on the location of the seed point and, thus, cannot be simply expressed by the auto-correlation function of its activity patterns as could be done in the statistical model.

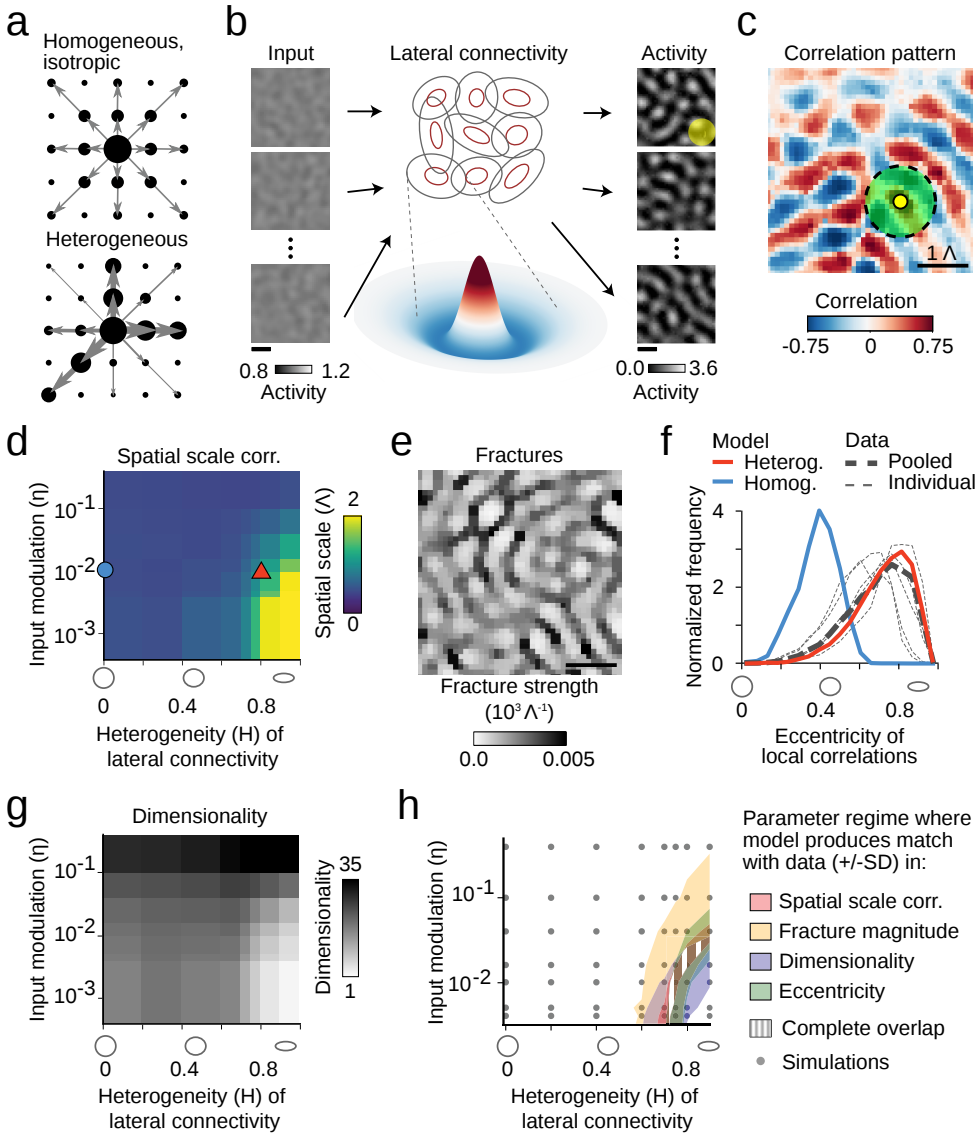

Figure 5.8: (Caption next page.)

5.3.3 Heterogeneity within network model

The observation that different seed points display different correlation patterns suggests that local network interactions might not be homogeneous across cortex. Instead variations in local connections can bias the interactions between neighboring domains, such that some show a stronger tendency to be co-active than others. Such biases can propagate through the network via multi-synaptic connections and induce correlations even between remote locations (**Fig. 5.8a**). Thus, local, but heterogeneous synaptic connections may *channel* the spread of activity across cortex, thereby constraining the overall layout of activity patterns, and explaining the observed pronounced correlations found between remote network domains.

To test the idea that heterogeneous local connections can produce long-range correlations by constraining the dimensionality of the set of network activity patterns, we modeled cortical spontaneous activity using a dynamical rate network[159,44,317,148], in which model units (representing a local pool of neurons) receive recurrent input from neighboring units weighted by an

Figure 5.8: (Previous page.) Circuit mechanism for long-range correlations in early cortex. **a** Homogenous local connections (arrow) induce moderate correlations with all nearby domains (black dots), whereas heterogeneity introduces biases, favouring some correlations (large dots) more than others (small dots). **b** A dynamical circuit model of spontaneous activity in the early cortex: a constant input modulated spatially by filtered noise is fed into a recurrent network with short-range, heterogeneous Mexican hat (MH) connectivity. It produces a set of modular output patterns with typical spatial scale Λ determined by the MH size (average MH size illustrated by the yellow circle). **c** Correlation pattern in model obtained for heterogeneity H=0.8 and input modulation η=0.016 (SD of noise component) shows long-range correlations in agreement with experiment (n=100 output patterns, 16% of modeled region shown). **d** The scale of correlations also increases with decreasing input modulation. Red triangle in (**d**): parameters used in (**c**). Blue circle in (**d**): isotropic, homogeneous connectivity, inconsistent with the range of correlations in experiment (compare **d**, **Fig. 4.6d** and **Fig. 5.7**). **e** Pronounced fracture pattern in the strongly heterogeneous regime (same parameters as in **c**). **f** Match of empirical data to model predictions of local correlation eccentricity (same parameters as in **c**). **g** Dimensionality of $N = 100$ output patterns produced by the model decreases with increasing heterogeneity and decreasing input modulation. **h** In the parameter regime where the spontaneous patterns of the model approach the empirically observed dimensionality, their short- and long-range correlation structure is in quantitative agreement with the experimental data. Shaded regions show parameter regimes in the model in which different properties lie within the range (mean±SD) of the experimental values (using 1Λ=1mm, linear interpolation between simulations). Scale bars: domain spacing 1Λ (**b**,**c**,**e**).

anisotropic Mexican hat function whose longer axis varies randomly across the cortical surface (**Fig. 5.8b**), thus, breaking rotational and translational symmetry and drastically shrinking the solution space of the activity patterns[428,464,353]. For this limited set of patterns the average over ensembles is not exchangable with the average over space, and thus cannot be replaced by it when calculating the correlation structure. This results in a seed point dependent correlation structure as observed in experimental data.

As in the homogeneous and isotropic network, the firing rate units obey the dynamics given in Eq. (5.35). Here the connectivity M was assumed to be short-range and follows an anisotropic Mexican hat structure, modeled as the difference of two elongated Gaussians, whose axis of elongation and scale vary discontinuously across space

$$\tilde{M}(\vec{x},\vec{y}) = \frac{1}{2\pi\sigma_1\sigma_2}\left(\exp\left(-\frac{1}{2}(R(\vec{x}-\vec{y}))^T\Sigma^{-1}R(\vec{x}-\vec{y})\right) - \frac{1}{\kappa^2}\exp\left(-\frac{1}{2\kappa^2}(R(\vec{x}-\vec{y}))^T\Sigma^{-1}R(\vec{x}-\vec{y})\right)\right), \quad (5.41)$$

$$M(\vec{x},\vec{y}) = \frac{\tilde{M}(\vec{x},\vec{y})}{\mathrm{Re}\left(\lambda_{\max}(\tilde{M})\right)} \quad (5.42)$$

with

$$\Sigma = \begin{pmatrix}\sigma_1^2 & 0\\ 0 & \sigma_2^2\end{pmatrix}, \quad (5.43)$$

$$R = \begin{pmatrix}\cos\phi & -\sin\phi\\ \sin\phi & \cos\phi\end{pmatrix}. \quad (5.44)$$

Here σ_1 and σ_2 ($\geq \sigma_1$) denote the SDs of the smaller Gaussian in the direction of its major and minor axis, respectively. For the larger Gaussian both SDs are scaled by a factor $\kappa > 1$. The level sets of both Gaussians are ellipses whose larger (smaller) axis is proportional to σ_1 (σ_2) and whose eccentricity ϵ measures the degree of elongation of the Mexican hat while the angle ϕ determines its orientation. For brevity the dependence of these parameters on cortical space $\vec{x}$ is suppressed in Eq. (5.41). M was normalized such that the real part of its maximal eigenvalue is equal to 1. For all simulations we set κ=2, τ=1 and γ=1.02 and used random initial conditions $r(\vec{x}, t = 0)$ drawn from a uniform distribution between 0 and 0.1.
We introduced the heterogeneity parameter H to parameterize and systematically vary the heterogeneity of the elongated Mexican hats across cortical space $\vec{x}$. The eccentricity ϵ was drawn from a normal distribution with mean $\langle\epsilon\rangle$ and standard deviation σ_ϵ both depending linearly on H ($\langle\epsilon\rangle$=H, σ_ϵ=0.13 H). The size of σ_1 was drawn from a normal distribution with SD $0.1\langle\sigma_1\rangle H$ and mean $\langle\sigma_1\rangle$=1.8. The orientation ϕ of the Mexican hat axis was drawn from a uniform distribution between 0° and 180°. These three parameters were drawn independently at each location.
As above, the input drive J was assumed to be constant in time for simplicity. J is modulated in space using a band-pass filtered Gaussian random field G with spatial scale Λ, zero mean and unit SD[231]

$$\tilde{J}(\vec{x}) = 1 + \eta\, G(\vec{x}). \tag{5.45}$$

We varied the input modulation η between 0.004 and 0.4, the regime over which we observed a smooth transition from an input-dominated system to a system dominated by the recurrent connections. Different spontaneous events were obtained by using different realizations of input drive J and different initial conditions (same connectivity M). All other parameters and the numerical implementation were identical to the homogeneous isotropic model described in the previous section.

5.3.4 Heterogeneous network model captures features of early spontaneous activity

For sufficiently strong connections, the network activity evolved towards a modular pattern with roughly alternating patches of active and non-active domains (**Fig. 5.8b**, *right*). In the regime of a considerable heterogeneous connectivity and moderate input modulation, the model produced pronounced long-range correlations (**Fig. 5.8c**; **Fig. 5.9**; **Fig. 5.12a,b**) and fractures (**Fig. 5.8e**) in quantitative agreement with experimental data (**Fig. 5.12c,d**; **Fig. 5.9**). While the dimensionality of the input patterns to the network is high, the dimensionality of the generated set of activity patterns in the heterogeneous regime was much smaller and approached values close to those observed in experiment (**Fig. 5.9**; **Fig. 5.12e,f**). In a similar regime the model also matched the spatial scale of long-range correlations and the fracture strengths. These results are consistent with the statistical model suggesting that low dimensionality, long-range correlations and pronounced fractures are intimately connected (**Fig. 5.1**). Notably, the dynamical network model predicts that the spatial structure of the correlation peak around the seed point is anisotropic, which was confirmed quantitatively by our data (**Fig. 5.8e**; **Fig. 5.12g,h**; see also Section 4.2.9 in Chapter 4). Thus, our dynamical model describes a plausible mechanism for how the early cortex, even in the absence of long-range horizontal connections, could produce spontaneous activity that is correlated over large distances.

The dynamical network model even reproduced qualitative aspects of the spatial distribution of the anisotropic local neighbourhood of correlations around the seed point but failed to capture the decay of this distribution. In the experimental data, we observed that the eccentricity and orientation of the ellipse which we fitted to the local correlation domain around each seed

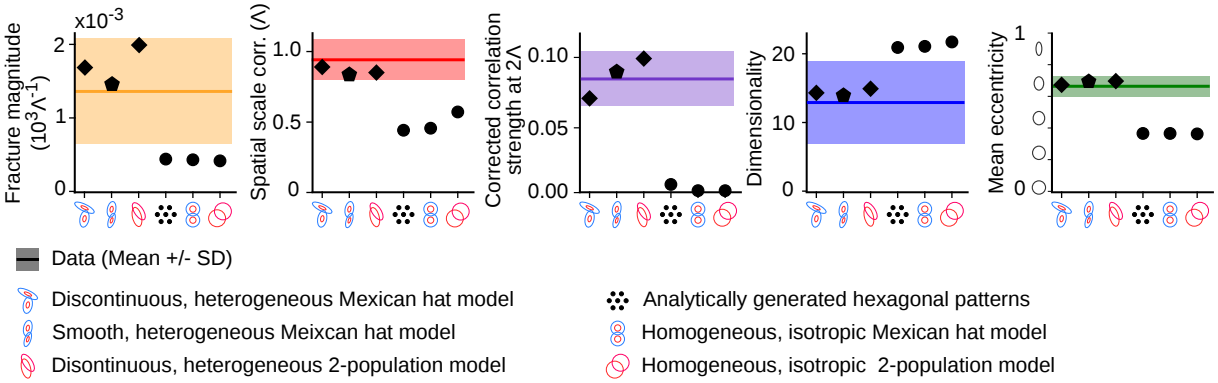

Figure 5.9: Quantitative comparison of statistical and network models with experimental data. Shown are (from *left* to *right*; mean (solid line) ±SD (shaded region) from experimental data of earliest age group): the fracture strength, the spatial scale of correlations, the average at correlation peaks at 2Λ subtracted by the shuffle average correlation, the dimensionality, and the mean eccentricity. The heterogeneous network models (diamond and pentagon) all lie within the experimentally observed range of values for all five quantities, while this is not the case for models with homogenous, isotropic connectivity (circle).

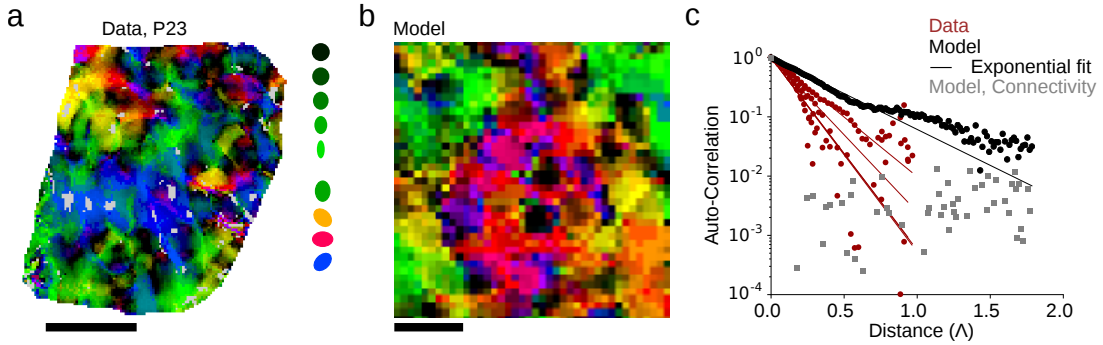

Figure 5.10: Dynamical network model reproduces overall structure qualitatively but fails to capture correlation length of spatial distribution of local anisotropies. **a-b** Distribution of eccentricity (saturation) and orientation (hue) of local correlation neighbourhood around seed point varies across cortical space **a** in the experimental data (P23, seven days prior to eye-opening) and **b** in the model. Gray values indicate that local correlations could not be adequately fitted by ellipse. **c** In both model and experimental data the auto-correlation of the local anisotropies decays exponentially with distance. The correlation length determined by an exponential fit (straight line) to the decay differs between model (black) and experimental data (red). As comparison the decay of the eccentricity of the model connectivity (uncorrelated in space; gray) is shown. Scale bar is 1 mm (**a**) and 1 Λ (**b**).

point varied smoothly across visual cortex (**Fig. 5.10a**). Notably, the spatial distribution of these two properties did not show a typical spatial scale but instead the autocorrelation decayed exponentially. The dynamical network model generated spatially distributed anisotropies that resembled the experimental data (**Fig. 5.10b**) and also showed an exponential decay of the autocorrelation (**Fig. 5.10c**) but with a longer correlation length. Thus, the model describes the spatial distribution of the anisotropy of the local correlations only qualitatively.
The smooth change of the anisotropy of the local correlations is not inherited by the underlying

heterogeneous network connectivity. The heterogeneity of the network connectivity was chosen such that the eccentricity and orientation of the Gaussian connectivity profiles change uncorrelated from unit to unit. Thus, the auto-correlation of the anisotropy of the local connectivity decays non-exponentially and on a significantly faster spatial scale (gray markers in **Fig. 5.10c**) than the anisotropy of the local correlation domain.

5.3.5 Summary

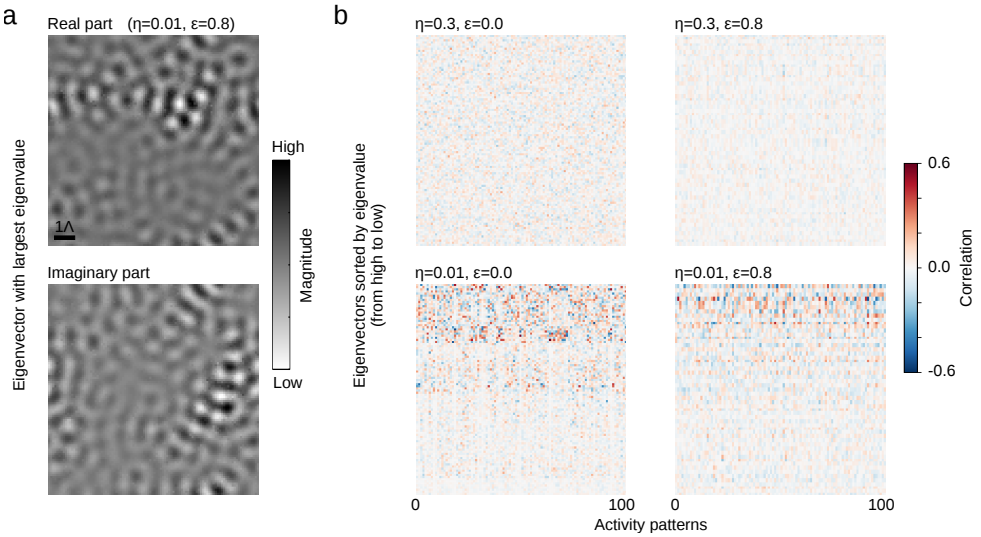

Figure 5.11: Network activity pattern show distributed overlap with system's eigenvectors. **a** Example of spatially localized real (*top*) and imaginary (*bottom*) part of eigenvector with largest eigenvalue for $\eta = 0.01, \epsilon = 0.8$. **b** *Bottom*: 100 activity patterns generated by using different initial conditions are correlated in a distributed manner to the eigenvectors with larger eigenvalues (top of matrix) independent of strength of network heterogeneity. *Top*: In networks that are dominated by feedforward input activity patterns are less strongly correlated with systems' eigenvectors.

All in all, the dynamical model demonstrated that long-range correlations can arise in the early cortex as an emergent property via multi-synaptic short-range interactions that tend to favor certain spatially extended activity patterns at the expense of others. By confining the space of possible large-scale activity patterns, long-range order was established in the form of distributed coactive domains, explaining our observation of long-range spontaneous correlations in the early visual cortex.
The dynamical network model was able to generate activity patterns which quantitatively agree in several key features with the experimental data. In a regime of high heterogeneity and intermediate input modulation the network model quantitatively matched the experimental values of the dimensionality of the spontaneous activity patterns, the spatial scale of their correlations, the fracture strength and the anisotropy of the local correlations.
The dynamical model captured certain aspects of the statistical model. First, in both model types activity patterns are generated that were modular. In the statistical model modularity was obtained by assuming that the spectrum of the Gaussian random fields exhibits a peak at a certain frequency. In the dynamical model activity patterns with a domain spacing formed due to a Turing instability. Note that in the dynamical network model we did not match the spectral width of the activity patterns to the experimental data. Second, in model 1 of the

statistical model we assumed that a limited number of basis patterns underly the formation of spontaneous activity patterns and determine their dimensionality. In the dynamical model these basis patterns are approximately given by the patterns of the eigenvectors of the network interaction matrix (**Fig. 5.11a**). The network activity patterns overlapped strongest with the eigenvectors with the highest eigenvalues and only little with eigenvectors with low eigenvalues (**Fig. 5.11b**). This distributed overlap can be interpreted as that the network activity patterns are approximately superpositions of the eigenvectors with high eigenvalues. However, in contrast to the basis patterns of the statistical model the eigenvectors of the interaction in the dynamical network were localized in space for a moderate strength of heterogeneity (**Fig. 5.11a**). Moreover, the network activity patterns also showed an overlap with the layout of the external input drive. In contrast to model 2 of the statistical model where the active domains of the activity patterns were maximally random distributed, the dynamical network model generated activity patterns whose layout was largely dominated by the maximal eigenvectors and therefore the layout of active domains is constrained to a subspace of all possible patterns.

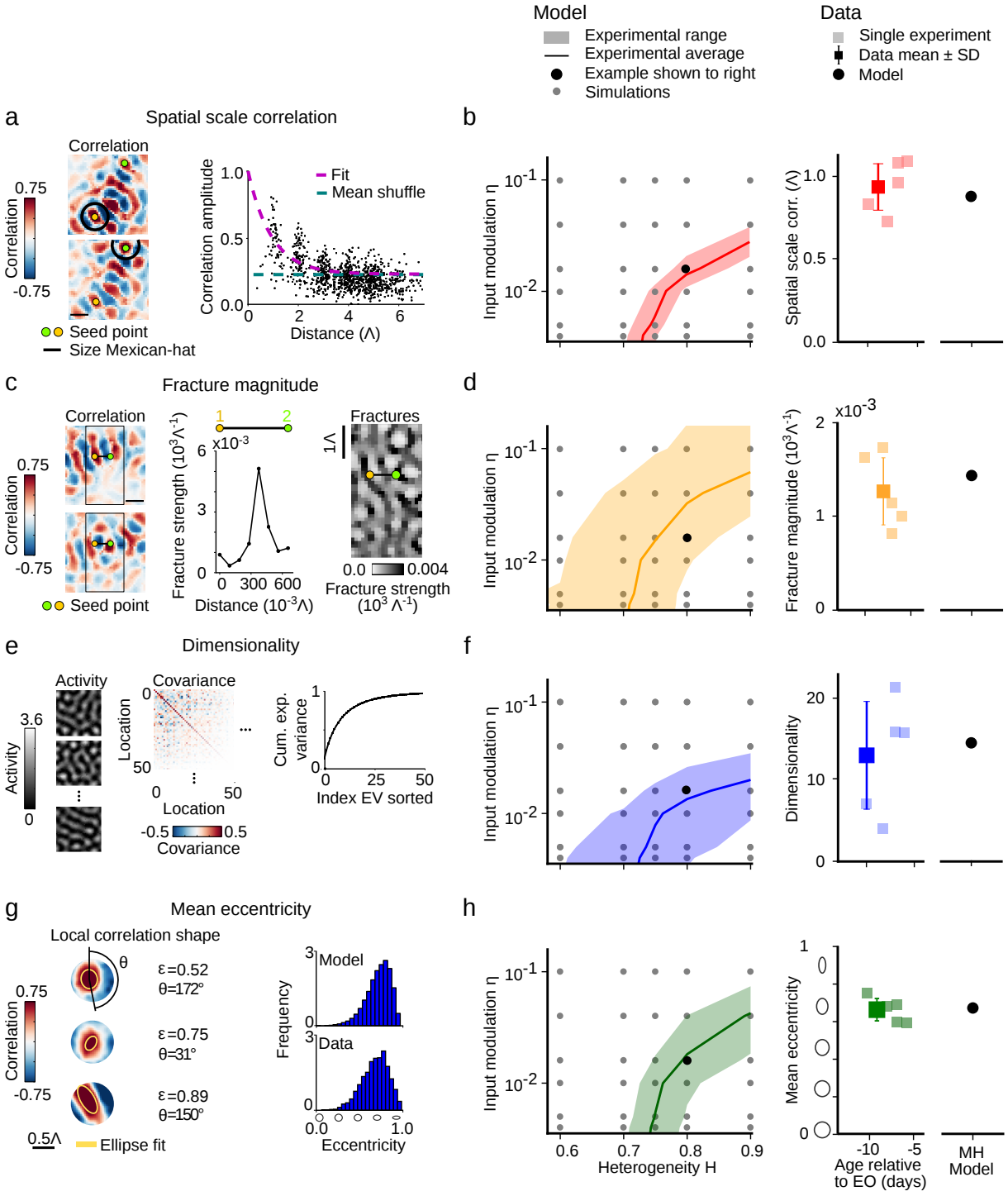

Figure 5.12: (Caption on next page.)

Figure 5.12: (Previous page.) Comparison of early in vivo spontaneous data to dynamical model. **a,c,e,g**: Model analysis; **b,d,f,h**: Comparison model vs. experiment (also compare **Fig. 5.8h**). **a** Long-range organization of correlation patterns (*left*) is quantified by fitting an exponential decay to the peaks (local maxima) in the correlation pattern as a function of their distance to the seed point, using all correlation patterns. **b** *Left*: Shaded region in the diagram with systematically varied heterogeneity and input modulation indicates the parameter settings in which the model values for correlation pattern scale lie within the interval (mean±SD) given by the experimental data (n=4 animals, 5 experiments). The parameter setting of the example shown in **Fig. 5.8c** (marked by red triangle) is highlighted. *Right*: Comparison of dimensionality for indicated model parameters and experimental data. **c** The geometrical layout of correlation patterns (*left*) can change drastically over only a short distance (*middle*). Rate of change reveals organization of fractures (*right*). Region of fractures shown is highlighted by black box in correlation patterns (*left*). **d** Comparison of fracture magnitude with experimental data. **e** Covariance matrix (*middle*) over 100 spontaneous activity events (*left*) shows that different locations co-vary. A moderate number of components (*right*) is needed to explain 75% of the variance indicating low dimensional activity patterns. **f** Comparison of dimensionality for model with experimental data. **g** *Left*: The anisotropic structure of local correlation (i.e. the peak around the seed point) is quantified by fitting an ellipse to the 0.7 contour line (least-square fit) and computing its eccentricity. *Right*: The eccentricity of local correlation shows a similar distribution in data and model. **h** Comparison of eccentricity of local correlation with experimental data.

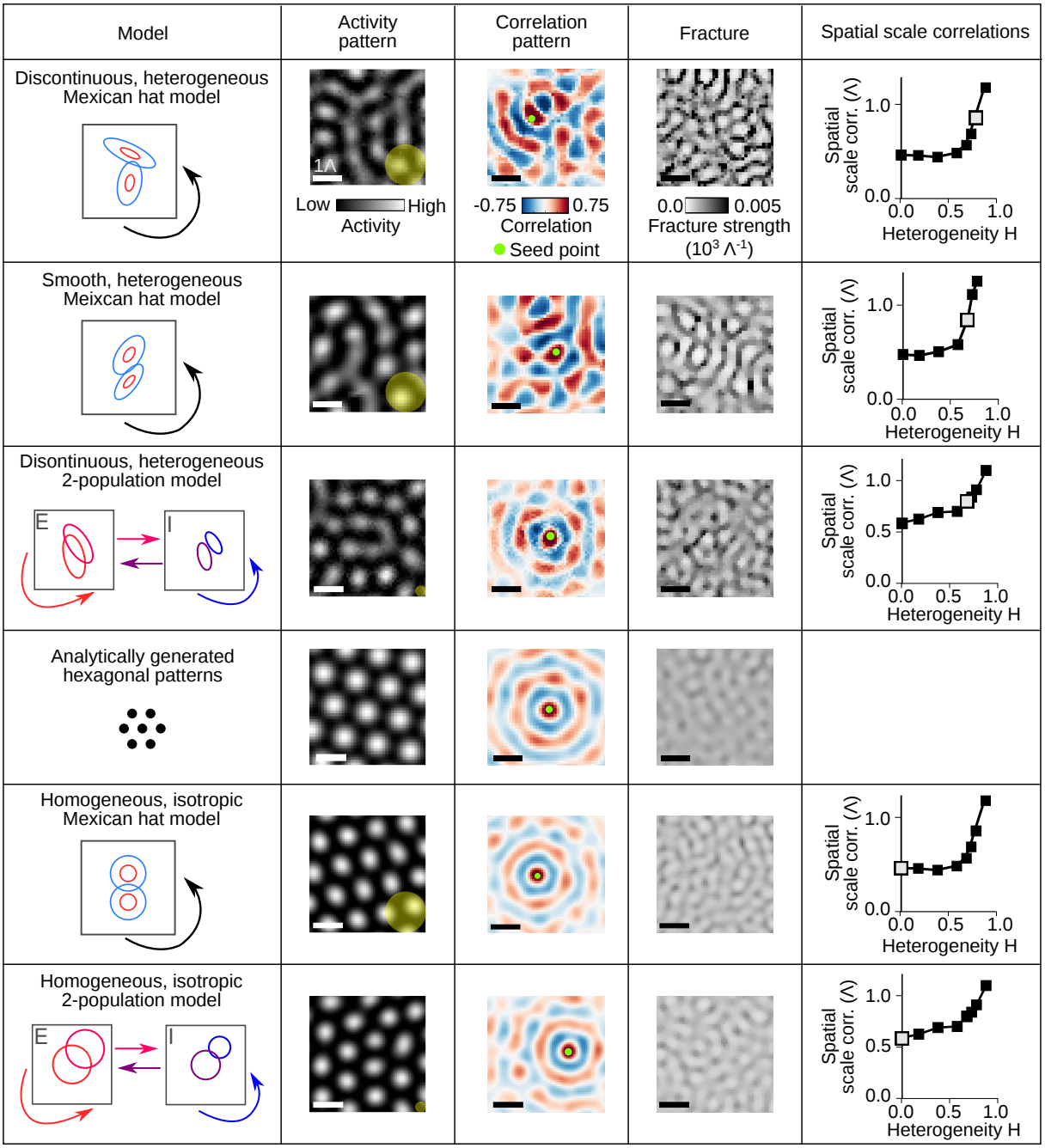

Figure 5.13: Caption on next page.)

Figure 5.13: (Previous page.) Systematic overview over different variants of the two types of circuit models studied, showing the correlation structure they produce. Columns (*left* to *right*): schematic diagram of model, a typical activity pattern, a representative correlation pattern, correlation fractures, and the spatial scale of correlations for the value of heterogeneity of connections, H, used (open symbol) and for varying H (closed symbols). Rows (*top* to *bottom*): (1) The model shown in **Fig. 5.8** (Mexican hat connectivity, H=0.8, η=0.016). (2) As in (1), but here the properties of the Mexican hat vary smoothly across space, on a spatial scale Λ marked by the scale bar on the activity pattern. Results are similar to the discontinuous version (1). (3) The model with two separate populations for inhibitory and excitatory neurons in the discontinuous, heterogeneous regime, analogous to (1) (H=0.7, η=0.01). In the heterogeneous regime, all three models (1-3) agree quantitatively with experiment. (4) Ideal hexagonal patterns, sampled from the distribution known to be the solution set for isotropic, homogeneous Mexican hat connectivity. Rows (5) and (6): Numerical solutions of the isotropic homogeneous versions of models (1) and (3) respectively. For (4)-(6) the correlation structure is inconsistent with experiment. The yellow circle on top of the activity patterns indicates the size of the average local connectivity (MH models only). All scalebars are 1Λ.

5.4 Long-range correlations from short-range connections without Mexican hat profile

In the previous section we showed that lateral connections that are short-range but heterogeneous can produce activity patterns that are correlated over an extended distance in space (**Fig. 5.8c-e**). This mechanism provides a potential explanation for the long-range correlation structure we observed in early ferret visual cortex at a stage in development before long-range anatomical connections form. In our model the lateral connections were assumed such as to support the formation of active domains, reflecting our observation that spontaneous activity in the early visual cortex is always modular. The dynamical mechanism we assumed for generating modular patterns of activity is in a broader context known known as the Turing-mechanism[430,152,296]: modular patterns arise from a spatially homogeneous state by amplifying spatially heterogeneous perturbations through dynamical feedback loops mediated by the recurrent connections[130].
Since the focus of the network model lies on the mechanisms causing active modules to be correlated over larger distances, we chose a generic local circuit motive known to implement the Turing-mechanism, the so-called Mexican hat connectivity (local excitation with lateral inhibition). Although there is evidence for such a motif from studies using glutamate uncaging in slices of ferret visual cortex at developmental stages similar to those we examined[108,80], other studies using paired recordings in slices of adult rat cortex[265], suggested that in fact the spatial range of inhibition is smaller than the range of excitation. This raises two important questions, to be addressed in the following. First, can lateral connections without a Mexican hat profile, i.e. with inhibition that is more short-range than excitation, produce modular patterns of activity? Second, would in this case heterogeneity in the lateral connections induce long-range correlations as it does in the model based on Mexican hat connectivity which is studied in **Fig. 5.8**?
In the following, we first describe a network model based on previous work[226,14] that produces modular activity patterns from local connections that do not exhibit a Mexican hat profile. The model consists of an excitatory and an inhibitory neural population and neurons are linked via local lateral connections (with Gaussian profiles). We consider a regime in which the range of connections formed by excitatory neurons is more than 30% larger than that of inhibitory neurons. We show that this model produces activity patterns very similar to those obtained in the one-population model with Mexican hat connectivity in **Fig. 5.8**.
In a second step, we ask whether this two-population model can produce long-range network correlations despite its only local lateral connections. We find that it can indeed account quantitatively for all aspects of the spontaneous activity correlation structure that we observe in the early visual cortex. It does so when the connectivity is sufficiently heterogeneous across space, i.e. when the connectivity parameters vary considerably across neurons, analogous to the heterogeneity assumed in the one-population model in **Fig. 5.8**. Both models produce very similar results indicating that the effect of heterogeneity is largely independent from the specific form of network interactions generating modular activity.

5.4.1 Modular activity through lateral connections without Mexican hat profile

Here we show in numerical simulations that modular activity emerges within a network model of two populations in the absence of lateral inhibition. Spontaneous activity in the early visual

cortex was modeled by the following rate dynamics:

$$\tau \frac{\mathrm{d}u_E(\vec{x})}{\mathrm{d}t} = -u_E(\vec{x}) + \left[\gamma \sum_{\vec{y}} \left(M_{EE}(\vec{x},\vec{y})u_E(\vec{y}) - M_{EI}(\vec{x},\vec{y})u_I(\vec{y})\right) + J_E(\vec{x})\right]_+, \tag{5.46}$$

$$\tau \frac{\mathrm{d}u_I(\vec{x})}{\mathrm{d}t} = -u_I(\vec{x}) + \left[\gamma \sum_{\vec{y}} \left(M_{IE}(\vec{x},\vec{y})u_E(\vec{y}) - M_{II}(\vec{x},\vec{y})u_I(\vec{y})\right) + J_I(\vec{x})\right]_+, \tag{5.47}$$

$$\text{with} \quad [x]_+ = \begin{cases} x & \text{if} \quad x > 0 \\ 0 & \text{else} \end{cases} \tag{5.48}$$

where $u_E(\vec{x})$ ($u_I(\vec{x})$) is the average firing rate of an excitatory (inhibitory) unit at location $\vec{x}$ in a two-dimensional model of cortex. τ is the neuronal time constant and assumed to be the same for excitation and inhibition. $M(\vec{x},\vec{y})_{KL}$ are the synaptic weights connecting locations $\vec{x}$ and $\vec{y}$ from populations L to K (where $K, L \in \{E, I\}$), $J_K(\vec{x})$ is the input to location $\vec{x}$ in population K and γ is a factor controlling the overall strength of synaptic weights. The sum goes over all locations $\vec{y}$ within the network. The excitatory and inhibitory units are uniformly distributed across the space with equal density.

The connectivity $M(\vec{x},\vec{y})$ consists of the four synaptic weight matrices $M_{KL}(\vec{x},\vec{y})$ that were assumed to be short-range and modeled by isotropic Gaussians:

$$M(\vec{x},\vec{y}) = \frac{\tilde{M}(\vec{x},\vec{y})}{\mathrm{Re}\left(\lambda_{\max}(\tilde{M})\right)} \tag{5.49}$$

$$\tilde{M}(\vec{x},\vec{y}) = \begin{pmatrix} M_{EE}(\vec{x},\vec{y}) & M_{EI}(\vec{x},\vec{y}) \\ M_{IE}(\vec{x},\vec{y}) & M_{II}(\vec{x},\vec{y}) \end{pmatrix}, \tag{5.50}$$

$$M_{KL}(\vec{x},\vec{y}) = \frac{a_{KL}}{2\pi\sigma_{KL}^2} \exp\left(-\frac{|\vec{x}-\vec{y}|^2}{2\sigma_{KL}^2}\right). \tag{5.51}$$

$M(\vec{x},\vec{y})$ was normalized such that the real part of its maximal eigenvalue is equal to 1. σ_{KL} denotes the SD of the Gaussian and a_{KL} denotes the connectivity strength. Note that the connectivity is isotropic and identical for each unit. Thus, the network connectivity is rotation and translation invariant.

For all simulations we set $\tau = 1$, $\gamma = 1.02$ and used random intial conditions $u_E(\vec{x}, t = 0), u_I(\vec{x}, t = 0)$ drawn from a Gaussian distribution of zero mean and SD of 1. The input drive was assumed to be constant in time and space:

$$J_E(\vec{x}) = J_I(\vec{x}) = J = 1. \tag{5.52}$$

We integrated the model dynamics until a near steady-state of the dynamics was reached (simulation time $T = 500\tau$). We obtained different spontaneous events by varying the initial conditions and kept the same realization of the connectivity matrix and the input. To numerically integrate the dynamics we used the fourth-order Runge-Kutta scheme with a time step $dt = 0.15\tau$ in a square region of size 80x80 using periodic boundary conditions. As above, the simulations were performed on GPUs (GeForce GTX TITAN Black and GeForce GTX TITAN X). The code was implemented in Python and Theano.

The activity patterns produced by this model were modular and exhibited a regular, hexagonal structure, similar to the solutions obtained for the simpler model with isotropic Mexican hat connectivity[130,52] studied in **Fig. 5.8** (compare **Fig. 5.14b,e**). The active modules for the

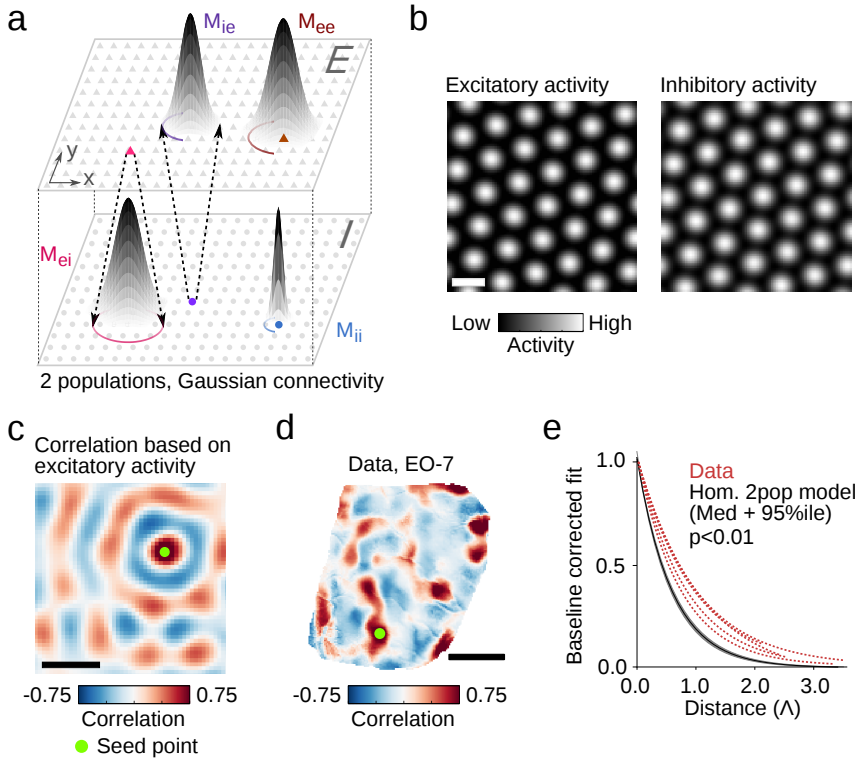

Figure 5.14: A two-population network with homogeneous and isotropic connections generates modular and regular activity patterns, but does not account for the long-range correlations observed in early visual cortex. **a** An excitatory (E) and inhibitory (I) population. Connections within E and from E to I both follow the same isotropic Gaussian profile. Connections from I also follow Gaussian profiles, but have a shorter spatial range. **b** Representative solution of excitatory (*left*) and inhibitory (*right*) population (parameter setting: a_{EE}=22.2, a_{EI}=a_{IE}=21.6, a_{II}=20.8, σ_e=1.9, σ_{EI}= 1.4, σ_{II}=0.6; simulations performed on a 80x80 grid). **c** Correlation pattern for the excitatory population across $N = 100$ activity patterns. **d** Representative example of a correlation pattern observed in ferret visual cortex 7 days prior to eye-opening (same as in **Fig. 5.7d**). **e** For the correlation patterns in the early cortex the peak values decay significantly slower with spatial distance from the seed points (fits, dashed red; N=5) than in the model (109 patterns, p<0.009; black and gray shaded area: mean±95 percentile) and in an ensemble of randomly shifted and rotated ideal hexagonal patterns (100 patterns, p<0.01; not shown). To assess significance we used bootstrap tests for all three comparisons see Section 3.10.1 in Chapter 3. All correlations were baseline corrected, see Section 3.10.1 in Chapter 3. Scale bars: domain spacing 1Λ (**b**,**c**); 1 mm (**d**).

excitatory population showed a similar orientation and phase as those of the inhibitory population (**Fig. 5.14e**). Different solutions (obtained using different initial conditions) consisted of translated and rotated versions of the same hexagonal pattern, reflecting the symmetries of the connectivity structure. The formation of hexagonal patterns is typical for two-dimensional systems with Turing instability characterized by translation and rotation symmetry and a broken z-symmetry (here the activity u)[104]. In our numerical simulations, hexagonal activity patterns occurred for a broad range of connectivity parameters. In particular, we could also obtain this type of solutions when setting σ_{II} to similar value as σ_{EI}, such that the range of connectivity from inhibition to excitation is similar to that from inhibition to inhibition, and setting the strengths a_{II} and a_{EI} such that the inhibition to excitation is comparable or slightly stronger

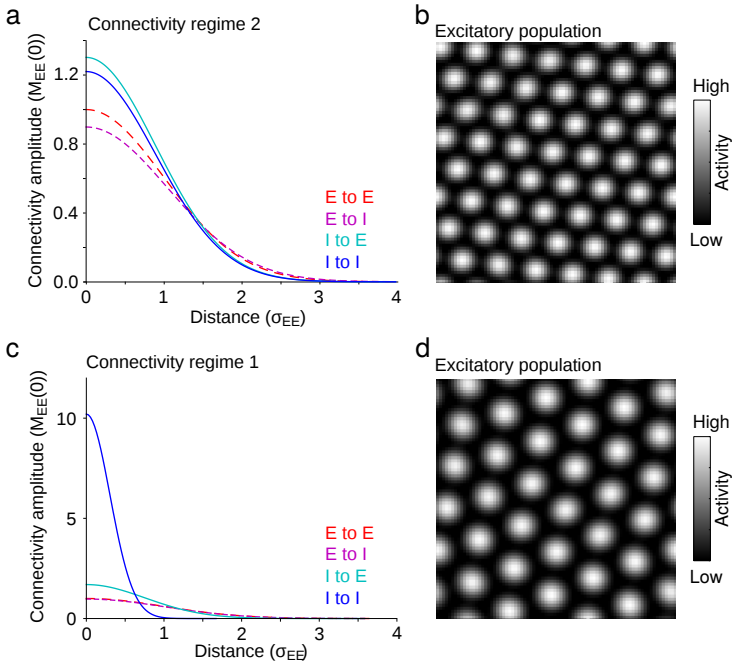

Figure 5.15: Modular activity in a regime where inhibition (I) to excitation (E) has a similar spatial range as inhibition to inhibition and slightly stronger magnitude. **a** The assumed radial dependence of connectivity profiles M_{KL}, with K, L in $\{E, I\}$, to study this regime (referred to as connectivity regime 2): a_{EE}=21.4, a_{IE}=21.05, a_{EI}=22.2, a_{II}=20.8, σ_{EE}=2.0, σ_{IE}=2.2, σ_{EI}=1.8, σ_{II}=1.8. **b** A representative steady state solution. **c,d** For comparison, the regime previously used in **Fig. 5.14**, referred to as connectivity regime 1 (a_{EE}=22.2, a_{IE}=21.6, a_{EI}=21.6, a_{II}=20.8, σ_{EE} =1.9, σ_{IE}=1.9, σ_{EI}=1.4, σ_{II} =0.6): The connectivity profiles (**c**) and a representative solution (**d**). Note that the solutions obtained for these two connectivity regimes are qualitatively very similar. Note further that for both regimes the spatial range of excitation is broader compared to inhibition, while the total sum of connectivity strength (integrated over space) is similar for all four connectivities.

than inhibition to inhibition[393,345] (**Fig. 5.15**). Thus, we conclude that lateral connections can produce modular patterns of activity, even if inhibition extends over a shorter range than excitation. In Chapter 6 we will consider in detail the mechanism underlying the formation of spatially modulated activity in the absence of lateral inhibition.

5.4.2 Heterogeneity in the connections induces long-range correlations consistent with the experimental data

Importantly, the correlation structure for an ensemble of solutions of the model described above decays on a significantly shorter range, when compared to size-matched sets of activity patterns measured in the early visual cortex (**Fig. 5.14h**). The reason for this is that the ensemble of patterns this model produces reflects the symmetries of the underlying dynamics and thus consists of all translated and rotated versions of a hexagonal pattern. The same applies to the one-population model with Mexican hat connectivity (**Fig. 5.7a** and previous section) and also to an ideal hexagonal ensemble, synthesized by applying (uniformly distributed) random translations and rotations to a hexagonal solution of the model. Thus, while both models can account for the fact that spontaneous activity is modular, their correlation structure is

inconsistent with the experimental data (**Fig. 5.9**, **Fig. 5.14d**). Therefore, we next asked whether introducing heterogeneity in the two-population model above (Eqs. (5.46) and (5.47)) induces correlations that are long-range, as in the case of the one-population Mexican hat model in **Fig. 5.8**. As before, we introduced heterogeneity by making the Gaussian connectivity matrices M_{KL} anisotropic by varying the strength of elongation, the orientation and the size of its axis across space (discontinuously, as in the one-population Mexican hat model):

$$M(\vec{x},\vec{y}) = \begin{pmatrix} M_{EE}(\vec{x},\vec{y}) & M_{EI}(\vec{x},\vec{y}) \\ M_{IE}(\vec{x},\vec{y}) & M_{II}(\vec{x},\vec{y}) \end{pmatrix}, \tag{5.53}$$

$$M_{KL}(\vec{x},\vec{y}) = \frac{a_{KL}}{2\pi\sigma^1_{KL}\sigma^2_{KL}} \exp\left(-\frac{1}{2}(R(\vec{x}-\vec{y}))^T\Sigma^{-1}_{KL}R(\vec{x}-\vec{y})\right), \tag{5.54}$$

$$\text{with} \quad \Sigma_{KL} = \begin{pmatrix} (\sigma^1_{KL})^2 & 0 \\ 0 & (\sigma^2_{KL})^2 \end{pmatrix}, \tag{5.55}$$

$$R = \begin{pmatrix} \cos(\phi) & -\sin(\phi) \\ \sin(\phi) & \cos(\phi) \end{pmatrix}, \quad K,L \in \{E,I\}. \tag{5.56}$$

Here, $M_{KL}(\vec{x},\vec{y})$ is the connectivity from location $\vec{y}$ in population n to location $\vec{x}$ in population m. The quantities σ^1_{KL} and σ^2_{KL} denote the SD of the Gaussian in the direction of its major and minor axis, respectively. The angle ϕ determines the orientation of the elongated Gaussian. The dependence of these parameters on cortical space $\vec{x}$ is suppressed for clarity. a_{KL} denotes the connectivity strength.

To systematically study the effect of heterogeneity, we defined a heterogeneity parameter H and used the eccentricity ϵ as the measure of the degree of elongation of the Gaussians, as above (see Eq. (4.6) in Section 4.2.9 in Chapter 4). To construct the network connectivity, at each location $\vec{x}$ the eccentricity was drawn from a normal distribution with mean $\langle\epsilon\rangle$ and standard deviation $\langle\sigma_\epsilon\rangle$ both depending linearly on H ($\langle\epsilon\rangle = H$, $\langle\sigma_\epsilon\rangle = 0.025H$). The σ^1_{KL} were drawn from normal distributions with average values $\sigma_{EE} = \sigma_{IE} = 1.9$, $\sigma_{EI} = 1.4$, $\sigma_{II} = 0.6$ respectively, and identical SD equal to $0.003H$. The orientation ϕ of the Gaussian was drawn from a uniform distribution between 0° and 180°. All parameters were drawn independently at each location $\vec{x}$ and were, apart from the offsets σ^1_{KL}, identical for all four Gaussians $M_{KL}(\vec{x},\vec{y})$. Finally, each synthesized matrix M was normalized such that the real part of its principle eigenvalue was equal to 1.

To model a spontaneous event we applied to the excitatory and the inhibitory population the input drive

$$J_K(\vec{x}) = 1 + \eta\, G_K(\vec{x}), \quad K \in \{E,I\} \tag{5.57}$$

which was constant in time and randomly modulated across space. G is Gaussian white noise field band-pass filtered around the domain spacing Λ which is the dominant scale of activity patterns for the homogeneous isotropic case ($H = 0$). The realization of the Gaussian noise G_K was different for the excitatory and inhibitory population. Different spontaneous events were obtained by using different realizations of input drive J_K and different initial conditions (same connectivity M). We systematically varied the input modulation strength η between 0.0004 and 0.4. All other parameters and the numerical implementation were identical to the homogeneous isotropic model described in the previous section.

We observed that introducing heterogeneity into this network yields results very similar to those shown in **Fig. 5.8** for the Mexican hat model. For high values of heterogeneity H and intermediate input modulation η the heterogeneous two-population model accounted quantitatively

for all aspects of the correlation structure that we observed in the early visual cortex (**Fig. 5.9**; **Fig. 5.13**). We thus conclude that lateral connections that are short-range but heterogeneous can produce modular patterns of activity that are correlated over an extended distance in space. The effect of heterogeneity is to induce long-range network correlations and this mechanisms appears independent from the specific form of network interactions that produce modular activity.

5.5 Influence of long-range lateral connections on the spatial scale of correlations

In the previous sections we presented and implemented a mechanism in a dynamical network model to generate long-range correlations in the absence of long-range anatomical connections as observed in our experimental data. In addition to the presence of long-range correlations already during the early development, we further observed that their spatial scale remained fairly constant during development, although the growth and maturation of the excitatory long-range lateral anatomical connections over the observed course of cortical development leads one to expect that the spatial scale of correlations might increase. Here, we study the influence of long-range connections on the spatial scale of correlations and incorporate them into the dynamical Mexican hat model.

To generate a connectivity matrix with long-range connections, we first simulated a network with only short-range connections. We then build a second network with long-range connections assuming that these long-range connections are proportional to the correlation structure of the original network with only local connectivity (**Fig. 5.16a,b**). We introduced lateral connections only between locations which showed a larger absolute correlation than the baseline level (see Section 3.8 in Chapter 3). To generate clustered long-range lateral connections as observed experimentally[48], we applied dilation and erosion on the thresholded correlation structure to remove noisy and localized correlations above threshold. We then applied a Gaussian filter (with standard deviation of $\Lambda/2$) to further smoothen the regions above threshold. The strength of the connections scaled linearly with the correlation coefficients such that positive correlations between two locations lead to excitatory connections between those locations, whereas negative correlations lead to inhibitory connections. Although, it has been observed that especially excitatory neurons exhibit long-range connections[48], there is also experimental evidence in carnivore visual cortex (unlike to rodent V1[211,265]) demonstrating that also inhibitory neurons can form long-range, intercolumnar connections[291,359,444].

When taking into account long-range lateral connections, we found an increase in the spatial scale of the correlation structure for fixed heterogeneity H and fixed input modulation η (**Fig. 5.16c**). If in addition the input modulation was increased (**Fig. 5.16d,e**), the spatial scale of the resulting correlations remained similar to the spatial scale observed in models with only local connections, and matched the spatial scale observed *in vivo* (**Fig. 5.16f**). An increase in input modulation would be consistent with the strengthening of feed-forward connections into the cortex during development and might explain the consistency of the spatial scale of the correlations throughout development. However, there are other fundamental changes in the circuit organization at this early stage in development, e.g. changes in inhibitory inputs, feedback inputs, modulatory inputs and intrinsic properties of the neurons that could also influence the spatial scale of the correlations.

All in all, these results demonstrate that the spatial scale of the spontaneous correlations does not necessarily need to increase with growing lateral connections. Rather our experimental observations are in line with the behaviour of our network model assuming that together with the maturation of lateral connectivity the input modulation is increasing. The Mexican hat model

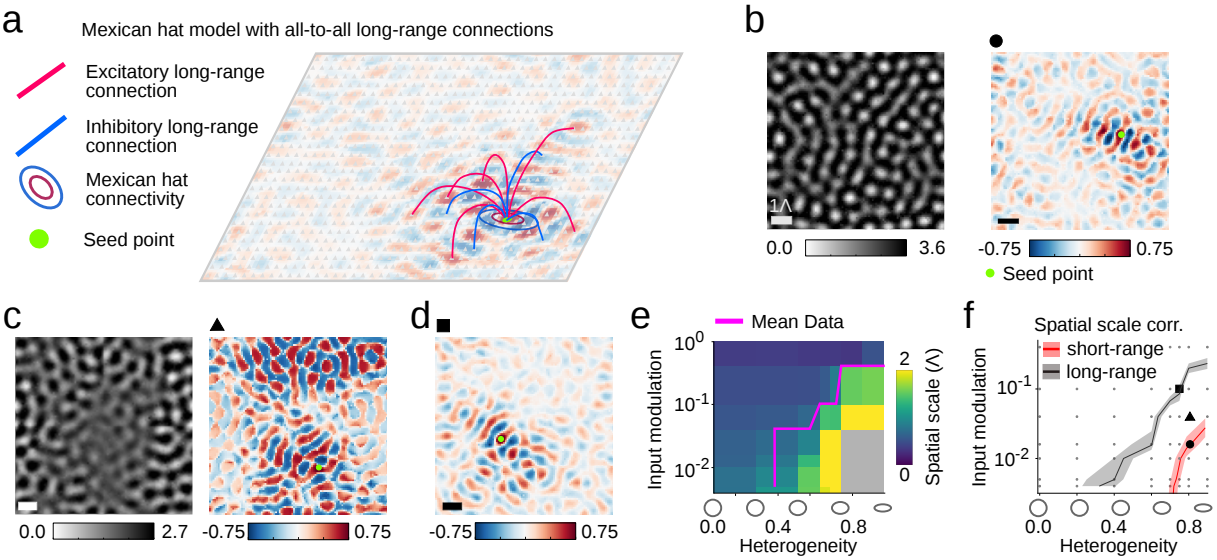

Figure 5.16: Extending the one-population model in **Fig. 5.8** to include anatomical long-range connections can produce a correlation range consistent with experiment, if the input modulation is sufficiently large. **a** Schematic of model: long-range connections are assumed to be proportional to the correlation structure of the model with local connectivity. **b** Activity and correlation pattern in the model with only local connectivity (heterogeneity $H = 0.8$, input modulation $\eta = 0.016$). **c** Activity and correlation pattern in the same model, but with long-range connections ($H = 0.8$, $\eta = 0.03$). Note that the range of correlations has increased considerably. **d** The same, after increasing the input modulation ($H = 0.75$, $\eta = 0.1$). The range of correlations is now similar to (**b**) and to the value we observe in ferret visual cortex after eye opening. **e** Similarly to the model in **Fig. 5.8**, the spatial scale in the network with non-local connections increases with heterogeneity H and decreases with input modulation η. The grey-colored area indicates the regime where all 100 simulated activity patterns (patterns similar in their layout to example in (**c**), *left*) were nearly identical (dimensionality equal to zero). **f** The regime in which the model with non-local connections matches the data lies at higher input modulation compared to the network model with only local connections. Black markers indicate the parameter settings used in **b-d**. Scale bar is 1Λ.

gives thus a simple explanation of the experimental results *in vivo* .

5.6 Network models are consistent with properties of activity after silencing LGN

After inactivating LGN spontaneous activity was still prominently present in visual cortex and showed a similar spatial correlation structure with a similar spatial scale as the spontaneous activity prior of inactivation (see Chapter 4). Our observation that spontaneous activity in the visual cortex is not completely abolished after silencing LGN suggests that spontaneous activity is in parts also elicited by input sources that do not involve afferents from LGN, such as other cortical areas, the non-specific thalamus, or the cholinergic system. Consistent with this hypothesis, we observed that individual spontaneous events are diverse, not only in terms of intensity and spatial extent (as described in Chapter 3 and Chapter 4), but also in terms of the velocity with which the activity expands across the imaging field of view at the onset of an event (Chapter 4). Importantly, the fact that the structure of spontaneous correlations remains

largely intact after silencing LGN suggests that this structure is primarily determined by the networks in visual cortex rather than by external input drive, as it is unlikely that these inputs from different sources (including those from LGN) impose a similar correlation structure onto the cortex.
Here, we study LGN inactivation in the framework of the dynamical Mexican hat model. In our model, the effect of silencing LGN does not simply correspond to setting $J(x) = 0$ (i.e. zero input) as there might be potential other input sources to visual cortex. However, assuming that the LGN is involved in a considerable fraction of inputs to visual cortex driving spontaneous events, it seems plausible to expect that silencing LGN reduces the external input drive $J(x)$ during an event (i.e. $0 < J_{\text{silence}}(x) < J(x)$). In the model reducing the input drive $J(x)$ by a simple scaling factor reduces the strength of the evoked activity patterns by a proportional amount, but keeps the correlation structure unchanged, in line with the empirical observations (compare **Fig. 4.17g**). This is because the neurons in the model operate at the threshold of excitability, i.e. in the rectifier nonlinearity in Eq. (5.35) the threshold is set equal to zero. Choosing a slightly different threshold than zero would only mildly change the structure of correlations in our model. More strongly the range of correlations depends on the strength of the spatial modulation η of the input, relative to its spatial average. However, currently, it is unclear whether this relative input modulation is different for the different input drives prior to and after LGN inactivation. The results from our silencing experiments, showing that correlation range is largely unaffected by eliminating the inputs from LGN, may suggest different inputs to exhibit comparable degrees of spatial modulation. Testing this hypothesis would require measuring the spatial distribution of activity in axons with identified origin, which is beyond the scope of this work. In summary, our finding that the spatial range of spontaneous correlations remains large after silencing LGN is captured by the network model.

5.7 Discussion

In this chapter we shed light on the conundrum presented by our analysis of the early spontaneous activity: long-range correlated activity in the early cortex is generated through intracortical circuits in the absence of long-range horizontal connectivity. Within a minimal statistical model (variant 1) we first revealed a close relationship between the dimensionality of an ensemble of activity patterns and its average values of peak correlations at large distances which indicated that constraining the space of activity patterns might lead to long-range correlations. Setting the dimensionality as a parameter of the model further showed that the correlation magnitude at some distance to the seed point, the fracture strength and the eccentricity of the local correlations all decreased with increasing dimensionality. These results generalize as shown in a second variant of the statistical model where we intrinsically increased the dimensionality of an ensemble of Gaussian random fields by increasing the spectral width which lead to a decrease in the spatial scale of correlations. Our dynamical model used these results and suggests a powerful solution by showing that long-range correlations can arise as an emergent property in heterogeneous circuits via multi-synaptic short-range interactions that tend to favor certain spatially extended activity patterns at the expense of others. By confining the space of possible large-scale activity patterns to a low-dimensional subspace, long-range order is established in the form of distributed coactive domains, explaining our observation of long-range spontaneous correlations in the early visual cortex. Furthermore the activity patterns generated by the dynamical network model quantitatively matched the experimentallly observed values in fracture strength, dimensionality and anisotropy of the local correlations. These results also suggest that the high degree of local precision that is evident in mature distributed network interactions could derive from the origin of network structure in early local interactions that seed the subsequent

emergence of clustered long-range horizontal connections via Hebbian plasticity mechanisms.
The dynamical network model required two distinct mechanisms to generate activity patterns that match the experimental data. First, the Turing mechanism for pattern formation yields modular activity patterns of a typical spatial scale as observed in experimental data. Second, considering the results from the statistical model demonstrating a close relationship between dimensionality and scale of correlations, we introduced heterogeneity into the network based on previous work that showed that network heterogeneity breaks the network's line attractor[428,464,353]. Increasing heterogeneity led to a decrease in the dimensionality of the network activity which in turn led to an increase in the spatial scale of the correlations. Importantly, the network heterogeneity was essential for the emergence of long-range correlation structure as a homogeneous network failed to generate long-range correlations. Intriguingly, when fitting the spatial scale of correlations the heterogeneous network matched quantitatively the experimental data in its dimensionality, its strength of spontaneous fractures and its eccentricity of local correlations over a broad range of parameters.
Networks with the distance dependent homogeneous Mexican hat (lateral inhibition and local excitation) connectivity have a long history in modeling. They are typically used to describe the emergence of functional maps[411,134,287,302,226,163,21] as well as modular activity[148]. Here, we used the Mexican hat as a simple connectivity to generate activity patterns that exhibit a spatial modulation around a certain spatial frequency as it was observed in the experimental data. However, the assumption of the Mexican hat connectivity which has yet to be experimentally demonstrated was not critical for the emergence of long-range correlations. We showed in a network with two populations that even if the interaction range of the inhibitory population is spatially more confined than the excitatory interaction range, modular activity forms which is consistent with recordings in mature cortical slices[265]. Moreover, a heterogeneous connectivity scheme in this model that varies from unit to unit led to long-range correlations in the network activity. Thus, similar to the Mexican hat model the two population model quantitatively matched the experimental observations.
Previous work examined how heterogeneity shapes properties of the network dynamics and showed that various kinds of heterogeneity ranging from the variability in neuronal parameters to the unreliability of synapses can enhance speed, responsiveness and robustness of networks[260]. Other work demonstrated that the information capacity of a heterogeneous network is not limited by noise correlations but scales linearly with the system size[378]. Recent work suggested to distinguish between network heterogeneity (induced by coupling, e.g. differences in synaptic coupling) and intrinsic heterogeneity (variability in cellular properties that exist without coupling to other neurons, e.g. variability in spiking threshold)[288,283]. The relationship between these two types of heterogeneity influenced the firing rate distribution in a network model[283]. Although heterogeneity locks the system into only a low number of states, homeostatic mechanisms can compensate for this heterogeneity by scaling the synaptic weights such that heterogeneity in cellular excitability and synaptic inputs are balanced out[251]. Here, we used that network heterogeneity breaks the symmetry of the system and thus constrains the spatial layout of network activity. Increasing the heterogeneity leads to an increased confinement of the activity to a low-dimensional manifold. For an intermediate level of heterogeneity the dimensionality of an ensemble of activity patterns is such that their long-range correlations quantitatively match the experimental data.
Our observation that spontaneous activity in the visual cortex is not completely abolished after silencing LGN suggests that spontaneous activity is in parts also elicited by other sources than LGN. In the network model the effect of silencing LGN would therefore not correspond to setting the input drive to zero. Assuming that the LGN is involved in a considerable fraction of inputs to visual cortex driving spontaneous events, it seems plausible to expect that silencing LGN has two effects: (1) a reduction of the frequency of spontaneous events and (2) a reduc-

tion of external input drive during an event. The network model was not intended to address the frequency of spontaneous events (effect 1), but to address the specific question of whether long-range correlations can arise in a cortex comprising only local horizontal connections. An extension of the model in which for example the strength of the input drive is not constant across a simulation but distributed such that only in a certain fraction of events a spatial pattern is forming could capture a reduction of the frequency of spontaneous events.
Similarly, the dynamical network model used here does not describe the temporal dynamics within a spontaneous event nor how a spontaneous event is initialized from a low activity state. Instead the network model was constructed to explain the emergence of long-range correlations in the absence of long-range connections based on the assessment of the spatial layout of activity patterns. An extension of the network model would be required to additionally describe (1) the dynamical switching from one event to another, and (2) the temporal dynamics within one event.
We assessed the influence of long-range connections (of the order of several wavelengths) on the formation of long-range correlations and showed that adding long-range connectivity does not necessarily increase the correlation strength between two distant locations. We demonstrated that multiple parameter regimes exist where the correlation strength remains constant. In particular, an additional increase in the input modulation together with a growing range in lateral connectivity left the spatial scale of correlations unchanged. However, there are a number of fundamental changes in circuit organization that occur during the developmental stage we are considering, e.g. changes in feedforward inputs, inhibitory inputs, feedback inputs, modulatory inputs, and intrinsic properties of the neurons that could influence the spatial scale of correlations. Thus, although our dynamical model gives a simple interpretation of the experimental observation, further changes in the cortical circuit might contribute to the stability of the spatial scale of the correlations across age.
We assumed here an attractor-type network model. Previous work argued that the timescale of attractor network models might be too slow to describe the seemingly fast dynamics of spontaneous activity[235,317]. Instead networks based on balanced amplification with a faster timescale were proposed to model spontaneous activity[317]. However, here we focused on the confinement of the spatial layout of the activity patterns and did not aim to describe the temporal dynamics of spontaneous activity. To this end, an attractor-type network might be a sufficiently good approximation to describe spontaneous activity patterns.
Previous work showed that networks describing spiking activity formed spatially modulated activity patterns assuming long-ranging inhibition[363,188]. Here we used a network model of firing rate units for (1) its simplicity and theoretical tractability, and (2) because we aimed to compare the results of the rate model to imaging data whose signal is roughly proportional to the firing rate of a population of neurons. It might still be instructive to study the influence of network heterogeneity in a spiking network (e.g. as done in[251] for dynamical balance of excitation and inhibition) on the dimensionality of spiking activity and the spatial scale of its correlations.
Overall, we demonstrated that low dimensionality in the spontaneous activity could serve as an organizing principle and be sufficient to explain the observed features of spontaneous activity. Moreover, our results suggest that the formation of spatially modulated network activity does not necessarily require fast inhibition or the interaction range of inhibition to be larger than the one of excitation. In Chapter 6 we will systematically study under which conditions a network with a biologically plausible connectivity can lead to the formation of modular cortical activity.

Chapter 6

Modelling modular cortical activity

Cortical activity patterns in primates and carnivores typically comprise domains of coactive neurons with an approximately regular spacing on the order of 1 mm. Such modular organization is seen in spontaneous activity early in the developing cortex and persists even after deactivation of LGN suggesting a cortical origin[389]. In fact, several classical models have shown that modular activity patterns can emerge from an intracortical mechanism involving lateral inhibition. However, these network models could not be experimentally tested, so far. Moreover, their mechanism is either based on short-range excitation and longer-ranging inhibition (Mexican hat connectivity)[129] or relies on fast inhibition[346,226] both of which appears to be in conflict with current experimental evidence. Here we show by using linear stability analysis that spatially localized self-inhibition relaxes the constraints on the connectivity structure in a network model, such that biologically more plausible network motives with shorter ranging inhibition than excitation robustly generate modular activity. Importantly, we also provide several predictions from our model to make the class of network models experimentally testable using recent technological advancements in imaging and manipulation of cortical circuits. A critical prediction of our model is the decrease in spacing of active domains when the total amount of inhibition increases. Indeed, consistent with an increase of inhibition in the developing visual cortex[440], we observe that the spacing of spontaneously active domains decreases with age in early ferret visual cortex. Together, these results provide an experimentally testable mechanism of how cortical circuits with short-range inhibition can form modular activity.

6.1 Introduction

Understanding how patterns of neural activity arise from neural circuits is a key problem of current computational and systems neuroscience. A fundamental characteristic of the cortex of primates and carnivores is that activity patterns are modular (columnar): individual neurons tend to be co-active in spatially localized domains and these active domains form orderly patterns across the cortical surface with a typical spacing between adjacent domains of roughly 1 mm. This mode of organization of cortical activity has been revealed in classical studies of the functional architecture of visual cortex[193,43,436,213]. Moreover, it has been found that spontaneous activity in visual cortex is spatially modulated to a degree similar to visually evoked activity[429,344,235,146,310,327,389], and consistently so already at early stages in development[389]. Despite its robust appearance fundamental to the functional organization of cortex, the mechanism by which brain circuits produce modular cortical activity remains elusive.

Intriguingly, the modular organization of spontaneous cortical activity remains intact after silencing spontaneous activity in the retina, and even after inactivation of LGN[389], demonstrating

that this fundamental property is not imposed to the cortex by feed-forward circuits. Alternatively, its origin could lie within the cortex itself. In fact, several dynamical network models[287,130,412,28,129,71,44] (see also Chapter 2) describe the formation of modular activity patterns using an intracortical mechanism based on local facilitation and lateral suppression enabling the network to robustly produce spatially modulated activity, and in a broader context is known as the Turing mechanism[430,152,296]. A straightforward way to implement this mechanism is through a specific from of recurrent circuitry consisting of local excitation and lateral inhibition (sometimes called a 'Mexican hat' connectivity profile)[287,412,28,71,44]. Local excitation amplifies locally elevated activity fluctuations whereas lateral inhibition suppresses activity nearby, such that adjacent active domains can arise at a distance roughly twice the extent of lateral inhibition. However, while there is some experimental support for this type of organization in early ferret visual cortex[108,80], several other lines of evidence indicate that the lateral extent of inhibitory connections tends to be shorter than excitatory connections[280,281,279,278,265]. This issue could potentially be resolved by disynaptic inhibition, involving an excitatory-to-inhibitory connection followed by an inhibitory synapse to excitatory neurons. This alternative requires fast inhibition[346,14,226,21], which again appears problematic, as the timescale of synaptic transmission of inhibitory neurons is typically slower than that of excitatory neurons[335,136,90,219,47].

Here we show that weak local self-inhibition can circumvent these problems, resulting in the robust formation of modular activity, yet within a circuitry that does not suffer from the above limitations and that appears consistent with current experimental evidence. Such local self-inhibition could, for instance, be mediated by inhibitory autapses[431], which are formed massively by fast-spiking PV+ inhibitory interneurons in visual cortex[418] and in barrel cortex[24]. Based on the classical theoretical framework of rate units[447,446], we first show using linear stability analysis that local self-inhibition broadens considerably the parameter regime in which modular activity arises. We then extend this minimal model by assuming a more realistic scheme of self-inhibition and demonstrate that already weak local self-inhibition is sufficient to promote spatially modulated activity. We confirm the proposed circuit mechanism and the analytically derived boundaries of the pattern forming regime by simulating the system's dynamics in one and two dimensions. These analyses show that local self-inhibition is a plausible robust mechanism for generating modular activity in the early developing cortex.

However, it is important to go beyond plausibility and to derive critical predictions of the modeling framework that are testable in experiment. This appears particularly relevant, as recent advancements in experimental techniques offer new opportunities to record and manipulate neuron-type-specific cortical activity. Only recently, cell type specific and highly sensitive activity sensors[81,185,209] in addition to optogenetical manipulation tools have been developed[70,421,282]. It is now also possible to combine these two techniques into an all-optical approach allowing to simultaneously readout and manipulate neuronal populations[128,362,6]. These technological advancements start to provide an unprecedented opportunity to critically assess the validity of not only the validity of the specific role of self-inhibition proposed here, but also general signatures of the broad class of models explaining the emergence of modular activity through lateral network connections.

To establish the prerequisites for performing such tests in future studies, we derive a set of specific predictions of the proposed network model. We show that applying a brief local input to the model network reveals an effective MH in the transient lateral spread of excitation and inhibition. Moreover, while domains of high excitatory activity are matched by co-localized domains of inhibitory activity, their amplitude can be several-fold weaker, depending on the connectivity parameters. Also the domain spacing can vary considerably across parameter space, even for a fixed width of the E to E connections, explaining the variability of the domain spacing across cortical areas and species[456,358,294,231,373]. Finally, we show that the model predicts the domain spacing to change when altering the strength of inhibition and suggest ways to perform

such manipulations. We argue that current technological advancements in the field make it now possible to experimentally test all these predictions and to critically study the mechanism and modeling framework studied here.

6.2 Modular activity without Mexican hat connectivity

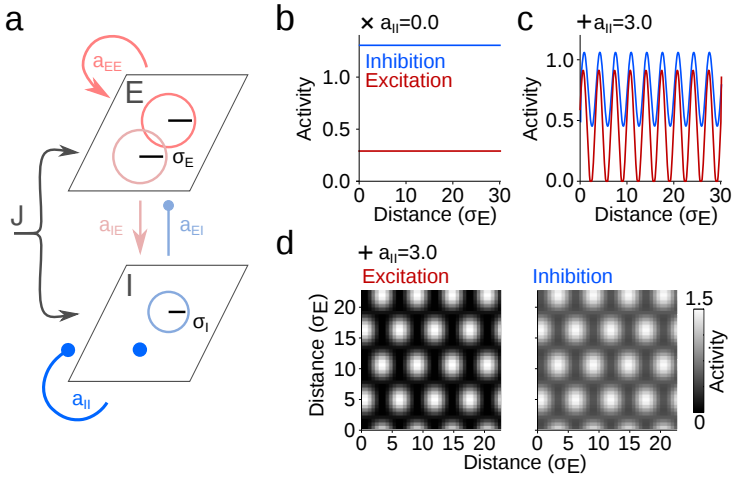

Figure 6.1: Local self-inhibition leads to modular network activity when inhibition has shorter range than excitation. **a** Schematic of network model of excitatory (E) and inhibitory (I) population. The connections between individual units follows a Gaussian profile (light colored circles). Self-inhibition (I to I; saturated blue) consists only of local connections. **b-d** Examples of simulated network solutions for excitatory (red) and inhibitory (blue) populations for the network model shown in (a). **b** In the absence of local self-inhibition ($a_{II} = 0$) the solution converges to a spatially homogeneous state. **c** Local self-inhibition (here $a_{II} = 3$) allows the network to generate spatially modulated patterns of activity. **d** In two dimensions the active domains are arranged as an hexagonal lattice. Parameters used are (**b**) $a_{EE} = 1.95, a_{IE} = 1.4, a_{EI} = 0.9, a_{II} = 0.0, \sigma_E = 1.3, \sigma_I = 1.2$, (**c**) $a_{EE} = 4.95, a_{IE} = 4.4, a_{EI} = 3.9, a_{II} = 0.0, \sigma_E = 1.3, \sigma_I = 1.2$ and (**d**) $a_{EE} = 4.95, a_{IE} = 4.4, a_{EI} = 3.9, a_{II} = 0.0, \sigma_E = 1.7, \sigma_I = 1.5$.

To investigate how networks without a Mexican hat-like connectivity can form modular activity, we study a standard Wilson-Cowan type network model with rate units[447,446,130,129,226,14] (see also Chapter 2). The network model contains two populations of excitatory (E) and inhibitory (I) rate units which are interconnected with each other[446,129]. Each excitatory unit is connected to nearby (excitatory and inhibitory) units via a distance dependent Gaussian connectivity profile (**Fig. 6.1a**). Each inhibitory unit is connected via a Gaussian connectivity profile to nearby excitatory units and only locally coupled to itself (**Fig. 6.1a**; this restriction will be dropped below). Each unit receives the same constant input $J > 0$ (**Fig. 6.1a**). The system's dynamics are then described by

$$\tau_E \frac{\mathrm{d}u_E(\vec{x},t)}{\mathrm{d}t} = -u_E(\vec{x},t) + f\left(\int \mathrm{d}\vec{y}\,(a_{EE}M_{EE}(\vec{x},\vec{y})u_E(\vec{y},t) - a_{EI}M_{EI}(\vec{x},\vec{y})u_I(\vec{y},t)) + J\right), \tag{6.1}$$

$$\tau_I \frac{\mathrm{d}u_I(\vec{x},t)}{\mathrm{d}t} = -u_I(\vec{x},t) + f\left(\int \mathrm{d}\vec{y}\,(a_{IE}M_{IE}(\vec{x},\vec{y})u_E(\vec{y},t)) - a_{II}u_I(\vec{x},t) + J\right) \tag{6.2}$$

where $u_E(\vec{x},t)$ ($u_I(\vec{x},t)$) is the average activity of an excitatory (inhibitory) unit in a column at location $\vec{x}$ in the two-dimensional plane. $M_{KL}(\vec{x},\vec{y})$ are the synaptic weight profiles connecting locations $\vec{x}$ and $\vec{y}$ from population L to K ($L,K \in \{E,I\}$) and the integral is taken over all locations $\vec{y}$ within the network. $M_{KL}(\vec{x},\vec{y})$ are modelled by Gaussian kernels, apart from local self-inhibition, which is modelled by a delta distribution:

$$M(\vec{x},\vec{y}) = \begin{pmatrix} a_{EE}M_{EE}(\vec{x},\vec{y}) & -a_{EI}M_{EI}(\vec{x},\vec{y}) \\ a_{IE}M_{IE}(\vec{x},\vec{y}) & -a_{II}M_{II}(\vec{x},\vec{y}) \end{pmatrix}, \tag{6.3}$$

$$M_{KL}(\vec{x},\vec{y}) = M_{KL}(|\vec{x}-\vec{y}|) = \frac{1}{2\pi\sigma_L^2}\exp\left(-\frac{|\vec{x}-\vec{y}|^2}{2\sigma_L^2}\right), \tag{6.4}$$

$$M_{II}(\vec{x},\vec{y}) = \delta(\vec{x}-\vec{y}). \tag{6.5}$$

Here σ_L denotes the standard deviation (SD) and a_{KL} the amplitude of the Gaussian describing the connectivity from population L to K, respectively. Note that the spatial range of excitatory connections to inhibitory and excitatory units is identical. Note further that the connectivity profiles and the inputs are isotropic and identical for all units, hence, the dynamical equations are rotation and translation symmetric. As we are interested in the behaviour of the network as a function of the range of inhibition relative to excitation, we introduce the ratio of the variances $r = \sigma_I^2/\sigma_E^2$. For $r > 1$ lateral inhibition extends further than excitation (Mexican hat connectivity profile). For $r < 1$ inhibition is of shorter range than excitation, which can be argued is the more relevant regime in cortex. For concreteness f is taken to be the rectifying function. τ_E and τ_I describe the time constants for excitation and inhibition, respectively. In the following we assume $\tau_E = \tau_I = \tau$. The more general case where $\tau_E \neq \tau_I$ is addressed below. Altogether, the network has six connectivity parameters, which we combine below to a set of three effective parameters determining the network's behaviour in generating modulated activity.
The discretized network used for simulations consist of N (N^2 in two dimensions) excitatory and inhibitory firing rate units, respectively. The units are equally distributed in one dimension along a line in the interval $0 \leq x \leq 1$ and in two dimensions in a square of $0 \leq x \leq 1, 0 \leq y \leq 1$. The position of the j-th unit is then $x_j = \frac{j}{N-1}$ ($y_j = \frac{j}{N-1}$) where $j \in 0,\ldots,N-1$. For all simulations we set $J = 1$ and use random initial conditions $u_E(\vec{x},t=0), u_I(\vec{x},t=0)$ drawn from a truncated Gaussian distribution of zero mean and SD of 0.1. To model an activity pattern, we integrate the network dynamics until a near steady state of the dynamics is reached. The results in **Fig. 6.1** and **Fig. 6.6g** are obtained for an integration time of 500 τ. Often integration only up to $\approx 50\ \tau$ resulted already in a near steady state solution. We integrated the dynamics using a 4th order Runge-Kutta method either in a line of size $N = 256$ (1D) or in a square region with $N = 50$ units (2D) using periodic boundary conditions. The time step was dt=0.15τ. The simulations were performed on the GPUs GeForce GTX TITAN Black and GeForce GTX TITAN X. The code was implemented in Python. We used standard libraries numpy and scipy.
In numerical simulations, we find that without local self-inhibition, the network typically remains in a spatially homogeneous state when inhibition acts on a shorter scale than excitation (**Fig. 6.1b**). In contrast with local self-inhibition, the network can robustly generate spatially modulated activity patterns in one (**Fig. 6.1c**) and two dimensions (**Fig. 6.1d**). In two dimensions the active domains tile the plane in a regular, hexagonal grid (**Fig. 6.1d**). This is consistent with previous work which has shown that hexagonal patterns are the solutions of a two-dimensional network model with isotropic and homogeneous Mexican hat connectivity and similar nonlinearity[130,52]. Note that the patterns emerging in the excitatory and the inhibitory population exhibit the same phase in space but a slightly different amplitude in modulation. This behaviour is studied in more detail below. Thus, local self-inhibition appears to have an

important effect on the spatial structure of network activity, promoting the formation of modular activity patterns.

6.2.1 Local self-inhibition broadens the regime of modular activity

In the following we show that local self-inhibition broadens the parameter regime in which modular activity forms. To determine this parameter regime, we follow the classical recipe of first computing the spatially homogenous fixed points of the network dynamics and then deriving the conditions under which these constant solutions become unstable towards spatially modulated patterns[430,130,133,131,132,129,226,14]. To this end, we perform linear stability analysis around the spatially homogeneous state.

Spatially homogeneous solutions

First, following the methods outlined in previous work (e.g.[130,129,226,14]) we derive the spatially homogeneous fixed point and then study the conditions for which this solution is dynamically unstable towards spatially structured perturbations. The spatially homogeneous fixed points are obtained by setting the excitatory and inhibitory activities in Eqs. (5.46) and (5.47) to be constant in time and space as

$$\frac{\mathrm{d}\bar{u}_E}{\mathrm{d}t} \stackrel{!}{=} 0 = -\bar{u}_E + [a_{EE}\bar{u}_E - a_{EI}\bar{u}_I + J]_+ \,, \tag{6.6}$$

$$\frac{\mathrm{d}\bar{u}_I}{\mathrm{d}t} \stackrel{!}{=} 0 = -\bar{u}_I + [a_{IE}\bar{u}_E - a_{II}\bar{u}_I + J]_+ \,. \tag{6.7}$$

Solving these equations for $\bar{u}_E$ and $\bar{u}_I$ we obtain the following spatially homogeneous stationary solutions

$$\bar{u}_E = J\frac{1 + a_{II} - a_{EI}}{(1 + a_{II})(1 - a_{EE}) + a_{EI}a_{IE}} \tag{6.8}$$

$$\bar{u}_I = J\frac{1 + a_{IE} - a_{EE}}{(1 + a_{II})(1 - a_{EE}) + a_{EI}a_{IE}} \tag{6.9}$$

$$\text{assuming} \quad a_{EI}a_{IE} > (a_{II} + 1)(a_{EE} - 1), \tag{6.10}$$

$$a_{II} + 1 > a_{EI}, \tag{6.11}$$

$$a_{IE} + 1 > a_{EE}. \tag{6.12}$$

The constraints in Eqs. (6.10) to (6.12) ensure that the argument of the nonlinearity in Eqs. (6.6) and (6.7) is positive for $J > 0$. Note that, a positive spatially homogeneous fixed point solution exists also for flipped signs in conditions (6.10) to (6.12). However, in the following, we will consider only the case when Eq. (6.10) holds. This ensures that the baseline activity in the network does not diverge.
A negative input J changes the sign of the conditions in Eqs. (6.11) and (6.12). For $J = 0$ the fixed point solutions are zero and the nonlinearity suppresses the growth of activity patterns.

Formation of activity patterns in network with local self-inhibition

To study the emergence of modular activity patterns in the network (Eqs. (5.46) and (5.47)), we analyze the conditions for which the spatially homogeneous steady state solutions become unstable against random perturbations[430,129]. In particular, we are interested in a stationary instability without temporal oscillations in the activity. To this end, we consider the linearized dynamics around the fixed points given in Eqs. (6.8), (6.9). We define $u_E(\vec{x}, t) = \bar{u}_E + \epsilon w_E(\vec{x}, t)$

and $u_I(\vec{x},t) = \bar{u}_I + \epsilon w_I(\vec{x},t)$ with $\epsilon \ll 1$. Since the linear dynamics are translation invariant, their eigenfunctions or modes are plane waves. We are considering a stationary instability of the dynamics that results into spatially periodic and time invariant patterns by amplifying those modes through the recurrent network that have positive eigenvalues. For simplicity, we limit ourselves to the case where the baseline activity does not diverge in time which corresponds to the eigenvalue being negative at zero frequency. The linearized dynamics are then given by

$$\frac{\mathrm{d}}{\mathrm{d}t} w_E(\vec{x},t) = \left(-w_E(\vec{x},t) + \int d\vec{y}\, (a_{EE} M_{EE}(\vec{x}-\vec{y}) w_E(\vec{y},t) - a_{EI} M_{EI}(\vec{x}-\vec{y}) w_I(\vec{y},t)) \right) \tag{6.13}$$

$$\frac{\mathrm{d}}{\mathrm{d}t} w_I(\vec{x},t) = \left(-(1+a_{II})\, w_I(\vec{x},t) + \int d\vec{y}\, (a_{IE} M_{IE}(\vec{x}-\vec{y}) w_E(\vec{y},t)) \right) \tag{6.14}$$

where the contributions from the fixed point vanish according to Eqs. (6.6) and (6.7) and ϵ is cancelled out. The linearized dynamics are translation invariant, therefore their eigenfunctions are plane waves. Thus we expand the perturbations $(w_E(\vec{x},t), w_I(\vec{x},t))^T$ into their Fourier series, since this allows us to study which modes are growing or decaying in the system. We use

$$\begin{pmatrix} w_E(\vec{x},t) \\ w_I(\vec{x},t) \end{pmatrix} = \frac{1}{(2\pi)^{d/2}} \int \mathrm{d}\vec{k}\; e^{-i\vec{k}\vec{x}} \begin{pmatrix} \tilde{w}_E(\vec{k},t) \\ \tilde{w}_I(\vec{k},t) \end{pmatrix} \tag{6.15}$$

where d denotes the system's dimension and $\vec{k}$ is the wave vector. Plugging these expressions into Eqs. (6.13) and (6.14) of the dynamics yields

$$\begin{aligned} \int \mathrm{d}\vec{k}\; e^{-i\vec{k}\vec{x}} \frac{\mathrm{d}}{\mathrm{d}t} \begin{pmatrix} \tilde{w}_E(\vec{k},t) \\ \tilde{w}_I(\vec{k},t) \end{pmatrix} &= - \int \mathrm{d}\vec{k}\; e^{-i\vec{k}\vec{x}} \begin{pmatrix} \tilde{w}_E(\vec{k},t) \\ \tilde{w}_I(\vec{k},t) \end{pmatrix} \\ &\quad + \int \mathrm{d}\vec{k} \int d\vec{y}\, e^{-i\vec{k}\vec{y}} \begin{pmatrix} a_{EE} M_{EE}(\vec{x}-\vec{y}) & -a_{EI} M_{EI}(\vec{x}-\vec{y}) \\ a_{IE} M_{IE}(\vec{x}-\vec{y}) & -1-a_{II} \end{pmatrix} \begin{pmatrix} \tilde{w}_E(\vec{k},t) \\ \tilde{w}_I(\vec{k},t) \end{pmatrix}. \end{aligned} \tag{6.16}$$

Since individual Fourier modes are orthogonal to each other, the equation above has to hold for each mode independently. We solve the integral over $\vec{y}$ on the right hand side to

$$\begin{aligned} &\frac{\mathrm{d}}{\mathrm{d}t} \begin{pmatrix} \tilde{w}_E(\vec{k},t) \\ \tilde{w}_I(\vec{k},t) \end{pmatrix} = \begin{pmatrix} a_{EE}\tilde{M}_{EE}(k) - 1 & -a_{EI}\tilde{M}_{EI}(k) \\ a_{IE}\tilde{M}_{IE}(k) & -1-a_{II} \end{pmatrix} \begin{pmatrix} \tilde{w}_E(\vec{k},t) \\ \tilde{w}_I(\vec{k},t) \end{pmatrix} = B_l \begin{pmatrix} \tilde{w}_E(\vec{k},t) \\ \tilde{w}_I(\vec{k},t) \end{pmatrix} \\ &\text{with} \quad \tilde{M}_{KL}(k) = e^{-\frac{k^2\sigma_L^2}{2}}, \quad K,L \in \{E,I\} \end{aligned} \tag{6.17}$$

and the wave number (spatial frequency) $k = |\vec{k}|$. $\tilde{M}_{KL}(k)$ is the Fourier transform of $M_{KL}(|\vec{x}-\vec{y}|)$. In the above system of equations we define the matrix B_l (l stands for local self-inhibition) combining the connection matrix and the decay terms. To solve this system of equations, we diagonalize B_l and project the system into its eigenbasis

$$\frac{\mathrm{d}}{\mathrm{d}t} \begin{pmatrix} \tilde{w}_E(\vec{k},t) \\ \tilde{w}_I(\vec{k},t) \end{pmatrix} = B_l \begin{pmatrix} \tilde{w}_E(\vec{k},t) \\ \tilde{w}_I(\vec{k},t) \end{pmatrix} = S \begin{pmatrix} \lambda_1 & 0 \\ 0 & \lambda_2 \end{pmatrix} S^{-1} \begin{pmatrix} \tilde{w}_E(\vec{k},t) \\ \tilde{w}_I(\vec{k},t) \end{pmatrix} \tag{6.18}$$

$$\overset{\cdot S^{-1}}{\Rightarrow} \frac{\mathrm{d}}{\mathrm{d}t} \begin{pmatrix} \tilde{v}_1(\vec{k},t) \\ \tilde{v}_2(\vec{k},t) \end{pmatrix} = \begin{pmatrix} \lambda_1 & 0 \\ 0 & \lambda_2 \end{pmatrix} \begin{pmatrix} \tilde{v}_1(\vec{k},t) \\ \tilde{v}_2(\vec{k},t) \end{pmatrix} \tag{6.19}$$

where we have defined $(\tilde{v}_1(\vec{k},t),\tilde{v}_2(\vec{k},t))^T = S^{-1}(\tilde{w}_E(\vec{k},t),\tilde{w}_I(\vec{k},t))^T$. The columns of S consist of the right eigenvectors (not normalized) of B_l, and S^{-1} being its inverse

$$S = \begin{pmatrix} c_1(k)+c_2(k) & c_1(k)-c_2(k) \\ 1 & 1 \end{pmatrix}, \tag{6.20}$$

$$S^{-1} = \frac{1}{2c_2(k)} \begin{pmatrix} 1 & -c_1(k)+c_2(k) \\ -1 & c_1(k)+c_2(k) \end{pmatrix} \tag{6.21}$$

with

$$c_1(k) = \frac{1}{2a_{IE}\tilde{M}_{IE}(k)} \left(a_{EE}\tilde{M}_{EE}(k) + a_{II} \right), \tag{6.22}$$

$$c_2(k) = \frac{1}{2a_{IE}\tilde{M}_{IE}(k)} \sqrt{\left(a_{EE}\tilde{M}_{EE}(k) + a_{II} \right)^2 - 4a_{IE}a_{EI}\tilde{M}_{IE}(k)\tilde{M}_{EI}(k)}. \tag{6.23}$$

The definition of S, S^{-1}, c_1 and c_2 proves to be useful further below. The eigenvalues are denoted by λ_1, λ_2 (with the larger eigenvalue being λ_1) and are given by

$$\lambda_1(k) = \frac{1}{2}\left(T(k) + \sqrt{T(k)^2 - 4\,D(k)} \right) \tag{6.24}$$

$$\lambda_2(k) = \frac{1}{2}\left(T(k) - \sqrt{T(k)^2 - 4\,D(k)} \right) \tag{6.25}$$

$$\text{with} \quad T(k) = a_{EE}\tilde{M}_{EE}(k) - 2 - a_{II} = \lambda_1 + \lambda_2, \tag{6.26}$$

$$D(k) = (1 - a_{EE}\tilde{M}_{EE}(k))(1 + a_{II}) + a_{IE}a_{EI}\tilde{M}_{IE}(k)\tilde{M}_{EI}(k) = \lambda_1\lambda_2 \tag{6.27}$$

where D denotes the determinant and T denotes the trace of B_l. The system in Eq. (6.19) can be solved by an exponential Ansatz of the following form

$$\begin{pmatrix} \tilde{v}_1(\vec{k},t) \\ \tilde{v}_2(\vec{k},t) \end{pmatrix} = \begin{pmatrix} e^{\lambda_1(k)t}\ \tilde{v}_1(\vec{k},t=0) \\ e^{\lambda_2(k)t}\ \tilde{v}_2(\vec{k},t=0) \end{pmatrix} \tag{6.28}$$

where $\tilde{v}_{1,2}(\vec{k},t=0)$ denote the initial conditions of the system. By transforming this solution back, we obtain the solutions for the Fourier coefficients $\tilde{w}_E, \tilde{w}_I$

$$\begin{pmatrix} \tilde{w}_E(\vec{k},t) \\ \tilde{w}_I(\vec{k},t) \end{pmatrix} = S \begin{pmatrix} \tilde{v}_1(\vec{k},t) \\ \tilde{v}_2(\vec{k},t) \end{pmatrix} = \begin{pmatrix} (c_1(k)+c_2(k))\tilde{v}_1(\vec{k},t) + (c_1(k)-c_2(k))\tilde{v}_2(\vec{k},t) \\ \tilde{v}_1(\vec{k},t) + \tilde{v}_2(\vec{k},t) \end{pmatrix}. \tag{6.29}$$

The full solution in state space is then given by

$$\begin{pmatrix} w_E(\vec{x},t) \\ w_I(\vec{x},t) \end{pmatrix} = \frac{1}{(2\pi)^{d/2}} \int \mathrm{d}\vec{k}\, e^{i\vec{k}\vec{x}} \left(\tilde{v}_1(\vec{k},0) \begin{pmatrix} (c_1(k)+c_2(k)) \\ 1 \end{pmatrix} e^{\lambda_1(k)t} + \tilde{v}_2(\vec{k},0) \begin{pmatrix} (c_1(k)-c_2(k)) \\ 1 \end{pmatrix} e^{\lambda_2(k)t} \right). \tag{6.30}$$

The coefficients describe whether individual modes in the perturbation $w_{E/I}(\vec{x},t)$ grow or decay during time. The expressions for $w_{E/I}(\vec{x},t)$ contain two time dependent terms. Depending on the sign of the eigenvalues $\lambda_{1,2}(k)$ these terms either grow (positive sign) or decay (negative sign) with time. The system's dominant modes at long times are those which grow maximally and their frequencies are determined by the location of the maximum of the larger eigenvalue λ_1. Note that the dominant modes of excitation and inhibition share the same spatial frequency. For the network to form modular activity, a mode at finite frequency k must have a positive

maximal growth rate, while the zero frequency mode is unstable corresponding to a negative eigenvalue at $k = 0$. In general, it would be sufficient to require that the eigenvalue at zero frequency is smaller than the one at peak frequency. Here, we will consider only the former case, but similar considerations can be given for the latter case.
In the following we determine how the sign of λ_1 behaves as a function of k depending on the network connectivity. To this end, we study the behaviour of trace and determinant as their signs fully determine the sign of the eigenvalues and are analytically more tractable. The condition that the eigenvalue must be negative at $k = 0$ corresponds to a positive determinant at zero frequency. Note that we derived this condition already in the calculation of the positive fixed points for positive input (Eq. (6.10)). For the determinant to be positive both eigenvalues have to share the same sign. In the case that both eigenvalues are positive at zero frequency, the trace must also be positive at $k = 0$. However, a positive trace at $k = 0$ leads to an oscillatory instability from a spatially homogeneous equilibrium[129,14], as the eigenvalues become complex, whereas we are interested in a stationary instability. Thus, we consider only the case where eigenvalue and trace at $k = 0$ are negative. As $\tilde{M}_{KL}(k = 0) = 1$, the two requirements that the trace is negative and the determinant is positive at $k = 0$ yield the following two constraints on the connectivity parameters

$$a_{EE} < \frac{a_{EI}a_{IE}}{1 + a_{II}} + 1 = s + 1, \tag{6.31}$$

$$a_{EE} < 2 + a_{II} \tag{6.32}$$

where we introduced the effective parameter $s = \frac{a_{EI}a_{IE}}{1 + a_{II}}$. The parameter s describes the coupling strengths a_{EI}, a_{IE} between the excitatory and inhibitory population normalized by the self-inhibitory connectivity strength a_{II}. Note that for fixed a_{EE} the condition in Eq. (6.32) becomes a lower bound for the connectivity strength a_{II}.
Second, we require that the determinant D becomes negative for an interval of finite frequencies, such that one of the eigenvalues becomes positive (**Fig. 6.6b-c**). As $D(k) \to 1$ for $k \to \infty$, this means that D needs to exhibit a negative minimum at a finite frequency. Setting the derivative of D w.r.t. k to zero, we solve for the location of the minimum $k_{\min}$. The equation for $k_{\min}$ is cubic in k and leads to the following relevant solution

$$k_{\min} = \frac{\sqrt{2\log\left(\frac{(\sigma_I^2+\sigma_E^2)a_{EI}a_{IE}}{(1+a_{II})a_{EE}\sigma_E^2}\right)}}{\sigma_I} = \frac{\sqrt{2\log\left(\frac{(r+1)s}{a_{EE}}\right)}}{\sigma_E\sqrt{r}} \tag{6.33}$$

where we introduce the second effective parameter which is the squared ratio between the inhibitory and excitatory spatial scale $r = \sigma_I^2/\sigma_E^2$. $k_{\min}$ is real (**Fig. 6.6b**) only if the argument of the logarithm is greater than 1 which requires

$$a_{EE} < s\,(1 + r). \tag{6.34}$$

Next, plugging the expression for $k_{\min}$ into the determinant shows that the minimum at $k_{\min}$ is negative only for

$$a_{EE} > (1 + r)\left(\frac{s^{\frac{1}{r}}}{r}\right)^{\frac{r}{1+r}} = (1 + r)\; s^{\frac{1}{1+r}}\left(\frac{1}{r}\right)^{\frac{r}{1+r}}. \tag{6.35}$$

Note that conditions in Eqs. (6.31), (6.34) and (6.35) only depend on the three effective variables a_{EE}, s and r. The conditions in Eqs. (6.31) and (6.34) describe an upper bound for a_{EE} whereas the condition in Eq. (6.35) describes a lower bound for a_{EE}. Thus, these three conditions can

only hold simultaneously if the right hand side of both conditions (6.31) and (6.34) is greater than the right hand side of condition (6.35). To assess for which parameter settings this holds, we first compare the right hand side of Eqs. (6.34) and (6.35)

$$s(1+r) > (1+r)\, s^{\frac{1}{1+r}} \left(\frac{1}{r}\right)^{\frac{r}{1+r}} \tag{6.36}$$

$$s^{\frac{r}{1+r}} > \left(\frac{1}{r}\right)^{\frac{r}{1+r}} \tag{6.37}$$

$$s > \frac{1}{r}. \tag{6.38}$$

Thus, in the regime where modular patterns form, the effective parameters s and r need to satisfy $s > \frac{1}{r}$ for the conditions in Eqs. (6.34) and (6.35) to simultaneously hold. Moreover, for $s > \frac{1}{r}$ the right hand side of Eq. (6.34) is always larger than the one of Eq. (6.31). Thus, if Eq. (6.31) holds, then Eq. (6.34) is also automatically satisfied. Generating modular network activity therefore requires only the three conditions in Eqs. (6.31), (6.32) and (6.35) to be satisfied. These conditions outline the pattern forming regime in the parameter space of the network connectivity. Taken together, in the two previous sections we derived in total five conditions for the six network parameters $a_{EE}, a_{EI}, a_{IE}, a_{II}, \sigma_E$ and σ_I. These conditions can be divided into two groups. The constraints in Eqs. (6.31) and (6.35) define the pattern forming regime. They depend on three effective parameters a_{EE}, s and r which is visualized and analyzed in **Fig. 6.3**. The remaining three conditions in Eqs. (6.11), (6.12) and (6.32) guarantee the existence of a constant and positive fixed point and specify values for the original parameters a_{IE}, a_{EI} and a_{II}. The ability of the network to form modular activity does not depend on the absolute values of σ_E and σ_I, but only on their ratio r, as changing σ_E or σ_I independently can always be compensated for by rescaling the network.
Moreover, for a given set of parameter values a^*_{EE}, s^*, r^* within the pattern forming regime, we can always find values for a_{EI}, a_{IE}, a_{II} that satisfy the constraints in Eqs. (6.11), (6.12) and (6.32), using the following recipe. First, we choose a value for $a_{II} = a^*_{II}$ such that Eq. (6.32) is fulfilled. Next, we choose a value for $a_{EI} = a^*_{EI}$ satisfying Eq. (6.11). With this choice the value of a_{IE} is $a^*_{IE} = \frac{s^*(1+a^*_{II})}{a^*_{EI}}$. Using the conditions in Eqs. (6.11) and (6.31), we show that this value in fact obeys the remaining condition (6.12)

$$a^*_{IE} = \frac{s^*(1+a^*_{II})}{a^*_{EI}} \overset{Eq.(6.31)}{>} \frac{(a^*_{EE}-1)(1+a^*_{II})}{a^*_{EI}} \overset{Eq.(6.11)}{>} (a^*_{EE}-1). \tag{6.39}$$

Thus, for all sets of values a^*_{EE}, s^*, r^* in the pattern forming regime it is possible to obtain a set of values for a_{EI}, a_{IE}, a_{II} such that the additional conditions in Eqs. (6.11), (6.12) and (6.32) are satisfied. Together, this leads to the following parameter regime that supports the formation of modular activity (see also[226])

$$a_{EE} < 2 + a_{II}, \tag{6.40}$$

$$a_{EE} < s + 1, \tag{6.41}$$

$$a_{EE} > (1+r)\, s^{\frac{1}{1+r}} r^{\frac{-r}{1+r}} \tag{6.42}$$

The conditions in Eqs. (6.41) and (6.42) depend only on the three effective variables a_{EE}, r and s which are combinations of the original six connectivity parameters. Only Eq. (6.40) depends explicitly on a_{II}, relating it to the coefficient a_{EE}. Thus, for a fixed value of a_{II} condition (6.40) defines the upper bound for a_{EE}, and the two conditions in Eqs. (6.41) and (6.42) define two other boundaries of the parameter regime in which spatially modulated activity can form.

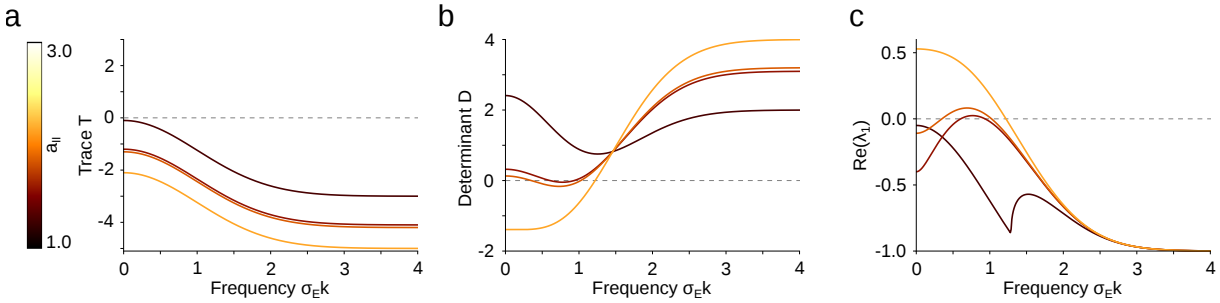

Figure 6.2: Increasing strength of self-inhibition a_{II} leads to positive peak in the maximal eigenvalue at finite frequencies. **a** Trace $T(k)$ as a function of normalized wave number $\sigma_E k$ for increasing values of self-inhibition a_{II} from 1 (black) to 3.0 (yellow) (other connectivity parameters kept fixed). Gray dashed line marks zero. **b** The determinant $D(k)$ is negative for finite frequencies at intermediate values of a_{II}. Further increasing a_{II} leads to a negative value of the determinant also at zero frequency. **c** The frequency intervals where the determinant is negative coincide with a positive real part of the larger eigenvalue $\lambda_1(k)$, and thus a positive growth rate for plane waves in this frequency band. The red and orange lines are within the pattern forming regime, whereas the black and yellow lines lie outside. (**a,b,c**) Parameters used are $a_{EE} = 2.9, a_{IE} = 2.7, a_{EI} = 2.3, r = 0.9$.

Note also that if Eqs. (6.41) and (6.42) are satisfied, there is always a value a_{II} for which Eq. (6.40) holds. Thus, the linear stability analysis determines a region in parameters space which in the following we call the pattern forming regime for which modular network activity can form. Importantly, its boundaries are determined by the three effective parameters a_{EE}, s and r.

Local self-inhibition extends the pattern forming regime into biologically plausible parameter region

To systematically determine the influence of local self-inhibition on the size and location of the pattern forming regime, we visualize its boundaries (Eqs. (6.41) and (6.42)) in the three-dimensional space spanned by a_{EE}, r, and the coupling strength $a_{EI}a_{IE}$ (**Fig. 6.3a**). Here, we use $a_{EI}a_{IE}$ instead of the effective variable s to illustrate the difference in extension of the pattern forming regime between networks with different strengths a_{II}. In **Fig. 6.3a** the pattern forming regime lies inbetween the red (corresponding to Eq. (6.41)) and the black surface (Eq. (6.42)). Without self-inhibition ($a_{II} = 0$), the pattern forming regime is limited to the parameter region with $r > 1$ (see below). In this case modular activity only forms in a regime with Mexican hat like connectivity consistent with previous results[129,226,14]. Intriguingly, adding local self-inhibition ($a_{II} = 1$) expands the pattern forming regime such that connectivity settings where inhibition is of shorter range than excitation ($r < 1$) also lead to modular activity (**Fig. 6.3a**, *right*). A cut through the three-dimensional pattern forming regime at fixed a_{II} highlights the notable increase in the relevant parameter regime where inhibition acts on a shorter range than excitation from a network without self-inhibition (gray) to nonzero self-inhibition (blue; $a_{II} = 3$; **Fig. 6.3b**). For all networks we fix $a_{II} = a_{EE} - 1.95$ (compare to Eq. (6.40)) to be able to compare them. Other parametrizations of a_{II} hold qualitatively similar results.
Next, we quantify the increase in size of the pattern forming regime in the relevant parameter regime ($r < 1$). To this end, we systematically increase a_{II} and determine the area A between the intersection point $r*$ of the boundaries (Eqs. (6.41) and (6.42)) and $r = 1$ (e.g. dashed region in **Fig. 6.3c**). If the pattern forming regime does not extend to values with $r < 1$ as is the case when the excitatory to excitatory interaction strength is below a minimal value

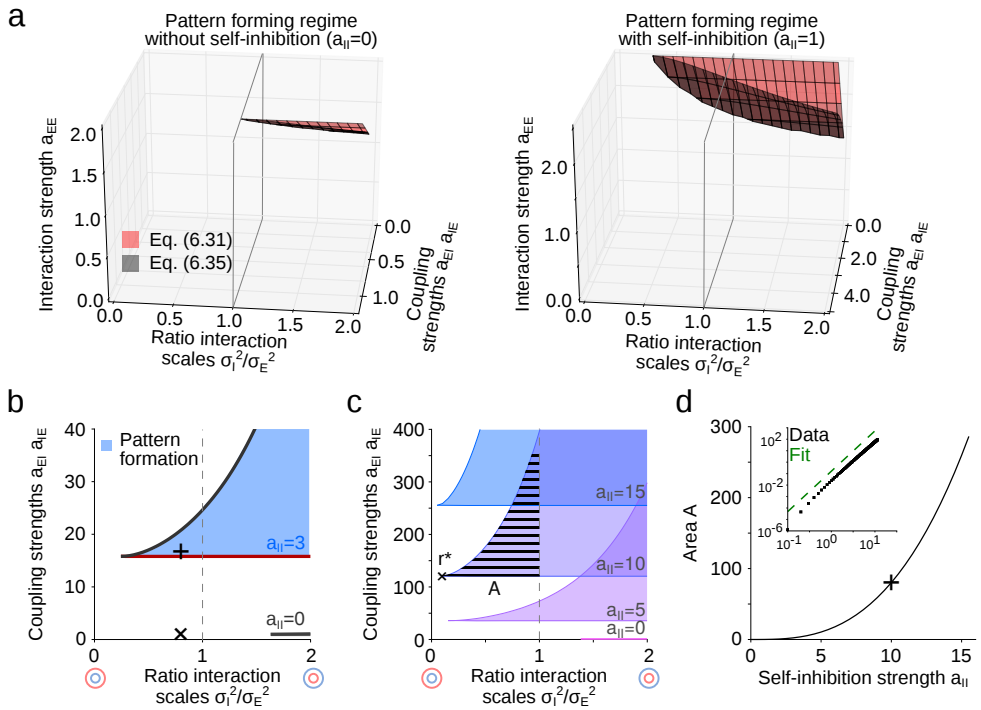

Figure 6.3: Phase diagram of parameter regime allowing for the formation of spatially modulated activity. **a** 3d phase diagram of the pattern forming regime. The two surfaces correspond to the conditions given in Eqs. (6.41) (red) and (6.42) (black) and contain the pattern forming regime. *Left:* without self-inhibition ($a_{II} = 0$) the pattern forming regime is constrained to a parameter region with lateral inhibition ($\sigma_I > \sigma_E$). *Right*: with self-inhibition ($a_{II} = 1.0$) this regime is extended such that connectivity settings with local inhibition ($\sigma_I < \sigma_E$) lead to spatially modulated activity. The gray lines indicate when the spatial range of excitation equals that of inhibition. Note that the pattern forming regime is plotted as a function of $a_{EI}a_{IE}$, to be able to compare the regimes for different values of a_{II}. **b** Two-dimensional cut through 3d phase diagram shown in (**a**) for $a_{EE} = a_{II} + 1.95$. For $a_{II} = 0$ the pattern formation regime (gray colored region in the lower right) is constrained to a parameter regime with lateral inhibition ($\sigma_I > \sigma_E$). Increasing self-inhibition ($a_{II} = 3$) expands the pattern forming regime (blue shaded area) such that connectivity settings with local inhibition allow for patterns to form. The two markers identify parameter settings within (+) and outside (×) of the pattern forming regime, whose simulated solutions are shown in **Fig. 6.1**. **c** Increasing the strength of self-inhibition a_{II} leads to an increase in size of the pattern forming regime A within the parameter region with local inhibition. We quantify the size of the pattern forming regime by the integral A from the intersection point r^* of the two conditions given in Eqs. (6.41) and (6.42) to $r = 1$ (exemplary dashed area for $a_{II} = 10$). **d** Region A increases smoothly with increasing self-inhibition strength a_{II}. The cross denotes the size of the dashed area shown in (**c**).

($a_{EE} < 2$; see **Fig. 6.3d**), we set $A = 0$. We observe that already very weak local self-inhibition leads the pattern forming regime to extend into the parameter region where inhibition acts on a shorter scale than excitation (**Fig. 6.3d**). This area A increases supralinearly as a power law with exponent of 3.13 ± 0.02 (see inset in **Fig. 6.3d**) in the limit of large a_{II}.
To derive those results, we assumed a Gaussian connectivity profile in the network. Using exponential profiles leads to qualitatively very similar results (see below). Furthermore, we assumed here that excitation and inhibition share the same time constant. Repeating the same analysis as above for different time constants, shows that an inhibitory time constant that is greater (smaller) than the excitatory time constant reduces (enlarges) the pattern forming regime in the region of $r < 1$. This reduction can be compensated, however, by choosing a sufficiently strong local self-inhibition (see below). Here, we assumed a Gaussian connectivity profile. Using an exponential profile instead leads to qualitatively very similar results (**Fig. 6.5**). To obtain modular activity patterns in a regime where inhibition is more short-ranged than excitation, we assumed a purely local self-inhibition. Alternative connectivity schemes such as a motif where the inhibitory to inhibitory connections are spatially more localized than the connections from inhibitory to excitatory units, allow similarly the formation of modular activity patterns in the absence of long-range inhibition[389] (Methods).
In summary, the presence of local self-inhibition in the wiring diagram of the network extends the pattern forming regime and relaxes the constraints on the connectivity parameters, especially on the relative spatial scales of excitatory and inhibitory interactions. Importantly, a network with short-range inhibition and an inhibitory time constant equivalent to the excitatory time constant can form spatially modulated activity patterns. Thus, local self-inhibition consolidates the requirements on the connectivity settings for forming modular network activity with experimental data[136,265].
A key difference between a network with and without local self-inhibition is that including self-inhibition relaxes the constraint on the magnitude of self-excitation $a_{EE} < 2 + a_{II}$ (see Eq. (6.32)). We show that for a network without self-inhibition ($a_{II} = 0$; $a_{EE} < 2$) the pattern forming regime is restriced to a parameter region where the range of inhibition exceeds excitation ($r > 1$). Previously we found $s > \frac{1}{r}$ in the pattern forming regime. Thus, if $r < 1$, then $s > 1$. With $a_{EE} < 2$, condition (6.35) then implies

$$2 > (1 + r)\, s^{\frac{1}{1+r}} \left(\frac{1}{r}\right)^{\frac{r}{1+r}}. \tag{6.43}$$

To test whether values of $r < 1$ exist for which this condition holds, we use $s > \frac{1}{r}$

$$\begin{aligned} 2 &> (1 + r)\, s^{\frac{1}{1+r}} \left(\frac{1}{r}\right)^{\frac{r}{1+r}} && (6.44)\\ &> (1 + r)\, s^{\frac{1}{1+r}} \left(\frac{1}{r}\right)^{\frac{r}{1+r}}\Bigg|_{s=1/r} && (6.45)\\ &> 1 + \frac{1}{r} && (6.46)\\ \Rightarrow r &> 1 && (6.47) \end{aligned}$$

Thus, this condition only holds for inhibition whose spatial range exceeds excitation. We therefore conclude that the network without self-inhibition does not form spatially modulated activity patterns for $r < 1$ but requires inhibition of larger spatial range than excitation.
On the other hand if $a_{II} > 0$ choosing $a_{EE} > 2$ but satisfying the condition $a_{EE} < 2 + a_{II}$ (Eq. (6.32)), we show that there exists a regime where modular patterns with shorter inhibiton than

excitation ($r < 1$) form. To this end, we compare Eqs. (6.31) and (6.32) which for convenience we state again here

$$a_{EE} < s + 1, \tag{6.48}$$

$$a_{EE} < a_{II} + 2. \tag{6.49}$$

For $a_{II} > 0$, we can choose $a_{EE} > 2$. To also satisfy Eq. (6.31), we require a value $s > a_{EE} - 1 > 1$ by assuming $r < 1$ which is consistent with $s > \frac{1}{r}$. To test whether the remaining condition (Eq. (6.35)) holds, we use as derived before

$$a_{EE} > (1 + r)\, s^{\frac{1}{1+r}} \left(\frac{1}{r}\right)^{\frac{r}{1+r}} \tag{6.50}$$

$$> 1 + \frac{1}{r} \tag{6.51}$$

which is consistent with Eq. (6.32) as $s > \frac{1}{r}$. Thus, the conditions in Eqs. (6.31) to (6.35) are simultaneously satisfied for a parameter setting where inhibition acts on a smaller spatial scale than excitation ($r < 1$) for sufficiently large self-excitation ($a_{EE} > 2$).

Influence of negative network input on pattern forming regime

So far, we discussed the case when the network input is positive ($J > 0$). Here we briefly discuss how applying a negative input changes the conditions for the formation of modular activity. First, when determining the spatially homogeneous fixed point solutions, two of the three conditions (Eqs. (6.11) and (6.12)) on the connectivity parameters change their sign and become

$$a_{II} + 1 < a_{EI} \tag{6.52}$$

$$\text{and} \quad a_{IE} + 1 < a_{EE}. \tag{6.53}$$

Importantly, the sign of the input does not affect the derivation of the conditions for the pattern forming regime based on the linear stability analysis. Therefore the size and location of the pattern forming regime remains unchanged for $J < 0$. However, the conditions in Eqs. (6.52) and (6.53) now lead to different connectivity parameters a_{KL}. To find a complete set of connectivity parameters that fulfills all five conditions, we first choose a value $a_{II} = a^*_{II}$ satisfying Eq. (6.32), and $a_{IE} = a^*_{IE}$ satisfying Eq. (6.53). This leads to $a^*_{EI} = \frac{s^*(1+a^*_{II})}{a^*_{IE}}$ fulfilling the remaining condition (6.52)

$$a^*_{EI} = \frac{s^*(1 + a^*_{II})}{a^*_{IE}} \overset{Eq.(6.31)}{>} \frac{(a^*_{EE} - 1)(1 + a^*_{II})}{a^*_{EI}} \overset{Eq.(6.53)}{>} (a^*_{II} + 1). \tag{6.54}$$

Thus, in the pattern forming regime it is always possible to find a set of connectivity parameters (a_{KL}, σ_L) that satisfy all conditions, irrespective of whether the input J is positive or negative, as the fixed points are positive and allow for facilitation of local activity fluctuations and suppression of fluctuations further away.

6.2.2 Influence of local inhibition on the formation of modular activity

In the main part of this work we demonstrated that a network with purely local inhibition forms modular activity even if inhibition acts on a shorter range than excitation. However, in cortical circuits inhibitory interneurons are not only coupled to themselves but also to their neighbours following certain motifs[345]. Here we study an alternative form of self-inhibition by

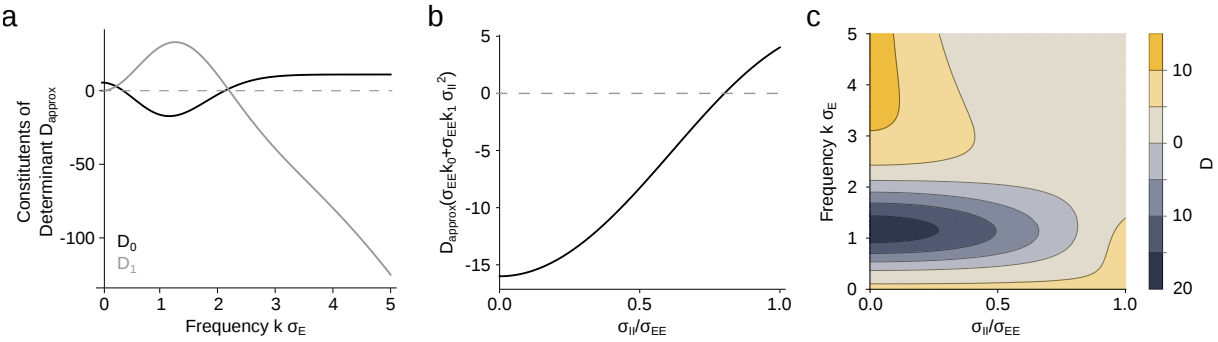

Figure 6.4: Robust formation of modular activity when spatial extent of self-inhibition is nonzero and small. **a** Expansion terms of determinant. D_0 (black) denotes zeroth order term exhibiting a negative minimum at a finite frequency whereas second order term D_1 (gray) shows at a similar frequency a positive peak. **b** The determinant's minimum becomes positive for increasing σ_{II}. **c** Over a large regime of σ_{II} the determinant D exhibits a negative minimum until for sufficiently large σ_{II} the minimum in the determinant first becomes positive and then vanishes. Parameters used are $a_{EE} = 11.4, a_{IE} = 11.0, a_{EI} = 10.9, a_{II} = 10.0, r = 0.8$.

assuming that self-inhibitory connections are spatially extended. In the following we study how a nonzero spatial range of self-inhibition influences the conditions for the pattern forming regime derived above, and how large it can be to still allow for the formation of modular activity. The network is based on the network model obeying the dynamics given in Eqs. (5.46) and (5.47). The full inhibitory to inhibitory connectivity M_{II} now consists of a spatially extended term M^s_{II} with Gaussian profile and width σ_{II} (analogous to Eq. (6.4)). We assume that the inhibitory interaction range is more short-range than excitation ($\sigma_{EI}, \sigma_{II} < \sigma_{EE} = \sigma_{IE}$). The trace (compare to Eq. (6.26)) of the linearized network dynamics is given by

$$T(k) = a_{EE}\tilde{M}_{EE}(k) - a_{II}\tilde{M}_{II}(k) - 2 \tag{6.55}$$

Note that for $\sigma_{II} < \sigma_{EE}$ the trace has its maximal value at $k = 0$ independent of σ_{II}. Thus, increasing σ_{II} neither changes the sign of the trace nor the conditions for the pattern forming regime derived from the trace.

Next, we consider the influence of σ_{II} on the determinant of the linearized system. To form modular activity the determinant is required to exhibit a minimum with negative value at a finite frequency. Therefore, we examine how the existence of this minimum and its sign depend on σ_{II}. To this end, we first expand the determinant in a Taylor series around $\sigma_{II} = 0$ up to $\mathcal{O}(\sigma^2_{II})$ and then solve for the location of its minimum. For the expanded determinant we obtain

$$D_{\text{approx}}(k) = D_0(k) + \sigma^2_{II} D_1(k) \tag{6.56}$$

$$\text{with} \quad D_1(k) = \frac{a_{II}}{2}(-1 + a_{EE}\tilde{M}_{EE}(k))k^2 \tag{6.57}$$

where $D_0(k)$ corresponds to the determinant of the network with purely local self-inhibition defined in Eq. (6.27), and $\tilde{M}_{KL}(k)$ is the Fourier transform of the connectivity profile from population L to K with $K, L \in \{E, I\}$. As mentioned above $D_0(k)$ exhibits a negative minimum at a finite frequency whereas the higher order term $D_1(k)$ shows a positive peak at similar frequencies (**Fig. 6.4a**). We conclude, that increasing σ_{II} leads to a diminishment of the negative peak eventually leading to positive values of the minimum. To confirm this intuition, we next determine the location of the minimum which we assume to be given by $k_{\min} = k_0 + \sigma^2 k_1$. k_0 coincides with the location of the minimum in the network with purely local self-inhibition

(see Eq. (6.33)), and k_1 describes the change in peak location after increasing σ_{II}. Setting the derivative of $D_{\text{approx}}(k)$ w.r.t the frequency to zero yields:

$$k_0 = \pm \frac{\sqrt{2 \log\left(\frac{s(1+r)}{a_{EE}}\right)}}{\sigma_{EI}}, \tag{6.58}$$

$$k_1 = -a_{II} \frac{r\left(-a_{EE} + \left(\frac{s(1+r)}{a_{EE}}\right)^{1/r}\right) + a_{EE} \log\left(\frac{s(1+r)}{a_{EE}}\right)}{\sqrt{2} a_{EE}(1+a_{II}) \sigma_{EI}^3 r \sqrt{\log\left(\frac{s(1+r)}{a_{EE}}\right)}} \tag{6.59}$$

Plugging this expression for $k_{\min}$ into $D_{\text{approx}}(k)$ shows that the value of the determinant's minimum remains negative for increasing σ_{II} over a relatively long interval (**Fig. 6.4b**). For sufficiently large σ_{II} it eventually becomes positive (**Fig. 6.4b**). Considering the full expression of the determinant reveals that for increasing σ_{II}, initially the negative peak in the determinant is preserved. However, as σ_{II} starts to approach the value of σ_{EI}, the peak first becomes positive and eventually vanishes (**Fig. 6.4c**). A numerical analysis of a network with spatially extended self-inhibition where inhibitory to inhibitory connections are spatially more constrained than inhibitory to excitatory connections was given previously[389].

6.2.3 Different time constants for excitation and inhibition

So far, we assumed that excitation and inhibition share the same time constant. However, the decay time constant of the most abundant receptor in cortex GABA_A is typically larger than the time constant of AMPA receptors[335,136,90,219,47]. Therefore, we analyse here how different time constants τ_E and τ_I affect the conditions for the formation of modular activity. Applying again linear stability analysis around the spatially homogeneous fixed points, yields new conditions on the connectivity parameters. The trace T_τ and determinant D_τ change to

$$D_\tau(k) = \frac{1}{\tau} D(k), \tag{6.60}$$

$$T_\tau(k) = T(k) + \left(1 - \frac{1}{\tau}\right)(M_{II}(k) + 1) \tag{6.61}$$

setting $\tau = \frac{\tau_I}{\tau_E}$. D denotes the determinant and T the trace of the network with $\tau_E = \tau_I$ (see Eqs. (6.27) and (6.26)). The sign of the determinant and its derivative are unaffected by introducing a different time scale for inhibition and excitation. Thus, the conditions which we derived for the determinant in the previous section remain the same (see Eqs. (6.31), (6.34), (6.35)). Requiring that the trace is negative for $k = 0$, however, leads to the following new condition (compare to [129,226])

$$a_{EE} < 1 + \frac{1}{\tau}(a_{II} + 1). \tag{6.62}$$

For $\tau = 1$ we recover the previously derived condition (see Eq. (6.32)). Irrespective of τ a nonzero a_{II} enlarges the range of possible a_{EE} and thus the pattern forming regime. If $\tau < 1$ ($\tau_E > \tau_I$) which is the configuration studied in[226], the additional factor of $\frac{1}{\tau}$ relaxes the constraint on a_{EE} and allows choosing larger values for a_{EE}. In contrast, $\tau > 1$ ($\tau_E < \tau_I$) reduces the pattern forming regime, but this can always be compensated by choosing a sufficiently strong local self-inhibition.

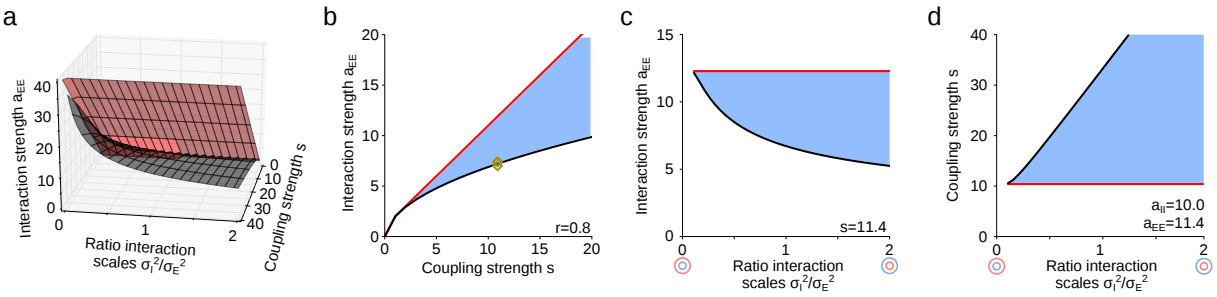

Figure 6.5: Pattern forming regime in the network with exponential connectivity profile extends to biologically plausible parameter region. **a** 3d phase diagram of the pattern forming regime as a function of a_{EE}, r and s which is bounded by the red surface (Eq. (6.65) and (6.67)) and the black surface (Eq. (6.68)). **b-d** 2d projections of the 2d phase diagram in (**b**) with one parameter fixed, respectively. Red (black) line corresponds to red (black) surface in (**b**). **b** Phase diagram as a function of a_{EE} and s for $r = 0.8$. Markers denote parameter settings that were numerically simulated to test boundaries of pattern forming regime. Parameters used are $s = 10.9$ and $a_{EE} = 7.2$ (green), $a_{EE} = 7.4$ (yellow). **c** Phase diagram as a function of a_{EE} and r for $s = 11.4$. **d** Phase diagram as a function of s and r for $a_{II} = 10.0, a_{EE} = 11.4$. Note that modular activity also forms for $r < 1$.

6.2.4 Exponential connectivity profile

In the previous network we have modelled the connectivity between units assuming its distanced-dependence in form of a Gaussian function. However, there is experimental evidence suggesting that connection weights are better described by an exponental distribution[359,80,108]. To test the influence of the specific spatial profile of the network connectivity on the formation of modular activity, we consider here a network for which connection strength decays as an exponential function of the distance between units. For simplicity we assume only local self-inhibition to obtain closed form expressions for the boundaries of the pattern forming regime. Adding a spatially extended self-inhibition leads to qualitatively similar results. The connectivity is then assumed to be

$$M_{KL}(\vec{x}-\vec{y}) = \frac{1}{2\sigma_L} e^{-\frac{|\vec{x}-\vec{y}|}{\sigma_L}} \quad \text{for} \quad K, L \in \{E, I\}, \tag{6.63}$$

$$M_{II}(\vec{x}-\vec{y}) = \delta(\vec{x}-\vec{y}). \tag{6.64}$$

Linearizing the network dynamics around the fixed points (Eqs. (6.8) and (6.9)) yields the following conditions analogous to Eqs. (6.31), (6.32), (6.34) and (6.35):

$$a_{EE} < \frac{a_{EI}a_{IE}}{1+a_{II}} + 1 = s + 1, \tag{6.65}$$

$$a_{EE} < a_{II} + 2, \tag{6.66}$$

$$a_{EE}(1-r) < \frac{a_{EI}a_{IE}}{1+a_{II}} = s, \tag{6.67}$$

$$a_{EE} > \frac{2\sqrt{r\,s} - 1 + r}{r}. \tag{6.68}$$

As before, we defined $r = \sigma_I^2/\sigma_E^2$ and $s = \frac{a_{EI}a_{IE}}{1+a_{II}}$. Note that the constraints for the zero frequency mode $k = 0$ (in Eqs. (6.65), (6.66)) are unchanged compared to the network with Gaussian connectivity profiles (see Eqs. (6.31) and (6.32)).

For completenes we give here the location of the minimum of the determinant (compare to Eq. (6.33) for the network with Gaussian connectivity profile)

$$k_{\min} = \frac{1}{\sigma_E\sqrt{r}}\left(1 - \frac{s}{a_{EE}} + \sqrt{\frac{s}{a_{EE}}\left(\frac{s}{a_{EE}} - 1 + r\right)}\right)^{\frac{1}{2}}. \tag{6.69}$$

Analogous to the network with a Gaussian connectivity profile, we test here whether all of these four conditions can hold simultaneously. To this end, we compare the right hand sides of Eqs. (6.67) and (6.68) which must satisfy

$$s > \frac{2\sqrt{r\,s} - 1 + r}{r}(1 - r) \tag{6.70}$$

$$\Rightarrow s > \frac{(r-1)^2}{r} \tag{6.71}$$

Next, we compare Eqs. (6.65) and (6.68) and obtain

$$s + 1 > \frac{2\sqrt{r\,s} - 1 + r}{r} \tag{6.72}$$

$$\Rightarrow s > \frac{1}{r} \tag{6.73}$$

This relation between s and r is analogous to the network with a Gaussian connectivity profile (see Eq. (6.38)). For $r < 2$, it is $\frac{1}{r} > \frac{(r-1)^2}{r}$, and the condition in Eq. (6.67) is trivially satisfied if Eq. (6.65) holds. Thus, in the regime where inhibition acts on a shorter spatial range than excitation, only the three conditions in Eqs. (6.65), (6.66) and (6.68) need to be considered to find the boundaries of the pattern forming regime. This is analogous to the network with Gaussian connectivity profile. As **Fig. 6.5** suggests, the pattern forming regime also extends into the region of connectivity parameters where inhibition is spatially more constrained than excitation. We tested the analytically derived boundary conditions for the formation of modular activity using numerical simulations. Parameter settings satisfying the conditions derived above result in modular activity pattern whereas parameter settings outside of the pattern forming regime yield either spatially homogeneous or diverging solutions (exemplary settings indicated in **Fig. 6.5b**).

6.3 Including spatially extended self-inhibition, already weak local self-inhibition allows for modular activity

In the previous section we showed that a network model with purely local self-inhibition robustly forms modular activity even if inhibition is of shorter range than excitation. However, local self-inhibition accounts only for a part of the total self-inhibitory connectivity. Here we study a biologically more plausible network model by adding spatially extended self-inhibition and assess how strong the local relative to the spatially extended self-inhibition must be to form modular activity in the absence of Mexican hat-like connectivity. The network is based on the network model with purely local self-inhibition obeying the dynamics given in Eqs. (6.1) and (6.2). The full inhibitory to inhibitory connectivity M_{II} now consists of a local term denoted by M^l_{II} and a spatially extended term M^s_{II} with Gaussian profile and width:

$$M_{II}(\vec{x},\vec{y}) = a^l_{II}M^l_{II}(\vec{x},\vec{y}) + a^s_{II}M^s_{II}(\vec{x},\vec{y}), \tag{6.74}$$

$$M^l_{II}(\vec{x},\vec{y}) = \delta(\vec{x} - \vec{y}), \tag{6.75}$$

$$M^s_{II}(\vec{x},\vec{y}) = \frac{1}{2\pi\sigma_I^2}e^{-\frac{(\vec{x}-\vec{y})^2}{2\sigma_I^2}} \tag{6.76}$$

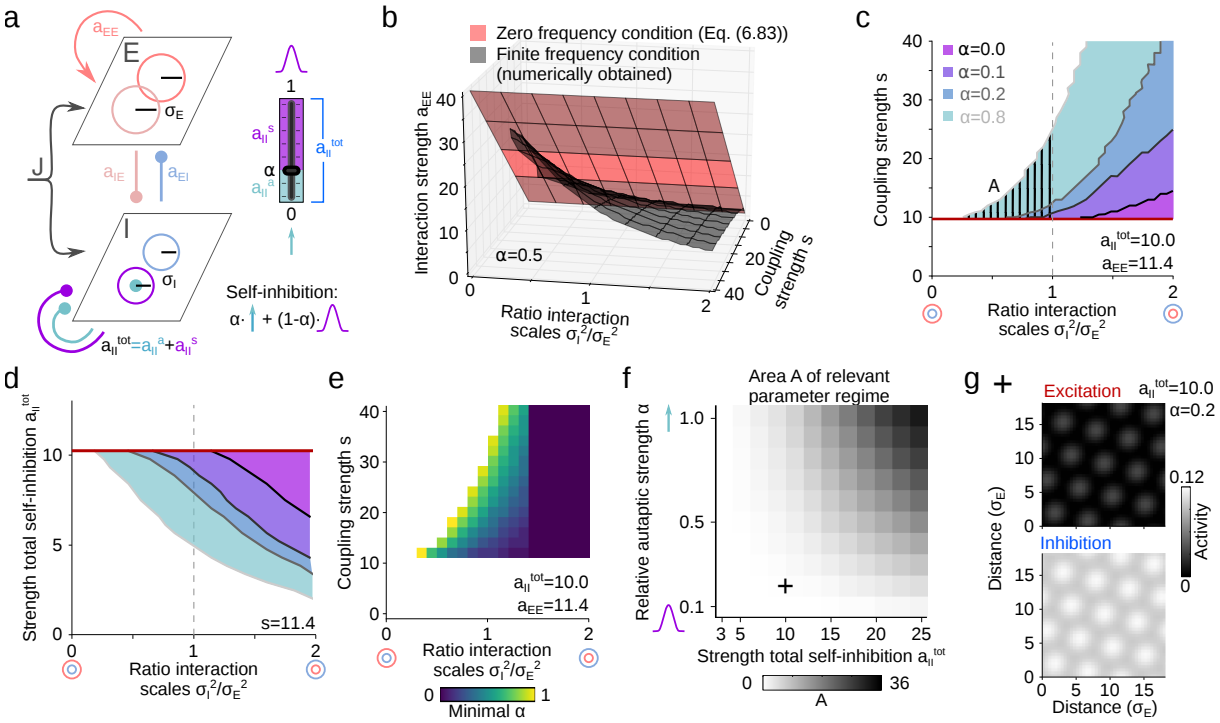

Figure 6.6: Weak local self-inhibition in extended network model is sufficient for modular network activity when inhibition has shorter range than excitation. **a** Schematic of extended network model of excitatory (E) and inhibitory (I) population. The connectivity between individual units follows a Gaussian profile (colored circles). The self-inhibition consists of a spatially distributed term (purple) with strength a_{II}^s and a local term (green) with strength a_{II}^l. These two terms combined give the total self-inhibitory strength a_{II}^{tot} (blue). The relative strength of local self-inhibition is given by α. **b** 3d phase diagram of the pattern forming regime as a function of a_{EE}, $r = \sigma_I^2/\sigma_E^2$ and $s = (a_{EI}a_{IE})/(1 + a_{II}^{\text{tot}})$. The pattern forming regime is contained between the red surface corresponding to condition (6.85), and the black surface which is obtained numerically requiring that the eigenvalue of the linearized dynamics is positive around a finite frequency. Here $\alpha = 0.5$. **c-d** 2d projections of the 3d phase diagram in (**b**) with one parameter fixed, respectively. Red (gray) line corresponds to red (black) surface in (**b**). **c** Phase diagram as a function of r and s for $a_{EE} = 11.4, a_{II}^{\text{tot}} = 10.0$. Note that modular activity can form when inhibition has shorter range than excitation ($r < 1$) for sufficiently strong α. The dashed area A indicates the region of the pattern forming regime where $r < 1$. **d** Phase diagram as a function of r and a_{EE} for $s = 11.4, a_{II}^{\text{tot}} = a_{EE} - 1.4$. **e** Phase diagram for $a_{EE} = 11.4, a_{II}^{\text{tot}} = 10.0$ showing the minimal relative autaptic strength α that is required for the network to form modular activity. **f** With increasing relative strength α and increasing total strength a_{II}^{tot} of self-inhibition, area A increases (with $a_{EE} = 1.4 + a_{II}^{\text{tot}}$). The cross indicates the parameter setting shaded in (**c**). **g** Examples of simulated solutions of extended network for excitatory (*top*) and inhibitory (*bottom*) populations. Parameters used are $a_{EE} = 11.4, a_{IE} = 11.5, a_{EI} = 10.9, a_{II}^{\text{tot}} = 10.0, \alpha = 0.2, \sigma_E = 0.055, \sigma_I = 0.048$.

where a^l_{II} denotes the strength of the local self-inhibition and a^s_{II} describes the strength of the spatially extended self-inhibition. We assume the same spatial scale σ_I for inhibitory to inhibitory and inhibitory to excitatory connections (**Fig. 6.6a**).
First, we investigate how the spatially extended self-inhibition influences the boundaries of the pattern forming regime. In particular, we assess how the relative strengths of the two self-inhibition terms, a^l_{II} and a^s_{II}, change the boundaries relative to r. To this end, analogous to the model with purely local self-inhibition we determine the conditions for a finite wavelength instability by applying linear stability analysis around the spatially homogeneous fixed point solutions[430,130,129,226,14]. Spatially homogeneous fixed points are now given by

$$\bar{u}_E = J\frac{1 + a^l_{II} + a^s_{II} - a_{EI}}{(1 + a^l_{II} + a^s_{II})(1 - a_{EE}) + a_{EI}a_{IE}} \tag{6.77}$$

$$\bar{u}_I = J\frac{1 + a_{IE} - a_{EE}}{(1 + a^l_{II} + a^s_{II})(1 - a_{EE}) + a_{EI}a_{IE}} \tag{6.78}$$

$$\text{assuming that} \quad a_{EI}a_{IE} > (a^l_{II} + a^s_{II} + 1)(a_{EE} - 1), \tag{6.79}$$

$$a^l_{II} + a^s_{II} + 1 > a_{EI} \tag{6.80}$$

$$a_{IE} + 1 > a_{EE} \tag{6.81}$$

Note that these fixed points are similar to the fixed points in the model with only local self-inhibition except that the sum of the local and spatially extended self-inhibition replaces the purely local term. For the eigenvalues $\lambda_{1/2}$, trace T and determinant D we obtain

$$\lambda_{1/2}(k) = \frac{1}{2}\left(T(k) \pm \sqrt{T(k)^2 - 4\,D(k)}\right) \tag{6.82}$$

$$\text{with} \quad T(k) = a_{EE}\tilde{M}_{EE}(k) - a^s_{II}\tilde{M}^s_{II}(k) - a^l_{II} - 2, \tag{6.83}$$

$$D(k) = (1 + a^s_{II}\tilde{M}^s_{II}(k) + a^l_{II})(1 - a_{EE}\tilde{M}_{EE}(k)) + a_{IE}a_{EI}\tilde{M}_{IE}(k)\tilde{M}_{EI}(k). \tag{6.84}$$

Unlike in the minimal network model, the parameter region for the pattern forming regime cannot be expressed in closed form. We can write down the conditions that the eigenvalue is negative at $k = 0$ which corresponds to the trace $T(k = 0)$ being negative and the determinant $D(k = 0)$ being positive at zero frequency

$$a_{EE} < s + 1, \tag{6.85}$$

$$a_{EE} < a^l_{II} + a^s_{II} + 2 \tag{6.86}$$

where the normalized coupling strength is now defined as $s = \frac{a_{EI}a_{IE}}{1+a^s_{II}+a^l_{II}}$. Note that the sum of the strengths of the self-inhibitory connectivity $a^s_{II} + a^l_{II}$ replaces the local self-inhibitory weight a_{II} in the corresponding condition of the model with only local self-inhibition. Analogous to the case there, an increase in the total strength of self-inhibition $a^{\text{tot}}_{II} = a^l_{II} + a^s_{II}$ relaxes the upper limit on the interaction strength a_{EE}. To differentiate between the relative contributions of the local and the spatially extended self-inhibition, we parametrize the relative strengths of both terms as

$$a^s_{II} = (1 - \alpha)\, a_{II}, \tag{6.87}$$

$$a^l_{II} = \alpha\, a_{II}. \tag{6.88}$$

α tunes the strength of the local connections relative to the strength of the spatially extended connectivity. For $\alpha = 0$ the local connectivity term vanishes, for $\alpha = 1$ the inhibitory to inhibitory connections consist only of the local connectivity term (corresponding to the minimal

network model), and for $\alpha = 0.5$ both terms are equally strong. Importantly, for all values of α the sum of the self-inhibitory connectivity strengths a_{II}^{tot} remains the same. This parametrization allows us to assess the influence of the total and the relative self-inhibitory strength, respectively, on the formation of modular activity.

Next, we solve numerically for the remaining condition which requires the eigenvalue of the system's linearized dynamics to be positive for some interval around a finite frequency. Unlike in the model with purely local self-inhibition, this condition depends directly on a_{II}^{tot} and α. Thus, to visualize the pattern forming regime we use Eq. (6.86) to choose an appropriate value for a_{II}^{tot} and systematically vary α. In **Fig. 6.6b** we combine the numerical results with the analytically derived condition (Eq. (6.85)) to show the boundaries of the pattern forming regime in the parameter space of the three effective parameters a_{EE}, s and r, as before. The red surface shows the analytically derived condition given in Eq. (6.85) and the black surface is numerically obtained. The boundaries are shown for a network where the local and the spatially extended self-inhibitory terms have equal strength ($\alpha = 0.5$). With this setting the pattern forming regime extends into the parameter region where inhibition has a shorter range than excitation. This is not the case in the absence of local self-inhibition ($\alpha = 0$, $a_{II}^{\text{tot}} = a_{II}^{s} = 10.0$; purple area in **Fig. 6.6c**), consistent with previous studies [226,14]. However, a relative strength of local self-inhibition of $\alpha = 0.1$ - that means the local part provides 10% of the strength of total self-inhibition - is already sufficient to considerably extend the pattern forming regime into the parameter region where inhibition is of shorter range than excitation. Further increasing α leads to a further extension of the pattern forming regime by shifting the second condition (gray lines in **Fig. 6.6c**) even further into the regime of short range inhibition. The condition derived for the zero frequency mode remains unchanged when increasing α (red line in **Fig. 6.6c**).

Furthermore, just as in the model with purely local self-inhibition, increasing the total strength of self-inhibition a_{II}^{tot} while keeping the relative strength α fixed, also increases the size of the pattern forming regime in the region where inhibition has shorter range than excitation (**Fig. 6.6d**). The minimal strength of local self-inhibition decreases with an increase in the spatial range of inhibition compared to excitation and with a decrease in the coupling strength s (**Fig. 6.6e**). In a parameter region where inhibition has a noticable larger range than excitation (Mexican hat regime) a local self-inhibition term is not required anymore to form modular activity (dark blue colored region on the right side of **Fig. 6.6e**). To quantify the influence of α and a_{II}^{tot} on the extension of the pattern forming regime into the region of short-range inhibition, we determine the size A of this regime by integrating numerically from the intersection point of the two boundaries of the pattern forming regime to $r = 1$ while systematically varying α and a_{II}^{tot} (see shaded region in **Fig. 6.6c** and **Fig. 6.6f**). We find that both increasing the total strength self-inhibition and only its local part increases A (**Fig. 6.6f**). Lastly, we corroborate the boundaries of the pattern forming regime with numerical simulations. For parameter settings within the pattern forming regime the network generates modular and hexagonally arranged activity domains in the excitatory and inhibitory populations (**Fig. 6.6g**) as in the model with purely local self-inhibition.

To visualize the phase diagram and when estimating the size A of the relevant area of the pattern forming regime, we set $a_{II}^{\text{tot}} = a_{EE} - 1.4$ and choose a specific value for α to determine a_{II}^{s} and a_{II}^{l} since the conditions we solve numerically not only depend on the three effective variables a_{EE}, s and r but also directly on a_{II}^{s} and a_{II}^{l}. The results shown in **Fig. 6.6** are qualitatively similar for different parametrizations of α and a_{II}^{tot}.

In summary, we find that already for weak local self-inhibition a_{II}^{l} the network robustly generates modular activity even in a regime where inhibition has shorter range than excitation. Thus, also in the presence of spatially distributed self-inhibition localized self-inhibitory connections robustly support the formation of modular activity.

6.4 Model predictions to test model class

The analyses above demonstrate that local self-inhibition facilitates the formation of modular activity with a connectivity structure where inhibition is more short-range than excitation, thus making this general model class a plausible candidate for explaining how modular activity arises in the early cortex. In the remainder of this paper, we characterize the solutions of this model further, study several implications and derive critical, experimentally testable predictions, to provide the basis for a rigorous empirical test of this model class in the near future.

6.4.1 Effective Mexican hat profile in population activity

To begin with, we seek to obtain a better understanding of the basic mechanism that underlies the formation of modular activity in our network model. As pointed out before[129,226], even in the absence of an anatomical Mexican hat, an effective Mexican hat can arise if the disynaptic inhibition combining connections from E to I and from I to E extends further in space than the connections E to E. However, this mechanism requires a fast time scale of inhibition, which appears problematic given the relative slow dynamics associated with the synaptic transmission of GABA-ergic neurons[335,136,90,219,47]. Local self-inhibition offers an alternative possibility, as the following argument based on the linearized model equations shows. Local self-inhibition effectively increases the linear decay term of the inhibitory dynamics to $-(1 + a_{II})u_I(\vec{x}, t)$. Equivalently (after appropriately rescaling a_{KL} and J) this reduces the effective inhibitory time constant to $\tau_I/(1 + a_{II})$ such that the dynamics for inhibitory activity u_I reads

$$\frac{\tau_I}{1 + a_{II}} \frac{\mathrm{d}u_I(\vec{x}, t)}{\mathrm{d}t} = -u_I(\vec{x}, t) + \int \mathrm{d}\vec{y} \left(\frac{a_{IE}}{1 + a_{II}} M_{IE}(\vec{x}, \vec{y}) u_E(\vec{y}, t) \right) + \frac{J}{1 + a_{II}} \tag{6.89}$$

This suggests that local self-inhibition decreases the effective inhibitory time constant to a point that disynaptic lateral inhibition extends further than excitation, leading to the formation of modular network activity even if inhibition has shorter range than excitation.
To make this argument more explicit and rigorous, we consider the impulse response of the network with purely local self-inhibition, i.e. the transient response of the network to a brief, localized input applied to the excitatory population, starting from a spatially homogeneous fixed point. We observe that shortly after the application of the input, the activity spreads laterally in both the excitatory and inhibitory population (**Fig. 6.7a**). However, the activity of the inhibitory population spreads faster, resulting in a broader peak than in the excitatory population over a transient period (**Fig. 6.7b,c**). **Fig. 6.7b** shows the difference in lateral spread of activation between the excitatory and inhibitory population as a function of time. The lateral spread is measured by the wavelength of the response, which we estimated both in numerical simulations and from the analytical approximation derived above (**Fig. 6.7a**). Over time, this difference approaches zero, i.e. the lateral spread in both populations becomes matched (**Fig. 6.7b**). The difference in lateral spread between excitation and inhibition results in a Mexican hat-like input to both populations (shown for excitation in **Fig. 6.7d**). If the fixed point is unstable (the case shown in **Fig. 6.7a-d**) a spatially periodic (modular) pattern forms (**Fig. 6.7a,b**). If the homogenous fixed point is stable (the case shown in **Fig. 6.7e**), the amplitude of the inhibitory activity exceeds that of the excitatory activity and the activation decays to zero. In both cases we observe that transiently the network generates a Mexican hat-like response with a more localized activation in the excitatory population and a wider activation of inhibitory units (**Fig. 6.7**).
In the following we briefly give the mathematical derivation of the impulse responses in the network. We apply the pulse like input at time point t_0 centered at x_0 to the excitatory

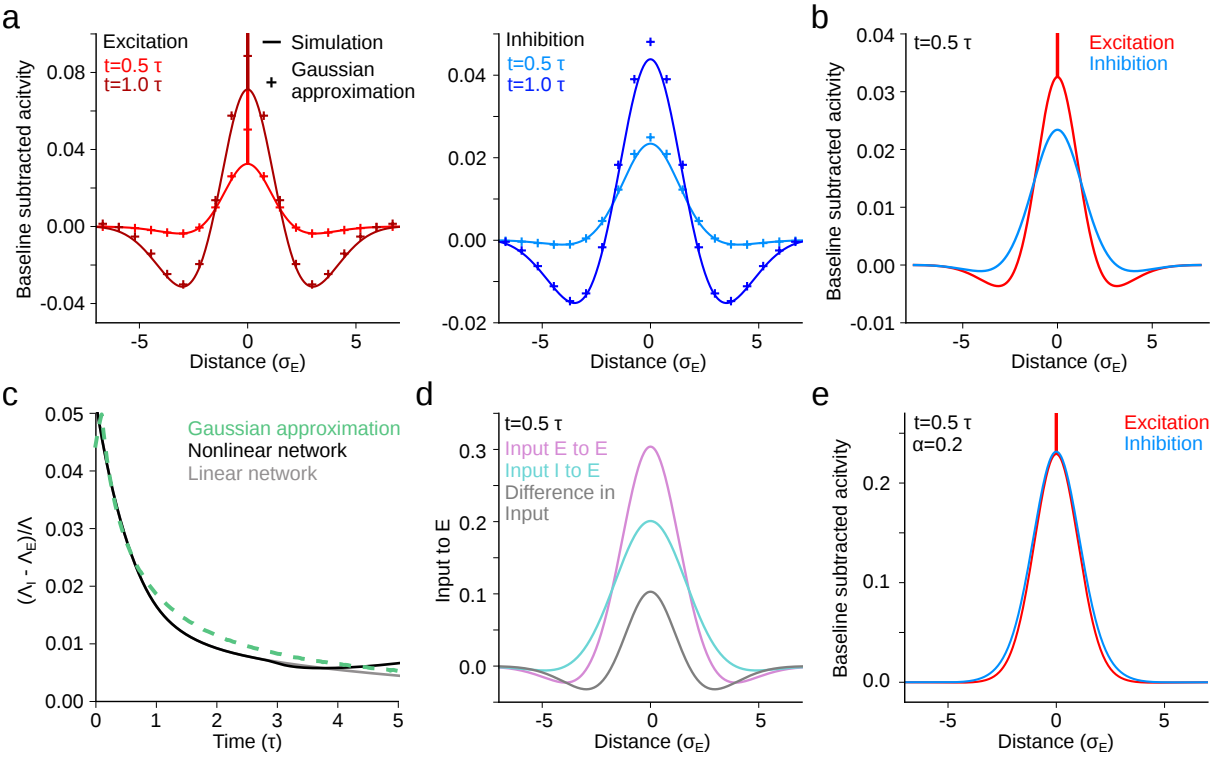

Figure 6.7: Effective Mexican hat-like activity to pulse-like stimulation. **a** Response of excitatory (*left*) and inhibitory (*right*) population to a pulse like stimulus at $t = 0$ at two different time points. The Gaussian approximation (cross; see Eqs. (6.103) and (6.104)) quantitatively agrees with the activity obtained in a simulated network (line). **b** The impulse input evokes an initially spatially localised response that is broader in inhibition (blue) than in excitation (red). Response at $t = 0.5\tau$. **c** The width of the inhibitory response (Λ_I) is larger than of the excitatory response (Λ_E). Over time this difference approaches zero. The difference in response widths obtained from the Gaussian approximation (green) agrees well for the linear regime of the nonlinear network (black) and the linear network (gray). Here the difference of the response widths is normalized by the wavelength Λ of the maximally amplified mode. In the simulations the response widths $\Lambda_{E/I}$ are obtained by fitting a plane wave with wavelength $\Lambda_{E/I}$ weighted by a Gaussian envelope to the responses (Eq. (6.106)). **d** Input to excitatory population has Mexican hat profile. Input from excitation (purple) is more spatially localized than inhibitory input (turquoise). **e** Impulse response for parameter settings outside of pattern forming regime. Here inhibition dominates the responses and leads to the decay of activity in time. Parameters used are $a_{EE} = 11.4, a_{IE} = 11.0, a_{EI} = 10.9, a_{II} = 10.0, \sigma_E = 0.066, \sigma_I = 0.058$ and $\alpha = 1$ (**a-d**), $\alpha = 0.2$ (**e**).

population around the spatially homogeneous fixed points. Since we are interested in the initial response, we consider the linearized equations for the dynamics (see Eqs. (6.13) and (6.14)) which read in one dimension

$$\begin{aligned}\frac{\mathrm{d}}{\mathrm{d}t}\begin{pmatrix}u_E(x,t)\\u_I(x,t)\end{pmatrix} - \int \mathrm{d}y \begin{pmatrix}a_{EE}M_{EE}(x-y)u_E(y,t) & -a_{EI}M_{EI}(x-y)u_I(y,t)\\ a_{IE}M_{IE}(x-y)u_E(y,t) & -a_{II}M_{II}(x-y)u_I(y,t)\end{pmatrix}\\ - \begin{pmatrix}u_E(x,t) & 0\\ 0 & u_I(x,t)\end{pmatrix} = \begin{pmatrix}1\\0\end{pmatrix}\delta(x-x_0)\,\delta(t-t_0).\end{aligned} \tag{6.90}$$

The system's impulse response is given by the Green's functions $(G_E(x,t), G_I(x,t))^T$. We solve for $G_E(x,t), G_I(x,t)$ by first applying a Fourier transformation to the system's equations to transform the convolution operator into a product between the Fourier transformed Green's functions $\tilde{\vec{G}}(k,t) = (\tilde{G}_E(k,t), \tilde{G}_I(k,t))^T$ and the Fourier transformed connectivity profiles $\tilde{M}_{KL}(k)$ (with $K, L \in \{E, I\}$). Next, we diagonalize these set of equations and obtain

$$\frac{\mathrm{d}}{\mathrm{d}t}\tilde{\vec{F}}(k,t) - \begin{pmatrix}\lambda_1(k) & 0\\ 0 & \lambda_2(k)\end{pmatrix}\tilde{\vec{F}}(k,t) = \sqrt{2\pi}\; S^{-1}\begin{pmatrix}1\\0\end{pmatrix} e^{-ikx_0}\;\delta(t-t_0) \tag{6.91}$$

where we have used $\tilde{\vec{F}}(k,t) = S^{-1}\;\tilde{\vec{G}}(k,t)$ with S^{-1} being defined previously. These dynamics are solved by an exponential ansatz and requiring that the solution is constant prior to giving the input pulse

$$\begin{aligned}\tilde{\vec{F}}(k,t) &= \sqrt{2\pi}\begin{pmatrix}\bar{u}_E\\ \bar{u}_I\end{pmatrix}\delta(k)\Theta(t_0-t) + \vec{a}(\vec{k})e^{\vec{b}(\vec{k})t}\;\Theta(t-t_0)\\ &= \sqrt{2\pi}\begin{pmatrix}\bar{u}_E\\ \bar{u}_I\end{pmatrix}\delta(k)\Theta(t_0-t) + \frac{\sqrt{2\pi}}{2c_2(k)}e^{-ikx_0}\begin{pmatrix}e^{\lambda_1(k)(t-t_0)}\\ -e^{\lambda_2(k)(t-t_0)}\end{pmatrix}\Theta(t-t_0).\end{aligned} \tag{6.92}$$

Prior to stimulus onset at t_0 the solution consists of a term that is constant in space, whereas afterwards it consists of an exponentially decaying response in time. To assess the widths of the inhibitory and excitatory response in cortical space, we consider the spatial form of the second term. To this end, we transform $\tilde{\vec{F}}(k,t)$ back to the Green's function of the excitatory and inhibitory population in cortical space. For simplicity, we omit in the following the constant term. We first transform $\tilde{\vec{F}}(k,t)$ from the eigenspace of the dynamics back to the space of the excitatory and inhibitory populations:

$$\begin{aligned}\tilde{\vec{G}}(k,t) &= S\;\tilde{\vec{F}}(k,t)\\ &= \frac{\sqrt{2\pi}}{2c_2}e^{-ikx_0}\begin{pmatrix}(c_1+c_2)e^{\lambda_1(t-t_0)} - (c_1-c_2)e^{\lambda_2(t-t_0)}\\ e^{\lambda_1(t-t_0)} - e^{\lambda_2(t-t_0)}\end{pmatrix}\Theta(t-t_0).\end{aligned} \tag{6.93}$$

Here we used S^{-1} in Eq. (6.21). c_1, c_2 are defined in Eqs. (6.22), (6.23). For brevity we omit the dependencies on the frequency k of $c_1, c_2, \lambda_1, \lambda_2$ in the equations above. Next, to obtain the Green's functions in cortical space, we apply the inverse Fourier transform

$$\begin{pmatrix}G_E(x,t)\\ G_I(x,t)\end{pmatrix} = \frac{1}{\sqrt{2\pi}}\int \mathrm{d}k\;\tilde{\vec{G}}(k,t)\;e^{ikx}. \tag{6.94}$$

As we are interested in the width of the excitatory and inhibitory responses, we consider in the following only the time and frequency dependent first term in Eq. (6.93). To solve the integral in the above equation, we apply two approximations to $\tilde{\vec{G}}(k,t)$. First, we assume that the larger eigenvalue $\lambda_1(k)$ exhibits a positive peak at some finite frequency whereas $\lambda_2(k) < \lambda_1(k)$ for all

k (see **Fig. 6.2**). Second, we approximate the exponential function in Eq. (6.93) by a Gaussian distribution.
Due to the first approximation, the terms in Eq. (6.93) that are proportional to $e^{\lambda_1(k)(t-t_0)}$ will dominate the contribution to the Fourier integral. We therefore neglect the remaining term that is proportional to $e^{\lambda_2(k)(t-t_0)}$. To simplify the expressions below, we define the following functions

$$g(k) = \frac{1}{2c_2(k)}, \tag{6.95}$$

$$f(k) = g(k)\ (c_1(k) + c_2(k)). \tag{6.96}$$

The Fourier transform of the Green's function for the excitatory population then becomes

$$\begin{aligned} G_E(x,t) &= \frac{1}{\sqrt{2\pi}} \int \mathrm{d}k\ \tilde{G}_E(k,t) e^{ikx} \\ &\approx \Theta(t-t_0) \int \mathrm{d}k\ e^{ik(x-x_0)} e^{\lambda_1(k)(t-t_0)}\ f(k) \\ &= \Theta(t-t_0) \int \mathrm{d}k\ e^{ik(x-x_0)} e^{\lambda_1(k)(t-t_0)+\log(f(k))}. \end{aligned} \tag{6.97}$$

The exponential function exhibits two peaks at k_f and $-k_f$. To solve this integral, we use Laplace's method and approximate these peaks with two Gaussian functions centered around k_f and $-k_f$. Note that the argument of the exponential function is time-dependent and that for sufficiently large times the logarithmic term only weakly alters this peak. For small times the logarithmic term monotonically increases with frequency and dominates. Thus the Gaussian function approximates the original function only poorly. To obtain the Gaussian approximation, we expand the argument of the exponential function in a Taylor series up to second order neglecting contributions from frequencies further away from $k_f, -k_f$. Therefore the expression simplifies to an integral over one Gaussian:

$$G_E(x,t) = \Theta(t-t_0) \int \mathrm{d}k\ \Big(e^{\lambda_1(k_f)(t-t_0)+\log(f(k_f))+\frac{1}{2}(\lambda_1''(t-t_0)+\frac{f''f-f'^2}{f^2})|_{k_f}(k-k_f)^2} + \tag{6.98}$$

$$+\ e^{\lambda_1(-k_f)(t-t_0)+\log(f(-k_f))+\frac{1}{2}(\lambda_1''(t-t_0)+\frac{f''f-f'^2}{f^2})|_{-k_f}(k+k_f)^2} \Big) e^{ik(x-x_0)} \tag{6.99}$$

$$= 2\ \Theta(t-t_0) e^{\lambda_1(k_f)(t-t_0)+\log(f(k_f))}\, \mathrm{Re}\left(\int \mathrm{d}k\ e^{ik(x-x_0)}\ e^{\frac{1}{2}(\lambda_1''(t-t_0)+\frac{f''f-f'^2}{f^2})|_{k_f}(k-k_f)^2} \right) + h.o.t. \tag{6.100}$$

where we have used that the real part of the second term of the integral is point symmetric to the first term whereas the imaginary part vanishes. The prefactor in the argument of the exponential function is the variance of the Gaussian envelope of the response in cortical space

$$\left(\sigma_E^{\mathrm{eff}}\right)^2 = -\left(\lambda_1''(k)(t-t_0) + \frac{f''(k)f(k) - f'(k)^2}{f(k)^2} \right)\Bigg|_{k_f}. \tag{6.101}$$

Plugging this expression into the integral yields

$$G_E(x,t) = 2\ \Theta(t-t_0) e^{\lambda_1(k_f)(t-t_0)} f(k_f)\, \mathrm{Re}\left(\int \mathrm{d}k\ e^{ik(x-x_0)} e^{\frac{1}{2}(k-k_f)^2\left(\sigma_E^{\mathrm{eff}}\right)^2} \right) + h.o.t. \tag{6.102}$$

$$= \frac{2\sqrt{2\pi}}{\sigma_E^{\mathrm{eff}}}\ f(k_f)\Theta(t-t_0)\ e^{\lambda_1(k_f)(t-t_0)}\ \cos(k_f(x-x_0))\ e^{-\frac{1}{2}(x-x_0)^2\left(\sigma_E^{\mathrm{eff}}\right)^{-2}} + h.o.t. \tag{6.103}$$

Eq. (6.103) shows that the impulse response consists of a plane wave that is damped in space by a Gaussian and exponentially decaying in time. The spatial frequency k_f describes the width of the excitatory response to a pulse like stimulus. The response width increases (k_f decreases) in time and depends via derivatives of $\lambda_1(k)$ and $f(k)$ directly on the connectivity parameters. The analogous calculation for the inhibitory response yields

$$G_I(x,t) = \frac{2\sqrt{2\pi}}{\sigma_I^{\text{eff}}}\, g(k_g)\, \Theta(t-t_0)\, e^{\lambda_1(k_g)(t-t_0)}\, \cos(k_g(x-x_0))\, e^{-\frac{1}{2}(x-x_0)^2\left(\sigma_I^{\text{eff}}\right)^{-2}} + h.o. \quad (6.104)$$

$$\text{with} \quad \left(\sigma_I^{\text{eff}}\right)^2 = -\left(\lambda_1''(k)(t-t_0) + \frac{g''(k)g(k) - g'(k)^2}{g(k)^2}\right)\Bigg|_{k_g}. \quad (6.105)$$

Here k_g denotes the peak location of the argument in the exponential function of $\tilde{G}_I(k,t)$. Closed-form expressions for k_f and k_g cannot be derived. Thus, also the variance of the responses of the excitatory and inhibitory populations $\left(\sigma_E^{\text{eff}}\right)^2, \left(\sigma_I^{\text{eff}}\right)^2$ are not analytically tractable. We therefore numerically determine values for k_f and k_g and assess their difference as a function of time $t-t_0$ (**Fig. 6.7**). To determine the widths of simulated excitatory and inhibitory impulse responses, we fit a plane wave weighted by a distance-dependent Gaussian profile to the responses

$$p_{E/I}(x) = \cos(\Lambda_{E/I}^{-1}(x-x_0))e^{-\frac{(x-x_0)^2}{2\sigma_{E/I}^{\text{eff}}}} \quad (6.106)$$

where Λ_E (Λ_I) denotes the fitted domain spacing of the excitatory (inhibitory) activity which we take as the width in response in **Fig. 6.7** and **Fig. 6.8**.

In the simulations we find that the inhibitory response is typically broader than the excitatory response (**Fig. 6.7a-c**) leading to a Mexican hat shaped input to the excitatory population (**Fig. 6.7d**). Although we cannot express k_f and k_g in closed form, we can show that within the pattern forming regime the inhibitory response is always broader than the excitatory response. To this end, we compare the equations defining k_f (see Eq. (6.97)) and k_g (see Eq. (6.93)) given by the derivative of the arguments of the exponential function in the solution of the Green's functions. The frequencies are given by

$$\frac{\mathrm{d}}{\mathrm{d}k}\left(\lambda_1(k)(t-t_0) + \log\left(\frac{c_1(k)+c_2(k)}{2c_2(k)}\right)\right)\Bigg|_{k_f} \stackrel{!}{=} 0 \quad (6.107)$$

$$\frac{\mathrm{d}}{\mathrm{d}k}\left(\lambda_1(k)(t-t_0) + \log\left(\frac{1}{2c_2(k)}\right)\right)\Bigg|_{k_g} \stackrel{!}{=} 0 \quad (6.108)$$

As k_f and k_g depend on time, we will consider in the following how different time scales influence both frequencies. First, in the limit of large times the term proportional to the time after stimulus onset dominates each equation leading k_f and k_g to converge to the frequency of the maximum in the eigenvalue. Thus, as k_f and k_g converge to the same value, the excitatory and inhibitory response approach the same width as well. In contrast, for very small times after stimulus onset, the terms independent of time dominate. These terms, however, do not show a peak like behaviour as a function of frequency. Thus, the Gaussian approximation is valid only after some time (approximated to be 0.1τ in **Fig. 6.8**). Next, we will therefore consider an intermediate time scale where the first term proportional to $t-t_0$ dominates such that the left hand side exhibits a peak-like behaviour at a finite frequency. We note that, Eqs. (6.107) and (6.108) only differ in the numerator of their logarithms. After applying the derivative, we rewrite these two equations as

$$\lambda_1(k)'(t-t_0) - \frac{c_2(k)'}{c_2(k)} = \begin{cases} -\frac{c_1(k)'+c_2(k)'}{c_1(k)+c_2(k)} & \text{for} \quad k_f \\ 0 \quad \text{for} \quad k_g, \end{cases} \quad (6.109)$$

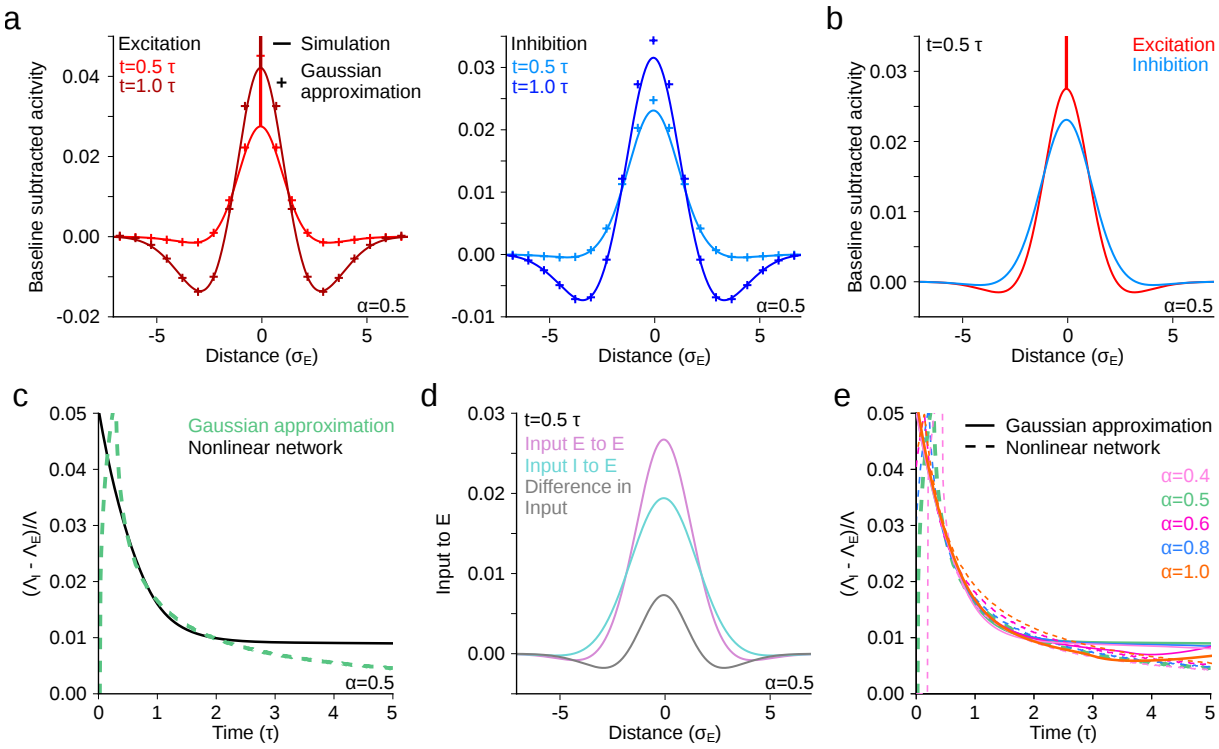

Figure 6.8: Extended network model also generates effective Mexican hat-like response activity to pulse like stimulation. **a** Response of excitatory (*left*) and inhibitory (*right*) population to a pulse like stimulus at $t = 0$ for two different time points. The Gaussian approximation (cross) quantitatively agrees with the activity obtained in a simulated network (line). **b** The impulse input evokes an initially spatially localized response that is broader in inhibition (blue) than in excitation (red). **c** Difference of width of the inhibitory response (Λ_I) and the excitatory response (Λ_E) approaches zero over time. The difference in response widths obtained from the Gaussian approximation (dashed green) agrees well for the linear regime of the nonlinear network (black). Here the difference of the response widths is normalised by the wavelength Λ of the maximally amplified mode. The response widths $\Lambda_{E/I}$ are obtained by fitting a plane wave with wavelength $\Lambda_{E/I}$ weighted by a Gaussian envelope to the simulated responses. **d** Input to excitatory population has Mexican hat profile. Input from excitation (purple) is more spatially localized than inhibitory input (teal). **e** For different strengths of local self-inhibition α the differential response width between excitation and inhibition varies only little. Parameters used are $a_{EE} = 11.4, a_{IE} = 11.0, a_{EI} = 10.9, a_{II} = 10.0, \sigma_E = 0.066, \sigma_I = 0.058$; (**a-d**) $\alpha = 0.5$.

To gain an understanding of these terms, we use from the definitions of $c_1(k), c_2(k)$ (Eqs. (6.22) and (6.23)) that $c_1(k) > 0$ and $c_2(k) > 0$ for all k. Further, both functions $c_1(k), c_2(k)$ rise monotonically with k. Thus, $-\frac{c_1(k)'+c_2(k)'}{c_1(k)+c_2(k)} < 0$ for all k. Second, the left hand side in the equation above must exhibit a change in sign from positive to negative reflecting the peak in its antiderivativ. Per definition the left hand side reaches zero at k_g, but reaches $-\frac{c_1(k)'+c_2(k)'}{c_1(k)+c_2(k)} < 0$ only at a higher frequency k_f. This shows that $k_f > k_g$ and yields the observed Mexican hat-shape of the excitatory and inhibitory responses.
In the following, we demonstrate that the extended network model generates Mexican hat-like responses to pulse-like stimuli analogous to the network with purely local inhibition. First, we extend the previously obtained results to the network with local and spatially extended self-inhibition by replacing the local self-inhibitory term $a_{II}\tilde{M}_{II}(\vec{k})$ with the full term $a^s_{II}\tilde{M}_{II}(\vec{k}) + a^l_{II}$. We find that the inhibitory and excitatory responses agree equally well with the Gaussian approximation (**Fig. 6.8a**). Analogous to the network with purely local self-inhibition the inhibitory response is broader than the excitatory response (**Fig. 6.8b**) and their difference approaches zero over time (**Fig. 6.8c**). The input to the excitatory population shows a Mexican hat-like profile (**Fig. 6.8d**). Intriguingly, the difference in response width between excitation and inhibition remains fairly robust against varying the local self-inhibition strength α (**Fig. 6.8e**). In the following we give an intuition why this is the case. In our approximation the frequencies k_f and k_g are dominated by the location of the maximum of the eigenvalue which can be approximated by the location of the minimum of the determinant. Dividing the determinant explicitly in the terms dependent and independent of α yields:

$$\begin{aligned} D(k) = (1 + a_{II}) \left(s\tilde{M}_{EI}(\vec{k})\tilde{M}_{IE}(\vec{k}) + 1 - a_{EE}\tilde{M}_{EE}(\vec{k}) \right) + \\ a_{II}(\alpha - 1) \left((a_{EE}\tilde{M}_{EE}(\vec{k}) - 1)\tilde{M}_{II}(\vec{k}) + 1 - a_{EE}\tilde{M}_{EE}(\vec{k}) \right). \end{aligned} \tag{6.110}$$

From this we find that both parts are composed of very similar terms. Indeed, the second part closely matches the shape of the first part only shifted by a constant depending on α (**Fig. 6.9**). Thus, instead of modifying the location of the minimum, the second term effectively acts as a multiplying factor to the first term. Therefore the location of the maximum of the maximal

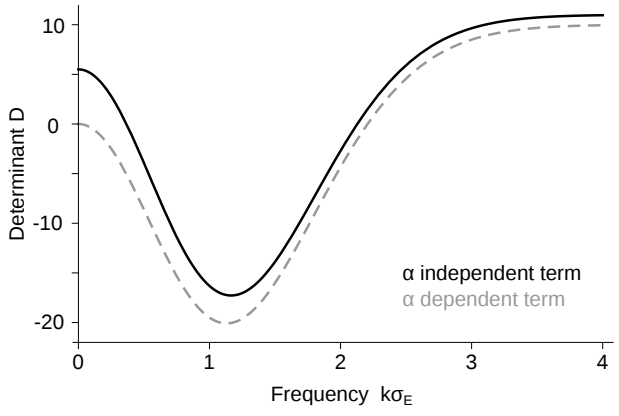

Figure 6.9: Peak in determinant remains stable when varying the strength of local self-inhibition. Dividing the determinant into its α independent part (black solid line) and the part multiplied by α (gray dashed line; compare Eq. (6.110)) shows that both terms exhibit their peak at nearly the same frequency. The location of the local minimum of the entire determinant is thus changed only little when varying α. Parameters used are $a_{EE} = 11.4, a_{IE} = 11.0, a_{EI} = 10.9, a^{\text{tot}}_{II} = 10.0, r = 0.8$.

eigenvalue also changes only little when varying α. This in turn leads to frequencies k_f and k_g which remain robust against changes in α.

6.4.2 Intimate relationship between excitatory and inhibitory activity

From cortical studies it is currently unclear whether the activity of inhibitory neurons is modular to a similar degree as has been observed for pyramidal neurons and whether the activity of inhibitory neurons is largest inside the domains showing high excitatory cell activity or in between these domains[231,445,444,389]. Our model makes several specific and testable predictions about the spatial relationship of domains of activity in excitatory and inhibitory neural populations as well as the relative magnitude of spatial modulation of activity.

The active domains in the excitatory and inhibitory populations are aligned with each other

The excitatory and inhibitory activity patterns are oriented such that their low and high activity domains are aligned, respectively (**Fig. 6.1**; to be shown below). This behaviour is due to two features of the dynamics. First, the dynamics ensure that the individual modes that form the excitatory and inhibitory activity patterns differ only in amplitude but not in phase. Second, as the activity patterns are dominated by the spatial frequency that is maximally amplified by the recurrency the difference in amplitude is (approximately) the same for all modes. Taken together, the activity patterns must then be co-localized with only a difference in amplitude and baseline.
In the following we provide a formal argument for the co-alignment between excitation and inhibition focusing on the case with only local self-inhibition. We assume that in general the excitatory and inhibitory activities can be described by a sum of N Fourier modes with wave vectors $\vec{k}_j$ whose modulus is their spatial frequency k_j. Considering the linearized dynamics (Eqs. (6.13) and (6.14)), the activity is thus expressed by

$$u_E(\vec{x},t) = \sum_{j=1}^{N} c_j \; e^{\lambda_1(k_j)t} \cos(\vec{k}_j\vec{x}), \tag{6.111}$$

$$u_I(\vec{x},t) = \sum_{j=1}^{N} d_j \; e^{\lambda_1(k_j)t} \cos(\vec{k}_j\vec{x} + \phi_j). \tag{6.112}$$

where the term for the smaller eigenvalue λ_2 has again been neglected assuming that $\lambda_1(k_{\max}) >> \lambda_2(k_{\max})$ (compare to Eq. (6.93)). c_j and d_j are coefficients. We suppose that the activity patterns grow around the spatially homogeneous fixed points $\bar{u}_E, \bar{u}_I$ and are shifted to each other by a constant phase $\phi_j = \vec{k}_j\vec{x}_0$ determined by the shift $\vec{x}_0$ in x, y space. To assess under which phase shift ϕ_j the excitatory and inhibitory activity patterns can grow, we plug the expressions for $u_E(\vec{x},t)$ and $u_I(\vec{x},t)$ into the dynamics of the linearized system (Eqs. (6.13) and (6.14)) and obtain

$$\begin{aligned}\sum_j e^{\lambda_1(k_j)t} \Bigg[-\lambda_1(k_j) \begin{pmatrix} c_j \cos(\vec{k}_j\vec{x}) \\ d_j \cos(\vec{k}_j\vec{x}+\phi_j) \end{pmatrix} - \begin{pmatrix} c_j \cos(\vec{k}_j\vec{x}) \\ d_j \cos(\vec{k}_j\vec{x}+\phi_j) \end{pmatrix} + \\ + \begin{pmatrix} a_{EE}\tilde{M}_{EE}(k_j) & -a_{EI}\tilde{M}_{EI}(k_j) \\ a_{IE}\tilde{M}_{IE}(k_j) & -a_{II} \end{pmatrix} \begin{pmatrix} c_j \cos(\vec{k}_j\vec{x}) \\ d_j \cos(\vec{k}_j\vec{x}+\phi_j) \end{pmatrix} \Bigg] = 0\end{aligned} \tag{6.113}$$

where we solved the integral over the connectivity matrix. As cosine and sine are orthogonal to each other for different $\vec{k}_j$, the set of equations must hold for each mode independently for all

$\vec{x}$. Then, rewriting the cosine containing the phase shift as the weighted sum of a cosine and a sine yields

$$\begin{aligned} 0 &= [(-\lambda_1(k_j) + a_{EE}\tilde{M}_{EE}(k_j) - 1)\ c_j - a_{EI}\tilde{M}_{EI}(k_j)\ d_j \cos\phi_j] \cos(\vec{k}_j\vec{x}) + \\ &\quad + a_{EI}\tilde{M}_{EI}(k_j)\ d_j \sin(\vec{k}_j\vec{x}) \sin\phi_j \\ 0 &= [a_{IE}\tilde{M}_{IE}(k_j)\ c_j + (-\lambda_1(k_j) - a_{II} - 1) d_j \cos\phi_j] \cos(\vec{k}_j\vec{x}) - \\ &\quad - (-\lambda_1(k_j) - a_{II} - 1) d_j \sin(\vec{k}_j\vec{x}) \sin\phi_j \end{aligned} \tag{6.114}$$

In the following, we determine how ϕ_j must be chosen such that the equations above are satisfied. The terms proportional to $\sin(\vec{k}_j\vec{x})$ vanish only if either $d_j = 0$ or $\phi_j = n_j\pi$ with $n_j \in \mathbb{N}$. If $d_j = 0$, then the terms proportional to $\cos(\vec{k}_j\vec{x})$ only vanish for $c_j = 0$. To obtain a nontrivial solution with nonzero coefficients c_j, d_j the phase shift ϕ_j must therefore be a multiple of π. Then, only the terms proportional to $\cos(\vec{k}_j\vec{x})$ are left and the coefficients must satisfy

$$0 = [-\lambda_1(k_j) + a_{EE}\tilde{M}_{EE}(k_j) - 1]\ c_j - a_{EI}\tilde{M}_{EI}(k_j)\ d_j(-1)^{n_j} \tag{6.115}$$

$$0 = a_{IE}\tilde{M}_{IE}(k_j)\ c_j + [-\lambda_1(k_j) - a_{II} - 1] d_j(-1)^{n_j}. \tag{6.116}$$

Next, by solving these equations for d_j, we can relate the two coefficients by

$$d_j(-1)^{n_j} = c_j \frac{-\lambda_1(k_j) + a_{EE}\tilde{M}_{EE}(k_j) - 1}{a_{EI}\tilde{M}_{EI}(k_j)} \tag{6.117}$$

$$d_j(-1)^{n_j} = c_j \frac{a_{IE}\tilde{M}_{IE}(k_j)}{\lambda_1(k_j) + a_{II} + 1} \tag{6.118}$$

Using the expression for $\lambda_1(k)$ we show that the right hand sides of these equations are in fact equivalent. Note that the fraction on the right hand side denotes the ratio of the amplitudes of inhibitory to excitatory activity and is consistent with the formal derivation of the amplitude ratio given in the next section. Plugging this result into the expression for the inhibitory activity (Eq. (6.112)) yields

$$\begin{aligned} u_I(\vec{x}, t) &= \sum_{j=1}^{N} d_j(-1)^{n_j} e^{\lambda_1(k_j)} \cos(\vec{k}_j\vec{x}) \\ &= \sum_{j=1}^{N} c_j \frac{a_{IE}\tilde{M}_{IE}(k_j)}{\lambda_1(k_j) + a_{II} + 1} e^{\lambda_1(k_j)} \cos(\vec{k}_j\vec{x}). \end{aligned} \tag{6.119}$$

Comparing this expression to the excitatory activity (Eq. (6.111)) shows that each Fourier mode only differs in its amplitude, but importantly not by a phase shift. Assuming that the activity patterns are dominated by the fastest growing mode with frequency $k_{\max}$, the prefactor becomes independent of j and the inhibitory activity pattern can be expressed by the excitatory activity pattern

$$u_I(\vec{x}, t) = \frac{a_{IE}\tilde{M}_{IE}(k_{\max})}{\lambda_1(k_{\max}) + a_{II} + 1} \sum_{j=1}^{N} c_j e^{\lambda_1(k_{\max})} \cos(\vec{k}_j\vec{x}) \tag{6.120}$$

$$= \frac{a_{IE}\tilde{M}_{IE}(k_{\max})}{\lambda_1(k_{\max}) + a_{II} + 1} u_E(\vec{x}, t) \tag{6.121}$$

This result shows that the inhibitory activity does not exhibit a phase shift compared to excitation but instead the active domains in the excitatory and inhibitory activity align and only

differ in their amplitude and baseline.
Simulations of the full dynamics suggest that this result also holds for the nonlinear case. Moreover, considering the nonlinear equations we can make a similar argument. Again we assume that the excitatory and inhibitory patterns are dominated by modes with a frequency around $k_{\max}$. The argument of the rectifying nonlinearity is then the sum of these modes weighted by the coefficients and the connectivity matrix plus a constant. These activity patterns can potentially exhibit a phase shift compared to the activity patterns outside of the nonlinearity. However, applying the rectification conserves the location of the domains of peak activity (assuming they are positive). Further, the rectification conserves the peak frequency in the spectrum of the activity patterns but also leads to modes with higher order frequencies of lower amplitude. Thus, we can directly compare the phase of the pattern within the nonlinearity with the one outside which leads to the same comparison as in the linear case. Moreover, an anti-phasic solution where the excitatory activity pattern is shifted relative to the inhibitory activity by π is not stable. In such a scenario the amplitude of the excitatory activity would grow because it is excited by excitatory units from within the peak region and is inhibited by inhibitory units in the regions of low activity. In contrast the inhibitory activity would change such as to co-align with the excitatory activity pattern. The peaks in the inhibitory activity that are shifted relative to the peaks in the excitatory activity would decay due to the input from inhibitory units and little input from excitatory units in this region whereas inhibitory activity would inrease at the location of the excitatory activity peaks.

Amplitude ratio between excitation and inhibition

While in the model both the excitatory and inhibitory activity is always modular, the amplitude of spatial modulation can be relatively weak in the inhibitory population depending on the connectivity parameters. **Fig. 6.10** suggests that the amplitudes of the spatial modulation of excitatory and inhibitory activity can vary considerably across the pattern forming regime. To obtain an approximate closed-form expression we consider the linear dynamics around the unstable constant fixed point solution (with only local self-inhibition). Our estimate is based on the fastest growing mode approximated by the frequency $k_{\max}$. Following previous results the solution of the linearized dynamics in Fourier space for any mode is given by

$$\begin{pmatrix} \tilde{u}_E(\vec{k},t) \\ \tilde{u}_I(\vec{k},t) \end{pmatrix} = \tilde{v}_1(\vec{k},0) \begin{pmatrix} c_1(k)+c_2(k) \\ 1 \end{pmatrix} e^{\lambda_1(k)t} \tag{6.122}$$

where the term for the smaller eigenvalue λ_2 has been neglected assuming that $\lambda_1(k_{\max}) > \lambda_2(k_{\max})$ (compare to Eq. (6.93)). For sufficiently large times, the fastest growing mode for both excitation and inhibition is given by $k_{\max}$. In this limit, the ratio in amplitude between excitation and inhibition is given by the following time-independent expression

$$\begin{aligned} \left.\frac{u_E(\vec{k},t)}{u_I(\vec{k},t)}\right|_{k_{\max}} &= c_1(k_{\max}) + c_2(k_{\max}) \\ &= \frac{1}{2a_{IE}\tilde{M}_{IE}(k)} \left(a_{EE}\tilde{M}_{EE}(k) + a_{II} + \sqrt{\left(a_{EE}\tilde{M}_{EE}(k)+a_{II}\right)^2 - 4a_{IE}a_{EI}\tilde{M}_{IE}(k)\tilde{M}_{EI}(k)} \right)\Bigg|_{k=k_{\max}} \\ &= \frac{1}{2a_{IE}} \left(a_{EE} + a_{II}\, e^{\frac{k^2\sigma_E^2}{2}} + \sqrt{\left(a_{EE} + a_{II}\, e^{\frac{k^2\sigma_E^2}{2}}\right)^2 - 4a_{IE}a_{EI}\, e^{\frac{k^2(\sigma_E^2-\sigma_I^2)}{2}}} \right)\Bigg|_{k=k_{\max}} \end{aligned} \tag{6.123}$$

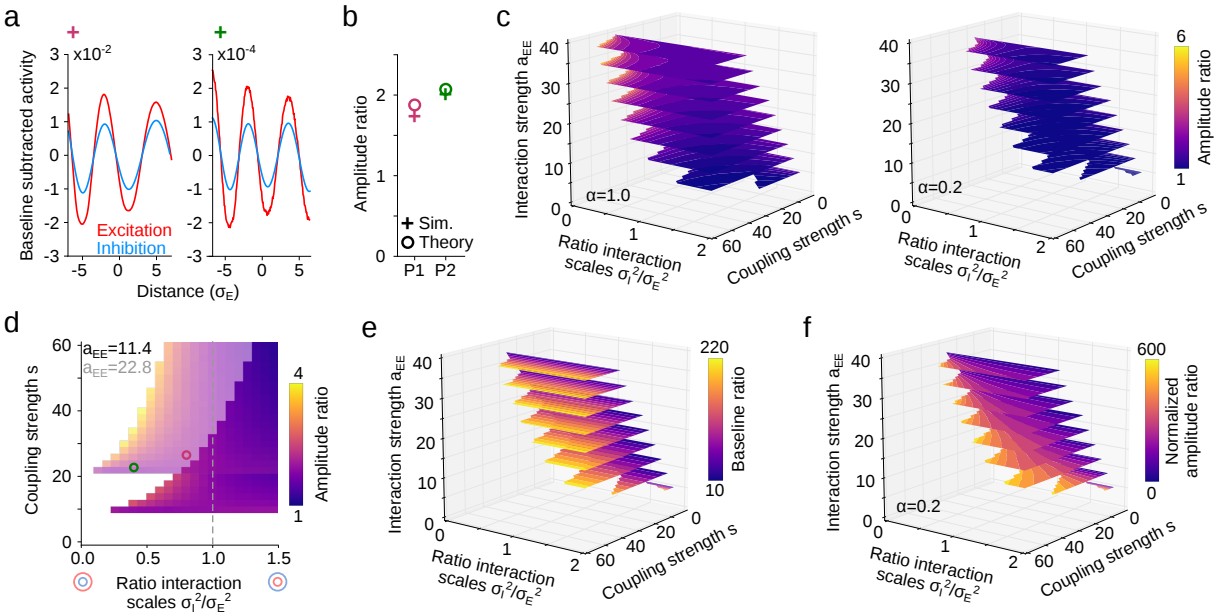

Figure 6.10: Excitatory population displays higher amplitude modulation of its spatial pattern than inhibition. **a** Network simulations with different connectivity settings leading to different ratios between the amplitudes of the excitatory (red) and inhibitory (blue) activity. Parameter settings used are $a_{EE} = 22.8, a_{EI} = 22.4, a_{II} = 21.4$ and in *left*: $a_{IE} = 26.5, \sigma_E = 0.063, \sigma_I = 0.058$ $(r = 0.8)$, *right*: $a_{IE} = 22.7, \sigma_E = 0.053, \sigma_I = 0.035$ $(r = 0.4)$. **b** Ratio of amplitude modulation obtained from solutions of linearized dynamics (circle) compared to simulations (cross). Parameters used are same as in (**a**) *right* (blue) and *left* (orange). **c** 3d phase diagram of amplitude ratio of activity between excitatory and inhibitory population for $\alpha = 1$ (*left*) and $\alpha = 0.2$ (*right*). Values are only shown within pattern forming regime. **d** 2d phase diagram of amplitude ratio for $a_{II} = a_{EE} - 1.95, a_{IE} = a_{EE} - 0.99, a_{EI}a_{IE} = s\,(1 + a_{II})$ and $a_{EE} = 11.4$ (solid) and $a_{EE} = 22.8$ (transparent). **e** Ratio of baseline activity between excitation and inhibition. **f** Amplitude ratio normalized by baseline activity.

With this expression we can systematically assess the modulation ratio as a function of the three effective parameters a_{EE}, s and r (**Fig. 6.10**). Since the ratio also explicitly depends on $a_{II}, a_{EI}a_{IE}, \sigma_E$ and σ_I, we set $\sigma_E = 1$ and used $a_{II} = a_{EE} - 1.95$, $a_{IE} = a_{EE} - 0.95$. Other parametrizations lead to qualitatively similar results. Note that this expression of the amplitude ratio is consistent with the expression obtained in the formal derivation of the co-alignment between excitation and inhibition given above.

Comparing the spatial modulation of the excitatory and inhibitory activity patterns in our simulations, we find that they co-vary, but differ in the amplitude of their modulation (**Fig. 6.10a**). We corroborate the ratio of their amplitudes from simulations (crosses in **Fig. 6.10b**) with an analytical approximation (circles in **Fig. 6.10b**; from Eq. (6.123) above). Intriguingly, the amplitude ratio varies notably up to a factor 6 across parameter space (**Fig. 6.10c,d**). It increases with increasing coupling strength s, but decreases with a_{EE} and with r (**Fig. 6.10c,d**). Note that we normalized the amplitude modulation by the baseline activity of each population (**Fig. 6.10e,f**), respectively, before calculating the modulation ratio, to provide a more robust measure of comparison with experiment (see Discussion).

6.4.3 The spacing of active domains is consistent with experimental data

In the following we investigate how well the domain spacing of the network activity corresponds to experimental data. The domain spacing is a feature of modular activity that can be very precisely determined in experiments[229,230,231]. Applying this sensitive readout to patterns of early spontaneous activity[389] yields a precise measure of the experimentally observed domain spacing.

Estimating the spacing between active domains

Fig. 6.11 suggests that within the pattern forming regime the spacing Λ of the active domains in the modular pattern can vary considerably. Expressed in units of σ_E, the spatial wavelength can be approximated by $\Lambda = 2\pi/(k_{\max}\sigma_E)$ where $k_{\max}$ is the location of the frequency at the maximum of the larger eigenvalue $\lambda_1(k)$ (Eq. (6.24); **Fig. 6.11**). We determine $k_{\max}$ by setting the derivative of the maximal eigenvalue λ_1 (Eq. (6.24); local self-inhibition) w.r.t. k to zero which yields

$$a_{EI}a_{IE}\,(1+r)^2\,\tilde{M}_{EI}(k) - (1+r)\,a_{EE}\,a_{II} - a_{EE}^2 r\,\tilde{M}_{EE}(k)\Big|_{k=k_{\max}} = 0. \tag{6.124}$$

$k_{\max}$ is a function of $a_{EI}a_{IE}, r, a_{EE}, a_{II}$. This equation cannot be solved analytically for $k_{\max}$. Instead, to assess the boundaries within the parameter space that allows to form modular activity, we solve it numerically by systematically varying the three effective parameters a_{EE}, s and r and fixing a_{II} such that it satisfies constraint Eq. (6.32) which fixes the coupling strengths to $a_{EI}a_{IE} = s\,(1 + a_{II})$.

Comparing domain spacing between model and experimental data

First, we characterize the domain spacing Λ of the modular network activity. Interestingly, we find that the domain spacing is not simply proportional to the interaction range of the excitatory population σ_E, but can vary considerably for a given σ_E (**Fig. 6.11a,b**). We corroborate the values of the domain spacing obtained in simulations (crosses in **Fig. 6.11a**, right) with the theoretically expected value for the domain spacing based on the peak location of the maximal eigenvalue of the linearized system (circles in **Fig. 6.11a**, right and **Fig. 6.11b**). To visualize the range in domain spacing as a function of the network connectivity, we plot Λ as a function of the three effective variables a_{EE}, s and r. We find that it varies at least by a factor of 6 within the chosen parameter regime (**Fig. 6.11**). To visualize Λ we choose the following parametrizations $a_{II} = a_{EE} - 1.95$, $a_{EI}a_{IE} = s(1 + a_{II})$. We take care of the dependency on σ_E, by expressing Λ in units of σ_E ($\Lambda \Rightarrow \Lambda/\sigma_E$). With this formulation we can express σ_I in terms of r. Choosing a different parametrization of a_{II} yields qualitatively similar results. A cut through the 3d phase diagram of Λ for a fixed a_{EE} shows that the wavelength increases with increasing r and a_{EE}, and with decreasing s (**Fig. 6.11d**).
Next, we compare the domain spacing Λ of the network model to experimental data. To assess whether the model values for Λ are in agreement with experimentally observed values, we compare them to the domain spacing observed in early ferret visual cortex normalized by the measured width of excitatory connectivity. Importantly, we compare the model to data from the early cortex since at early stages in development the anatomical long-range connections are only immaturely developed, and therefore the horizontal connectivity is well described by local connections as assumed in our network model. The typical spatial scale of activity patterns in visual cortex of young ferrets is about 1 mm[389], while the scale of excitatory connections lies at around 250 µm[80]. This yields an experimentally observed domain spacing on the order of 4 σ_E which is consistent with model values in a broad parameter regime, in particular also in a

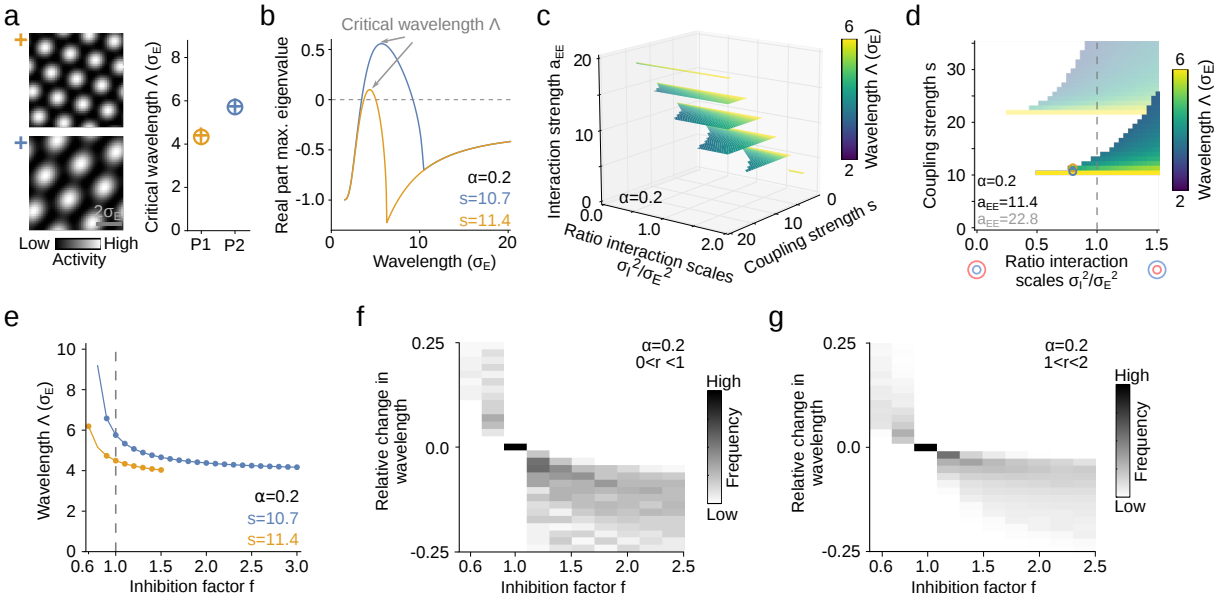

Figure 6.11: Domain spacing varies considerably across phase diagram. **a** Different connectivity settings lead to activity patterns (*left*) with different critical wavelengths (i.e. spacing between active domains). Parameters used for simulations are $a_{EE} = 11.4, a_{EI} = 10.9, a_{II}^{\text{tot}} = 10.0, \alpha = 0.2, \sigma_E = 2.2, \sigma_I = 1.9$ and *top*: $a_{IE} = 11.5$ (orange), *bottom*: $a_{IE} = 10.8$ (blue). Critical wavelength Λ (*right*) obtained from peaks in spectrum of simulated solutions (cross) and from the peak location of the real part of the larger eigenvalue λ_1 of the linearized system (circle) match. **b** Λ is analytically derived from the peak location of the real part of eigenvalue λ_1 of the linearized system. **c** 3d phase diagram displaying Λ. Values are only shown within pattern forming regime. The wavelength is plotted in units of σ_E. **d** 2d diagram of Λ for fixed $a_{EE} = 11.4$. The wavelength increases with increasing ratio of spatial scale σ_I^2/σ_E^2 and with decreasing value of s. Note that the wavelength depends also directly on a_{II}^{tot} and the product $a_{EI}a_{IE}$. Here, we set $a_{II}^{\text{tot}} = a_{EE} - 1.95$ and $a_{EI}a_{IE} = s\,(1 + a_{II}^{\text{tot}})$. **e** When increasing inhibition by a factor ($a_{EI} \to f a_{EI}$, $a_{II}^{\text{tot}} \to f a_{II}^{\text{tot}}$), Λ decreases. Same parameters used as in (**a**). **f-g** Change in critical wavelength induced by change in inhibitory strength. Distribution taken over parameter region shown in (**c**) up to $r = 1$ (**f**) and for $1 < r < 2$ (**g**). Here $\alpha = 0.2$.

regime where $r < 1$ (**Fig. 6.11c,d**).
The large range of values of the domain spacing in the model is itself consistent with the variability observed in the domain spacing between different species and cortical areas, e.g. the domain spacing varies between 0.5 mm in primary visual cortex of tree shrew[231] and marmoset[358,294] to 2 mm in secondary visual cortex of owl monkey[456]. Thus, changes in the connectivity parameters between species and cortical areas potentially explain the observed variability in the domain spacing.

6.4.4 Manipulating inhibition and its effect on activity domain spacing

The spacing of active domains can be measured with high accuracy in experimental data [229,230,231]. Using widefield calcium imaging, it could be assessed whether the domain spacing changes when transiently altering connectivity parameters. For instance, systematically changing the overall strength in inhibition is possible in the network and in experiment using pharmacological [184] or optogenetical tools [70,421,282,84]. We therefore investigate how Λ changes

as a function of inhibition strength in the network. We increase (decrease) network inhibition by increasing (decreasing) the connectivity strengths a_{EI} and a_{II} by a factor f. After systematically varying f we determine for each new setting the domain spacing. Increasing network inhibition leads to a robust decrease in the critical wavelength Λ (**Fig. 6.11e**). By determining the relative change in domain spacing over a broad regime of parameter settings (region used is shown in **Fig. 6.11c**), we obtain a distribution over the change in Λ. This distribution allows to determine the expected change in Λ for a given change in network inhibition, e.g. an increase in inhibition by 50% yields a decrease in domain spacing by about 25% (**Fig. 6.11f,g**). Even without the precise knowledge of the connectivity parameters in cortex we are able to compare the experimentally observed change with the expected change in the model. This prediction cannot distinguish between a network with Mexican hat-like connectivity and connectivity where the inhibitory interaction range is greather than that of excitation, as the domain spacing Λ robustly decreases with increasing inhibition independent on the specific parameter region (**Fig. 6.11f,g**). Therefore, the prediction allows to test the network class.

The decrease in spacing of active domains when the total amount of inhibition increases is a

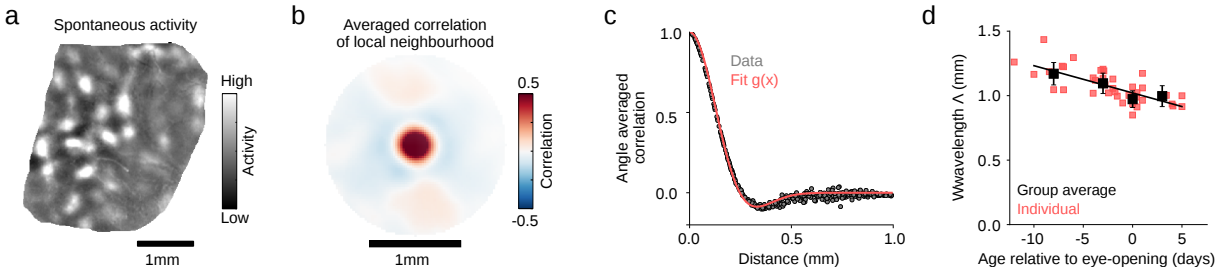

Figure 6.12: The spacing between spontaneously active domains decreases with age in the early ferret visual cortex. **a** Example of spontaneous activity pattern in ferret visual cortex at eye-opening (EO). **b** 2D spatial correlation function of spontaneous activity averaged across all locations within field of view. **c** Its radial average (gray) with fit $g(x) = \exp(-\frac{x^2}{2\sigma^2})\cos(\frac{2\pi}{\Lambda}x)$ (red) to estimate the spacing of active domains Λ. **d** Λ decreases with age during period of increasing inhibition[440]. Individual animals (red) and average across age groups (age<-5,<-1,=EO,¿EO; black). Scale bar: 1 mm (**a,b**).

critical prediction of our model. Indeed, consistent with an increase of inhibition in the developing visual cortex[440], we observe that the spacing of spontaneously active domains decreases with age in early ferret visual cortex. In this analysis we determined the domain spacing in spontaneous activity across development (compare Section 4.2.6 in Chapter 4). To this end, we computed the correlation patterns for each seed point across the spontaneous activity patterns and averaged these after centering each to its seed point (**Fig. 6.12a,b**). This average correlation pattern was then integrated over its angular dependence to obtain the average correlation as a function of distance to the seed point (**Fig. 6.12c**). Next, we fitted a Gabor function $g(x)$ (Eq. (4.4); a Gaussian function modulated by a plane wave) to these correlation coefficients. Each fit yields a value for the domain spacing Λ (**Fig. 6.12d**). Consistent with the increase of inhibition during the development of visual cortex, the domain spacing in spontaneous activity decreases.

To experimentally test this prediction a combination of techniques for the read-out and manipulation of cortical activity is required. There are several possible methods of how to potentially achieve this. As described before, one possibility is to use an all-optical approach combining fluorescence imaging and optogenetics with fluorescent markers and cell-type specific optogenetic actuators that are cross-talk free and highly sensitive[443,354,189,336,210,240,110,209].

Imaging cortical activity before and during optogenetical manipulation of inhibitory neurons reveals potential changes in domain spacing. Alternatively, Neuropixels probes together with optogenetical tools similarly allow to assess the change in domain spacing after manipulating inhibition. Instead of an optogenetical manipulation it might also be possible to use pharmacological tools such as GABA enhancing benzodiazepines[184], or inverse GABA agonists such as DMCM[184] or the antagonist picrotoxin[323,333].
Combining these three experimental measurements of the amplitude ratio, the domain spacing and the change in domain spacing after manipulating network inhibition, allows to test whether the network model provides a parameter regime that is in agreement with all of these three observables. In summary, we provided three clear predictions to critically test our suggested network model. Using recent technological advancements in the field makes the predicted observables now experimentally accessible.

6.5 Discussion

Here we proposed a novel mechanism for the formation of spatially modulated (modular) activity patterns. To assess the plausibility of the mechanism, we studied a neural network consisting of recurrently interconnected excitatory and inhibitory populations. We derived the boundaries of the parameter regime in which modular activity patterns form and verified the derived results with numerical simulations. We showed that self-inhibition broadens the regime in which the network robustly and reliably displays modular activity patterns extending towards a region where the spatial range of inhibition is smaller compared to excitation. While these calculations were performed using Gaussian connectivity profiles, we showed that similar results are obtained for exponential profiles. Moreover, by considering a biologically more plausible extension of the minimal network which incorporated both local and spatially extended self-inhibition, we demonstrated that already the presence of relatively weak local self-inhibtion led to the robust formation of activity patterns. We observed the formation of patterns across a broad range of connectivity settings including the regime in which excitatory connections to excitatory and inhibitory neurons are equally strong, whereas inhibition connects more strongly to excitatory than to inhibitory pools consistent with previous experimental results[393,345].
Recurrent network models describing the formation of modular activity have been extensively studied in the past and have been demonstrated to be able to generate modular activity assuming specific network architectures. Most of these models assumed a Mexican hat-type connectivity ensuring long-range inhibition and local excitation between units to generate activity patterns (e.g.[287,412,134,28,71,302,163]). However, experimental evidence for an anatomical Mexican hat is controversial. One of the few indications was based on glutamate uncaging experiments in slices of visual cortex in young ferrets[108]. In contrast electrode recordings in auditory cortex of adult mice indicate that the spatial scale of inhibition is more constrained than the one of excitation, whereas the spatial range of excitatory connections to inhibitory and excitatory neurons is similar[265]. Studies of layer 2/3 slices of ferret striate cortex show that the spatial extent of inhibitory inputs shrinks during the development to 300 µm[80] which is below the spatial range of excitation of typically 500 µm[108] in ferrets. Therefore, the anatomical studies appear inconsistent with a Mexican hat like distributed connectivity profile and it remains unclear whether lateral connections in cortex support the formation of modular activity.
To circumvent this issue previous work suggested to introduce fast inhibition to enable the formation of patterns in the absence of lateral inhibition[346,226]. These studies found that in the regime of local inhibition ($\sigma_I < \sigma_E$) a network with a fast or instantaneous inhibitory timescale amplifies spatial fluctuations and leads to the formation of modular activity patterns. In this

setup modular activity forms since fast inhibitory units have a large effective spatial range via a disynaptic path that exceeds the excitatory range, thus resulting in an effective Mexican hat like connectivity profile. However, experimental evidence is inconsistent with the assumption of fast inhibition. The typical decay time constant of the most abundant receptor in cortex $GABA_A$ is larger than the timescale of AMPA receptors[335,136,90,219,47]. Further, in the case of non-instantaneous inhibitory units the disynaptic path (E to I to E), leads to a transmission delay compared to the monosynaptic E to E transmission which was shown to impair the formation of modular activity[316,21]. Only carefully tuned transmission delays that are specific for transmission from E to E, E to I and I to E lead to the formation of such activity[21]. Here we argued that local self-inhibitory connections effectively shorten the inhibitory timescale. Thus, by adapting the strength and range of self-inhibition modular activity can form even when the timescale of inhibition is of the same order of magnitude as the one of excitation.

A plausible implementation of the proposed mechanism is provided by autapses on inhibitory neurons. Anatomical studies have shown that autapses are abundantly present on inhibitory fast-spiking PV+ basket cells in visual cortex of cat[418] and somatosensory cortex of rat[24]. They are functioning comparable to synapses[24,96]. So far, relatively little is known about the function of autapses and they are only rarely included into the wiring diagram[431]. Currently, they are thought to play a role in maintaining spiking precision of neurons and contributing to the pace of whole cortical circuits[23]. It has further been suggested that autapses are well suited to self-control local excitability, or even control excitability on a sub-cellular level[208,24]. Autaptic self-inhibition provides a simple and direct disinhibition scheme for pyramidal neurons and a fast mechanism for feedback inhibition in inhibitory neurons[114]. Here we suggested a further function of autapses, namely to provide the network with the ability to robustly form spatially modulated activity patterns.

Our model analysis also allows us to derive several previously not described predictions, providing a critical test of the proposed model class. This appears particularly relevant, as recent advancements in experimental techniques offer new opportunities to manipulate and record neuron-type-specific cortical activity.

First, to illuminate the mechanism underlying the formation of modular activity, we assessed the response property of the network by applying a pulse-like input to the excitatory population. The response in inhibition spreads faster than in excitation resulting in a broader peak over a transient period. Thus, transiently the network generates a Mexican hat-like activity with a more localized response in the excitatory population and a wider response in inhibitory units. Using modern methods that allow now increasingly precise experiments manipulating local groups of neurons and their simultaneous imaging, it is possible to experimentally test for a Mexican hat-like profile in cortical activity. To this end, one could locally perturb the activity of a single or a small group of excitatory neurons, and record the response of neighbouring excitatory and inhibitory neurons. Optogenetical tools allow to specifically manipulate individual cells[70,421,282,84] whose activity can be simultaneously imaged using fluorescence indicators with little spectral overlap to the optogenetic actuators and advanced microscopies[443,354,189,336,210,240,110,209]. Since we expressed the response widths of excitation and inhibition in terms of the domain spacing, even a quantitative comparison to experimental data can be achieved. Importantly, testing this effective Mexican hat in the population activity allows to illuminate the key underlying mechanism of this class of network models.

Second, we found that the excitatory and inhibitory activity patterns are co-aligned consistent with previous work [130], but may differ in the amplitude of their modulation. The current technological advancements make it possible to measure co-alignment and amplitude ratio between inhibition and excitation. A potential approach would be to use widefield or 2-photon imaging to assess the modular cortical activity in carnivores[389] or primates[375] of excitatory and inhibitory neurons. To this end, Calcium indicators can be constructed to specifically target

excitatory and inhibitory neurons[117,176,295] and by using dual-color imaging to simultaneously record both activities in two separate channels [210,110,209]. Another approach would be to densely label cortical neurons and to retrieve the information about cell type either by using a spectrally separate fluorescent marker in one of the populations[343], or by applying post-hoc a molecular analysis of the imaged neurons[237]. Current approaches also allow to specifically label individual subclasses of inhibitory interneurons[176,295]. Comparing the alignment of their activity to the excitatory activity pattern might shed light on potential differences in their tasks. Moreover, the newly developed high-density Neuropixels probes allow to readout the activity of several hundreds of neurons with high sensitivity[222]. Previous studies suggest that cell types can be inferred based on the densely sampled extracellular waveform[216]. Alternatively, the information about cell types can be obtained by opto-tagging genetically identified neuron types[222,400]. The Neuropixels recordings might allow to compare the alignment of excitation and inhbition along one dimension with high temporal and spatial precision. Note, however, that when using fluorescent markers to assess the cortical activity several factors might confound the comparison in the amplitude modulation of excitatory and inhibitory activity. Different expression levels of the indicator in excitatory versus inhibitory neurons could lead to an artificial total increase in one of the activities relative to the other. Similarly, the underlying transformation from an action potential to the observed fluorescence signal might be different in excitatory and inhibitory neurons.

Third, the spacing of active domains in this model is consistent with an estimate based on experimental data[109,80,108,389]. In order to compare the model values with the experimental data, we determined the domain spacing of the activity patterns in units of the range of the excitatory connectivity resulting in a domain spacing of about 4 σ_E^{ferret}[109,108,389]. This is consistent with the range of the domain spacing in the model of 2 to 7 σ_E. Moreover, our model shows a wide range of values of the domain spacing which is consistent with the high variability of domain spacing in cortical activity of different species and cortical areas[109,80,231,108,389].

Fourth, the model predicts that with increasing strength of network inhibition the domain spacing of modular activity patterns decreases. It is possible to experimentally test this prediction by estimating the domain spacing of cortical activity which can be robustly and reliably done by analysing spontaneous activity already in early cortex[389] using recently developed genetically encoded and cell-type specific[343,237] activity sensors with high sensitivity[81,185,209]. To assess the influence of the strength of network inhibition on the domain spacing, inhibition in cortex can be manipulated using either pharmacological or optogenetical methods[70,421,282]. Only recently, the imaging of calcium or voltage sensors and optogenetical methods have been combined into an all-optical approach allowing to simultaneously readout and manipulate neuronal populations[128,362]. Thus, by simultaneously imaging cortical activity and activating[244,166] or inactivating[442,87,444,36,175] inhibitory interneurons in cortex, a potential change in the domain spacing can be measured as a function of the change in network inhibition and be compared to the change in domain spacing as predicted by the model. In addition, combining the experimental measurements of the amplitude ratio, the domain spacing and its change after manipulating network inhibition allows to test whether there is a parameter regime that quantitatively matches all three of these observables.

In conclusion, we suggest a mechanism that extends the parameter regime such that the classically proposed model class succesfully forms modular activity patterns even when inhibition is more short-ranged than excitation. Moreover, our predictions make this model class experimentally testable.

Chapter 7

Summary and Outlook

Cortical activity exhibits two key features across many different brain areas and species: it is often modular and correlated between distant cortical regions. So far, it has been unclear how activity with these two fundamental properties emerges during development. To address this question, I analyzed chronic imaging data of spontaneous and visually evoked activity in primary visual cortex of ferret. The data analysis was complemented by computational modelling of neural networks investigating mechanisms for the emergence of modular and long-range correlated activity in early circuits. In this thesis I showed that spontaneous activity in the mature cortex exhibits a long-range correlation structure that is tightly related to the mature functional organization over large distances and at a fine spatial scale. I then demonstrated that distributed, long-range correlated network activity is already present in the early cortex prior to the maturation of long-range lateral connections. I provided a solution to this apparent conundrum by showing in a network model that long-range correlations can emerge from purely local lateral connections in the presence of network heterogeneity. Moreover, the empirical data I am analyzing shows that cortical activity is modular early in development. I proposed a mechanism which allows modular activity to form in a network with biologically plausible connectivity. Combining both network models yields activity patterns that quantitatively match several characteristic features of long-range network behaviour observed in our experimental data.

In previous studies anatomical evidence in support of a fundamental modular structure for distributed network interactions in visual cortex has been demonstrated by documenting the orientation specificity of long-range horizontal connections[154,285,48]. Such an organization has also been suggested by the similarity of spontaneous activity to the modular patterns of activity evoked with grating stimuli[235,327] imaged with voltage sensitive dyes. However, it remained unclear over which cortical range and up to which fine spatial scale the similarity between spontaneous and evoked activity holds[159]. Our analysis of spontaneous activity in mature visual cortex extends these observations by showing that both the fine and large scale organization of network interactions measured by the circuit's correlation structure of spontaneous activity closely resembles the layout of orientation domains in ferret visual cortex. A remarkable degree of precision is evident in the correlated activity of long-range network interactions, such that the activity patterns of a local cortical area accurately predict the structure of local functional architecture millimeters away. Even the finest-scale topographic features of orientation maps - fractures or pinwheel centers - are accurately reflected in the long-range network interactions evident from correlated spontaneous activity. These results, together with the stability of large-scale correlation patterns across awake and anesthetized states, demonstrate an exceptional degree of functional coherence in cortical networks, a coherence that possibly transcends the columnar scale and likely ensures reliable distributed neural representations of sensory input.

In this thesis we used spontaneous activity to probe distributed network early in their devel-

opment. By analyzing spontaneous patterns of activity imaged prior to eye opening and prior to the formation of the orientation preference map and the maturation of long-range horizontal connections, I showed that modular network correlations already extend over distances comparable to what is observed in the mature cortex. The possibility that such long-range correlations would be present at these early stages of development has, to our knowledge, never been considered. Given the strong association of modular activity patterns with the modular arrangement of long-range horizontal connections in mature cortex[154,285,48], it seems surprising to find robust long-range modular patterns of correlated activity as early as 10 days prior to eye opening, when horizontal connections have not fully developed yet[46,122,364]. The correlated patterns of activity at this developmental stage are not identical to the patterns found in the mature cortex, but instead undergo significant refinement in the period prior to eye opening. Indeed, developmental changes in the patterns of correlated activity are likely to reflect ongoing maturation of multiple features of circuit organization including the emergence of long-range horizontal connections[439]. Nevertheless, the presence of such long-range modular correlation patterns in the absence of a well-developed horizontal network in layer 2/3 challenges the necessity of long-range anatomical connections for generating distributed modular network activity.

Although network correlations refine considerably during development, they exhibit already early in development a modular pattern that is predictive of the mature functional architecture. Up to 10 days prior to eye-opening spontaneous activity is already modular and shows some signatures of the functional organization of the mature cortex. The modular patterns of spontaneous activity early in development and their relation to the mature circuit organization has not been described before. The resemblance of early network correlations with the mature functional layout is consistent with the idea of self-organized cortical activity.

It has been unclear whether the long-range correlated and modular activity patterns are generated mainly by feed-forward inputs, via an intracortical mechanism or by feed-back inputs. The retinal and thalamic inactivation experiments performed by our collaborators in the laboratory of David Fitzpatrick at the Max Planck Florida Institute establish that early correlated patterns of spontaneous activity can be generated by visual cortex in the absence of input from retina or LGN. The observed drop in the frequency of spontaneous events after LGN inactivation suggests that LGN triggers intrinsic cortical spontaneous events (see also [284]). This is consistent with previous work in cortical slices demonstrating that slow cortical oscillations ($\sim$0.1 Hz) can be generated within cortex itself[368,423]. The presence of modular correlation patterns distributed over distances comparable to those found with intact feedforward inputs provides evidence that already immature cortical circuits have the capacity to generate long-range modular patterns of activity. It is important to emphasize that these observations do not rule out a causal role for feedforward inputs in establishing modular cortical network structure. Patterns of retinal and geniculocortical activity could play a critical role in guiding the development of these cortical activity patterns (e.g.[311,69,75,201]), but they are clearly not required for their expression. Together, these results demonstrate that early cortical circuits generate structured long-range correlations that are refined over development to form mature distributed functional networks, thereby linking the fine-scale functional architecture with distant network organization.

These results, however, present a challenging puzzle: long-range correlated activity in the early cortex is generated through intracortical circuits in the absence of long-range horizontal connectivity. I addressed this conundrum by first formulating a statistical model describing an ensemble of spatially extended, spontaneous activity patterns. I showed that decreasing the dimensionality of this ensemble of activity patterns leads to an increase in the range over which domains were correlated. Thus, it can be concluded that a low-dimensional ensemble of spatially extended activity patterns exhibit a long-range correlation structure. This suggests that a mechanism is implemented in the early cortical circuit that confines the dimensionality of activity patterns thus providing the early cortex with the ability to generate distributed network

activity in the absence of long-range anatomical connectivity.
Next, I implemented such a mechanism in a dynamical network model suggesting a simple and robust solution by showing that long-range correlations can arise as an emergent property in heterogeneous circuits. They emerge via multi-synaptic short-range interactions that tend to favor certain spatially extended activity patterns at the expense of others. In the dynamical network model we started by choosing the lateral connections such as to support the formation of active domains, reflecting our observation that spontaneous activity in the early visual cortex is always modular. The dynamical mechanism used for generating modular activity is known as the Turing-mechanism[430]: modular patterns arise from a spatially homogeneous state by amplifying spatially heterogeneous perturbations around a typical spatial scale through dynamical feedback loops mediated by the recurrent connections[130]. Since the focus of our study lies on the mechanisms causing active modules to be correlated over larger distances, a generic local circuit motive known to implement the Turing-mechanism, the so-called Mexican hat connectivity (local excitation with lateral inhibition), was chosen. Although there is evidence for such a motive from studies using glutamate uncaging in slices of ferret visual cortex at a developmental stage similar to those I examine in this thesis[80,108], other studies using paired recordings in slices of adult rat cortex[265], suggest that in fact the spatial range of inhibition is smaller than the range of excitation. To address this issue I investigated a second dynamical network model consisting of two populations which are connected with a wiring diagram that is consistent with current experimental data (local inhibition and spatially more extended excitation)[265]. In both network models introducing heterogeneity confines their output activity to a low dimensional subset of possible activity patterns.
As predicted by the statistical model this low dimensionality leads to a long-range correlation structure in the activity patterns that matches quantitatively that observed in experimental data. The relation between the dimensionality of the ensemble of activity patterns and other properties of spontaneous correlations, such as the eccentricity of the local correlations and their fracture strength, suggest that low dimensionality acts as an organizational principle of the activity in cerebral cortex. Both network models generate activity patterns with a long-range correlation structure, indicating that the effect of heterogeneity is largely independent from the specific form of network interactions generating modular activity. Importantly, the correlation structure for an ensemble of solutions of the homogeneous model decays on a significantly shorter range, when compared to size-matched sets of activity patterns measured in the early visual cortex. The reason for this is that the ensemble of patterns the homogeneous model produces reflects the symmetries of the underlying dynamics and thus consists of all translated and rotated versions of a hexagonal pattern. The model predicts that increasing the heterogeneity of local connections increases the spatial extent of spontaneous correlations. Future experiments could test this prediction by experimentally manipulating the amount of heterogeneity within the cortical circuit. By optogenetically activating random sets of sparsely distributed neurons, the local structure of funcitonal lateral interactions might become more heterogeneous. The idea that long-range order in cortical networks has its origin in short-range interactions has to the author's knowledge not been suggested in previous studies.
Notably, the dynamical network with local inhibition and spatially more extended excitation that was used to describe the formation of long-range correlated activity also generates modular activity patterns. This stands in contrast to previous models which required a network to exhibit either long-range or fast inhibition for it to form modular activity[287,411,28,71,44,163,346,14,226,21]. However, experimental evidence for lateral or fast inhibition has been limited[80,108,329]. To shed light on the underlying mechanism I systematically analyzed the requirements on the architecture of the dynamical network model to form modular network activity. I showed that modular activity patterns are generated when introducing local self-inhibition into a network with a biologically plausible architecture where inhibition acts on a smaller spatial scale than excitation.

Already with relatively weak local self-inhibition the network robustly and reliably displayed modular activity patterns over a broad range of connectivity settings, including a regime where the spatial scale of inhibition was smaller than the spatial scale of excitation, and when the time scale of inhibition was equal to the one of excitation. Long range, disynaptic or fast inhibition as suggested in previous studies[411,28,71,163,134,287,302,226,14] were not required to produce this effect. A natural way to implement local self-inhibition in cortical circuits are autapses[431], i.e. synapses formed between a neuron and a branch of its own axon. Autapses have been observed in large numbers especially in visual cortex of cat[418] and somatosensory cortex of rat[24], both of which exhibit modular activity. This suggests that the presence of a sufficient amount of autapses leads to the emergence of modular activity patterns.

To critically test the proposed model class and the specific mechanism, I derived several previously not described predictions. Recent advancements in experimental techniques offer new possibilities to manipulate and record neuron-type-specific cortical activity. First, to illuminate the mechanism underlying the formation of modular activity, we assessed the network response to a pulse-like input to the excitatory population. The response in inhibition spread faster than in excitation resulting in a broader peak over a transient period, thus, generating a Mexican hat-like activity with a more localized response in the excitatory population and a wider response in inhibitory units. Using methods that allow now increasingly precise manipulations of local groups of neurons and their simultaneous imaging, it is possible to experimentally test for a Mexican hat-like profile in cortical activity. To this end, one could locally perturb the activity of a single or a small group of excitatory neurons, and record the response of neighbouring excitatory and inhibitory neurons. Optogenetical tools allow to specifically manipulate individual cells[70,421,282,84] whose activity can be simultaneously imaged using fluorescence indicators with little spectral overlap to the optogenetic actuators and advanced microscopies[443,354,189,336,210,240,110]. Second, the model predicts that the domain spacing decreases with increasing strength of network inhbition. Measuring the domain spacing of cortical activity experimentally has been done for several years[231]. In order to determine the domain spacing at a stage during development when lateral long-range connections have not maturated yet, spontaneous activity could be used as a readout as it is present as a strong signal in e.g. immature ferret visual cortex[86,389]. Spontaneous cortical activity can be reliably imaged by the recent development of highly sensitive genetically encoded Calcium indicators which enable reliable single trial imaging of cortical activity[81]. Using state-of-the-art recording technology it becomes now possible to simultaneously measure the domain spacing of cortical activity and manipulate cortical circuits such as to modulate inhibition strength[128,362]. Optogenetic methods offer the possibility to manipulate the activity in a precisely targeted subset of neurons, e.g. in inhibitory interneurons[70,421,282] to study the effect of network inhibition on the domain spacing. Third, the model predicts that the activity patterns of the excitatory and inhibitory population are co-aligned, and that the amplitude modulations of excitatory and inhibitory activity can differ from each other. By imaging the excitatory and inhibitory neuronal populations separately[237,343,282] using, e.g. neuron type specific Calcium indicators, it would be possible to study whether excitatory and inhibitory activity is co-aligned or shifted to each other. In addition this might allow to test the potential difference in amplitude modulation between excitatory and inhibitory activity. Moreover, the range of values of the domain spacing of the modular network activity was found to be consistent with values from experimental data[109,80,108,389]. The domain spacing in the network model can vary by a factor of about 5. This variability is consistent with the broad range of values found in different cortical areas and species varying from 0.5 to 2 mm[86,231,373,389]. Together, I provided a network mechanism that generates modular activity with a biologically plausible network connectivity and several predictions to critically test this mechanism.

Thus, in this thesis I showed that early cortical circuits exhibit quantitatively similar properties to the mature network. This finding suggests that the high degree of local precision that is

evident in mature distributed network interactions could originate from the network structure in early local interactions that seed the subsequent emergence of clustered long-range horizontal connections via activity-dependent, e.g. Hebbian plasticity mechanisms. This would be consistent with previous experimental work in ferret visual cortex showing that spontaneous activity in the early cortex is required for the maturation of orientation selectivity[76]. However, it remains unclear whether the patterns of ongoing activity play an instructive role in this process or if they are permissive.

I took first steps to understand how the spatial layout of the orientation preference map is forming and how the structure of spontaneous correlations is reorganized. From a self-organizational point of view there are several hypothesis of how the layout of network activity is shaped during development. Potentially spontaneous activity could drive the development of network activity via plasticity mechanisms or, alternatively, visually evoked activity might dominate its development. A third possibility is that the influence of spontaneous and evoked activity on the development of cortical activity could be interrelated[269]. To disentangle these scenarios the first step in a future experiment could be to chronically image spontaneous and visually evoked activity over the period of prior to after eye-opening. These simultaneous recordings allow to study if spontaneous activity contains information not only about the current immature organization of orientation selectivity but also about the future layout of orientation domains that is not reflected in its early structure. Preliminary results indicate that spontaneous activity indeed contains signatures of the mature orientation map that are not yet present in early evoked responses indicating that spontaneous activity supports shaping mature cortical activity.

Based on the hypothesis that cortical activity self-organizes during development, a dynamic network model could be used to approach the question whether and how spontaneous activity influences map development. To test the hypothesis that spontaneous activity shapes mature cortical activity, spontaneous correlations could be used to describe the interactions between cortical locations as they can be interpreted as the average cortical activity over long times. This assumption is consistent with previous theoretical work demonstrating that spontaneous dynamics can form and maintain neuronal assemblies[269]. Preliminary results show that this model captures aspects of the reorganization in orientation preference observed *in vivo*, suggesting that the early patterns of spontaneous cortical activity shape the development of orientation selectivity in the visual cortex.

To validate this result the structure of early spontaneous activity correlation could be perturbed to study potential consequences for the layout of the mature orientation preference map. Taking advantage of the advancement of optogenetic tools it might be possible to increase spontaneous correlations between a specifically targeted subset of neurons by increasing their synchronous activity and test whether this subset's similarity in orientation preference increases as predicted by the correlation-based model. A combination of perturbation experiments and computational modeling might be able to address the question of how spontaneous activity influences the development of the mature functional cortical organization in the future.

In summary, in this thesis I first analyzed imaging data to quantitatively describe properties of spontaneous activity during development. In the second step I used self-organizational network models that are based on simple interactions between units to shed light on the underlying mechanisms for the emergence of observed properties in the experimental data, in particular the long-range correlation structure in spontaneous activity in early development prior to the maturation of long-range anatomical connections and its modular organization in the absence of lateral inhibition. In addition, I provided several predictions to make these network models experimentally testable.

As the main interest in this thesis lies in the emergence of features of population activity, I considered models that approximated cortical circuits on a network level by coarse-graining and decreasing their complexity. Approximations included modeling the firing rate instead of individ-

ual action potentials, neglecting the neuronal morphology, neglecting differences in the various types of inhibitory interneurons which differ in morphology, connectivity, dynamics, etc., and simplifying the feed-forward and feedback input structure. These approximations allowed us to determine key mechanisms underlying experimental observations, and make simple predictions to test these mechanisms. However, those simplified network models stand in stark contrast to the complex and heterogeneous nature of cortical circuits and their activity and further experiments are required to test our proposed mechanisms. Alternatively, we could describe the complex cortical circuits as precisely as possible by building a complicated model with many parameters and obtaining numerical predictions. Typically, this approach leads to a large number of parameters which cannot be all faithfully measured, and to complex sets of equations which are generally not analytically solvable. These results cannot be easily interpreted due to their complexity and large number of parameters. Importantly, to understand the mechanism behind a model we need to simplify the system but still preserve its essential features by constraining the number of parameters to only a few factors[264,165]. However, it is currently unclear which features are important and how many to faithfully describe brain activity.

Describing a complex system by a simplified model has proven to be exceptionally effective in physics. An often cited success story is the Ising model for magnetic systems[212]. It describes the phase behaviour of a magnet qualitatively correct, and is even quantitatively correct near the critical point. The reason a simplified description is successful in physical systems is that microscopic models generally *flow* towards simpler models when coarse-grained and eventually converge[142] with increasing scale to a fixed point. Their large-scale behaviour, which in the Ising model is the magnetization, is then described by those fixed points. This transition towards simple macroscopic descriptions of a system is formalized by the renormalization group which systematically investigates the changes of a system when viewed at different scales. Using renormalization group the system's observables can be determined to be relevant or irrelevant for the description of the system's macroscopic behaviour. An observable is said to be relevant if its magnitude increases during the progress of coarse-graining, whereas the observable is irrelevant if its magnitude decreases. Remarkably, most observables in physical systems are irrelevant and the large scale behaviour is dominated by only a small set of observables. Often microscopically different models flow towards the same large-scale behaviour by sharing the same relevant observables and only differing in their irrelevant observables. These models are part of the same universality class.

Currently there is ongoing work to study if and how these techniques from physics can be applied to problems in neuroscience to potentially find a low-dimensional description of neural activity that can be understood. Recent studies investigated the scaling behaviour in e.g. network models of cortical circuits[424,425]. Their goal is to determine whether network models have effectively a low dimension or can be described by a small set of relevant parameters similar to physical systems. In an alternative approach renormalization group was directly applied to experimental data[50,300]. The authors suggested an empirical method that aims to provide a framework that not only interprets but also predicts and stimulates new experiments. Nevertheless, further theoretical and experimental work is required to illuminate if the dynamics of cortical activity can be understood in terms of basic principles. Here we added but one building block contributing to our understanding of the intricate brain activity. We characterized spontaneous and visually evoked activity and extracted quantifiable features. Based on these results we investigated fundamental mechanisms that can reproduce these features and proposed predictions to experimentally test them. The great advantage of a model is to provide a way of how to think about an observation or a mechanism. Ideally this leads to generating new hypotheses and ideas resulting in further advancement of understanding. Taken all this combined it might be desirable to try to formulate effective theories to illuminate the mechanisms underlying the complex system of the brain.

Bibliography

[1] LF Abbott, K Rajan, and H Sompolinsky. "Interactions between Intrinsic and Stimulus-Evoked Activity in Recurrent Neural Networks". In: *The Dynamic Brain: An Exploration of Neuronal Variability and Its Functional Significance*. 2011. arXiv: 0912.3832.

[2] M Abeles and MH Goldstein Jr. "Functional architecture in cat primary auditory cortex: columnar organization and organization according to depth". In: *Journal of Neurophysiology* **33** (1970), pp. 172–187.

[3] P Abrahamsen. *A review of Gaussian random fields and correlation functions*. Vol. 1. Norsk Regnesentral/Norwegian Computing Center, 1997, p. 70. arXiv: arXiv:1011.1669v3.

[4] M Abramowitz and IA Stegun. *Handbook of mathematical functions with formulas, graphs and mathematical tables*. 1964.

[5] JB Ackman, TJ Burbridge, and MC Crair. "Retinal waves coordinate patterned activity throughout the developing visual system". In: *Nature* **490** (2012), pp. 219–225. arXiv: NIHMS150003.

[6] Y Adam, JJ Kim, S Lou, Y Zhao, ME Xie, D Brinks, H Wu, MA Mostajo-Radji, S Kheifets, V Parot, S Chettih, KJ Williams, B Gmeiner, SL Farhi, L Madisen, EK Buchanan, I Kinsella, D Zhou, L Paninski, CD Harvey, H Zeng, P Arlotta, RE Campbell, and AE Cohen. "Voltage imaging and optogenetics reveal behaviour-dependent changes in hippocampal dynamics". In: *Nature* **569** (2019), pp. 413–417.

[7] H Adelsberger, O Garaschuk, and A Konnerth. "Cortical calcium waves in resting newborn mice". In: *Nature Neuroscience* **8** (2005), p. 988.

[8] Y Ahmadian, DB Rubin, and KD Miller. "Analysis of the stabilized supralinear network". In: *Neural Computation* **25** (2013), pp. 1994–2037.

[9] B Ahmed, JC Anderson, KAC Martin, and JC Nelson. "Map of the synapses onto layer 4 basket cells of the primary visual cortex of the cat". In: *J Comparative Neurology* **380** (1997), pp. 230–242.

[10] L Aitkin, D Anderson, and JF Brugge. "Tonotopic Organization and Discharge Characteristics of Single Neurons in Nuclei of the Lateral Lemniscus of the Cat". In: *J Physiology* **33** (1970), pp. 421–440.

[11] CJ Akerman. "Depolarizing GABAergic Conductances Regulate the Balance of Excitation to Inhibition in the Developing Retinotectal Circuit In Vivo". In: *Journal of Neuroscience* **26** (2006), pp. 5117–5130.

[12] CJ Akerman, D Smyth, and ID Thompson. "Visual experience before eye-opening and the development of the retinogeniculate pathway". In: *Neuron* **36** (2002), pp. 869–879.

[13] A Akrouh and D Kerschensteiner. "Intersecting circuits generate precisely patterned retinal waves". In: *Neuron* **79** (2013), pp. 322–334.

[14] R Ali, J Harris, and B Ermentrout. "Pattern formation in oscillatory media without lateral inhibition". In: *Physical Review E* **94** (2016), p. 012412.

[15] HJ Alitto and WM Usrey. "Corticothalamic feedback and sensory processing". In: *Current Opinion in Neurobiology* **13** (2003), pp. 440–445.

[16] KL Allendoerfer and CJ Shatz. "The Subplate, a Transient Neocortical Structure: Its Role in the Development of Connections between Thalamus and Cortex". In: *Annual Review of Neuroscience* **17** (1994), pp. 185–218.

[17] C Allene, A Cattani, JB Ackman, P Bonifazi, L Aniksztejn, Y Ben-Ari, and R Cossart. "Sequential Generation of Two Distinct Synapse-Driven Network Patterns in Developing Neocortex". In: *Journal of Neuroscience* **28** (2008), pp. 12851–12863.

[18] JMM Alonso and LM Martinez. "Functional connectivity between simple cells and complex cells in cat striate cortex." In: *Nature neuroscience* **1** (1998), p. 395.

[19] Si Amari. "Dynamics of pattern formation in lateral-inhibition type neural fields". In: *Biological Cybernetics* **27** (1977), pp. 77–87.

[20] PA Anderson, J Olavarria, and RC Van Sluyters. "The overall pattern of ocular dominance bands in cat visual cortex." In: *J Neurosci* **8** (1988), pp. 2183–2200.

[21] J Antolík. "Rapid Long-Range Disynaptic Inhibition Explains the Formation of Cortical Orientation Maps". In: *Frontiers in Neural Circuits* **11** (2017), p. 21.

[22] DA Arroyo and MB Feller. "Spatiotemporal Features of Retinal Waves Instruct the Wiring of the Visual Circuitry". In: *Frontiers in Neural Circuits* **10** (2016), p. 54.

[23] A Bacci and JR Huguenard. "Enhancement of spike-timing precision by autaptic transmission in neocortical inhibitory interneurons". In: *Neuron* **49** (2006), pp. 119–130.

[24] A Bacci, JR Huguenard, and Da Prince. "Functional autaptic neurotransmission in fast-spiking interneurons: a novel form of feedback inhibition in the neocortex." In: *Journal of Neuroscience* **23** (2003), pp. 859–866.

[25] T Baden, P Berens, K Franke, MR Rosón, M Bethge, and T Euler. "The functional diversity of retinal ganglion cells in the mouse". In: *Nature* **529** (2016), pp. 345–350. arXiv: 15334406.

[26] Y Banitt, KAC Martin, and I Segev. "A biologically realistic model of contrast-invariant orientation tuning by thalamocortical synaptic depression". In: *J Neuroscience* **27** (2007), pp. 10230–10239.

[27] J Barral and AD Reyes. "Synaptic scaling rule preserves excitatory-inhibitory balance and salient neuronal network dynamics". In: *Nature Neuroscience* **19** (2016), pp. 1690–1696.

[28] HG Barrow, AJ Bray, and JM Budd. "A Self-Organizing Model of "Color Blob" Formation". In: *Neural Computation* **8** (1996), pp. 1427–1448.

[29] B Bathellier, L Ushakova, and S Rumpel. "Discrete Neocortical Dynamics Predict Behavioral Categorization of Sounds". In: *Neuron* **76** (2012), pp. 435–49.

[30] RJ Bell and P Dean. "Atomic vibrations in vitreous silica". In: *Discussions of the Faraday Society* **50** (1970), pp. 55–61.

[31] Y Ben-Ari, E Cherubini, R Corradetti, and JL Gaiarsa. “Giant synaptic potentials in immature rat CA3 hippocampal neurones.” In: *The Journal of Physiology* **416** (1989), pp. 303–325.

[32] R Ben-Yishai, RL Bar-Or, and H Sompolinsky. “Theory of orientation tuning in visual cortex”. In: *PNAS* **92** (1995), pp. 3844–3848.

[33] LA Benevento and GP Standage. “Demonstration of lack of dorsal lateral geniculate nucleus input to extrastriate areas MT and Visual 2 in the macaque monkey”. In: *Brain Research* **252** (1982), pp. 161–166.

[34] I Benjumeda, A Escalante, C Law, D Morales, G Chauvin, G Muca, Y Coca, J Marquez, G Lopez-Bendito, A Kania, L Martinez, and E Herrera. “Uncoupling of EphA/ephrinA Signaling and Spontaneous Activity in Neural Circuit Wiring”. In: *Journal of Neuroscience* **33** (2013), pp. 18208–18218.

[35] P Berkes, G Orban, M Lengyel, and J Fiser. “Spontaneous Cortical Activity Reveals Hallmarks of an Optimal Internal Model of the Environment”. In: *Science* **331** (2011), pp. 83–87.

[36] A Berndt, SY Lee, C Ramakrishnan, and K Deisseroth. “Structure-guided transformation of channelrhodopsin into a light-activated chloride channel”. In: *Science* **344** (2014), pp. 420–424. arXiv: `NIHMS150003`.

[37] T Binzegger, RJ Douglas, and KAC Martin. “A Quantitative Map of the Circuit of Cat Primary Visual Cortex”. In: *J Neuroscience* **24** (2004), pp. 8441–8453.

[38] JK Bizley, FR Nodal, I Nelken, and AJ King. “Functional organization of ferret auditory cortex”. In: *Cerebral Cortex* **15** (2005), pp. 1637–1653.

[39] P Blaesse, MS Airaksinen, C Rivera, and K Kaila. “Cation-Chloride Cotransporters and Neuronal Function”. In: *Neuron* **61** (2009), pp. 820–838.

[40] C Blakemore and EA Tobin. “Lateral inhibition between orientation detectors in the cat’s visual cortex”. In: *Experimental Brain Research* **15** (1972), pp. 439–440.

[41] AG Blankenship, KJ Ford, J Johnson, RP Seal, RH Edwards, DR Copenhagen, and MB Feller. “Synaptic and Extrasynaptic Factors Governing Glutamatergic Retinal Waves”. In: *Neuron* **62** (2009), pp. 230–241.

[42] GG Blasdel and JS Lund. “Termination of afferent axons in macaque striate cortex”. In: *The Journal of Neuroscience* **3** (1983), pp. 1389–1413.

[43] GG Blasdel and G Salama. “Voltage-sensitive dyes reveal a modular organization in monkey striate cortex”. In: *Nature* **321** (1986), p. 579.

[44] B Blumenfeld, D Bibitchkov, and M Tsodyks. “Neural network model of the primary visual cortex: From functional architecture to lateral connectivity and back”. In: *Journal of Computational Neuroscience* **20** (2006), pp. 219–241.

[45] T Bonhoeffer and A Grinvald. “Iso-orientation domains in cat visual cortex are arranged in pinwheel-like patterns”. In: *Nature* **353** (1991), pp. 429–431.

[46] V Borrell and EM Callaway. “Reorganization of exuberant axonal arbors contributes to the development of laminar specificity in ferret visual cortex.” In: *Journal of Neuroscience* **22** (2002), pp. 6682–6695.

[47] JG Borst, F Helmchen, and B Sakmann. “Pre- and postsynaptic whole-cell recordings in the medial nucleus of the trapezoid body of the rat.” In: *The Journal of Physiology* **489** (1995), pp. 825–840.

[48] WH Bosking, Y Zhang, B Schofield, and D Fitzpatrick. "Orientation selectivity and the arrangement of horizontal connections in tree shrew striate cortex." In: *Journal of Neuroscience* **17** (1997), pp. 2112–27.

[49] DB Bowling and CR Michael. "Projection patterns of single physiologically characterized optic tract fibres in cat". In: *Nature* **286** (1980), pp. 899–902. arXiv: `arXiv:1011.1669v3`.

[50] S Bradde and W Bialek. "PCA Meets RG". In: *Journal of Statistical Physics* **167** (2017), pp. 462–475. arXiv: `arXiv:1610.09733v1`.

[51] V Braitenberg and A Schüz. *Anatomy of the Cortex - Statistics and Geometry*. Vol. 18. 1991, p. 203.

[52] PC Bressloff, JD Cowan, M Golubitsky, PJ Thomas, and MC Wiener. "Geometric visual hallucinations, Euclidean symmetry and the functional architecture of striate cortex". In: *Philosophical Transactions of the Royal Society B: Biological Sciences* **356** (2001), pp. 299–330.

[53] PC Bressloff. "Integro-differential equations and the stability of neural networks with dendritic structure". In: *Biological Cybernetics* **73** (1995), pp. 281–290.

[54] PC Bressloff. "New mechanism for neural pattern formation". In: *Physical Review Letters* **76** (1996), pp. 4644–4647.

[55] PC Bressloff. "Pattern formation in visual cortex". In: *Les Houches Summer School Proceedings*. 2003, pp. 477–574.

[56] PC Bressloff and Ma De Souza Silva. "Neural pattern formation in networks with dendritic structure". In: *Physica D: Nonlinear Phenomena* **115** (1998), pp. 124–144.

[57] N Brunel. "Dynamics of Sparsely Connected Networks of Excitatory and Inhibitory Spiking Neurons". In: *Journal of Computational Neuroscience* **8** (2000), pp. 183–208.

[58] EK Buchanan, I Kinsella, D Zhou, R Zhu, P Zhou, F Gerhard, J Ferrante, Y Ma, S Kim, M Shaik, Y Liang, R Lu, J Reimer, P Fahey, T Muhammad, G Dempsey, E Hillman, N Ji, A Tolias, and L Paninski. "Penalized matrix decomposition for denoising, compression, and improved demixing of functional imaging data". In: *arXiv preprint arXiv* **1807.06203** (2018), p. 334706. arXiv: `1807.06203`.

[59] J Bullier and GH Henry. "Laminar distribution of first-order neurons and afferent terminals in cat striate cortex". In: *Journal of Neurophysiology* **42** (1979), pp. 1271–1281.

[60] J Bullier and H Kennedy. "Projection of the Lateral Geniculate Nucleus onto Cortical Area V2 in the Macaque Monkey". In: *Experimental Brain Research* **53** (1983), pp. 168–172.

[61] TJ Burbridge, HP Xu, JB Ackman, X Ge, Y Zhang, MJ Ye, ZJ Zhou, J Xu, A Contractor, and MC Crair. "Visual circuit development requires patterned activity mediated by retinal acetylcholine receptors". In: *Neuron* **84** (2014), pp. 1049–1064.

[62] DA Butts. "Retinal Waves: Implications for Synaptic Learning Rules during Development". In: *The Neuroscientist* **8** (2002), pp. 243–253.

[63] DA Butts, PO Kanold, and CJ Shatz. "A burst-based "Hebbian" learning rule at retinogeniculate synapses links retinal waves to activity-dependent refinement". In: *PLoS Biology* **5** (2007), pp. 0651–0661.

[64] SR y Cajal. *Comparative study of the sensory areas of the human cortex*. Clark University, 1899, p. 80.

[65] EM Callaway. "Local circuits in primary visual cortex of the macaque monkey". In: *Annual Review of Neuroscience* **21** (1998), pp. 47–74.

[66] EM Callaway and LC Katz. “Effects of binocular deprivation on the development of clustered horizontal connections in cat striate cortex”. In: *PNAS* **88** (1991), pp. 745–749.

[67] EM Callaway and LC Katz. “Emergence and Refinement of Clustered Horizontal Connections in Cat Striate Cortex”. In: *J Neuroscience* **10** (1990), pp. 1134–1153.

[68] EM Callaway and AK Wiser. “Contributions of individual layer 2-5 spiny neurons to local circuits in macaque primary visual cortex”. In: *Visual Neuroscience* (1996).

[69] J Cang, R Renteria, M Kaneko, J Cang, and MP Stryker. “Development of Precise Maps in Visual Cortex Requires Patterned Spontaneous Activity in the Retina”. In: *Neuron* **48** (2005), pp. 797–809.

[70] JA Cardin, M Carlén, K Meletis, U Knoblich, F Zhang, K Deisseroth, LH Tsai, and CI Moore. “Targeted optogenetic stimulation and recording of neurons in vivo using cell-type-specific expression of Channelrhodopsin-2”. In: *Nature Protocols* **5** (2010), p. 247. arXiv: NIHMS150003.

[71] M Carreira-Perpiñán and GJ Goodhill. “Influence of lateral connections on the structure of cortical maps.” In: *Journal of neurophysiology* **92** (2004), pp. 2947–59.

[72] VA Casagrande. “A third parallel visual pathway to primate area V1”. In: *Trends in Neurosciences* **17** (1994), pp. 305–310.

[73] M Catsicas, V Bonness, D Becker, and P Mobbs. “Spontaneous Ca2+ transients and their transmission in the developing chick retina”. In: *Current Biology* **8** (1998), pp. 283–288.

[74] AA Cattani, VD Bonfardin, A Represa, Y Ben-Ari, and L Aniksztejn. “Generation of Slow Network Oscillations in the Developing Rat Hippocampus After Blockade of Glutamate Uptake”. In: *Journal of Neurophysiology* **98** (2007), pp. 2324–2336.

[75] B Chapman and I Gödecke. “Cortical cell orientation selectivity fails to develop in the absence of ON-center retinal ganglion cell activity.” In: *Journal of Neuroscience* **20** (2000), pp. 1922–1930. arXiv: NIHMS150003.

[76] B Chapman and MP Stryker. “Development of orientation selectivity in ferret visual cortex and effects of deprivation.” In: *Journal of Neuroscience* **13** (1993), pp. 5251–5262.

[77] B Chapman, MP Stryker, and T Bonhoeffer. “Development of orientation preference maps in ferret primary visual cortex.” In: *J Neuroscience* **16** (1996), pp. 6443–6453.

[78] B Chapman, KR Zahs, and MP Stryker. “Relation of cortical cell orientation selectivity to alignment of receptive fields of the geniculocortical afferents that arborize within a single orientation column in ferret visual cortex.” In: *J Neuroscience* **11** (1991), pp. 1347–1358.

[79] B Chattopadhyaya, G Di Cristo, CZ Wu, G Knott, S Kuhlman, Y Fu, RD Palmiter, and ZJ Huang. “GAD67-Mediated GABA Synthesis and Signaling Regulate Inhibitory Synaptic Innervation in the Visual Cortex”. In: *Neuron* **54** (2007), pp. 889–903. arXiv: NIHMS150003.

[80] B Chen, K Boukamel, JPY Kao, and B Roerig. “Spatial distribution of inhibitory synaptic connections during development of ferret primary visual cortex”. In: *Experimental brain research.* **160** (2005), pp. 496–509.

[81] TW Chen, TJ Wardill, Y Sun, SR Pulver, SL Renninger, A Baohan, ER Schreiter, RA Kerr, MB Orger, V Jayaraman, LL Looger, K Svoboda, and DS Kim. “Ultrasensitive fluorescent proteins for imaging neuronal activity”. In: *Nature* **499** (2013), pp. 295–300. arXiv: arXiv:1011.1669v3.

[82] X Chen, M Gabitto, Y Peng, NJP Ryba, and CS Zuker. “A gustotopic map of taste qualities in the mammalian brain”. In: *Science* **333** (2011), pp. 1262–1266. arXiv: NIHMS150003.

[83] A Cheng, UT Eysel, and TR Vidyasagar. "The role of the magnocellular pathway in serial deployment of visual attention". In: *European Journal of Neuroscience* **20** (2004), pp. 2188–2192.

[84] SN Chettih and CD Harvey. "Single-neuron perturbations reveal feature-specific competition in V1". In: *Nature* **567** (2019), pp. 334–340.

[85] C Chiu and M Weliky. "Relationship of correlated spontaneous activity to functional ocular dominance columns in the developing visual cortex". In: *Neuron* **35** (2002), pp. 1123–1134.

[86] C Chiu and M Weliky. "Spontaneous activity in developing ferret visual cortex in vivo." In: *Journal of Neuroscience* **21** (2001), pp. 8906–8914.

[87] BY Chow, X Han, AS Dobry, X Qian, AS Chuong, M Li, MA Henninger, GM Belfort, Y Lin, PE Monahan, and ES Boyden. "High-performance genetically targetable optical neural silencing by light-driven proton pumps". In: *Nature* **463** (2010), p. 98.

[88] N Chub and MJ O'Donovan. "Blockade and recovery of spontaneous rhythmic activity after application of neurotransmitter antagonists to spinal networks of the chick embryo." In: *Journal of Neuroscience* **18** (1998), pp. 294–306.

[89] PG Clarke and D Whitteridge. "The cortical visual areas of the sheep." In: *J Physiology* **256** (1976), pp. 497–508.

[90] JD Clements, RA Lester, G Tong, CE Jahr, and GL Westbrook. "The time course of glutamate in the synaptic cleft". In: *Science* **258** (1992), pp. 1498–1501.

[91] H Cline. "Sperry and Hebb: Oil and vinegar?" In: *Trends in Neurosciences* **26** (2003), pp. 655–661.

[92] D Cohen and M Segal. "Network bursts in hippocampal microcultures are terminated by exhaustion of vesicle pools". In: *J Neurophysiology* **106** (2011), pp. 2314–2321.

[93] MT Colonnese and R Khazipov. "Slow activity transients in infant rat visual cortex: a spreading synchronous oscillation patterned by retinal waves". In: *J Neuroscience* **30** (2010), pp. 4325–4337.

[94] GJ Condo and VA Casagrande. "Organization of cytochrome oxidase staining in the visual cortex of nocturnal primates (Galago crassicaudatus and Galago senegalensis): I. Adult Patterns". In: *Journal of Comparative Neurology* **293** (1990), pp. 632–645.

[95] M Conley and D Fitzpatrick. "Morphology of retinogeniculate axons in the macaque". In: *Visual Neuroscience* **2** (1989), pp. 287–296.

[96] WM Connelly and G Lees. "Modulation and function of the autaptic connections of layer V fast spiking interneurons in the rat neocortex". In: *Journal of Physiology* **588** (2010), pp. 2047–2063.

[97] R Corlew, MM Bosma, and WJ Moody. "Spontaneous, synchronous electrical activity in neonatal mouse cortical neurones". In: *Journal of Physiology* **560** (2004), pp. 377–390.

[98] NM da Costa and KAC Martin. "Selective targeting of the dendrites of corticothalamic cells by thalamic afferents in area 17 of the cat." In: *Journal of Neuroscience* **29** (2009), pp. 13919–13928.

[99] MC Crair, DC Gillespie, and MP Stryker. "The Role of Visual Experience in the Development of Columns in Cat Visual Cortex". In: *Science* **279** (1998), pp. 566–570.

[100] MC Crair, JC Horton, A Antonini, and MP Stryker. "Emergence of ocular dominance columns in cat visual cortex by 2 weeks of age." In: *J Comparative Neurology* **430** (2001), pp. 235–249.

[101] KS Cramer and M Sur. "Blockade of afferent impulse activity disrupts on/off sublamination in the ferret lateral geniculate nucleus". In: *Developmental Brain Research* **98** (1997), pp. 287–290.

[102] V Crépel, D Aronov, I Jorquera, A Represa, Y Ben-Ari, and R Cossart. "A Parturition-Associated Nonsynaptic Coherent Activity Pattern in the Developing Hippocampus". In: *Neuron* **54** (2007), pp. 105–120.

[103] HS Cresho, LM Rasco, GH Rose, and GJ Condo. "Blob-like pattern of cytochrome oxidase staining in ferret visual cortex". In: *Soc Neurosci Abstract* **18** (1992), p. 298.

[104] MC Cross and PC Hohenberg. "Pattern-Formation Outside of Equilibrium". In: *Reviews of Modern Physics* **65** (1993), pp. 851–1112.

[105] JC Crowley and LC Katz. "Early development of ocular dominance columns". In: *Science* **290** (2000), pp. 1321–1324.

[106] CA Curcio, KR Sloan, RE Kalina, and AE Hendrickson. "Human photoreceptor topography". In: *Journal of Comparative Neurology* **292** (1990), pp. 497–523.

[107] NM Da Costa and KAC Martin. "How Thalamus Connects to Spiny Stellate Cells in the Cat's Visual Cortex". In: *J Neuroscience* **31** (2011), pp. 2925–2937.

[108] MB Dalva. "Remodeling of inhibitory synaptic connections in developing ferret visual cortex". In: *Neural Development* **5** (2010), p. 5.

[109] MB Dalva and LC Katz. "Rearrangements of synaptic connections in visual cortex revealed by laser photostimulation". In: *Science* **265** (1994), pp. 255–258.

[110] H Dana, B Mohar, Y Sun, S Narayan, A Gordus, JP Hasseman, G Tsegaye, GT Holt, A Hu, D Walpita, R Patel, JJ Macklin, CI Bargmann, MB Ahrens, ER Schreiter, V Jayaraman, LL Looger, K Svoboda, and DS Kim. "Sensitive red protein calcium indicators for imaging neural activity". In: *eLife* **5** (2016), e12727.

[111] PMM Daniel and D Whitteridge. "The representation of the visual field on the cerebral cortex in monkeys". In: *The Journal of Physiology* **159** (1961), pp. 203–221.

[112] A Das and CD Gilbert. "Topography of contextual modulations mediated by short-range interactions in primary visual cortex". In: *Nature* **399** (1999), pp. 655–661.

[113] Ja De Carlos and DD O'Leary. "Growth and targeting of subplate axons and establishment of major cortical pathways." In: *Journal of Neuroscience* **12** (1992), pp. 1194–1211.

[114] C Deleuze, A Pazienti, and A Bacci. "Autaptic self-inhibition of cortical GABAergic neurons: Synaptic narcissism or useful introspection?" In: *Current Opinion in Neurobiology* **26** (2014), pp. 64–71.

[115] M Demarque, A Represa, Hé Becq, I Khalilov, Y Ben-Ari, and L Aniksztejn. "Paracrine Intercellular Communication by a Ca2+- and SNARE-Independent Release of GABA and Glutamate Prior to Synapse Formation". In: *Neuron* **36** (2002), pp. 1051–1061.

[116] EA Deyoe and DC Van Essen. "Segregation of efferent connections and receptive field properties in visual area V2 of the Macaque". In: *Nature* **317** (1985), pp. 58–61.

[117] J Dimidschstein, Q Chen, R Tremblay, SL Rogers, GA Saldi, L Guo, Q Xu, R Liu, C Lu, J Chu, JS Grimley, AR Krostag, A Kaykas, MC Avery, MS Rashid, M Baek, AL Jacob, GB Smith, DE Wilson, G Kosche, I Kruglikov, T Rusielewicz, VC Kotak, TM Mowery, SA Anderson, EM Callaway, JS Dasen, D Fitzpatrick, V Fossati, MA Long, S Noggle, JH Reynolds, DH Sanes, B Rudy, G Feng, and G Fishell. "A viral strategy for targeting and manipulating interneurons across vertebrate species". In: *Nature Neuroscience* **19** (2016), pp. 1743–1749.

[118] J Dormand and P Prince. "A family of embedded Runge-Kutta formulae". In: *Journal of Computational and Applied Mathematics* **6** (1980), pp. 19–26.

[119] RJ Douglas, M Mahowald, KA Martin, and KJ Stratford. "The role of synapses in cortical computation." In: *Journal of neurocytology* **25** (1996), pp. 893–911.

[120] JE Dowling and BB Boycott. "Organization of the Primate Retina: Electron Microscopy". In: *Proceedings of the Royal Society B: Biological Sciences* **166** (1966), pp. 80–111.

[121] E Dupont, IL Hanganu, W Kilb, S Hirsch, and HJ Luhmann. "Rapid developmental switch in the mechanisms driving early cortical columnar networks". In: *Nature* **439** (2006), pp. 79–83.

[122] JC Durack and LC Katz. "Development of Horizontal Projections in Layer 2/3 of Ferret Visual Cortex". In: *Cerebral cortex* **6** (1996), pp. 178–183.

[123] V Dzhala, G Valeeva, J Glykys, R Khazipov, and K Staley. "Traumatic Alterations in GABA Signaling Disrupt Hippocampal Network Activity in the Developing Brain". In: *Journal of Neuroscience* **32** (2012), pp. 4017–4031.

[124] A Edelstein, N Amodaj, K Hoover, R Vale, and N Stuurman. "Computer control of microscopes using manager". In: *Current Protocols in Molecular Biology*. 2010.

[125] B Efron. "Bootstrap Methods: Another Look at the Jackknife". In: *The Annals of Statistics* **7** (1979), pp. 1–26. arXiv: `arXiv:1306.3979v1`.

[126] SJ Eglen. "The role of retinal waves and synaptic normalization in retinogeniculate development." In: *Philosophical transactions of the Royal Society of London. Series B, Biological sciences* **354** (1999), pp. 497–506.

[127] AV Egorov and A Draguhn. "Development of coherent neuronal activity patterns in mammalian cortical networks: Common principles and local hetereogeneity". In: *Mechanisms of Development* **130** (2013), pp. 412–423.

[128] V Emiliani, AE Cohen, K Deisseroth, and M Häusser. "All-Optical Interrogation of Neural Circuits". In: *J Neuroscience* **35** (2015), pp. 13917–13926. arXiv: `arXiv:1011.1669v3`.

[129] B Ermentrout. "Neural networks as spatio-temporal pattern-forming systems". In: *Reports on Progress in Physics* **61** (1998), pp. 353–430.

[130] GB Ermentrout and JD Cowan. "A mathematical theory of visual hallucination patterns". In: *Biological Cybernetics* **34** (1979), pp. 137–150.

[131] GB Ermentrout and JD Cowan. "Large Scale Spatially Organized Activity in Neural Nets". In: *SIAM Journal on Applied Mathematics* **38** (1980), pp. 1–21.

[132] GB Ermentrout and JD Cowan. "Secondary Bifurcation in Neuronal Nets". In: *SIAM Journal on Applied Mathematics* **39** (1980), pp. 323–340.

[133] GB Ermentrout and JD Cowan. "Temporal oscillations in neuronal nets". In: *Journal of Mathematical Biology* **7** (1979), pp. 265–280.

[134] E Erwin, K Obermayer, and K Schulten. "Models of orientation and ocular dominance columns in the visual cortex: A critical comparison". In: *Neural Computation* **7** (1995), pp. 425–468.

[135] JS Espinosa and MP Stryker. "Development and Plasticity of the Primary Visual Cortex". In: *Neuron* **75** (2012), pp. 230–249.

[136] M Farrant and K Kaila. "The cellular, molecular and ionic basis of GABA_A receptor signalling". In: *Progress in Brain Research* **160** (2007), pp. 59–87.

[137] MS Farrell, S Recanatesi, G Lajoie, and E Shea-Brown. "Dynamic compression and expansion in a classifying recurrent network". In: *bioRxiv* (2019). arXiv: 564476.

[138] DJ Felleman and DC Van Essen. "Distributed hierarchical processing in the primate cerebral cortex". In: *Cerebral Cortex* **1** (1991), pp. 1–47.

[139] D Ferster, S Chung, and H Wheat. "Orientation selectivity of thalamic input to simple cells of cat visual cortex". In: *Nature* **380** (1996), pp. 249–252.

[140] E Fino, AM Packer, and R Yuste. "The logic of inhibitory connectivity in the neocortex". In: *Neuroscientist* **19** (2013), pp. 228–237. arXiv: NIHMS150003.

[141] A Firl, GS Sack, ZL Newman, H Tani, and MB Feller. "Extrasynaptic glutamate and inhibitory neurotransmission modulate ganglion cell participation during glutamatergic retinal waves". In: *Journal of Neurophysiology* **109** (2013), pp. 1969–1978.

[142] ME Fisher. "The renormalization group in the theory of critical behavior". In: *Reviews of Modern Physics* **46** (1974), p. 597.

[143] KJ Ford and MB Feller. "Assembly and disassembly of a retinal cholinergic network". In: *Visual Neuroscience* **29** (2012), pp. 61–71. arXiv: NIHMS150003.

[144] JM Fritschy and P Panzanelli. "Molecular and synaptic organization of GABAA receptors in the cerebellum: Effects of targeted subunit gene deletions". In: *Cerebellum* **5** (2006), pp. 275–285.

[145] RD Frostig. "What Does in Vivo Optical Imaging Tell Us about the Primary Visual Cortex in Primates?" In: *Primary Visual Cortex in Primates*. Ed. by Peters A. and R K.S. Boston, MA: Springer, 1994, pp. 331–358.

[146] M Fukushima, RC Saunders, DA Leopold, M Mishkin, and BB Averbeck. "Spontaneous High-Gamma Band Activity Reflects Functional Organization of Auditory Cortex in the Awake Macaque". In: *Neuron* **74** (2012), pp. 899–910. arXiv: NIHMS150003.

[147] K Funke and F Wörgötter. "On the significance of temporally structured activity in the dorsal lateral geniculate nucleus (LGN)". In: *Progress in Neurobiology* **53** (1997), pp. 67–119.

[148] RF Galán. "On how network architecture determines the dominant patterns of spontaneous neural activity". In: *PLoS ONE* **3** (2008). arXiv: 1203.2655.

[149] RAW Galuske and W Singer. "The origin and topography of long-range intrinsic projections in cat visual cortex: A developmental study". In: *Cerebral Cortex* **6** (1996), pp. 417–430.

[150] O Garaschuk, J Linn, J Eilers, and A Konnerth. "Large-scale oscillatory calcium waves in the immature cortex". In: *Nature Neuroscience* **3** (2000), p. 452.

[151] TJ Gawne, BJ Richmond, W Newsome, K Britten, MA Montemurro, NK Logothetis, and S Panzeri. "How independent are the messages carried by adjacent inferior temporal cortical neurons?" In: *Journal of Neuroscience* **13** (1993), pp. 2758–71.

[152] A Gierer and H Meinhardt. “A theory of biological pattern formation”. In: *Kybernetik* **12** (1972), pp. 30–39.

[153] CD Gilbert and TN Wiesel. “Clustered intrinsic connections in cat visual cortex.” In: *Journal of Neuroscience* **3** (1983), pp. 1116–1133.

[154] CD Gilbert and TN Wiesel. “Columnar specificity of intrinsic horizontal and corticocortical connections in cat visual cortex.” In: *Journal of Neuroscience* **9** (1989), pp. 2432–2442.

[155] CD Gilbert and TN Wiesel. “Morphology and intracortical projections of functionally characterised neurones in the cat visual cortex”. In: *Nature* **280** (1979), pp. 120–125.

[156] CD Gilbert. “Laminar differences in receptive field properties of cells in cat primary visual cortex”. In: *The Journal of Physiology* **268** (1977), pp. 391–421.

[157] SV Girman, Y Sauvé, and RD Lund. “Receptive field properties of single neurons in rat primary visual cortex”. In: *J Neurophysiology* **82** (1999), pp. 301–311.

[158] I Gödecke, DS Kim, T Bonhoeffer, and W Singer. “Development of orientation preference maps in area 18 of kitten visual cortex”. In: *European Journal of Neuroscience* **9** (1997), pp. 1754–1762.

[159] JA Goldberg, U Rokni, and H Sompolinsky. “Patterns of ongoing activity and the functional architecture of the primary visual cortex”. In: *Neuron* **42** (2004), pp. 489–500.

[160] MH Goldstein, M Abeles, RL Daly, and J McIntosh. “Functional architecture in cat primary auditory cortex: tonotopic organization.” In: *Journal of Neurophysiology* **33** (1970), pp. 188–197.

[161] MA Goodale and AD Milner. “Separate visual pathways for perception and action”. In: *Trends in Neurosciences* **15** (1992), pp. 20–25.

[162] CS Goodman and CJ Shatz. “Developmental mechanisms that generate precise patterns of neuronal connectivity”. In: *Cell* **72** (1993), pp. 77–98. arXiv: 80006922130.

[163] A Grabska-Barwinska and C von der Malsburg. “Establishment of a scaffold for orientation maps in primary visual cortex of higher mammals”. In: *J Neuroscience* **28** (2008), pp. 249–257.

[164] A Grinvald, EE Lieke, RD Frostig, CD Gilbert, and TN Wiesel. “Functional architecture of cortex revealed by optical imaging of intrinsic signals”. In: *Nature* **324** (1986), pp. 361–364.

[165] J Gunawardena. “Biology is more theoretical than physics”. In: *Molecular Biology of the Cell* **24** (2013), pp. 1827–1829.

[166] LA Gunaydin, O Yizhar, A Berndt, VS Sohal, K Deisseroth, and P Hegemann. “Ultrafast optogenetic control”. In: *Nature Neuroscience* **13** (2010), p. 387.

[167] KM Hagihara, T Murakami, T Yoshida, Y Tagawa, and K Ohki. “Neuronal activity is not required for the initial formation and maturation of visual selectivity”. In: *Nature Neuroscience* **18** (2015).

[168] B Haider, A Duque, HA R, and M DA. “Neocortical Network Activity In Vivo Is Generated through a Dynamic Balance of Excitation and Inhibition”. In: *Journal of Neuroscience* **26** (2006), pp. 4535–4545. arXiv: NIHMS150003.

[169] F Han, N Caporale, and Y Dan. “Reverberation of Recent Visual Experience in Spontaneous Cortical Waves”. In: *Neuron* **60** (2008), pp. 321–327. arXiv: NIHMS150003.

[170] IL Hanganu, Y Ben-Ari, and R Khazipov. "Retinal Waves Trigger Spindle Bursts in the Neonatal Rat Visual Cortex". In: *J Neuroscience* **26** (2006), pp. 6728–6736.

[171] KD Harris and A Thiele. "Cortical state and attention". In: *Nature Reviews Neuroscience* **12** (2011), p. 509. arXiv: NIHMS150003.

[172] HK Hartline. "The receptive fields of optic nerve fibers". In: *American Journal of Physiology* **130** (1940), pp. 690–699.

[173] C Hartmann, A Lazar, B Nessler, and J Triesch. "Where's the Noise? Key Features of Spontaneous Activity and Neural Variability Arise through Learning in a Deterministic Network". In: *PLoS Computational Biology* **11** (2015), e1004640.

[174] Y Hata, T Tsumoto, H Sato, K Hagihara, and H Tamura. "Development of local horizontal interactions in cat visual cortex studied by cross-correlation analysis". In: *Journal of Neurophysiology* **69** (1993), pp. 40–56.

[175] M Häusser. "Optogenetics: The age of light". In: *Nature Methods* **11** (2014), p. 1012.

[176] M He, J Tucciarone, SH Lee, MJ Nigro, Y Kim, JM Levine, SM Kelly, I Krugikov, P Wu, Y Chen, L Gong, Y Hou, P Osten, B Rudy, and ZJ Huang. "Strategies and Tools for Combinatorial Targeting of GABAergic Neurons in Mouse Cerebral Cortex". In: *Neuron* **91** (2016), pp. 1228–1243.

[177] DO Hebb. *The Organization of Behavior*. New York: Wiley & Sons, 1949.

[178] S Hecht, S Shlaer, and MH Pirenne. "Energy, Quanta, and Vision." In: *The Journal of general physiology* **25** (1942), pp. 819–840.

[179] Z Henderson, L Finlay, and KC Wikler. "Development of Ganglion Cell Topography in Ferret Retina". In: *J Neuroscience* **8** (1988), pp. 1194–1205.

[180] AE Hendrickson, JR Wilson, and MP Ogren. "The neuroanatomical organization of pathways between the dorsal lateral geniculate nucleus and visual cortex in Old World and New World primates." In: *The Journal of Comparative Neurology* **182** (1978), pp. 123–136.

[181] SH Hendry and T Yoshioka. "A neurochemically distinct third channel in the macaque dorsal lateral geniculate nucleus". In: *Science* **264** (1994), pp. 575–577.

[182] G Hennequin, Y Ahmadian, DB Rubin, M Lengyel, and KD Miller. "The Dynamical Regime of Sensory Cortex: Stable Dynamics around a Single Stimulus-Tuned Attractor Account for Patterns of Noise Variability". In: *Neuron* **98** (2018), pp. 846–860.

[183] CA Henry, S Joshi, D Xing, RM Shapley, and MJ Hawken. "Functional Characterization of the Extraclassical Receptive Field in Macaque V1: Contrast, Orientation, and Temporal Dynamics". In: *Journal of Neuroscience* **33** (2013), pp. 6230–6242. arXiv: NIHMS150003.

[184] TK Hensch and MP Stryker. "Columnar Architecture Sculpted by GABA Circuits in Developing Cat Visual Cortex". In: *Science* **303** (2004), pp. 1678–1681.

[185] DR Hochbaum, Y Zhao, SL Farhi, N Klapoetke, CA Werley, V Kapoor, P Zou, JM Kralj, D MacLaurin, N Smedemark-Margulies, JL Saulnier, GL Boulting, C Straub, YK Cho, M Melkonian, GKS Wong, DJ Harrison, VN Murthy, BL Sabatini, ES Boyden, RE Campbell, and AE Cohen. "All-optical electrophysiology in mammalian neurons using engineered microbial rhodopsins". In: *Nature Methods* **11** (2014), p. 825. arXiv: NIHMS150003.

[186] KL Hoffman and BL McNaughton. "Coordinated reactivation of distributed memory traces in primate neocortex". In: *Science* **297** (2002), pp. 2070–2073.

[187] CD Holmgren, M Mukhtarov, AE Malkov, IY Popova, P Bregestovski, and Y Zilberter. "Energy substrate availability as a determinant of neuronal resting potential, GABA signaling and spontaneous network activity in the neonatal cortex in vitro". In: *Journal of Neurochemistry* **112** (2010), pp. 900–912.

[188] C Huang, D Ruff, R Pyle, R Rosenbaum, M Cohen, and BD Doiron. "Circuit-based models of shared variability in cortical networks". In: *bioRxiv* (2017), p. 217976. arXiv: 217976 [10.1101].

[189] X Huang, YM Elyada, WH Bosking, T Walker, and D Fitzpatrick. "Optogenetic Assessment of Horizontal Interactions in Primary Visual Cortex". In: *Journal of Neuroscience* **34** (2014), pp. 4976–4990.

[190] DH Hubel and MS Livingstone. "Segregation of form, color, and stereopsis in primate area 18." In: *Journal of Neuroscience* **7** (1987), pp. 3378–3415.

[191] DH Hubel and TN Wiesel. "Laminar and columnar distribution of geniculo-cortical fibers in the macaque monkey". In: *Journal of Comparative Neurology* **146** (1972), pp. 421–450.

[192] DH Hubel and TN Wiesel. "Receptive Fields and Functional Architecture in Two Nonstriate Visual Areas (18 and 19) of the Cat." In: *Journal of neurophysiology* **28** (1965), pp. 229–289.

[193] DH Hubel and TN Wiesel. "Receptive fields and functional architecture of monkey striate cortex." In: *The Journal of physiology* **195** (1968), pp. 215–243. arXiv: NIHMS150003.

[194] DH Hubel and TN Wiesel. "Receptive fields, binocular interaction and functional architecture in the cat's visual cortex". In: *J Physiology* **160** (1962), pp. 106–154.

[195] DH Hubel and TN Wiesel. "Receptive fields of cells in striate cortex of very young, visually inexperienced kittens". In: *J Physiology* **26** (1963), pp. 994–1002.

[196] DH Hubel and TN Wiesel. "Receptive fields of single neurones in the cat's striate cortex." In: *The Journal of physiology* **148** (1959), pp. 574–591.

[197] DH Hubel, TN Wiesel, and MP Stryker. "Anatomical demonstration of orientation columns in macaque monkey." In: *The Journal of comparative neurology* **177** (1978), pp. 361–380.

[198] DH Hubel and TN Wiesel. "Ferrier lecture. Functional architecture of macaque monkey visual cortex." In: *Philosophical Transactions of the Royal Society B* **198** (1977), pp. 1–59.

[199] DH Hubel and TN Wiesel. "Sequence regularity and geometry of orientation columns in the monkey striate cortex". In: *Journal of Comparative Neurology* **158** (1974), pp. 267–293.

[200] AD Huberman, MB Feller, and B Chapman. "Mechanisms Underlying Development of Visual Maps and Receptive Fields". In: *Annual Review of Neuroscience* **31** (2008), pp. 479–509.

[201] AD Huberman, CM Speer, and B Chapman. "Spontaneous Retinal Activity Mediates Development of Ocular Dominance Columns and Binocular Receptive Fields in V1". In: *Neuron* **52** (2006), pp. 247–254.

[202] AD Huberman, D Stellwagen, and B Chapman. "Decoupling eye-specific segregation from lamination in the lateral geniculate nucleus." In: *Journal of Neuroscience* **22** (2002), pp. 9419–29.

[203] AD Huberman, GY Wang, LC Liets, OA Collins, B Chapman, and LM Chalupa. "Eye-specific retinogeniculate segregation independent of normal neuronal activity". In: *Science* **300** (2003), pp. 994–998.

[204] P Hülsdunk. *Image registration in neural data*. Tech. rep. Goethe Universität Frankfurt, 2017, Master Thesis.

[205] C Humphries, E Liebenthal, and JR Binder. "Tonotopic organization of human auditory cortex". In: *NeuroImage* **50** (2010), pp. 1202–1211. arXiv: NIHMS150003.

[206] PR Huttenlocher. "Development of Neuronal Activity in Neocortex of the Kitten". In: *Nature* **211** (1966), pp. 91–92.

[207] PR Huttenlocher. "Development of cortical neuronal activity in the neonatal cat". In: *Experimental Neurology* **17** (1967), pp. 247–262.

[208] K Ikeda and JM Bekkers. "Autapses". In: *Current Biology* **16** (2006), R308.

[209] M Inoue, A Takeuchi, S Manita, S ichiro Horigane, M Sakamoto, R Kawakami, K Yamaguchi, K Otomo, H Yokoyama, R Kim, T Yokoyama, S Takemoto-Kimura, M Abe, M Okamura, Y Kondo, S Quirin, C Ramakrishnan, T Imamura, K Sakimura, T Nemoto, M Kano, H Fujii, K Deisseroth, K Kitamura, and H Bito. "Rational Engineering of XCaMPs, a Multicolor GECI Suite for In Vivo Imaging of Complex Brain Circuit Dynamics". In: *Cell* **177** (2019), pp. 1346–1360.

[210] M Inoue, A Takeuchi, SI Horigane, M Ohkura, K Gengyo-Ando, H Fujii, S Kamijo, S Takemoto-Kimura, M Kano, J Nakai, K Kitamura, and H Bito. "Rational design of a high-affinity, fast, red calcium indicator R-CaMP2". In: *Nature Methods* **12** (2015), p. 64.

[211] JS Isaacson and M Scanziani. "How inhibition shapes cortical activity". In: *Neuron* **72** (2011), pp. 231–243.

[212] E Ising. "Beitrag zur Theorie des Ferromagnetismus". In: *Zeitschrift für Physik* (1925).

[213] NP Issa, C Trepel, and MP Stryker. "Spatial frequency maps in cat visual cortex." In: *J Neuroscience* **20** (2000), pp. 8504–8514. arXiv: NIHMS150003.

[214] CA Jackson, JD Peduzzi, and TL Hickey. "Visual cortex development in the ferret. I. Genesis and migration of visual cortical neurons." In: *Journal of Neuroscience* **9** (1989), pp. 1242–1253.

[215] SK Jetti, N Vendrell-Llopis, and E Yaksi. "Spontaneous activity governs olfactory representations in spatially organized habenular microcircuits". In: *Current Biology* **24** (2014), pp. 434–439.

[216] X Jia, JH Siegle, C Bennett, SD Gale, DJ Denman, C Koch, and SR Olsen. "High-density extracellular probes reveal dendritic backpropagation and facilitate neuron classification". In: *Journal of Neurophysiology* **121** (2019), pp. 1831–1847.

[217] J Jin, Y Wang, HA Swadlow, and JM Alonso. "Population receptive fields of ON and OFF thalamic inputs to an orientation column in visual cortex." In: *Nature Neuroscience* **14** (2011), pp. 232–238.

[218] MR Joglekar, JF Mejias, GR Yang, and XJ Wang. "Inter-areal Balanced Amplification Enhances Signal Propagation in a Large-Scale Circuit Model of the Primate Cortex". In: *Neuron* **16** (2018), pp. 6402–6413.

[219] P Jonas, G Major, and B Sakmann. "Quantal components of unitary EPSCs at the mossy fibre synapse on CA3 pyramidal cells of rat hippocampus." In: *The Journal of Physiology* **472** (1993), pp. 615–663.

[220] M Judaš, G Sedmak, and M Pletikos. "Early history of subplate and interstitial neurons: From Theodor Meynert (1867) to the discovery of the subplate zone (1974)". In: *Journal of Anatomy* **217** (2010).

[221] M Judaš, G Sedmak, M Pletikos, and N Jovanov-Milošević. "Populations of subplate and interstitial neurons in fetal and adult human telencephalon". In: *Journal of Anatomy* **217** (2010), pp. 381–399.

[222] JJ Jun, NA Steinmetz, JH Siegle, DJ Denman, M Bauza, B Barbarits, AK Lee, CA Anastassiou, A Andrei, Ç Aydin, M Barbic, TJ Blanche, V Bonin, J Couto, B Dutta, SL Gratiy, DA Gutnisky, M Häusser, B Karsh, P Ledochowitsch, CM Lopez, C Mitelut, S Musa, M Okun, M Pachitariu, J Putzeys, PD Rich, C Rossant, WL Sun, K Svoboda, M Carandini, KD Harris, C Koch, J O'Keefe, and TD Harris. "Fully integrated silicon probes for high-density recording of neural activity". In: *Nature* **551** (2017), pp. 232–236.

[223] DM Kammen and AL Yuille. "Spontaneous symmetry-breaking energy functions and the emergence of orientation selective cortical cells". In: *Biological Cybernetics* **59** (1988), pp. 23–31.

[224] H Kamyshanska. "The influence of recurrent interactions on orientation discrimination in primary visual cortex". PhD thesis. Goethe University Frankfurt, 2018.

[225] K Kandler and LC Katz. "Coordination of neuronal activity in developing visual cortex by gap junction-mediated biochemical communication". In: *Journal of Neuroscience* **18** (1998), pp. 1419–1427.

[226] KK Kang, M Shelley, and H Sompolinsky. "Mexican hats and pinwheels in visual cortex". In: *Proceedings of the National Academy of Sciences* **100** (2003), pp. 2848–2853.

[227] PO Kanold and HJ Luhmann. "The Subplate and Early Cortical Circuits". In: *Annual Review of Neuroscience* **33** (2010), pp. 23–48.

[228] P Kanold. "Subplate neurons: crucial regulators of cortical development and plasticity". In: *Frontiers in Neuroanatomy* **3** (2009).

[229] M Kaschube, F Wolf, T Geisel, and S Löwel. "Genetic influence on quantitative features of neocortical architecture." In: *The Journal of Neuroscience* **22** (2002), pp. 7206–7217.

[230] M Kaschube, M Schnabel, F Wolf, S Loewel, and S Löwel. "Interareal coordination of columnar architectures during visual cortical development". In: *PNAS* **106** (2009), pp. 17205–17210. arXiv: `0801.4164`.

[231] M Kaschube, M Schnabel, S Löwel, DM Coppola, LE White, and F Wolf. "Universality in the evolution of orientation columns in the visual cortex". In: *Science* **330** (2010), pp. 1113–1116.

[232] LC Katz, CD Gilbert, and TN Wiesel. "Local circuits and ocular dominance columns in monkey striate cortex." In: *Journal of Neuroscience* **9** (1989), pp. 1389–1399.

[233] LC Katz and JC Crowley. "Development of cortical circuits: Lessons from ocular dominance columns". In: *Nature Reviews Neuroscience* **3** (2002), pp. 34–42.

[234] W Keil, KFKF Schmidt, S Löwel, M Kaschube, S Lowel, and M Kaschube. "Reorganization of columnar architecture in the growing visual cortex." In: *Proceedings of the National Academy of Sciences* **107** (2010), pp. 12293–12298. arXiv: `0905.2843`.

[235] T Kenet, D Bibitchkov, M Tsodyks, A Grinvald, and A Arieli. "Spontaneously emerging cortical representations of visual attributes." In: *Nature* **425** (2003), pp. 954–956.

[236] C Kennedy, MH Des Rosiers, O Sakurada, M Shinohara, M Reivich, JW Jehle, and L Sokoloff. "Metabolic mapping of the primary visual system of the monkey by means of the autoradiographic [14C]deoxyglucose technique." In: *Proceedings of the National Academy of Sciences of the United States of America* **73** (1976), pp. 4230–4235.

[237] AM Kerlin, ML Andermann, VK Berezovskii, and RC Reid. "Broadly Tuned Response Properties of Diverse Inhibitory Neuron Subtypes in Mouse Visual Cortex". In: *Neuron* **67** (2010), pp. 858–871.

[238] D Kerschensteiner. "Spontaneous network activity and synaptic development". In: *Neuroscientist* **20** (2014), pp. 272–290. arXiv: NIHMS150003.

[239] R Khazipov, A Sirota, X Leinekugel, GL Holmes, Y Ben-Ari, and G Buzsáki. "Early motor activity drives spindle bursts in the developing somatosensory cortex". In: *Nature* **432** (2004), p. 758.

[240] CK Kim, SJ Yang, N Pichamoorthy, NP Young, I Kauvar, JH Jennings, TN Lerner, A Berndt, SY Lee, C Ramakrishnan, TJ Davidson, M Inoue, H Bito, and K Deisseroth. "Simultaneous fast measurement of circuit dynamics at multiple sites across the mammalian brain". In: *Nature Methods* **13** (2016), pp. 325–328.

[241] JZ Kim, JM Soffer, AE Kahn, JM Vettel, F Pasqualetti, and DS Bassett. "Role of graph architecture in controlling dynamical networks with applications to neural systems". In: *Nature Physics* **14** (2018), pp. 91–98.

[242] LA Kirkby, GS Sack, A Firl, and MB Feller. "A Role for Correlated Spontaneous Activity in the Assembly of Neural Circuits". In: *Neuron* **80** (2013), pp. 1129–1144. arXiv: 15334406.

[243] ZF Kisvárday and UT Eysel. "Cellular organization of reciprocal patchy networks in layer III of cat visual cortex (area 17)". In: *Neuroscience* **46** (1992), pp. 275–286.

[244] NC Klapoetke, Y Murata, SS Kim, SR Pulver, A Birdsey-benson, YK Cho, TK Morimoto, AS Chuong, EJ Carpenter, Z Tian, J Wang, Y Xie, Z Yan, Y Zhang, BY Chow, B Surek, M Melkonian, V Jayaraman, M Constantine-Paton, GKsS Wong, and ES Boyden. "Independent optical excitation of distinct neural populations". In: *Nature Methods* **11** (2014), pp. 338–346. arXiv: NIHMS150003.

[245] T Kleindienst, J Winnubst, C Roth-Alpermann, T Bonhoeffer, and C Lohmann. "Activity-dependent clustering of functional synaptic inputs on developing hippocampal dendrites". In: *Neuron* **72** (2011), pp. 1012–1024.

[246] JJ Knierim and CV Essen. "Neuronal responses to static texture patterns in area V1 of the alert macaque monkey". In: *Neurophysiol* **67** (1992), pp. 961–980.

[247] SM Koch, CG Dela Cruz, TS Hnasko, RH Edwards, AD Huberman, and EM Ullian. "Pathway-Specific Genetic Attenuation of Glutamate Release Alters Select Features of Competition-Based Visual Circuit Refinement". In: *Neuron* **71** (2011), pp. 235–242.

[248] I Kostović and M Molliver. "A new interpretation of the laminar development of cerebral cortex: synaptogenesis in different layers of neopallium in the human fetus". In: *Anat Rec* **178** (1974).

[249] K Krug, CJ Akerman, and ID Thompson. "Responses of neurons in neonatal cortex and thalamus to patterned visual stimulation through the naturally closed lids." In: *Journal of Neurophysiology* **85** (2001), pp. 1436–1443.

[250] SW Kuffler. "Discharge patterns and functional organization of mammalian retina". In: *J Neurophysiology* **16** (1953), pp. 37–68.

[251] ID Landau, R Egger, VJ Dercksen, M Oberlaender, and H Sompolinsky. "The Impact of Structural Heterogeneity on Excitation-Inhibition Balance in Cortical Networks". In: *Neuron* **92** (2016), pp. 1106–1121.

[252] MI Law, KR Zahs, and MP Stryker. "Organization of primary visual cortex (area 17) in the ferret". In: *J Comparative Neurology* **278** (1988), pp. 157–180.

[253] A Lazar, G Pipa, and J Triesch. "SORN: A self-organizing recurrent neural network". In: *Frontiers in Computational Neuroscience* **3** (2009), p. 23.

[254] S Le Vay, TN Wiesel, and DH Hubel. "The development of ocular dominance columns in normal and visually deprived monkeys". In: *Journal of Comparative Neurology* **191** (1980), pp. 1–51.

[255] S LeVay, DH Hubel, and TN Wiesel. "The pattern of ocular dominance columns in macaque visual cortex revealed by a reduced silver stain". In: *Journal of Comparative Neurology* **159** (1975), pp. 559–575.

[256] H Lee, BK Brott, LA Kirkby, JD Adelson, S Cheng, MB Feller, A Datwani, and CJ Shatz. "Synapse elimination and learning rules co-regulated by MHC class i H2-Db". In: *Nature* **509** (2014), pp. 195–200. arXiv: 15334406.

[257] AH Leighton and C Lohmann. "The Wiring of Developing Sensory Circuits-From Patterned Spontaneous Activity to Synaptic Plasticity Mechanisms". In: *Frontiers in Neural Circuits* **10** (2016), p. 71.

[258] X Leinekugel, V Tseeb, Y Ben-Ari, and P Bregestovski. "Synaptic GABAA activation induces Ca2+ rise in pyramidal cells and interneurons from rat neonatal hippocampal slices." In: *The Journal of Physiology* **487** (1995), pp. 319–329.

[259] X Leinekugel, I Medina, I Khalilov, Y Ben-Ari, and R Khazipov. "Ca2+ oscillations mediated by the synergistic excitatory actions of GABA(A) and NMDA receptors in the neonatal hippocampus". In: *Neuron* **18** (1997), pp. 243–255.

[260] J Lengler, F Jug, and A Steger. "Reliable neuronal systems: The importance of heterogeneity". In: *PLoS ONE* **8** (2013), e80694.

[261] G Leuba and R Kraftsik. "Changes in volume, surface estimate, three-dimensional shape and total number of neurons of the human primary visual cortex from midgestation until old age". In: *Anatomy and Embryology* **190** (1994), pp. 351–366.

[262] S Levay, MP Stryker, and CJ Shatz. "Ocular dominance columns and their development in layer IV of the cat's visual cortex: A quantitative study". In: *Journal of Comparative Neurology* **179** (1978), pp. 223–244.

[263] AG Leventhal, RW Rodieck, and B Dreher. "Retinal ganglion cell classes in the Old World monkey: morphology and central projections." In: *Science* **213** (1981), pp. 1139–1142.

[264] R Levins. "The Strategy of Model Building in Population Biology". In: *American Sci* **54** (1966), pp. 421–431.

[265] RB Levy and AD Reyes. "Spatial profile of excitatory and inhibitory synaptic connectivity in mouse primary auditory cortex." In: *Journal of Neuroscience* **32** (2012), pp. 5609–5619.

[266] AD Lien and M Scanziani. "Tuned thalamic excitation is amplified by visual cortical circuits". In: *Nature Neuroscience* **16** (2013), pp. 1315–1323.

[267] DC Linden, RW Guillery, and J Cucchiaro. "The dorsal lateral geniculate nucleus of the normal ferret and its postnatal development". In: *J Comp Neurol* **203** (1981), pp. 189–211.

[268] R Linsker. "From basic network principles to neural architecture: emergence of spatial-opponent cells." In: *PNAS* **83** (1986), pp. 8390–8394.

[269] A Litwin-Kumar and B Doiron. "Formation and maintenance of neuronal assemblies through synaptic plasticity". In: *Nature Communications* **5** (2014), p. 5319.

[270] MS Livingstone and DH Hubel. "Anatomy and Physiology of a color system in the primate visual cortex". In: *J Neuroscience* **4** (1984), pp. 309–356.

[271] MS Livingstone and DH Hubel. "Psychophysical evidence for separate channels for the perception of form, color, movement, and depth." In: *Journal of Neuroscience* **7** (1987), pp. 3416–3468.

[272] S Löwel and W Singer. "The pattern of ocular dominance columns in flat-mounts of the cat visual cortex". In: *Experimental Brain Research* **68** (1987), pp. 661–666.

[273] S Löwel and W Singer. "Selection of Intrinsic Horizontal Connections in the Visual Cortex by Correlated Neuronal Activity". In: *Science* **255** (1992), pp. 209–212.

[274] A Luczak, P Barthó, and KD Harris. "Spontaneous Events Outline the Realm of Possible Sensory Responses in Neocortical Populations". In: *Neuron* **62** (2009), pp. 413–425. arXiv: `NIHMS150003`.

[275] HJ Luhmann, W Singer, and L Martinez-Millán. "Horizontal Interactions in Cat Striate Cortex: I. Anatomical Substrate and Postnatal Development". In: *European Journal of Neuroscience* **2** (1990), pp. 344–357.

[276] HJ Luhmann, W Kilb, and IL Hanganu-opatz. "Subplate cells : amplifiers of neuronal activity in the developing cerebral cortex". In: *Frontiers in Neuroanatomy* **3** (2009), p. 19.

[277] HJ Luhmann, A Sinning, JW Yang, V Reyes-Puerta, MC Stüttgen, S Kirischuk, W Kilb, K Imaizumi, and R Khazipov. "Spontaneous Neuronal Activity in Developing Neocortical Networks: From Single Cells to Large-Scale Interactions". In: *Frontiers in Neural Circuits* **10** (2016), p. 40.

[278] JS Lund. "Anatomical Organization of Macaque Monkey Striate Visual Cortex". In: *Annual Review of Neuroscience* **11** (1988), pp. 253–288.

[279] JS Lund and T Yoshioka. "Local circuit neurons of macaque monkey striate cortex: III. Neurons of laminae 4B, 4A, and 3B." In: *J Comp Neurol* **311** (1991), pp. 234–258.

[280] JS Lund. "Local circuit neurons of macaque monkey striate cortex: I. Neurons of laminae 4C and 5A." In: *Journal of Comparative Neurology* **257** (1987), pp. 60–92.

[281] JS Lund and CQ Wu. "Local circuit neurons of macaque monkey striate cortex: IV. Neurons of laminae 1-3a". In: *Journal of Comparative Neurology* **384** (1997), pp. 109–126.

[282] L Luo, EM Callaway, and K Svoboda. "Genetic Dissection of Neural Circuits: A Decade of Progress". In: *Neuron* **98** (2018), pp. 256–281.

[283] C Ly. "Firing rate dynamics in recurrent spiking neural networks with intrinsic and network heterogeneity". In: *Journal of Computational Neuroscience* **39** (2015), pp. 311–327. arXiv: `1505.03176`.

[284] JN MacLean, BO Watson, GB Aaron, and R Yuste. "Internal dynamics determine the cortical response to thalamic stimulation". In: *Neuron* **48** (2005), pp. 811–823.

[285] R Malach, Y Amir, M Harel, and A Grinvald. "Relationship between intrinsic connections and functional architecture revealed by optical imaging and in vivo targeted biocytin injections in primate striate cortex." In: *Proceedings of the National Academy of Sciences* **90** (1993), pp. 10469–10473.

[286] HA Mallot. "An overall description of retinotopic mapping in the cat's visual cortex areas 17, 18, and 19". In: *Biological Cybernetics* **52** (1985), pp. 45–51.

[287] C von der Malsburg. "Self-organization of orientation sensitive cells in the striate cortex." In: *Biological Cybernetics* **14** (1973), pp. 85–100.

[288] E Marder. "Variability, compensation, and modulation in neurons and circuits". In: *Proceedings of the National Academy of Sciences* **108** (2011), pp. 15542–15548.

[289] D Marr. "A theory of cerebellar cortex". In: *The Journal of Physiology* **202** (1969), pp. 437–470. arXiv: `NIHMS150003`.

[290] JR Martin, KL Rogers, C Chagneau, and P Brûlet. "In vivo bioluminescence imaging of Ca$ˆ{2+}$ signalling in brain of Drosophila". In: *PLoS ONE* **2** (2007), e275.

[291] KAC Martin, P Somogyi, and D Whitteridge. "Physiological and morphological properties of identified basket cells in the cat's visual cortex". In: *Experimental Brain Research* **50** (1983), pp. 193–200.

[292] KAC Martin. "The Wellcome Prize Lecture From Single Cells To Simple Circuits In The Cerebral Cortex". In: *Quarterly Journal of Experimental Physiology* **73** (1988), pp. 637–702.

[293] A Mason and A Larkman. "Correlations between morphology and electrophysiology of pyramidal neurons in slices of rat visual cortex. II. Electrophysiology". In: *The Journal of Neuroscience* **10** (1990), pp. 1415–1428.

[294] N McLoughlin and I Schiessl. "Orientation selectivity in the common marmoset (Callithrix jacchus): The periodicity of orientation columns in V1 and V2". In: *NeuroImage* **31** (2006), pp. 76–85.

[295] P Mehta, L Kreeger, DC Wylie, JJ Pattadkal, T Lusignan, MJ Davis, GF Turi, WK Li, MP Whitmire, Y Chen, BL Kajs, E Seidemann, NJ Priebe, A Losonczy, and BV Zemelman. "Functional Access to Neuron Subclasses in Rodent and Primate Forebrain". In: *Cell Reports* **26** (2019), pp. 2818–2832.

[296] H Meinhardt. "Turing's theory of morphogenesis of 1952 and the subsequent discovery of the crucial role of local self enhancement and long-range inhibition". In: *Interface Focus* **56** (2012), pp. 447–462.

[297] M Meister, ROL Wong, DA Baylor, and CJ Shatz. "Synchronous bursts of action potentials in ganglion cells of the developing mammalian retina." In: *Science* **252** (1991), pp. 939–943.

[298] M Meister, L Lagnado, and DA Baylor. "Concerted signaling by retinal ganglion cells". In: *Science* **270** (1995), pp. 1207–1210.

[299] MM Merzenich and JF Brugge. "Representation of the cochlear partition on the superior temporal plane of the macaque monkey". In: *Brain Research* **50** (1973), pp. 275–296. arXiv: `arXiv:1011.1669v3`.

[300] L Meshulam, JL Gauthier, CD Brody, DW Tank, and W Bialek. "Collective Behavior of Place and Non-place Neurons in the Hippocampal Network". In: *Neuron* **96** (2017), pp. 1178–1191. arXiv: `1612.08935`.

[301] C Metin, P Godement, and M Imbert. “The primary visual cortex in the mouse: receptive field properties and functional organization”. In: *Exp Brain Res* **69** (1988), pp. 594–612.

[302] R Miikkulainen, JA Bednar, Y Choe, and J Sirosh. *Computational maps in the visual cortex*. Springer Science & Business Media, 2005, pp. 1–538.

[303] JeK Miller, I Ayzenshtat, L Carrillo-Reid, and R Yuste. “Visual stimuli recruit intrinsically generated cortical ensembles”. In: *Proceedings of the National Academy of Sciences* **111** (2014), pp. 1–9.

[304] KD Miller. “A model for the development of simple cell receptive fields and the ordered arrangement of orientation columns through activity-dependent competition between ON- and OFF-center inputs.” In: *J Neuroscience* **14** (1994), pp. 409–441.

[305] KD Miller. “Understanding layer 4 of the cortical circuit: a model based on cat V1”. In: *Cerebral Cortex* **13** (2003), pp. 73–82.

[306] KD Miller, JB Keller, and MP Stryker. “Ocular dominance column development: analysis and simulation.” In: *Science* **245** (1989), pp. 605–15.

[307] D Miner and J Triesch. “Plasticity-Driven Self-Organization under Topological Constraints Accounts for Non-random Features of Cortical Synaptic Wiring”. In: *PLoS Computational Biology* **12** (2016), e1004759.

[308] M Minlebaev, Y Ben-Ari, and R Khazipov. “Network Mechanisms of Spindle-Burst Oscillations in the Neonatal Rat Barrel Cortex In Vivo”. In: *Journal of Neurophysiology* **97** (2007), pp. 692–700.

[309] M Minlebaev, M Colonnese, T Tsintsadze, A Sirota, and R Khazipov. “Early gamma oscillations synchronize developing thalamus and cortex”. In: *Science* **334** (2011), pp. 226–229.

[310] MH Mohajerani, AW Chan, M Mohsenvand, J Ledue, R Liu, DA McVea, JD Boyd, YT Wang, M Reimers, and TH Murphy. “Spontaneous cortical activity alternates between motifs defined by regional axonal projections”. In: *Nature Neuroscience* **16** (2013), pp. 1426–1435. arXiv: `NIHMS150003`.

[311] R Mooney, AA Penn, R Gallego, and CJ Shatz. “Thalamic relay of spontaneous retinal activity prior to vision”. In: *Neuron* **17** (1996), pp. 863–874.

[312] A Morel, PE Garraghty, and JH Kaas. “Tonotopic organization, architectonic fields, and connections of auditory cortex in macaque monkeys”. In: *Journal of Comparative Neurology* **335** (1993), pp. 437–459.

[313] V Mountcastle. “Modality and topographic properties of single neurons of cat’s somatic sensory cortex.” In: *Journal of neurophysiology* **20** (1957), pp. 408–34.

[314] G Muir-Robinson, BJ Hwang, and MB Feller. “Retinogeniculate axons undergo eye-specific segregation in the absence of eye-specific layers”. In: *Journal of Neuroscience* **22** (2002), pp. 5259–5264.

[315] DR Muir, NM Da Costa, CC Girardin, S Naaman, DB Omer, E Ruesch, A Grinvald, and RJ Douglas. “Embedding of Cortical Representations by the Superficial Patch System.” In: *Cerebral Cortex* **21** (2011), pp. 2244–2260.

[316] DR Muir and M Cook. *Anatomical constraints on lateral competition in columnar cortical architectures*. 2014. arXiv: `1309.2848v1`.

[317] BK Murphy and KD Miller. “Balanced Amplification: A New Mechanism of Selective Amplification of Neural Activity Patterns”. In: *Neuron* **61** (2009), pp. 635–648.

[318] EH Murphy and N Berman. "The rabbit and the cat: a comparison of some features of response properties of single cells in the primary visual cortex." In: *J Comparative Neurology* **188** (1979), pp. 401–427.

[319] KM Murphy, RC Van Sluyters, and DG Jones. "Cytochrome-oxidase activity in cat visual cortex: is it periodic." In: *Soc Neurosci Abstract* **16** (1990).

[320] KL Myhr, PD Lukasiewicz, and ROL Wong. "Mechanisms underlying developmental changes in the firing patterns of ON and OFF retinal ganglion cells during refinement of their central projections". In: *J Neurosci* **21** (2001), pp. 8664–8671.

[321] MM Nass and LN Cooper. "A theory for the development of feature detecting cells in visual cortex". In: *Biological Cybernetics* **19** (1975), pp. 1–18.

[322] Da Nelson and LC Katz. "Emergence of Functional Circuits in Ferret Visual Cortex Visualized by Optical Imaging". In: **15** (1995), pp. 23–34.

[323] CF Newland and SG Cull-Candy. "On the mechanism of action of picrotoxin on GABA receptor channels in dissociated sympathetic neurones of the rat." In: *The Journal of Physiology* **447** (1992), pp. 191–213.

[324] CM Niell and MP Stryker. "Highly selective receptive fields in mouse visual cortex." In: *J Neuroscience* **28** (2008), pp. 7520–7536.

[325] CM Niell and MP Stryker. "Modulation of Visual Responses by Behavioral State in Mouse Visual Cortex". In: *Neuron* **65** (2010), pp. 472–479. arXiv: `arXiv:1011.1669v3`.

[326] L Nurminen and A Angelucci. "Multiple components of surround modulation in primary visual cortex: Multiple neural circuits with multiple functions?" In: *Vision Research* **104** (2014), pp. 47–56.

[327] K O'Hashi, T Fekete, T Deneux, R Hildesheim, C van Leeuwen, and A Grinvald. "Inter-hemispheric Synchrony of Spontaneous Cortical States at the Cortical Column Level". In: *Cerebral Cortex* **28** (2017), pp. 1794–1807.

[328] LP O'Keefe, JB Levitt, DC Kiper, RM Shapley, and JA Movshon. "Functional Organization of Owl Monkey Lateral Geniculate Nucleus and Visual Cortex". In: *J Neurophysiology* **80** (1998), pp. 594–609.

[329] O Ohana, H Portner, and KAC Martin. "Fast recruitment of recurrent inhibition in the cat visual cortex". In: *PLoS ONE* **7** (2012), e40601.

[330] K Ohki, Y Matsuda, A Ajima, DS Kim, and S Tanaka. "Arrangement of orientation pinwheel centers around area 17/18 transition zone in cat visual cortex." In: *Cerebral cortex* **10** (2000), pp. 593–601.

[331] K Ohki, S Chung, YH Ch'ng, P Kara, and RC Reid. "Functional imaging with cellular resolution reveals precise micro-architecture in visual cortex." In: *Nature* **433** (2005), pp. 597–603.

[332] K Ohki, S Chung, P Kara, M Hübener, T Bonhoeffer, and RC Reid. "Highly ordered arrangement of single neurons in orientation pinwheels." In: *Nature* **442** (2006), pp. 925–928.

[333] RW Olsen. "Picrotoxin-like channel blockers of GABAA receptors". In: *Proceedings of the National Academy of Sciences* **103** (2006), pp. 6081–6082.

[334] O OpenStax College. *Anatomy & Physiology*. 2013.

[335] TS Otis and I Mody. "Modulation of decay kinetics and frequency of GABAA receptor-mediated spontaneous inhibitory postsynaptic currents in hippocampal neurons". In: *Neuroscience* **49** (1992), pp. 13–32.

[336] AM Packer, LE Russell, HWP Dalgleish, and M Häusser. "Simultaneous all-optical manipulation and recording of neural circuit activity with cellular resolution in vivo". In: *Nature Methods* **12** (2015), pp. 140–146.

[337] JG Parnavelas, RA Burne, and CS Lin. "Receptive field properties of neurons in the visual cortex of the rat." In: *Neuroscience Letters* **27** (1981), pp. 291–296.

[338] A Patrizi, B Scelfo, L Viltono, F Briatore, M Fukaya, M Watanabe, P Strata, F Varoqueaux, N Brose, JM Fritschy, and M Sassoè-Pognetto. "Synapse formation and clustering of neuroligin-2 in the absence of GABAA receptors." In: *Proceedings of the National Academy of Sciences of the United States of America* **105** (2008), pp. 13151–13156.

[339] N Patzke, GM Innocenti, and PR Manger. "The claustrum of the ferret: afferent and efferent connections to lower and higher order visual cortical areas". In: *Frontiers in Systems Neuroscience* **8** (2014), p. 31.

[340] JW Peirce. "PsychoPy-Psychophysics software in Python". In: *Journal of Neuroscience Methods* **162** (2007), pp. 8–13.

[341] AA Penn, PA Riquelme, MB Feller, and CJ Shatz. "Competition in retinogeniculate patterning driven by spontaneous activity". In: *Science* **279** (1998), pp. 2108–2112.

[342] V Pernice and RA da Silveira. "Interpretation of correlated neural variability from models of feed-forward and recurrent circuits". In: *PLoS Computational Biology* **14** (2018), e1005979.

[343] SP Peron, J Freeman, V Iyer, C Guo, and K Svoboda. "A Cellular Resolution Map of Barrel Cortex Activity during Tactile Behavior". In: *Neuron* **86** (2015), pp. 783–799.

[344] CCH Petersen, TTG Hahn, M Mehta, A Grinvald, and B Sakmann. "Interaction of sensory responses with spontaneous depolarization in layer 2/3 barrel cortex." In: *Proceedings of the National Academy of Sciences* **100** (2003), pp. 13638–13643.

[345] CK Pfeffer, M Xue, M He, ZJ Huang, and M Scanziani. "Inhibition of inhibition in visual cortex: The logic of connections between molecularly distinct interneurons". In: *Nature Neuroscience* **16** (2013), pp. 1068–1076. arXiv: `NIHMS150003`.

[346] DJ Pinto and BG Ermentrout. "Spatially structured activity in synaptically coupled neuronal networks: II. Lateral inhibition and standing pulses." In: *SIAM Journal on Applied Mathematics* **62** (2001), pp. 226–243.

[347] V Plerou, P Gopikrishnan, B Rosenow, LA Amaral, and HE Stanley. "Universal and nonuniversal properties of cross correlations in financial time series". In: *Physical Review Letters* **83** (1999), p. 1471.

[348] J Pokorny. "Review: Steady and pulsed pedestals, the how and why of post-receptoral pathway separation". In: *Journal of Vision* **11** (2011), pp. 7–7.

[349] RA Reale and TJ Imig. "Tonotopic organization in auditory cortex of the cat". In: *Journal of Comparative Neurology* **192** (1980), pp. 265–291.

[350] A Rebsam, TJ Petros, and CA Mason. "Switching retinogeniculate axon laterality leads to normal targeting but abnormal eye-specific segregation that is activity dependent". In: *Journal of Neuroscience* **29** (2009), pp. 14855–14863.

[351] S Recanatesi, GK Ocker, MA Buice, and E Shea-Brown. "Dimensionality in recurrent spiking networks: global trends in activity and local origins in connectivity". In: *bioRxiv* (2018). arXiv: `394684`.

[352] K Reinhold, AD Lien, and M Scanziani. "Distinct recurrent versus afferent dynamics in cortical visual processing". In: *Nature Neuroscience* **18** (2015), pp. 1789–1797.

[353] A Renart, P Song, and XJ Wang. "Robust spatial working memory through homeostatic synaptic scaling in heterogeneous cortical networks". In: *Neuron* **38** (2003), pp. 473–485.

[354] JP Rickgauer, K Deisseroth, and DW Tank. "Simultaneous cellular-resolution optical perturbation and imaging of place cell firing fields". In: *Nature Neuroscience* **17** (2014), pp. 1816–24.

[355] DM Rioch. "Studies on the diencephalon of carnivora part I. The nuclear configuration of the thalamus, epithalamus, and hypothalamus of the dog and cat". In: *Journal of Comparative Neurology* **49** (1929), pp. 1–119.

[356] KS Rockland and JS Lund. "Intrinsic laminar lattice connections in primate visual cortex". In: *Journal of Comparative Neurology* **216** (1983), pp. 303–318.

[357] KS Rockland and JS Lund. "Widespread periodic intrinsic connections in the tree shrew visual cortex." In: *Science* **215** (1982), pp. 1532–1534.

[358] AW Roe, K Fritsches, and JD Pettigrew. "Optical imaging of functional organization of V1 and V2 in marmoset visual cortex". In: *The Anatomical Record Part A: Discoveries in Molecular, Cellular, and Evolutionary Biology* **287A** (2005), pp. 1213–1225.

[359] B Roerig and B Chen. "Relationships of local inhibitory and excitatory circuits to orientation preference maps in ferret visual cortex." In: *Cerebral cortex* **12** (2002), pp. 187–98.

[360] GL Romani, SJ Williamson, and L Kaufman. "Tonotopic organization of the human auditory cortex". In: *Science* **216** (1982), pp. 1339–1340.

[361] SA Romano, T Pietri, V Pérez-Schuster, A Jouary, M Haudrechy, and G Sumbre. "Spontaneous neuronal network dynamics reveal circuit's functional adaptations for behavior". In: *Neuron* **85** (2015), pp. 1070–1085.

[362] E Ronzitti, C Ventalon, M Canepari, BC Forget, E Papagiakoumou, and V Emiliani. "Recent advances in patterned photostimulation for optogenetics". In: *Journal of Optics* **19** (2017), p. 113001.

[363] R Rosenbaum and B Doiron. "Balanced networks of spiking neurons with spatially dependent recurrent connections". In: *Physical Review X* **4** (2014), p. 021039. arXiv: 1308.6014.

[364] ES Ruthazer and MP Stryker. "The role of activity in the development of long-range horizontal connections in area 17 of the ferret." In: *Journal of Neuroscience* **16** (1996), pp. 7253–7269.

[365] S Sakata and KD Harris. "Laminar Structure of Spontaneous and Sensory-Evoked Population Activity in Auditory Cortex". In: *Neuron* **64** (2009), pp. 404–418.

[366] AB Saleem, EM Diamanti, J Fournier, KD Harris, and M Carandini. "Coherent encoding of subjective spatial position in visual cortex and hippocampus". In: *Nature* **562** (2018), pp. 124–127.

[367] SL Sally and JB Kelly. "Organization of auditory cortex in the albino rat: sound frequency." In: *Journal of neurophysiology* **59** (1988), pp. 1627–38.

[368] MV Sanchez-Vives and DA McCormick. "Cellular and network mechanisms of rhytmic recurrent activity in neocortex". In: *Nature Neuroscience* **3** (2000), pp. 1027–1034.

[369] KJ Sanderson, RW Guillery, and RM Shackelford. "Congenitally abnormal visual pathways in mink (Mustela vison) with reduced retinal pigment". In: *Journal of Comparative Neurology* **154** (1974), pp. 225–248.

[370] JR Sanes and M Yamagata. "Many Paths to Synaptic Specificity". In: *Annual Review of Cell and Developmental Biology* **25** (2009), pp. 161–195.

[371] JL Schnapf and DA Baylor. "How photoreceptor cells respond to light". In: *Scientific American* **256** (1987), pp. 40–47.

[372] E Schneidman, MJ Berry, R Segev, and W Bialek. "Weak pairwise correlations imply strongly correlated network states in a neural population". In: *Nature* **440** (2006), pp. 1007–1012. arXiv: `0512013 [q-bio]`.

[373] M Schottdorf, W Keil, D Coppola, and LE White. "Random Wiring, Ganglion Cell Mosaics, and the Functional Architecture of the Visual Cortex". In: *PLoS Computational Biology* **11** (2015), e1004602.

[374] G Sclar and RD Freeman. "Orientation selectivity in the cat's striate cortex is invariant with stimulus contrast". In: *Experimental Brain Research* **46** (1982), pp. 457–461.

[375] E Seidemann, Y Chen, Y Bai, SC Chen, P Mehta, BL Kajs, WS Geisler, and BV Zemelman. "Calcium imaging with genetically encoded indicators in behaving primates". In: *eLife* **5** (2016), e16178.

[376] F Sengpiel and PC Kind. "The Role of Activity in Development of the Visual System". In: *Current Biology* **12** (2002), pp. 818–826.

[377] F Sengpiel, P Stawinski, and T Bonhoeffer. "Influence of experience on orientation maps in cat visual cortex." In: *Nature Neuroscience* **2** (1999), pp. 727–732.

[378] M Shamir and H Sompolinsky. "Implications of neuronal diversity on population coding". In: *Neural Computation* **18** (2006), pp. 1951–1986.

[379] R Shapley and P Lennie. "Spatial frequency analysis in the visual system." In: *Annual review of neuroscience* **8** (1985), pp. 547–581.

[380] E Sharifullina and A Nistri. "Glutamate uptake block triggers deadly rhythmic bursting of neonatal rat hypoglossal motoneurons". In: *Journal of Physiology* **572** (2006), pp. 407–423.

[381] CJ Shatz. "The prenatal development of the cat's retinogeniculate pathway". In: *J Neurosci* **3** (1983), pp. 482–499.

[382] A Shmuel and A Grinvald. "Functional organization for direction of motion and its relationship to orientation maps in cat area 18." In: *Journal of Neuroscience* **16** (1996), pp. 6945–6964.

[383] F Siegel, JA Heimel, J Peters, and C Lohmann. "Peripheral and central inputs shape network dynamics in the developing visual cortex in vivo". In: *Current Biology* **22** (2012), pp. 253–258.

[384] AM Sillito, HE Jones, GL Gerstein, and DC West. "Feature-linked synchronization of thalamic relay cell firing induced by feedback from the visual cortex." In: *Nature* **369** (1994), pp. 479–482.

[385] ST Sipila, K Huttu, J Yamada, R Afzalov, J Voipio, P Blaesse, and K Kaila. "Compensatory Enhancement of Intrinsic Spiking upon NKCC1 Disruption in Neonatal Hippocampus". In: *Journal of Neuroscience* **29** (2009), pp. 6982–6988.

[386] BC Skottun, a Bradley, G Sclar, I Ohzawa, and RD Freeman. "The effects of contrast on visual orientation and spatial frequency discrimination: a comparison of single cells and behavior." In: *Journal of neurophysiology* **57** (1987), pp. 773–786.

[387] GB Smith and D Fitzpatrick. "Viral injection and cranial window implantation for in vivo two-photon imaging". In: *High-Resolution Imaging of Cellular Proteins*. New York, NY: Springer Verlag, 2016. Chap. 10, pp. 171–185.

[388] GB Smith, DE Whitney, and D Fitzpatrick. "Modular Representation of Luminance Polarity in the Superficial Layers of Primary Visual Cortex". In: *Neuron* **88** (2015), pp. 805–818.

[389] GB Smith, B Hein, DE Whitney, D Fitzpatrick, and M Kaschube. "Distributed network interactions and their emergence in developing neocortex". In: *Nature Neuroscience* **21** (2018), pp. 1600–1608.

[390] GB Smith, A Sederberg, YM Elyada, SD Van Hooser, M Kaschube, and D Fitzpatrick. "The development of cortical circuits for motion discrimination". In: *Nat Neurosci* **18** (2015), pp. 252–261.

[391] L Sokoloff. "Relation between Physiological Function and Energy Metabolism in the Central Nervous System". In: *Journal of Neurochemistry* **29** (1977), pp. 13–26.

[392] DC Somers, EV Todorov, AG Siapas, LJ Toth, DS Kim, and M Sur. "A local circuit approach to understanding integration of long-range inputs in primary visual cortex". In: *Cerebral Cortex* **8** (1998), pp. 204–217.

[393] P Somogyi, ZF Kisvárday, KA Martin, and D Whitteridge. "Synaptic connections of morphologically identified and physiologically characterized large basket cells in the striate cortex of cat". In: *Neuroscience* **10** (1983), pp. 261–294.

[394] CM Speer, C Sun, LC Liets, BK Stafford, B Chapman, and HJ Cheng. "Eye-specific retinogeniculate segregation proceeds normally following disruption of patterned spontaneous retinal activity". In: *Neural Development* **9** (2014), p. 25.

[395] NC Spitzer. "Electrical activity in early neuronal development". In: *Nature* **444** (2006), pp. 707–712.

[396] DW Sretavan and CJ Shatz. "Prenatal development of retinal ganglion cell axons: segregation into eye-specific layers within the cat's lateral geniculate nucleus." In: *Journal of Neuroscience* **6** (1986), pp. 234–51.

[397] RC Stacy. "Disruption and Recovery of Patterned Retinal Activity in the Absence of Acetylcholine". In: *Journal of Neuroscience* **25** (2005), pp. 9347–9357.

[398] BK Stafford, A Sher, AM Litke, and DA Feldheim. "Spatial-Temporal Patterns of Retinal Waves Underlying Activity-Dependent Refinement of Retinofugal Projections". In: *Neuron* **64** (2009), pp. 200–212.

[399] W Stammer. *Analysis of the Structure and Dynamics of Cortical Spontaneous Activity*. Tech. rep. 2018, Master Thesis.

[400] NA Steinmetz, C Koch, KD Harris, and M Carandini. "Challenges and opportunities for large-scale electrophysiology with Neuropixels probes." In: *Current opinion in neurobiology* **50** (2018), pp. 92–100.

[401] D Stellwagen and CJ Shatz. "An instructive role for retinal waves in the development of retinogeniculate connectivity". In: *Neuron* **33** (2002), pp. 357–367.

[402] D Stellwagen, CJ Shatz, and MB Feller. "Dynamics of retinal waves are controlled by cyclic AMP". In: *Neuron* **24** (1999), pp. 673–685.

[403] GS Stent. "A Physiological Mechanism for Hebb's Postulate of Learning". In: *Proceedings of the National Academy of Sciences* **70** (1973), pp. 997–1001.

[404] P Sterling. “Microcircuitry of the cat retina”. In: *Annual Review of Neuroscience* **6** (1983), pp. 149–185.

[405] KJ Stratford, K Tarczy-Hornoch, KAC Martin, NJ Bannister, and JJB Jack. “Excitatory synaptic inputs to spiny stellate cells in cat visual cortex”. In: *Nature* **382** (1996), pp. 258–261.

[406] C Stringer, M Pachitariu, N Steinmetz, M Carandini, and KD Harris. “High-dimensional geometry of population responses in visual cortex”. In: *Nature* **571** (2019), pp. 361–365.

[407] C Stringer, M Pachitariu, N Steinmetz, CB Reddy, M Carandini, and KD Harris. “Spontaneous behaviors drive multidimensional, brainwide activity.” In: *Science* **364** (2019), p. 100.

[408] SM Stringer, ET Rolls, TP Trappenberg, and IET De Araujo. “Self-organizing continuous attractor networks and path integration: One-dimensional models of head direction cells”. In: *Network: Computation in Neural Systems* **13** (2002), pp. 217–242.

[409] C Sun, CM Speer, GY Wang, B Chapman, and LM Chalupa. “Epibatidine application in vitro blocks retinal waves without silencing all retinal ganglion cell action potentials in developing retina of the mouse and ferret.” In: *Journal of neurophysiology* **100** (2008), pp. 3253–63.

[410] M Sur and CA Leamey. “Development and plasticity of cortical areas and networks”. In: *Nature Reviews Neuroscience* **2** (2001), pp. 251–262.

[411] NV Swindale. “A model for the formation of ocular dominance stripes.” In: *Proc R Soc Lond B Biol Sci.* **208** (1980), pp. 243–264.

[412] NV Swindale. “A model for the formation of orientation columns”. In: *Proc R Soc Lond B Biol Sci.* **215** (1982), pp. 211–230.

[413] NV Swindale, JA Matsubara, and MS Cynader. “Surface organization of orientation and direction selectivity in cat area 18.” In: *Journal of Neuroscience* **7** (1987), pp. 1414–1427.

[414] NV Swindale. “How Many Maps are there in Visual Cortex?” In: *Cerebral Cortex* **10** (2000), pp. 633–643.

[415] NV Swindale, D Shoham, A Grinvald, T Bonhoeffer, and M Hübener. “Visual cortex maps are optimized for uniform coverage”. In: *Nature Neuroscience* **3** (2000), pp. 822–826.

[416] MM Syed, S Lee, S He, and ZJ Zhou. “Spontaneous waves in the ventricular zone of developing mammalian retina.” In: *Journal of neurophysiology* **91** (2004), pp. 1999–2009.

[417] A Takeuchi and Si Amari. “Formation of topographic maps and columnar microstructures in nerve fields”. In: *Biological Cybernetics* **35** (1979), pp. 63–72.

[418] G Tamás, EH Buhl, and P Somogyi. “Massive autaptic self-innervation of GABAergic neurons in cat visual cortex.” In: *Journal of Neuroscience* **17** (1997), pp. 6352–6364.

[419] S Tanaka, J Ribot, K Imamura, and T Tani. “Orientation-restricted continuous visual exposure induces marked reorganization of orientation maps in early life.” In: *NeuroImage* **30** (2006), pp. 462–477.

[420] E Tang and DS Bassett. “Colloquium: Control of dynamics in brain networks”. In: *Reviews of Modern Physics* **90** (2018), p. 031003.

[421] H Taniguchi, M He, P Wu, S Kim, R Paik, K Sugino, D Kvitsani, Y Fu, J Lu, Y Lin, G Miyoshi, Y Shima, G Fishell, SB Nelson, and ZJ Huang. “A Resource of Cre Driver Lines for Genetic Targeting of GABAergic Neurons in Cerebral Cortex”. In: *Neuron* **71** (2011), pp. 995–1013. arXiv: NIHMS150003.

[422] SF Tavazoie and RC Reid. "Diverse receptive fields in the lateral geniculate nucleus during thalamocortical development". In: *Nature Neuroscience* **3** (2000), pp. 608–616.

[423] I Timofeev, F Grenier, M Bazhenov, T Sejnowski, and M Steriade. "Origin of Slow Cortical Oscillations in Deafferented Cortical Slabs". In: *Cerebral Cortex* **10** (2000), pp. 1185–1199.

[424] MK Transtrum, BB Machta, and JP Sethna. "Geometry of nonlinear least squares with applications to sloppy models and optimization". In: *Physical Review E* **83** (2011), p. 036701. arXiv: 1010.1449.

[425] MK Transtrum, BB Machta, KS Brown, BC Daniels, CR Myers, and JP Sethna. "Perspective: Sloppiness and emergent theories in physics, biology, and beyond". In: *Journal of Chemical Physics* **143** (2015). arXiv: 1501.07668v1.

[426] R Tremblay, S Lee, and B Rudy. "GABAergic Interneurons in the Neocortex: From Cellular Properties to Circuits". In: *Neuron* **91** (2016), pp. 260–292.

[427] TW Troyer, AE Krukowski, NJ Priebe, and KD Miller. "Contrast-Invariant Orientation Tuning in Cat Visual Cortex: Thalamocortical Input Tuning and Correlation-Based Intracortical Connectivity". In: *J Neuroscience* **18** (1998), pp. 5908–5927.

[428] M Tsodyks and T Sejnowski. "Associative memory and hippocampal place cells". In: *International Journal of Neural Systems* **6** (1995), pp. 81–86.

[429] M Tsodyks, T Kenet, A Grinvald, and A Arieli. "Linking spontaneous activity of single cortical neurons and the underlying functional architecture." In: *Science* **286** (1999), pp. 1943–1946.

[430] AM Turing. "The Chemical Basis of Morphogenesis". In: *Philosophical transactions of the Royal Society of London. Series B, Biological sciences* **237** (1952).

[431] H Van Der Loos and EM Glaser. "Autapses in neocortex cerebri: synapses between a pyramidal cell's axon and its own dendrites". In: *Brain Research* **48** (1972), pp. 355–360.

[432] SD Van Hooser, JAF Heimel, S Chung, SB Nelson, and LJ Toth. "Orientation selectivity without orientation maps in visual cortex of a highly visual mammal." In: *J Neuroscience* **25** (2005), pp. 19–28.

[433] C van Vreeswijk and H Sompolinsky. "Chaotic Balanced State in a Model of Cortical Circuits". In: *Neural Computation* **10** (1998), pp. 1321–1371.

[434] C van Vreeswijk and H Sompolinsky. "Chaos in neuronal networks with balanced excitatory and inhibitory activity." In: *Science* **274** (1996), pp. 1724–1726.

[435] AB Watson. "A formula for human retinal ganglion cell receptive field density as a function of visual field location." In: *Journal of vision* **14** (2014), pp. 1–17.

[436] M Weliky, WH Bosking, and D Fitzpatrick. "A systematic map of direction preference in primary visual cortex". In: *Nature* **379** (1996), pp. 725–728.

[437] M Weliky, LC Katz, and C Katz. "Correlational structure of spontaneous neuronal activity in the developing lateral geniculate nucleus in vivo." In: *Science* **285** (1999), pp. 599–604.

[438] G Westheimer, K Shimamura, and SP McKee. "Interference with line-orientation sensitivity." In: *Journal of the Optical Society of America* **66** (1976), pp. 332–8.

[439] LE White, DM Coppola, and D Fitzpatrick. "The contribution of sensory experience to the maturation of orientation selectivity in ferret visual cortex." In: *Nature* **411** (2001), pp. 1049–1052.

[440] LE White and D Fitzpatrick. “Vision and cortical map development.” In: *Neuron* **56** (2007), pp. 327–338.

[441] J Wielaard and P Sajda. “Extraclassical receptive field phenomena and short-range connectivity in V1”. In: *Cerebral Cortex* **16** (2006), pp. 1531–1545. arXiv: 0504027 [q-bio].

[442] J Wietek, JS Wiegert, N Adeishvili, F Schneider, H Watanabe, SP Tsunoda, A Vogt, M Elstner, TG Oertner, and P Hegemann. “Conversion of channelrhodopsin into a light-gated chloride channel”. In: *Science* **344** (2014), pp. 409–412.

[443] S Willadt, M Canepari, P Yan, LM Loew, and KE Vogt. “Combined optogenetics and voltage sensitive dye imaging at single cell resolution”. In: *Frontiers in Cellular Neuroscience* **8** (2014), p. 311.

[444] DE Wilson, B Scholl, and D Fitzpatrick. “Differential tuning of excitation and inhibition shapes direction selectivity in ferret visual cortex”. In: *Nature* **560** (2018), pp. 97–101.

[445] DE Wilson, GB Smith, AL Jacob, T Walker, J Dimidschstein, G Fishell, and D Fitzpatrick. “GABAergic Neurons in Ferret Visual Cortex Participate in Functionally Specific Networks”. In: *Neuron* **93** (2017), 1058–1065.e4.

[446] HR Wilson and JD Cowan. “A mathematical theory of the functional dynamics of cortical and thalamic nervous tissue”. In: *Biological Cybernetics* **13** (1973), pp. 55–80.

[447] HR Wilson and JD Cowan. “Excitatory and Inhibitory Interactions in Localized Populations of Model Neurons”. In: *Biophysical Journal* **12** (1972), pp. 1–24.

[448] J Winnubst, JE Cheyne, D Niculescu, and C Lohmann. “Spontaneous Activity Drives Local Synaptic Plasticity InVivo”. In: *Neuron* **87** (2015), pp. 399–411.

[449] ROL Wong and DM Oakley. “Changing patterns of spontaneous bursting activity of on and off retinal ganglion cells during development”. In: *Neuron* **16** (1996), pp. 1087–1095.

[450] ROL Wong. “Retinal Waves And Visual System Development”. In: *Annual Review of Neuroscience* **22** (1999), pp. 29–47.

[451] WT Wong, JR Sanes, and ROL Wong. “Developmentally regulated spontaneous activity in the embryonic chick retina.” In: *Journal of Neuroscience* **18** (1998), pp. 8839–8852.

[452] WT Wong, KL Myhr, ED Miller, and ROL Wong. “Developmental changes in the neurotransmitter regulation of correlated spontaneous retinal activity”. In: *J Neurosci* **20** (2000), pp. 351–360.

[453] HP Xu, M Furman, YS Mineur, H Chen, SL King, D Zenisek, ZJ Zhou, DA Butts, N Tian, MR Picciotto, and MC Crair. “An Instructive Role for Patterned Spontaneous Retinal Activity in Mouse Visual Map Development”. In: *Neuron* **70** (2011), pp. 1115–1127.

[454] HP Xu, TJ Burbridge, MG Chen, X Ge, Y Zhang, ZJ Zhou, and MC Crair. “Spatial pattern of spontaneous retinal waves instructs retinotopic map refinement more than activity frequency”. In: *Developmental Neurobiology* **75** (2015), pp. 621–640.

[455] X Xu, WH Bosking, LE White, D Fitzpatrick, and VA Casagrande. “Functional Organization of Visual Cortex in the Prosimian Bush Baby Revealed by Optical Imaging of Intrinsic Signals”. In: *J Neurophysiology* **94** (2005), pp. 2748–2762.

[456] X Xu, W Bosking, G Sáry, J Stefansic, D Shima, and VA Casagrande. “Functional organization of visual cortex in the owl monkey.” In: *J Neuroscience* **24** (2004), pp. 6237–6247.

[457] E Yacoub, N Harel, and K Ugurbil. “High-field fMRI unveils orientation columns in humans”. In: *Proceedings of the National Academy of Sciences* **105** (2008), pp. 10607–10612.

[458] JW Yang, IL Hanganu-Opatz, JJ Sun, and HJ Luhmann. "Three Patterns of Oscillatory Activity Differentially Synchronize Developing Neocortical Networks In Vivo". In: *Journal of Neuroscience* **29** (2009), pp. 9011–9025.

[459] JW Yang, S An, JJ Sun, V Reyes-Puerta, J Kindler, T Berger, W Kilb, and HJ Luhmann. "Thalamic network oscillations synchronize ontogenetic columns in the newborn rat barrel cortex". In: *Cerebral Cortex* **23** (2013), pp. 1299–1316.

[460] R Yuste, DA Nelson, WW Rubin, and LC Katz. "Neuronal domains in developing neocortex: Mechanisms of coactivation". In: *Neuron* **14** (1995), pp. 7–17.

[461] N Zeater, SK Cheong, SG Solomon, B Dreher, and PR Martin. "Binocular Visual Responses in the Primate Lateral Geniculate Nucleus". In: *Current Biology* **25** (2015), pp. 3190–3195.

[462] AJ Zhang and SM Wu. "Receptive Fields of Retinal Bipolar Cells Are Mediated by Heterogeneous Synaptic Circuitry". In: *Journal of Neuroscience* **29** (2009), pp. 789–797.

[463] J Zhang, JB Ackman, HP Xu, and MC Crair. "Visual map development depends on the temporal pattern of binocular activity in mice". In: *Nature Neuroscience* **15** (2012), pp. 298–307.

[464] K Zhang. "Representation of Spatial Orientation by the Intrinsic Dynamics of the Head-Direction Cell Ensemble: A Theory". In: *The Journal of Neuroscience* **16** (1996), pp. 2112–2126.

[465] JJ Zheng, ZJ Zhou, and S Lee. "A developmental switch in the excitability and functionality of the starburst network in the mammalian retina". In: *Neuron* **44** (2004), pp. 851–864.

[466] JJ Zheng, S Lee, and ZJ Zhou. "A transient network of intrinsically bursting starburst cells underlies the generation of retinal waves". In: *Nature Neuroscience* **9** (2006), pp. 363–371.

[467] K Zipser, Va Lamme, and PH Schiller. "Contextual modulation in primary visual cortex." In: *Journal of Neuroscience* **16** (1996), pp. 7376–7389.

[468] E Zohary, MN Shadlen, and WT Newsome. "Correlated neuronal discharge rate and its implications for psychophysical performance". In: *Nature* **370** (1994), pp. 140–143.